

MICROMECHANICAL SIMULATIONS OF HEART VALVE TISSUES

by

Hsiao-Ying Shadow Huang

BEng, National Chung-Hsing University, Taiwan, 1995

MS, University of Pittsburgh, 1997

Submitted to the Graduate Faculty of

The School of Engineering in partial fulfillment

of the requirements for the degree of

Doctor of Philosophy

University of Pittsburgh

2004

UNIVERSITY OF PITTSBURGH
SCHOOL OF ENGINEERING

This dissertation was presented

by

Hsiao-Ying Shadow Huang

It was defended on

January 06, 2004

and approved by

Anne M. Robertson, Associate Professor, Department of Mechanical Engineering

William S. Slaughter, Associate Professor, Department of Mechanical Engineering

Patrick Smolinski, Associate Professor, Department of Mechanical Engineering

David A. Vorp, Associate Professor, Department of Bioengineering

Dissertation Director: Michael S. Sacks, Associate Professor, Department of Bioengineering

Copyright by Hsiao-Ying Shadow Huang

© 2004

ABSTRACT

MICROMECHANICAL SIMULATIONS OF HEART VALVE TISSUES

Hsiao-Ying Shadow Huang, PhD

University of Pittsburgh, 2004

Heart valve disease is generally treated by surgical replacement with either a mechanical or bioprosthetic valve. While prosthetic valves perform remarkably well, having significantly reduced patient mortality since their inception in 1960, each type exhibits specific drawbacks. Specifically, thrombosis and anticoagulation in the case of mechanical valves; calcific and fatigue-related degeneration in bioprosthetic heart valve (BHV). In attempt to improve the durability of BHV, recent studies have focused on quantifying the biomechanical interactions between the organ, tissue, and cellular-level components in native heart valve and BHV tissues. Such data is considered fundamental to designing improved BHV, and ultimately may be useful in the design of tissue engineered heart valves (TEHV).

The goals of this research were two-fold: (1) to simulate layer-specific mechanical property changes incurred by the porcine BHV with fatigue, and (2) to simulate the cellular-level deformation of valve interstitial cells (VIC) nuclei under organ-level transvalvular pressures. For the first goal, parametric studies were conducted to isolate the effective moduli of the individual layers using finite element simulations of native and BHV tissues in flexure. The finite element simulations isolated fatigue-related changes in the overall effective modulus of

BHV tissues specifically to the collagen-rich fibrosa layer. These results may be useful in designing improved BHV, as novel fixatives and fixation methods may have the capacity to target specific layers of the BHV tissue.

For the second goal, cellular-level VIC nuclei deformations were quantified experimentally by analyzing images of histological sections prepared from native porcine aortic valves subjected to transvalvular pressures. Finite element simulations were conducted to quantify the relationship between organ-level transvalvular pressure, concomitant tissue-level strain, and ultimate cellular-level VIC nuclei deformation. The cellular-level image analysis studies uncovered layer-specific, positive relationships between VIC nuclei deformations and transvalvular pressure. These data were found to correlate with previously published data on the associated collagen fiber architecture, providing insight into the tissue-to-cellular level mechanical coupling predicted by the finite element simulations. These results may be useful in designing TEHV, as evidence suggests that the secretion and organization of extracellular matrix (ECM) (e.g., collagen) by the constituent cells of a TEHV can be modulated by mechanical deformation.

To the best of our knowledge, the simulations presented herein represent the first attempt to quantify layer-specific changes in porcine BHV tissue mechanical properties with fatigue. Moreover, we report the first information on the cellular-level deformation of VIC nuclei under transvalvular pressures, including experimental analysis of the native porcine aortic valve, as well as rigorous finite element simulations. These micromechanical simulations thus offer new data on the biomechanical behavior of heart valve tissues, and may contribute to the design of improved BHV and TEHV.

TABLE OF CONTENTS

ABSTRACT	IV
LIST OF TABLES	XI
LIST OF FIGURES	XIV
PREFACE	XXII
ACRONYMS	XXIV
NOMENCLATURE	XXV
1.0 INTRODUCTION	1
1.1 STRUCTURE, FUNCTION AND MECHANICAL PROPERTIES OF THE NATIVE AORTIC VALVE.....	3
1.1.1 Heart Anatomy.....	3
1.1.2 Valvular Anatomy.....	5
1.1.3 Fluid Dynamics.....	8
1.1.4 Tissue Structure and Composition.....	10
1.1.5 Mechanical Properties of Native Valve Tissue.....	12
1.1.6 Valvular Cells.....	16
1.2 AORTIC VALVE FUNCTION: A MULTI-SCALE BIOMECHANICS PROBLEM.....	20
1.2.1 Organ – Level.....	21
1.2.2 Tissue – Level.....	23

1.2.3	Cell – Level.....	25
1.3	HEART VALVE DISEASE.....	26
1.3.1	General Description and Statistics.....	26
1.3.2	Therapy for Aortic Valve Dysfunction.....	29
1.4	CURRENTLY AVAILABLE REPLACEMENT HEART VALVES.....	29
1.4.1	Mechanical Valves.....	30
1.4.2	Bioprosthetic Heart Valves.....	33
1.5	MECHANICAL PROPERTIES OF PORCINE BIOPROSTHETIC HEART VALVE.....	41
1.5.1	Effects of Chemical Treatment.....	41
1.5.2	Effects of Flex Fatigue.....	49
1.5.3	Limitations of Current Knowledge.....	53
1.6	ALTERNATIVELY HEART VALVE REPLACEMENTS: BIOHYBRID AND TISSUE ENGINEERING APPROACHES.....	54
1.6.1	Biohybrid Approaches.....	54
1.6.2	Tissue Engineering Approaches.....	56
1.6.3	Mayer Approach.....	57
1.6.4	Decellularized Approaches.....	57
1.6.5	Current Limitations of Tissue Engineered Heart Valve Approaches.....	58
1.7	NEED FOR MICROMECHANICAL MODELING OF THE HEART VALVE TISSUES.....	59
1.8	CURRENT STATE OF BIOMECHANICAL STUDIES OF EXTRACELLULAR MATRIX.....	61
1.8.1	Interaction of Extracellular Matrix and Cell.....	61
1.8.2	Constitutive Models of Soft Tissues.....	69

1.8.3	Constitutive Model of the Heart Valve Tissue	70
1.8.4	Numerical Studies of the Heart Valve Tissues	72
1.8.5	Limitations	75
1.9	MOTIVATION AND SPECIFIC CONTRIBUTION OF PRESENT STUDY	77
2.0	MODELING THE FLEXURAL BEHAVIOR OF THE NATIVE AORTIC AND THE PORCINE BIOPROSTHETIC HEART VALVE LEAFLET	79
2.1	OVERVIEW OF THE FINITE ELEMENT IMPLEMENTATION	79
2.1.1	Nonlinear Finite Element Modeling of Heart Valve Tissue Leaflet Flexural Behavior.....	80
2.1.2	User-Defined Material Properties	81
2.2	METHODS	83
2.2.1	Composite Model Development	84
2.2.2	Flexural Mechanical Behavior of Native Aortic Valve Leaflet.....	89
2.2.3	Flexural Mechanical Behavior of Porcine Bioprosthetic Heart Valve Leaflet	90
2.2.4	Changes in the Flexural Behavior of the Porcine Bioprosthetic Heart Valve with Fatigue.....	94
2.3	RESULTS	99
2.3.1	Validation of User-Defied Material Properties.....	99
2.3.2	Flexural Behavior of the Porcine Bioprosthetic Heart Valve	101
2.3.3	Flexural Behavior of the Porcine Bioprosthetic Heart Valve with Fatigue.....	105
2.4	SUMMARY	109
3.0	GEOMETRIC CHANGES IN HEART VALVE INTERSTITIAL CELL NUCLEI DUE TO TRANSVALVULAR PRESSURE.....	112
3.1	METHODS	113

3.1.1	Database and Specimen Preparation	113
3.1.2	Image Processing	118
3.1.3	Statistical Analyses	126
3.2	RESULTS	130
3.2.1	Aspect ratio of Valve Interstitial Cell Nuclei	130
3.2.2	Intra-Section and Intra-Slide Variability	131
3.2.3	Results of Intra-Pressure and Inter-Pressure Variability	135
3.2.4	Distribution of Nuclei Aspect Ratio	138
3.2.5	The Relationship of Nuclei Aspect Ratio and Collagen Fiber Architecture.....	145
3.3	SUMMARY.....	149
4.0	SIMULATION THE EFFECT OF TRANSVALVULAR PRESSURE ON THE VALVE INTERSTITIAL CELL NUCLEI GEOMETRY.....	152
4.1	MODEL DEVELOPMENT I: STRESS STATE OF HEART VALVE LEAFLET	152
4.2	FINITE ELEMENT MICROSCOPIC MODEL FORMULATION.....	157
4.2.1	Multi-Scale Modeling Considerations	157
4.2.2	Finite Element Simulations of the Interactions of Extracellular Matrix and Valve Interstitial Cell Nucleus	160
4.2.3	Material Moduli for the Valve Interstitial Cell and Extracellular Matrix.....	162
4.2.4	Predicted Aspect Ratios of Valve Interstitial Cell Nuclei	165
4.3	RESULTS	167
4.3.1	Parameter Values and Single Element Test.....	167
4.3.2	Effects of Valve Interstitial Cell Nucleus Material Property.....	172
4.3.3	Effects of Valve Interstitial Cell Nucleus Initial Geometry.....	174

4.3.4	Local Mechanical Environment of Valve Interstitial Cell Nucleus.....	179
4.4	SUMMARY.....	183
5.0	CONCLUSIONS AND FUTURE STUDIES.....	186
5.1	MODELING THE FLEXURAL BEHAVIOR OF PORCINE BHV TISSUES	186
5.1.1	Summary.....	186
5.1.2	Relation to Other Studies.....	187
5.1.3	Recommendations for Future Studies.....	188
5.2	GEOMETRIC CHANGES IN HEART VALVE INTERSTITIAL CELL NUCLEUS.....	189
5.2.1	Summary.....	189
5.2.2	Implications.....	191
5.2.3	Recommendations for Future Studies.....	194
	APPENDIX A: NONLINEAR FINITE ELEMENT SOLUTION PROCEDURE.....	197
	APPENDIX B: TRANSMURAL SURFACE STRAIN DURING BENDING.....	200
	APPENDIX C: PHOTOMICROGRAPH OF HISTOLOGY SECTIONS.....	205
	APPENDIX D: INTRA-SLIDE AND INTRA-PRESSURE VARIABILITY.....	229
	APPENDIX E: CALCULATION OF NUCLEI ASPECT RATIOS.....	239
	APPENDIX F: LOCAL MECHANICAL ENVIRONMENT OF VIC NUCLEI.....	241
	BIBLIOGRAPHY.....	244

LIST OF TABLES

Table Number		Page
Table 1-1	Material properties of the studies in the interaction of microscopic and microscopic models, in Which E represents elastic moduli, G represents shear moduli, and ν is Poisson's ratio.	64
Table 1-2	Micromechanical studies by other researchers: (a) Intervertebral disc (IVD), ⁽⁹⁵⁻⁹⁸⁾ (b) tissue equivalents (TEs), ⁽¹⁰⁴⁻¹⁰⁶⁾ (c) representative volume element (RVE). ^(100, 101, 107)	76
Table 2-1	Three different classes material property of the composite beam models based on the previous experimental findings (Figure 1-22). ⁽⁶⁶⁾	87
Table 2-2	Parametric study of chemical-treated uncycled porcine BHV leaflet flexural behavior.....	93
Table 2-3	Parametric study of different combinations of tensile and compressive moduli in AC and WC bending directions for uncycled flexural models. E represents the layer moduli, superscripts T and C represent tensile and compressive moduli, subscripts F and V represent the fibrosa and the ventricularis layer, A is the ratio of the tensile moduli to the compressive moduli in the fibrosa layer, and B is the ratio of the tensile moduli to the compressive moduli in the ventricularis layer, respectively.	94
Table 2-4	The M/I vs. $\Delta\kappa$ relationship of 200 million-cycles in AC and WC bending directions of fatigued porcine BHV. ^(3, 68)	95
Table 2-5	The material constants of the stiffness in the AC and BC bending directions of fatigued porcine BHV leaflet.....	96
Table 2-6	Parametric study of fatigued porcine BHV leaflet flexural behavior.	97
Table 2-7	A comparison of experimental effective stiffness to the individual layer moduli finite element results of the uncycled porcine BHV.....	101

Table 2-8	A comparison of effective stiffness of experimental results from equation (2.9) and (2.10) to the individual layer moduli finite element results of the fatigued porcine BHV at 200 million-cycles.	106
Table 2-9	Finite element results of layer moduli: the fatigued porcine BHV model (200 million cycles) predicted an approximately 50 % drop in AC bending direction (370 kPa to 180 kPa), with no substantial change in the WC bending direction (123.4 kPa to 132 kPa).....	109
Table 2-10	A summary of finite element results of individual layer moduli and addition information were presented in Table 2-7, Table 2-8, equations (2.9) and (2.10). Linear bi-modular stress-strain relationship was presented in black for uncycled BHV, and non-linear bi-modular stress-strain relationship was presented in red for fatigued BHV.....	111
Table 3-1	Summary of histological specimen database.	118
Table 3-2	Summary of statistical study performed to correlate the effects of transvalvular pressure on VIC nuclei dimensions from the available histological specimen database (Table 3-1). Study (1): the intra-image variability, study (2) the intra-section variability, study (3) the intra-slide variability, study (4) the intra-pressure variability, and study (5) the inter-pressure variability.....	127
Table 3-3	Calculated number of degrees of freedom of slide (DF_{slide}), the number of degrees of freedom of section (slide) ($DF_{section(slide)}$), and the number of degrees of freedom of error (DF_{error}) from the specimen database.	129
Table 3-4	Calculated $DF_{pressure}$, $DF_{slide(pressure)}$, $DF_{section(slide)}$, and DF_{error} from the specimen database.....	130
Table 3-5	Statistical results of ANOVA table for intra-slide and intra-section variability.	133
Table 3-6	Results from the ANOVA table and F-table for intra-slide and intra-pressure variability.	134
Table 3-7	Statistical results of ANOVA table for inter-pressure variability.....	137
Table 3-8	Results from ANOVA table and F-table for inter-pressure variability.....	137
Table 3-9	Calculation the VIC nuclei aspect ratio and its corresponding area under 0 mmHg	142
Table 3-10	Calculation the VIC nuclei aspect ratio and the corresponding areas under 4 mmHg and 90 mmHg pressure levels.....	144

Table 4-1	Loading conditions for finite element simulations under all transvalvular pressure levels.....	161
Table 4-2	Material property of the VIC nucleus, in which E represents elastic moduli in MPa, G represents shear moduli in MPa, and ν represents Poisson ratio.....	162
Table 4-3	Seven parameters of the Fung elastic constitutive model with convexity constraint: $c > 0$, $A_1 > A_3 $, $A_2 > A_3 $ and $A_1A_2A_4 + 2A_3A_6A_5 - A_5^2A_2 - A_6^2A_1 - A_3^2A_4 > 0$	167
Table 4-4	LEHI circular VIC nucleus microscopic model: results of the major axis lengths in the circumferential, radial, and transmural directions, calculation of aspect ratio and percent change in aspect ratio under 6 different pressure levels.	173
Table 4-5	LEHI elliptic VIC nucleus microscopic model: results of the major axis lengths in the circumferential, radial, and transmural directions, calculation of aspect ratio and percent change in aspect ratio under 6 different pressure levels.	174
Table 4-6	The differences of the percent change in aspect ratio (%) from the elliptic and circular VIC nucleus microscopic models to the experimental measured VIC nucleus percent change in aspect ratio.....	177
Table 4-7	Calculations of volume of two microscopic models under different pressure levels, in which all units in μm	178
Table 4-8	Stretches at the interface of the VIC nucleus and ECM and the stretches at the boundary of the elliptic microscopic model at 90mmHg pressure levels.....	185

LIST OF FIGURES

Figure Number		Page
Figure 1-1	Schematic of the heart showing its valves and chambers (image courtesy of the Mayo Foundation for Medical Education and Research: http://www.mayoclinic.com).	4
Figure 1-2	The normal tri-leaflet aortic valve is viewed from above in an intact aorta (image courtesy of the Mayo Foundation for Medical Education and Research: http://www.mayoclinic.com).	5
Figure 1-3	Schematic presentation of an aortic valve opened by a vertical incision through the noncoronary sinus. L, R, and N are the left, right and noncoronary leaflets, respectively. The dotted line is the line of leaflet coaptation (image courtesy of Thubrikar ⁽⁷⁾).	7
Figure 1-4	A schematic representation of a cross-section of the layered structure of the aortic leaflets. The relative proportions of the fibrosa (F), spongiosa (S), and ventricularis (V) are shown along with their major components.....	11
Figure 1-5	Actual (left panel) and a schematic (right panel) biaxial testing setup.....	14
Figure 1-6	The smaller circumferential strains were observed than the radial strains in the native aortic valve (adapted from Billiar and Sacks ⁽¹⁹⁾).	15
Figure 1-7	A micrograph of aortic valve surface stained in red for endothelial cells and stained in green for nuclei (image courtesy of Leask, <i>et al.</i> ⁽²⁸⁾)	17
Figure 1-8	A micrograph of aortic valve surface stained in blue for collagen fibers and stained in black for valve interstitial cell nuclei (image courtesy of Sacks <i>et al.</i> ⁽²⁹⁾).	18
Figure 1-9	A schematic of the role of biomechanics in aortic valve function, which occurs at multiple structural levels. At each structural level, biomechanics plays a functionally critical role.....	21

Figure 1-10	Two-dimensional schematic depicting blood flow streamlines in the aortic valve during peak systole. Note the junction between the aortic root, one leaflet, and one sinus (A). The vortical flow patterns generated in the sinus (B) assist in valve closure. Two organ-level structural features of the aortic valve are the circular sinotubular junction (C) and the nodulus (D).....	22
Figure 1-11	Two dimensional schematic depicting collagen fiber rotation (A to B) and un-crimping (B to C) during aortic valve closure and coaptation, respectively.	25
Figure 1-12	Arrow denotes scar tissue due to rheumatic fever (image courtesy of Dr. Richard B. Roberts of Cornell medical school).....	27
Figure 1-13	A buildup of calcium deposits on the aortic valve may lead to a narrowing of the valve, i.e. calcific aortic stenosis (image courtesy of the Mayo Foundation for Medical Education and Research: http://www.mayoclinic.com).....	28
Figure 1-14	Mechanical valve (image courtesy of Edwards Life Sciences: http://www.edwards.com).....	32
Figure 1-15	Stented porcine BHV (image courtesy of Edward Life Science: http://www.edwards.com/site).....	34
Figure 1-16	SALS device was used to quantitatively assess tissue fiber architecture.	39
Figure 1-17	A representative resultant angular distribution of scattered light intensity about the laser axis.....	39
Figure 1-18	SALS image of clinically explanted porcine BHV and x-ray image of calcified BHV.	40
Figure 1-19	Example of the bending experimental set-up. The rectangular (~0.75 mm x ~12 mm) strip of specimen was positioned between two posts and forced into three-point bending at the center.....	44
Figure 1-20	Schematic of heart valve tissue bending against (AC) and with (WC) the natural curvature of the leaflet. When the sample was bending in the AC direction, the fibrosa (F) was in tension and the ventricularis (V) was in compression, where S represents spongiosa. When the sample was bending in the WC direction, the ventricularis was in tension and the fibrosa was in compression.	45
Figure 1-21	Representative force measurement under the three-point bending test.	46
Figure 1-22	A representative M/I vs. $\Delta\kappa$ curve for native aortic valve leaflet demonstrated a linear response over the full range of flexure in both AC and WC directions. In contrast, and uncycled porcine BHV demonstrated a	

	profound bending direction dependent increase in stiffness in AC and WC directions. After 200×10^6 cycles, the AC direction stiffness dropped substantially (adapted from Sacks, <i>et al.</i> ^(3, 68)).	48
Figure 1-23	M/I versus $\Delta \kappa$ curve have different flexural behaviors at different cycles, and at 200 million-cycles leaflet demonstrated a non-linear response over the full range of flexure.	51
Figure 1-24	Changes in E_{eff} with the number of fatigue cycles (N) in the AC and WC bending direction, * = statistically significant ($p < 0.05$) different from 0 cycles. A substantial drop in stiffness with N was found only in the AC direction, with no statistically significant changes occurring in the WC direction (adapted from Sacks <i>et al.</i> ⁽⁶⁸⁾).	52
Figure 1-25	The multi-scale and axisymmetric finite element mesh (adapted from Baer, <i>et al.</i> ⁽⁹⁹⁾).	63
Figure 1-26	(a) RVE with one hole, representing a regular structure, and (b) ten random RVEs (adapted from Kouznetsova <i>et al.</i> ⁽¹⁰⁰⁾).	65
Figure 1-27	TE microscopic model was showed above, and macroscopic modes were shown by solid circles. ⁽¹⁰⁴⁾	66
Figure 1-28	Finite element models of muscle tissue (left panel) and myoblasts (right panel). ⁽¹⁰⁸⁾	68
Figure 1-29	The structural model is able to fully simulate the highly anisotropic and nonlinear in-plane biaxial mechanical behavior. ^(19, 116)	72
Figure 2-1	A flow chart for finite element implementation of solution-dependent variables.	82
Figure 2-2	Schematic diagram of the Cartesian coordinate representation of a two-layer porcine BHV specimen composite beam model.	84
Figure 2-3	Boundary conditions for the bi-layer composite beam model required to simulate the flexural behavior under three point bending, in which E_1 and E_2 represent different linear, or non-linear layer moduli.	85
Figure 2-4	The boundary conditions of the composite beam models were required to deflect 2.3 mm on the center of the beam in the AC bending direction and 0.95 mm in the WC bending direction based on the previous experiments. ⁽⁶⁶⁾	86
Figure 2-5	Class 1: The schematic analysis method for uni-modular, uni-layer and bi-layer composite beam models of native aortic valve leaflet under three-point bending in WC direction. Uni-modular, uni-layer and bi-layer composite	

	beams under three-point bending in AC direction were simulated but not shown in this figure.....	90
Figure 2-6	Class 2: The schematic analysis method for linear bi-modular, uni-layer and bi-layer composite beam models of porcine BHV leaflets under three-point bending in WC direction. Linear bi-modular, uni-layer and bi-layer composite beam under three-point bending in AC direction were simulated but not shown in this figure.....	91
Figure 2-7	Class 3: The schematic analysis method for non-linear bi-modular bi-layer composite beam models of fatigued porcine BHV leaflet under WC three-point bending direction. Non-linear bi-modular bi-layer composite beam under AC bending direction were simulated but not shown in this figure.	98
Figure 2-8	Custom code validation: the stress-strain relationship in a linear bi-modular composite beam model (Figure 2-6: A). The result of stress-strain relationship generated from the finite element solver verified custom coded material property ($E^T = 216$ kPa, $E^C = 72$ kPa, and $E^T = 3E^C$).	100
Figure 2-9	A comparison of the M/I vs. $\Delta\kappa$ curves from experimental data ^(3, 68) to the finite element results of the uncycled porcine BHV in both WC and AC bending directions ($r^2 = 0.962$ in AC bending direction and $r^2 = 0.96$ in WC bending direction).	102
Figure 2-10	The neutral axis shift for the composite beam model was from 0.5 to 0.74 in the AC bending direction, and the corresponding transmural strain distributions were showed above.....	103
Figure 2-11	The neutral axis shift for the composite beam model was from 0.5 to 0.57 in the WC bending direction, and the corresponding transmural strain distributions were showed above.....	104
Figure 2-12	From the experimental data, the neutral axis shifted from 0.54 to 0.64 in WC direction and from 0.54 to 0.84 in AC direction (sample size $n = 1$). The neutral axis shift for the composite beam models were from 0.5 to 0.57 in the WC direction, and from 0.5 to 0.74 in the AC direction (sample size $n = 1$).	105
Figure 2-13	Comparison of the M/I vs. $\Delta\kappa$ curves from experimental data ^(3, 68) to the finite element results of the fatigued porcine BHV in the AC bending direction ($r^2 = 0.852$) at 200-million cycles.	107
Figure 2-14	Comparison of the M/I vs. $\Delta\kappa$ curves from experimental data ^(3, 68) to the finite element results of the fatigued porcine BHV in the WC bending direction ($r^2 = 0.855$) at 200 million cycles.....	108

Figure 3-1	Three-dimensional native aortic valve tissue was prepared for two different cross-sectional specimens (center panel). In the left panel, radial-transmural cross-section was used, and in the right panel, circumferential-transmural cross-section was used for measuring the geometry of the VIC nuclei.	114
Figure 3-2	Hematoxylin and Eosin (H & E) and Masson stained the VIC nuclei all in black, and collagen in pink and blue, respectively.	115
Figure 3-3	A total of forty-eight slides of native aortic valve leaflets were prepared, covering 0, 1, 2, 4, 60, 90 mmHg transvalvular pressure levels. Each pressure level included eight slides, and each slide contained three sections (all sections prepared but not showed in the figure above), and five photomicrographs of histology sections were digitized for each section (all images for each section were digitized as shown in the dash-box).	116
Figure 3-4	Section was prepared including three layers of the aortic leaflet: fibrosa, spongiosa, and ventricularis transmurally. Five photomicrographs were digitized circumferentially for each section, and each image covered all three layers of the aortic valve.	117
Figure 3-5	A panoramic image was created by 4-5 over lapped images to cover all three layers transmurally. In order to achieve the best quality of the panoramic image, 50-70% range of over-lapping was required.	119
Figure 3-6	Sample of five panoramic photomicrographs in 0 mmHg along circumferential direction for one section.	120
Figure 3-7	A sample image of VIC nuclei inside the tissue under 90 mmHg was digitized by SigmaScan (SPSS, Inc. Chicago, Il). Local coordinates, the major-, minor-axis lengths, slope, area of deformed VICs were generated by the imaging software.	122
Figure 3-8	One sample image of VIC nuclei inside the tissue under 90mmHg transvalvular pressure and was prepared including three layers of the aortic leaflet: fibrosa, spongiosa, and ventricularis. Local coordinates were used for calculating the normalized thickness from ventricularis layer to fibrosa layer. A representative length of 10 μm was also shown above.	123
Figure 3-9	A schematic of a hypothesized prolate ellipsoidal cellular geometry in circumferential, radial, and transmural directions.	124
Figure 3-10	A schematic of a deformed VIC nucleus where major axis length = $2a$, and minor axis length = $2b$. From the given data, the moment of inertia of the deformed VIC nucleus was then calculated. ⁽¹⁴⁵⁾	125

Figure 3-11	A comparison of the VIC nuclei aspect ratios under six pressure levels. The barbells (●—●) indicate inter-pressure statistical differences, which were found everywhere except 0- and 1-mmHg, 2- and 4-mmHg, and 60- and 90-mmHg (ANOVA, $p < 0.001$).....	131
Figure 3-12	A representative results of cellular nuclei aspect ratio study of intra-slide variability under 0 mmHg pressure level, and the barbells (●—●) indicates statistical differences ($p < 0.05$).....	132
Figure 3-13	A representative results of cellular nuclei aspect ratios study of intra-pressure variability under 0 mmHg pressure level, and the barbells (●—●) indicates statistical differences ($p < 0.05$).....	136
Figure 3-14	Aspect ratios of cellular nuclei vs. normalized thickness for all the cellular nuclei data at zero-, low- and high-pressure levels. Statistically significant differences were found everywhere by comparing the VIC nuclei aspect ratios at 4 and 90 mmHg to those at 0 mmHg pressure levels. Statistically significant different were found everywhere by comparing the VIC nuclei aspect ratios at 4 mmHg to those at 90 mmHg. “N.S.” indicates no statistically significant differences ($p < 0.05$).....	139
Figure 3-15	Area of cellular nuclei vs. normalized thickness for all the cellular nuclei data for zero-, low- and high-pressure levels, in which (*) indicates statistically significant differences were found by comparing the VIC nuclei areas under 4 and 90 mmHg to those under 0 mmHg ($p < 0.05$).....	141
Figure 3-16	An schematic cellular deformation indicated that under the 0 mmHg pressure level, elongation of the cellular nuclei (aspect ratio from 1.75 to 2.25) along the normalized thickness (from 0.25 to 0.85) was found while the area of the cellular nuclei remained constant (area $\approx 18 \mu\text{m}^2$).	143
Figure 3-17	Orientation Index vs. transvalvular pressure, and VIC nuclei aspect ratio vs. transvalvular pressure. A trend was found associated with the fiber orientation and the deformed VIC nuclei aspect ratio.	146
Figure 3-18	VIC nuclei aspect ratio vs. OI in the ventricular layer.	148
Figure 3-19	VIC nuclei aspect ratio vs. OI in the fibrosa layer.....	148
Figure 3-20	The relationship of physiological transvalvular pressure measured <i>in vivo</i> and the corresponding VIC nuclei aspect ratios at a specific time point during valve operation. The VIC nuclei aspect ratios with consistent areas increased with the increasing transvalvular pressure.....	150
Figure 4-1	The heart valve leaflets are subjected to a uniform tension at the edge and a uniform lateral pressure. p represents the pressure per unit area of the	

	membrane and T represents the uniform traction per unit length of its boundary.	155
Figure 4-2	Finite element microscopic model of one circular VIC nucleus within its ECM.	158
Figure 4-3	The finite element microscopic model with elliptic VIC nucleus was showed above.	160
Figure 4-4	A representative undeformed, deformed circular and elliptic VIC nuclei finite element models, in which A, B, C, and D are the local coordinates at the interface of the VIC nuclei and ECM.	166
Figure 4-5	Results of the Fung elastic constitutive model with seven parameters under equal biaxial loading conditions (circumferential loading : radial loading = 1:1) and agreements were observed in the circumferential ($r^2 = 0.9832$) and radial directions ($r^2 = 0.9948$).	168
Figure 4-6	Results of the Fung elastic constitutive model with seven parameters under loading conditions of circumferential loading : radial loading = 1.5:1. Agreements were observed in the circumferential ($r^2 = 0.9913$) and radial directions ($r^2 = 0.9927$).	168
Figure 4-7	Results of the Fung elastic constitutive model with seven parameters under loading conditions of circumferential loading : radial loading = 2:1. Agreements were observed in the circumferential ($r^2 = 0.9936$) and radial directions ($r^2 = 0.9883$).	169
Figure 4-8	Results of the Fung elastic constitutive model with seven parameters under loading conditions of circumferential loading : radial loading = 2.5:1. Agreements were observed in the circumferential ($r^2 = 0.9946$) and radial directions ($r^2 = 0.9867$).	169
Figure 4-9	Results of the Fung elastic constitutive model with seven parameters under loading conditions of circumferential loading : radial loading = 3:1. Agreements were observed in the circumferential ($r^2 = 0.9948$) and radial directions ($r^2 = 0.9907$).	170
Figure 4-10	Results of the Fung elastic constitutive model with seven parameters under different biaxial loading conditions and agreements were observed in the circumferential ($r^2 = 0.9915$) and radial directions ($r^2 = 0.9906$) under different loading conditions.	170
Figure 4-11	A representative stress-strain relationship of single element test results under the equibiaxial loading condition comparing to the experimental data and the	

	constitutive model ($r^2 = 0.71$ and $r^2 = 0.72$ in the circumferential and radial directions, respectively).....	171
Figure 4-12	Parametric studies of varying the VIC nuclei material properties, and a comparison of percent change in the aspect ratio (%) versus different pressure levels was showed above.	173
Figure 4-13	A comparison of VIC nucleus aspect ratios measured experimentally and calculated form the finite element simulations.	175
Figure 4-14	A comparison of percent change in aspect ratio (%) measured experimentally and calculated form the finite element simulations.	177
Figure 4-15	Stress distributions in the circumferential and radial directions of the circular VIC nucleus microscopic model under 90 mmHg transvalvular pressure were showed above.....	180
Figure 4-16	Strain distributions in the circumferential and radial directions of the circular VIC nucleus microscopic model under 90 mmHg transvalvular pressure were showed above.....	181
Figure 4-17	Stress distributions in the circumferential and radial directions of the elliptic VIC nucleus microscopic model under 90 mmHg transvalvular pressure were showed above.....	181
Figure 4-18	Strain distributions in the circumferential and radial directions of the elliptic VIC nucleus microscopic model under 90 mmHg transvalvular pressure were showed above.....	182
Figure 4-19	Stress distributions in the circumferential and radial directions of the elliptic VIC nucleus microscopic model at 4 mmHg transvalvular pressure level were showed above.....	182
Figure 4-20	Strain distributions in the circumferential and radial directions of the elliptic VIC nucleus microscopic model at 4 mmHg transvalvular pressure level were showed above.....	183
Figure 4-21	Local circumferential stress states of circular VIC nucleus (left panel) and elliptic VIC nucleus (right panel) at 90 mmHg transvalvular pressure (Note: different legend scales were used in those two models).....	184
Figure 5-1	Two dimensional schematic depicting fiber straightening and compaction with corresponding VIC nucleus deformation induced from the ECM.	193

PREFACE

I would like to express my gratitude to my research advisor, Dr. Michael Sacks, for his support and encouragement throughout my Ph.D. study. His technical and editorial advice was essential to the completion of this dissertation and has taught me innumerable lessons and insights on the workings of academic research in general.

I would like to thank my committee members: Dr. Patrick Smolinski, Dr. Anne Robertson, Dr. David Vorp, and Dr. William Slaughter who is also my academic advisor, guided me through the dissertation process, never accepting less than my best efforts. Thank Wei Sun, Ph.D. for his efforts in the numerical coding. His remarkable research is invaluable to my final stages of the computational simulations. I would also like to thank my lab members for their cooperation and help in the Engineered Tissue Mechanics Lab.

To my parents, receive my deepest gratefulness and love for their dedication and the many years of support during my graduate studies that provided the foundation for this work and made my days in Pittsburgh pleasant. My thanks also go to my dear sister, my best friend, TsuHui Zoey Huang, it is not often that *she* finds a person that always finds the time for listening to her little problems and roadblocks that unavoidably crop up in the life, and vice versa. My little brother, my “Godfather”, YuanHan Rick Huang, this dissertation would not be possible without his constantly aggressive, precious criticizing and advice over the whole course of my

life. In addition, thank Thelma Chen, who always has faith in me, and thanks my friends, Mohammed Shihabi, Ahmed Al-Zahrani, Benjamin Pfoutz, and Osamah Al-Banyan, you have been the source of joy and blessing.

Special thank to Dr. Michael Kolar, to the opportunities for being his teaching assistant in the field of mechanism engineering design, kinematics analysis, mechanics of machinery, and etc, which inspire me the interests into the higher education instruction.

Last, but not least, my greatest appreciation to my very good friend, George Engelmayr, for his assistance in providing many valuable comments that improved the contents of this dissertation, and for his patience and wisdom made my last two-year graduate study much enjoyable.

ACRONYMS

AC	against curvature
ANOVA	analysis of variance
BHV	bioprosthetic heart valve
DF	degrees of freedom
ECM	extracellular matrix
GAGs	glycosaminoglycans
H & E	Hematoxylin and Eosin
OI	orientation index
RVE	representative volume element
SALS	small angle light scattering
TEHV	tissue engineered heart valve
VIC	valve interstitial cell
WC	with curvature

NOMENCLATURE

\mathbf{E}	Green strain tensor
E_{eff}	effective stiffness
E_F^C	bending stiffness in compression in the fibrosa layer
E_F^T	bending stiffness in tension in the fibrosa layer
E_V^C	bending stiffness in compression in the ventricularis layer
E_V^T	bending stiffness in tension in the ventricularis layer
ε	axial strain
I	moment of inertia
κ	curvature
$\Delta\kappa$	change in curvature
λ	stretch
M	moment
p	pressure
T	tension

1.0 INTRODUCTION

The primary diseases associated with the aortic valve are stenosis and insufficiency, for which the primary therapy is valve replacement. There were 96,000 heart valve replacements performed in 1999 in the United States alone. Bioprosthetic heart valves (BHV) offer significant advantages over mechanical valve prostheses, due to their low rate of thromboembolic complications and minimal need of chronic anticoagulation. However, they continue to suffer from degeneration over 10-15 years, resulting in either replacement or failure with consequent morbidity or mortality.⁽¹⁾ Although calcification is recognized as a leading cause of degeneration of BHV following long-term implantation, recent studies of clinical explants have revealed prominent and structural damage independent of calcification.⁽²⁾

Previous experimental results generated in our laboratory on porcine BHV indicated that *in vitro* accelerated wear testing experimental results in a dramatic loss in flexural stiffness.⁽³⁾ Moreover, these results demonstrated that the moment-curvature relationship shifted from linear to non-linear behavior with fatigue. However, the mechanism underlying this non-linear flexural behavior has yet to be explained. Sacks *et al.* have hypothesized that the occurrence of non-linearity resulted from preferential fatigue of the layers of the porcine BHV. These changes in mechanical properties correlated with the changes in collagen structure with fatigue.⁽³⁾ In order to address these issues, studies are underway in our laboratory to experimentally measure changes in layer mechanical properties with fatigue. However, changes

in porcine BHV layer moduli are potential highly complex and potentially can confound experimental measurements.

In addition to research efforts to improve current porcine BHV, in the long-term new technologies will have to be developed. This is especially the case in pediatric applications, where growth of the replacement valve is essential to eliminate the need for reoperations. Tissue engineering offers the potential to create cardiac replacement structures containing living cells, which have the potential for growth, and remodeling, overcoming the limitations of current pediatric heart valve devices. Despite promising initial results, significant questions remain. For example, cyclic mechanical stress applied to tissue engineering heart valve (TEHV) tissues has been shown to stimulate extra-cellular matrix (ECM) production.⁽⁴⁾ In order to understand and ultimately apply these results, fundamental information on the mechanical interaction of the native valve interstitial cells (VIC) with ECM needs to be obtained, which is the ultimate design paradigm. Yet, the internal and external stress environment of a heart valve, and how ECM stresses are transmitted to the VIC are completely unknown. Moreover, it is even unknown how VIC nuclei deformation response to the mechanical stresses is transmitted from the ECM in the native valve. The long-term goal of our laboratory is to understand heart valve micro-mechanics in order to inform the development of novel heart valve designs with improved performance. Clearly, an improved understanding of the micro-mechanics of both the native aortic valve leaflet and chemically treated BHV will help establish fundamental engineering principals to guide their design.

1.1 STRUCTURE, FUNCTION AND MECHANICAL PROPERTIES OF THE NATIVE AORTIC VALVE

1.1.1 Heart Anatomy

The primary function of the heart is to pump deoxygenated blood to the lungs and oxygenated blood from the lungs to rest of the body. The heart can be broken down into two main compartments; the left-heart and the right-heart. Each compartment has two chambers, a smaller chamber called an atrium and a larger chamber called a ventricle. The ventricles are the main pumps of the heart. Deoxygenated blood returns from the body to the right atrium via a large vein called the Vena Cava. It then flows into the right ventricle through a valve known as the “tricuspid valve,” named so because it has three flaps, or leaflets. The blood is then pumped into the lungs through the pulmonary valve and pulmonary artery. In the lungs the blood is loaded with oxygen. It then returns to the left side of the heart, via the pulmonary veins, to the left atrium. It is then pumped into the left ventricle through the mitral valve. Finally, the left ventricle pumps the oxygenated blood to the rest of the body through the aortic valve and aorta (Figure 1-1).

Chambers and valves of the heart

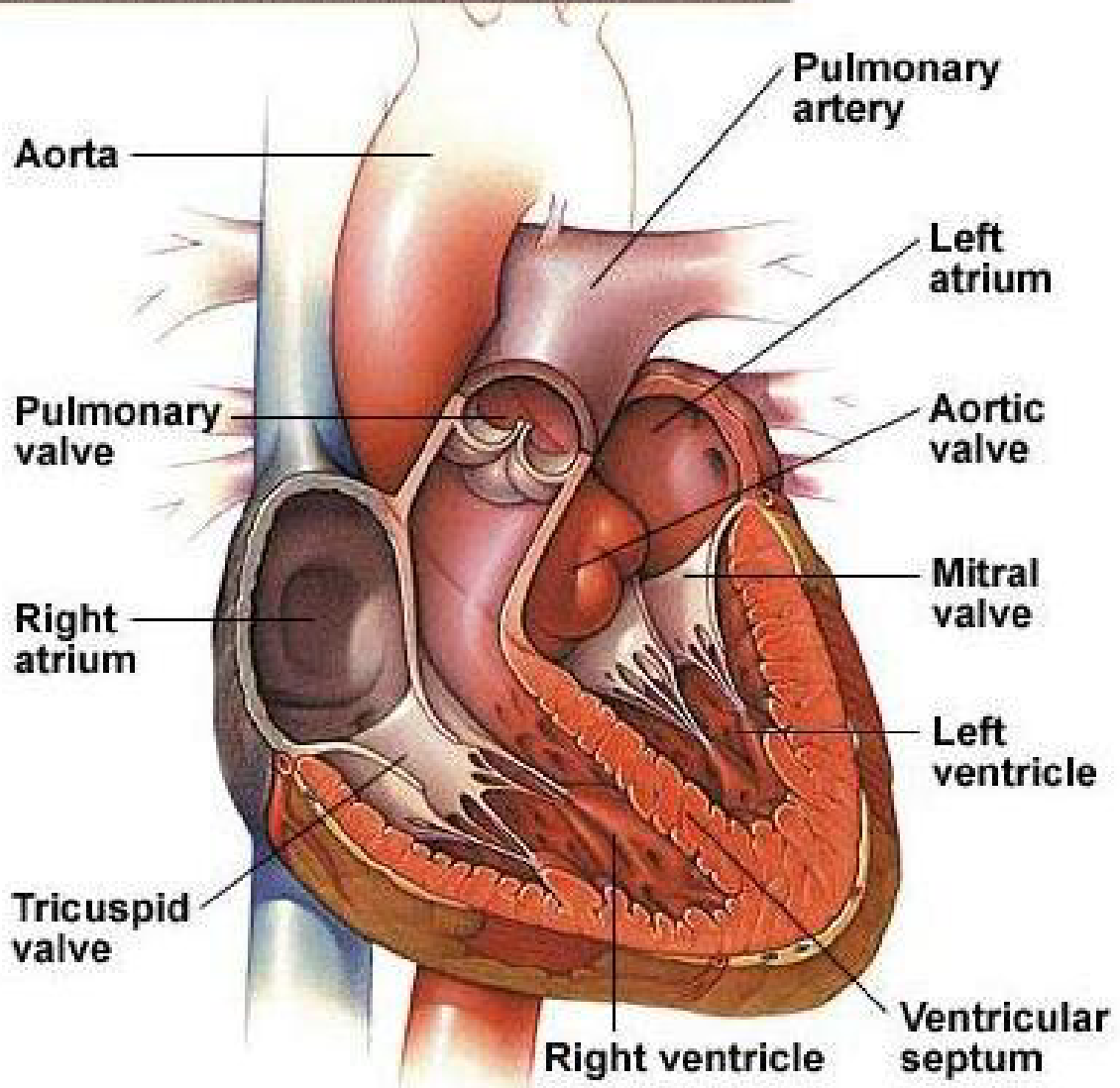


Figure 1-1 Schematic of the heart showing its valves and chambers (image courtesy of the Mayo Foundation for Medical Education and Research: <http://www.mayoclinic.com>).

1.1.2 Valvular Anatomy

The aortic valve is located at the junction between the outlet of the left ventricle of the heart and the inlet of the aorta. The gross structure of the normal aortic valve is generally conserved across mammalian species,⁽⁵⁾ and appears to follow directly from its physiological function: to prevent backwards (i.e., retrograde, regurgitant) flow into the left ventricle following the ejection of oxygenated blood from the left ventricle into the aorta. The aortic valve (as well as the pulmonary valve) is described as both tri-leaflet and semilunar, meaning that it consists of three discrete leaflets, or leaflets, and that each of the individual leaflets exhibit a gross semilunar, or half-moon, shape (Figure 1-2).



Figure 1-2 The normal tri-leaflet aortic valve is viewed from above in an intact aorta (image courtesy of the Mayo Foundation for Medical Education and Research: <http://www.mayoclinic.com>.)

The semilunar line of attachment of each of the three leaflets to the wall of the aorta (aortic root) is called the annulus fibrosis. The body of each leaflet extends from this peripheral

attachment to what is called the free edge. During valve closure, several millimeters of the free edge of each leaflet overlaps against an equal portion of the opposing leaflets, forming a seal against the backward flow of blood. This meeting of the individual leaflets during valve closure is termed coaptation, and the overlapping region is called the coapting surface of the leaflet, or lunula. Each of the ventricular surfaces of the aortic leaflets has a small nodule in the center of the free edge that marks the closure contact site. A circular ridge of thickened tissue circumscribes the aortic-pointing apices of the semilunar leaflets and marks the distal end of the aortic root and the proximal end of the aorta. These three apices at which the semilunar leaflets form a peripheral attachment are commonly referred to as the commissures, and the circle circumscribing these three points is called the sinutubular junction. Since each of the leaflets is roughly equal in size, the circumferential distance from commissure to commissure is approximately equal, and the commissures are located approximately 120 degrees apart from each other. The roughly triangular regions of the aortic root descending from each of the three commissures to the basal ring, and demarcated on either side by the semilunar lines of the annulus fibrosis of adjacent leaflets, are called the interleaflet triangles (Figure 1-3).⁽⁶⁾

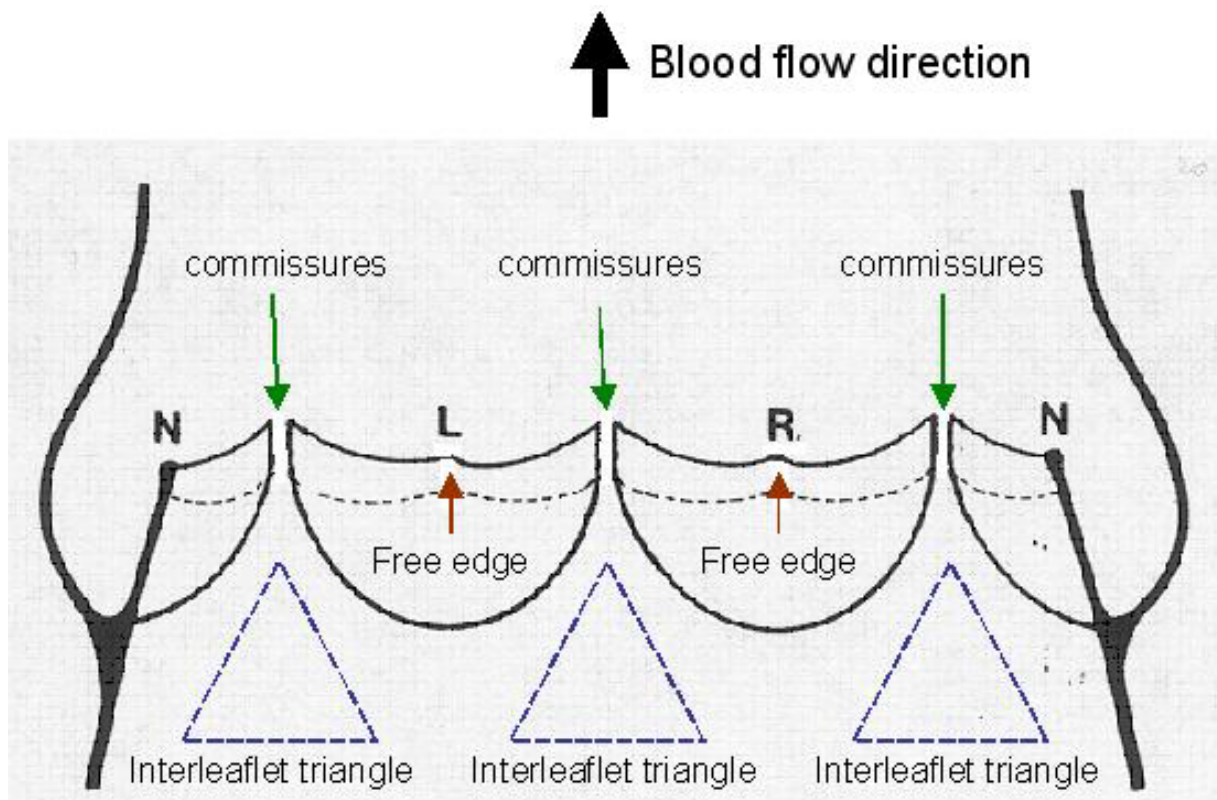


Figure 1-3 Schematic presentation of an aortic valve opened by a vertical incision through the noncoronary sinus. L, R, and N are the left, right and noncoronary leaflets, respectively. The dotted line is the line of leaflet coaptation (image courtesy of Thubrikar⁽⁷⁾).

The valves have two main functions: to allow the blood to flow through the heart smoothly, and, more importantly, to act as a check valve by preventing backflow of the blood, about 40 million times per year. As the heart muscle contracts and relaxes, the valves open and shut, letting blood flow into the ventricles and atria at alternate times. In the left ventricle, for example, after the left ventricle contracts, the aortic valve closes and the mitral valve opens, to allow blood to flow from the left atrium into the left ventricle, and as the left atrium contracts,

more blood flows into the left ventricle. When the left ventricle contracts again, the mitral valve closes and the aortic valve opens so blood flows into the aorta.

1.1.3 Fluid Dynamics

The aortic valve exists for the purpose of allowing blood to flow in one direction from the left ventricle to the aorta. It must serve the purpose without causing significant resistant to flow so as not to put an additional demand on the heart. It must work with almost 100% efficiency. Its opening and closing mechanisms must also not use a significant amount of energy. For these reasons, it is important to understand the fluid dynamics of the aortic valve. One of the early accounts of the role of fluid dynamics in the function of the aortic valve was given by Leonardo da Vinci.⁽⁸⁾ Henderson and Johnson,⁽⁹⁾ observed that under pulsatile flow the valve moves gradually towards closure during flow deceleration and finally closes without regurgitation.

Bellhouse *et al.*⁽¹⁰⁾ proposed a fluid dynamics model of the aortic valve, and the observations in the flow pattern of the model aortic valve could be summarized as follows: When the aortic valve opens rapidly, whereas the leaflets move into the sinuses and vortices form between the leaflets and the sinus walls. The leaflets project slightly into the sinuses. The flow enters the sinus at the sinus ridge, curl back along the sinus wall, along the leaflet, and flow out into the main stream. After peak systole the leaflets move away from the sinuses with gathering speed and the valve is almost closed before the end of systole. The trapped vortices reach maximum strength at peak systole, but decay slowly during the latter part of systole. After peak systole the flow decelerates. This deceleration causes the pressure on the sinus side of the leaflet

to be greater than that on the aortic side of the leaflet. Under the influence of this pressure difference, the leaflets start to move towards the closed position and the valve begins to close.

Thubrikar, *et al.*⁽¹¹⁾ related membrane stresses to the pressure difference across the leaflet and bending stresses to the leaflet curvature in aortic valve. Furthermore, Thubrikar, *et al.* compared the *in vivo* and *in vitro* study results of leaflet length with the pressure gradient changes. During diastole, they observed a change of leaflet length increased by 3.9% as the pressure gradient increased from 60 to 200 mmHg. *In vitro*, for an increase in stress that corresponded to an increase in pressure gradient from 60 to 200 mmHg, the leaflet length increased 8.7%. They concluded the increase was more than twice that measured *in vivo*, which indicates that during diastole the leaflet is much stiffer *in vivo* than *in vitro*. This stiffening appears to be due to stress in the circumferentially oriented collagen fibers of the leaflet, which prevents stretching in the radial direction. In systole, the lower elastic modulus reduces the flexion stresses, and in diastole, stiffening prevents the leaflet from prolapsing under pressure.

More recently, several studies on the fluid dynamics of the aortic valve stenosis and the aortic valve resistance have been published.⁽¹²⁻¹⁴⁾ Yearwood *et al.* studied the flow velocity profiles across the lumen of aortic in the presence of aortic stenosis. They observed that a strong systole jet bordered by transient vortices with intensely reversed flows was produced distal to severely stenotic aortic valves, becoming less intense with a lesser degree of stenosis. Burwash *et al.*⁽¹³⁾ investigated the effects of changing transvalvular volume flow rate on the aortic valve areas, calculated using both the Gorlin formula (a formula for calculating the area of the orifice of a cardiac valve, based on flow across the valve and the mean pressures in the chambers on either side of the valve) and the continuity equation in a model of chronic valvular aortic

stenosis. In both of the equations, valve areas were flow dependent indicators of stenosis severity and demonstrated linear relations with transvalvular volume flow rate. Furthermore, Antonini-Canterin *et al.*⁽¹⁴⁾ studied the transvalvular pressure gradient related to the aortic valve stenosis severity, and they concluded that transvalvular pressure gradient alone was insufficient to evaluate the aortic valve resistance since blood viscosity, turbulence and flow change should also be included.

1.1.4 Tissue Structure and Composition

The aortic valve leaflets are mostly (90%) water, but contain other components that lend it unique mechanical properties. The connective tissue proteins collagen and elastin are the main structural components, while the role of glycosaminoglycans (GAGs) and interstitial cells are less well understood. The internal collagen framework of the leaflets is arranged in three layers, the fibrosa, spongiosa and ventricularis (Figure 1-4). Towards the aortic surface is the fibrosa, consisting mainly of collagen fibers with scattered fibroblasts and a few fine elastin fibers. The collagen fiber bundles in the fibrosa are primarily arranged in a circumferential direction, that is, running from commissure to commissure. Both sides of the fibrosa are covered by loose fibroelastic tissue, usually containing mucopolysaccharides, and the entire valve is covered by endothelium. These circumferentially oriented, large diameter fibers are arranged in a corrugated manner that enables the leaflets to expand radially. During valve loading, the radial expansion enables the three leaflets to mate together and seal off the orifice.

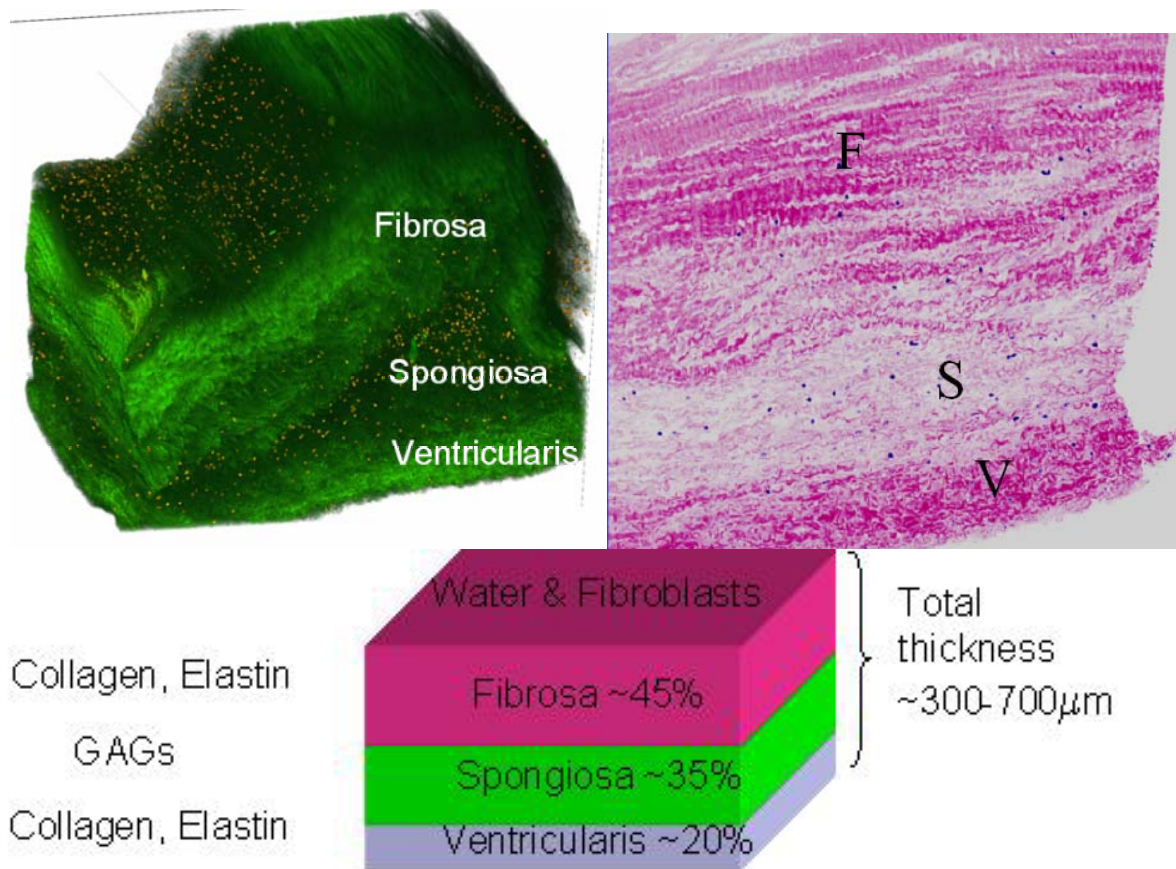


Figure 1-4 A schematic representation of a cross-section of the layered structure of the aortic leaflets. The relative proportions of the fibrosa (F), spongiosa (S), and ventricularis (V) are shown along with their major components.

In 1931, Gross and Kugel⁽¹⁵⁾ proposed that the loose connective tissue on the ventricular surface of the aortic valve the ventricularis. This layer is rich in elastin fibers and is continuous with the endocardium. The ventricularis consists mainly of sheet elastin and provides the tensile recoil necessary to retain the folded shape of the fibrosa. Elastin is believed to be primarily responsible for generating the preload in the ventricularis, and for maintaining the collagen fiber architecture in its neutral state. This relationship between the fibrosa and the

ventricularis requires the fibrosa to remain preloaded in compression and the ventricularis to remain in tension. Between the fibrosa and ventricularis is a very loosely organized spongiosa, consisting of collagen, elastin, and large amounts of proteoglycan. The specific function of the spongiosa at this time is not well understood, but it likely functions as a buffer zone to enable the localized movement and shearing between the fibrosa and the ventricularis during loading and unloading. Overall, the valve leaflets themselves are a fiber reinforced composite material. They consist mainly of strong collagen fiber bundles that run through the valve leaflets and attach to the walls of the aorta. During diastole, these fiber bundles transmit the forces imposed on the leaflets to the aortic wall.

1.1.5 Mechanical Properties of Native Valve Tissue

In light of the clinical relevance of aortic valve structure and function, a number of studies have focused specifically on the mechanical properties of the native valve leaflets, which are responsible for the efficiency and longevity of the valve.⁽¹⁶⁾ In one such study, Thubrikar *et al.*⁽¹¹⁾ studied the mode of deformation of the aortic valves, noting that the aortic leaflets undergo not only cyclic loading during valve operation, but also cyclic reversal of their inherent curvature. In the study, they computed the membrane stresses, due to the pressure differences across the leaflet, and the bending stresses, due to the curvature changes. They observed that in systole, the natural leaflet was not subjected to compressive stresses during the cardiac cycle.

Further more, Thubrikar *et al.*⁽¹⁶⁾ studied the stress-strain relationship of the aortic valve leaflets *in vitro*. For an increase in stress corresponding to an increase in pressure gradient, a 8.7 % increasing in the leaflet length was observed. This increase was more than twice that measured *in vivo*, indicating that during diastole the leaflet is much stiffer *in vivo* than *in vitro*.

Authors concluded the stiffening were due to stress in the circumferentially oriented collagen fibers of the leaflet, which prevents stretching in the radial direction. Moreover, the lower elastic modulus reduces the flexion stresses in systole, and in diastole, stiffening prevents the leaflet from prolapsing under pressure.

Lo *et al.*⁽¹⁷⁾ investigated the biaxial strain variability by calculating the distance between the markers in the sample in the radial and circumferential directions of native aortic valves. Highly anisotropic strain distributions from left to the right across the leaflets were observed in both circumferential and radial directions. In another study, Vesely and Boughner⁽¹⁸⁾ studied the relationship between the bending stiffness and the thickness (t) of the native aortic valves. Above and beyond the increase in flexural rigidity with t , which for a rectangular sample goes as the third power, they found that the bending stiffness increased in proportion to $t^{1.14}$, suggesting that the tissue is inherently stiffer in thicker leaflets. Moreover, they studied the neutral axis location of aortic valve under bending. The neutral axis lies in the fibrosa layer during bending was observed, suggesting a low compressive elastic modulus for the native aortic valve. A constant elastic modulus identical in tension and compression isotropic model was used to predict this neutral axis location.⁽¹⁸⁾ However, as mentioned in Section 1-1-2, the aortic valve consists of three distinct layers and each of these individual layers consists of different amounts of collagen, elastin, or glycosaminoglycans, which would be expected to yield different mechanical properties for the layers. Thus, in order to more fully understand the flexural mechanical properties of the native valve, further work is needed to model the mechanical properties of the individual layers.

In our laboratory, Billiar and Sacks⁽¹⁹⁾ studied the structure-function relationship of the native aortic valves with biaxial testing techniques. A detailed description of the biaxial testing device, including modifications to allow the test specimen to undergo in-plane shear, has been previously presented⁽²⁰⁻²⁴⁾ (Figure 1-5). Briefly, the video resolution is approximately 76 pixels/mm with a corresponding strain resolution of $\sim 0.5\%$. The axial forces and marker positions were continuously recorded at 15Hz with custom marker tracking software. Two loops of 000 nylon suture of equal length were attached to each side of the specimens with four stainless steel surgical staples. Small floats were attached to each staple to make the mounted sample neutrally buoyant. This procedure was completed in isotonic saline on a lab bench away from the biaxial testing device to minimize tissue deformation. The specimens were then mounted onto the biaxial device with the long and short dimensions of the sample aligned with the testing axes.

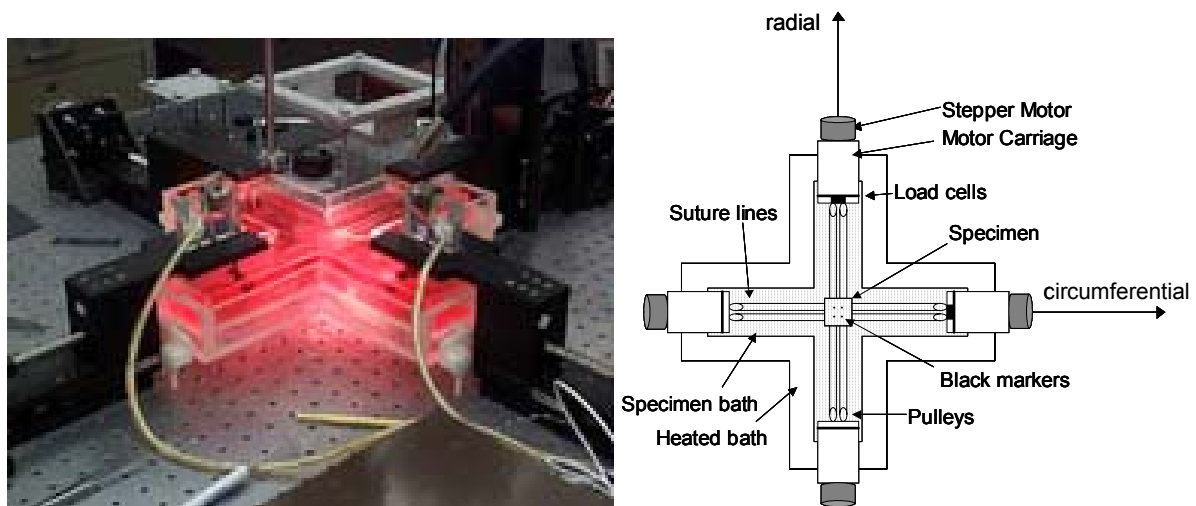


Figure 1-5 Actual (left panel) and a schematic (right panel) biaxial testing setup.

From the biaxial testing of the aortic valve, the smaller circumferential strains were observed than the radial strains (Figure 1-6), and authors explained the larger strain in radial direction was due to the large rotations of the circumferential aligned collagen fiber in the fibrosa layer. From the morphology of aortic valve, the larger strains in radial direction would facilitate the formation of a large coaptation area, while the circumferential strain could be explained by the extension to the crimped collagen fibers.⁽²⁵⁾

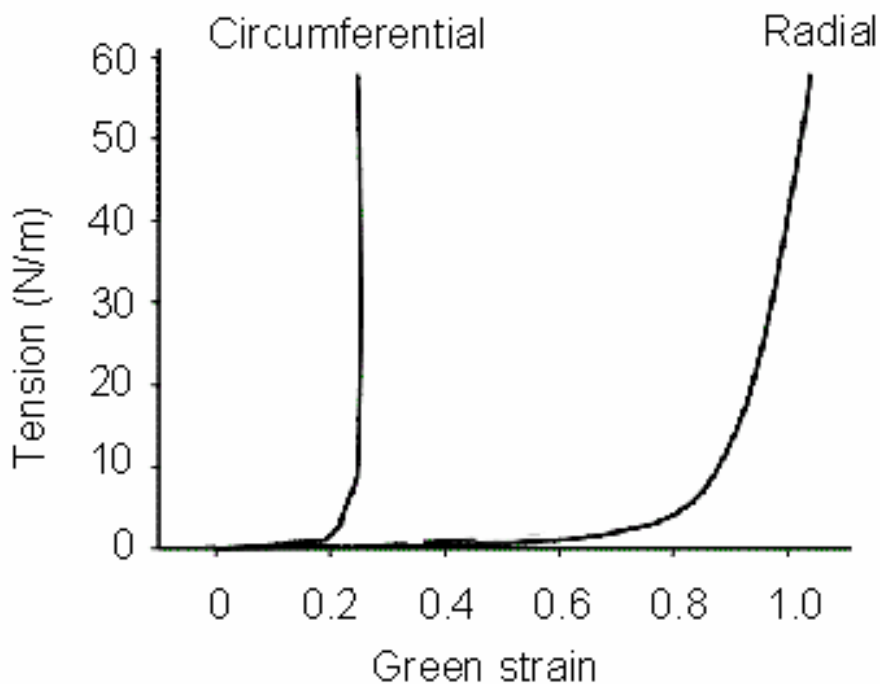


Figure 1-6 The smaller circumferential strains were observed than the radial strains in the native aortic valve (adapted from Billiar and Sacks⁽¹⁹⁾).

1.1.6 Valvular Cells

1.1.6.1 Valvular endothelial cell Heart valves have three distinct layers (fibrosa, spongiosa, and ventricularis), covered on both sides by a monolayer of endothelial cells. The endothelial cells of a normal heart valve are polygonal, aligned with the internal collagen framework of the valve, which is generally arranged circumferentially with the free edge of the leaflet (arranged across the direction of flow).⁽²⁶⁾ The aortic valve endothelial cells acts as a barrier between the blood and the stroma, including subendothelial fibroblasts of the normal heart valve (Figure 1-7),⁽²⁷⁾ and it has been shown that endothelial cell dysfunction is caused by mechanical forces, bacterial infection, autoantibodies, and circulating modulators of endothelial cell function.⁽²⁸⁾ Furthermore, evidence showed that the endothelial cell plays a critical role in the pathogenesis of valvular heart disease since endothelial cell dysfunction is a breakdown of the normal healing and regulatory functions, and has been linked to the pathogenesis of atherosclerosis, stroke, hypertension and thrombosis.⁽²⁸⁾

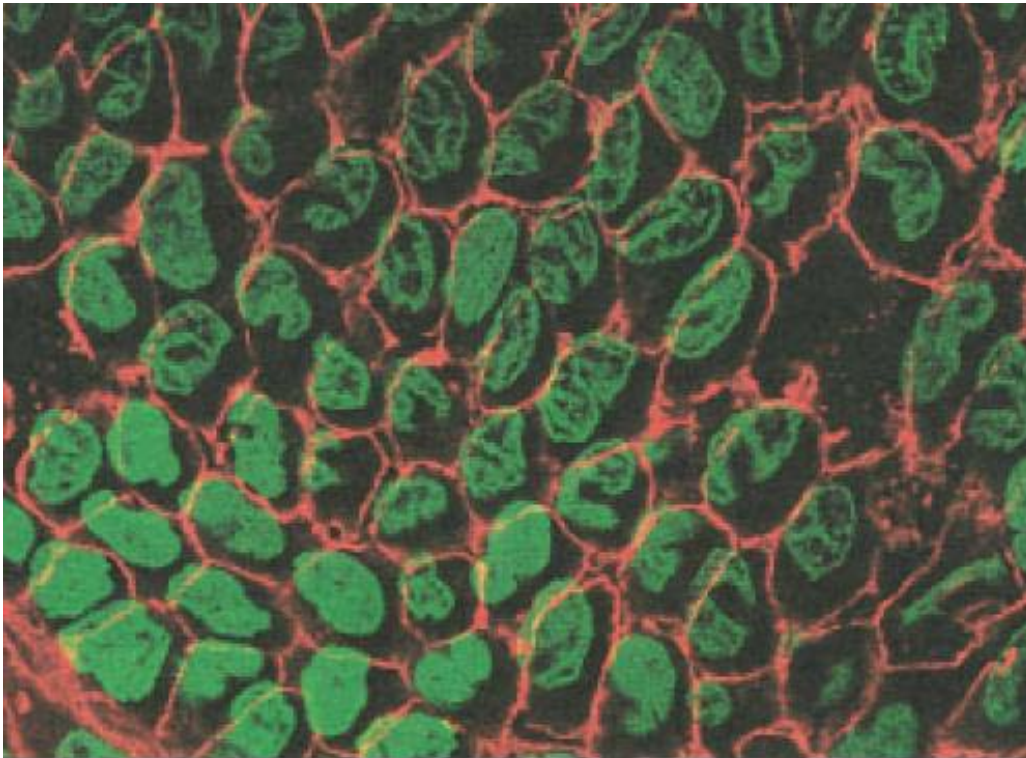


Figure 1-7 A micrograph of aortic valve surface stained in red for endothelial cells and stained in green for nuclei (image courtesy of Leask, *et al.*⁽²⁸⁾)

1.1.6.2 Valvular interstitial cell Many animal cells, including the VICs of heart valve leaflets, are surrounded by a dense ECM; an organized network of extracellular material that is present beyond the immediate vicinity of the plasma membrane. The mechanisms by which VICs interact with their ECM, however, remain unknown (Figure 1-8). Up to date, most of the studies of VIC focused on their phenotype or molecular characteristics *in vitro*.

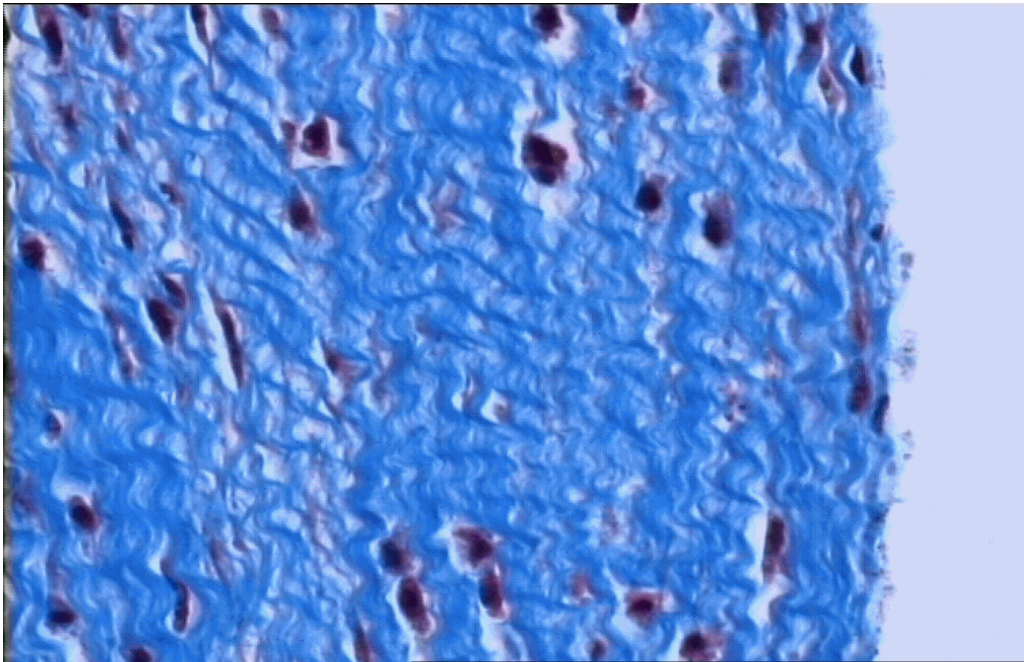


Figure 1-8 A micrograph of aortic valve surface stained in blue for collagen fibers and stained in black for valve interstitial cell nuclei (image courtesy of Sacks *et al.*⁽²⁹⁾)

The first study that characterized VIC was done by Filip *et al.*⁽³⁰⁾, who studied the ultrastructural features and functional properties. They observed that VICs have characteristics that classified them as intermediate between fibroblasts and smooth muscle cells. Specifically, like fibroblasts, VICs lack a basal lamina establishing direct and extensive contacts with collagen fibers, elastin microfibrils, and proteoglycans of the matrix. The cells have numerous slender and long processes, connected to one another, forming a complex cellular framework spanning the entire valve. Similar to smooth muscle cells, VICs are extensively coupled by communicating junctions as shown by thin sections, freeze-fracture, lanthanum staining, and carboxyfluorescein microinjection. The cells contain numerous bundles of actin filaments, which are decorated by the S1 fragment of heavy meromyosin. Furthermore, Messier *et al.*⁽³¹⁾

found that aortic VICs possessed characteristics of both fibroblasts (matrix secretion) and smooth muscle cells (contraction), and may be classified as myofibroblasts. The unusual features of the myofibroblasts may be central to lifelong aortic leaflet durability. They concluded VIC in aortic valve leaflets was a mix population of fibroblasts, myofibroblasts, and smooth muscle cells.

Mulholland *et al.*⁽³²⁾ also found that VIC has features of smooth muscle cells, but there is heterogeneity with respect to these smooth muscle cell markers. Since calcium is involved in the contraction of heart muscle and gene expression, Mulholland *et al.* hypothesized that the contractile ability of VICs may provide a passive structural support to maintain valve structure as it withstands dynamic hemodynamic forces. Roy *et al.*⁽³³⁾ studied the characteristics of the cultured aortic VICs with regards to the expression of myofibroblasts markers. In this study, authors observed that VICs express a number of genes whose products may have functional significance for heart valves. These include members of the contractile apparatus such as MHC and troponins. The presence of members of the frizzled family, which specify the orientation of cell polarization, in these cells could indicate that VICs are not randomly arranged in the valve tissue. From the gene expression of aortic VICs, an increase in intracellular levels of calcium in response to endothelial, indicating that these cells are capable of creating changes in the level of calcium.

This result was confirmed from Taylor *et al.*⁽³⁴⁾ Authors found VICs are responsible for maintaining the extracellular scaffold that provides the mechanical characteristics vital for sustaining the unique dynamic behavior of the valve. A number of cellular phenotypes were observed: some are sparsely arranged throughout the valve leaflets, while others are arranged in thin bundles. These cells express molecular markers similar to those of skeletal, cardiac and

smooth muscle cells and in particular, many VICs express smooth muscle alpha-actin, a marker of myofibroblasts. In this respect, these cells exhibit a profile which may allude to their role in valve function. Taken together these observations suggest that VICs may have contractile properties, which can account for a controlled tonus, actively correlated with the cyclically changing forces acting on valves during diastole and systole.

Overall, the valve leaflets form a dynamic regulator of blood flow through the chambers of the heart that can withstand large cyclic strains loads with little resistance to cardiac function. With disease, the endothelial and interstitial cell function and morphology change, alternating the valve's hemodynamics, compromising cardiac function. The understanding of the activation and response of the cells that results in valve operation is limited and requires more investigations.

1.2 AORTIC VALVE FUNCTION: A MULTI-SCALE BIOMECHANICS

PROBLEM

Since the physiological function of the aortic valve is mainly biomechanical in nature, understanding the biomechanics of the native valves is considered to be of great clinical and scientific importance. However, while the function of the aortic valve may appear deceptively simple—preventing backwards blood flow into the left ventricle—there is a growing appreciation in the academic and clinical community for the complex interplay of organ, tissue, and cellular level components required to orchestrate efficient valve performance and long-term durability. Clearly, a complete understanding the aortic valve function requires multi-length

scale approaches, and this perspective is central to the work presented herein, and thus warrants further discussion at each of the relevant scales: organ, tissue, and cellular (Figure 1-9).

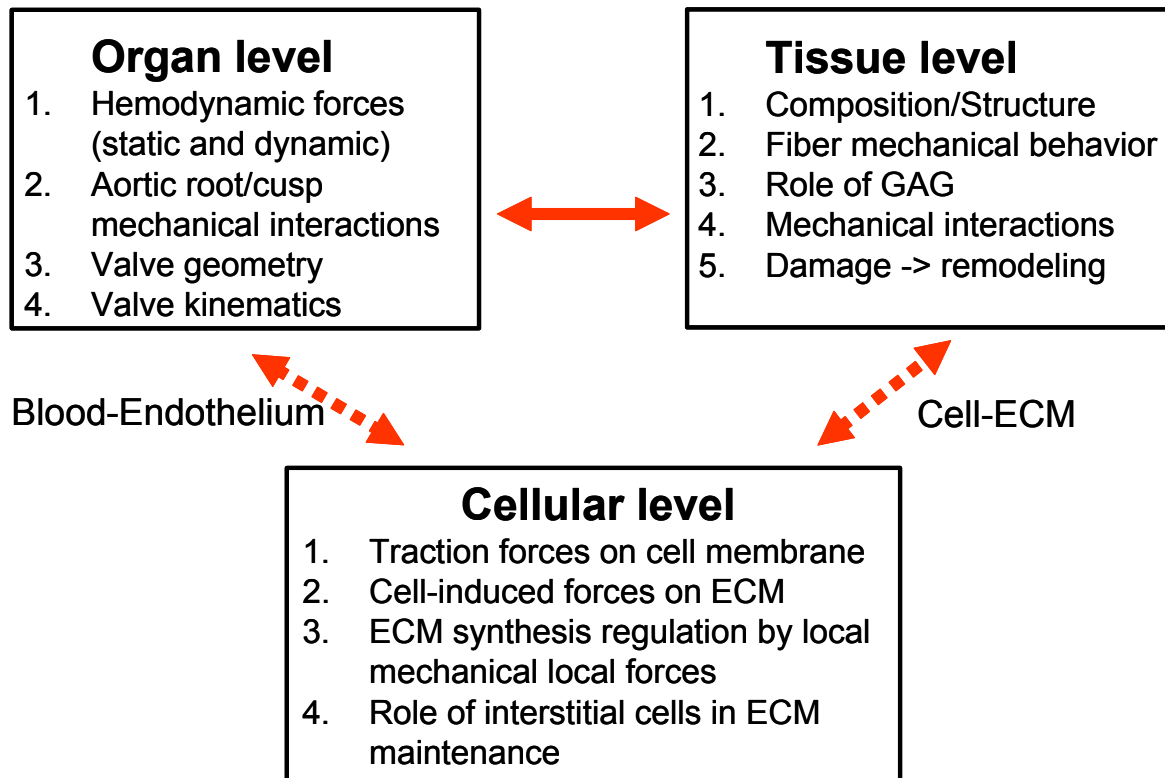


Figure 1-9 A schematic of the role of biomechanics in aortic valve function, which occurs at multiple structural levels. At each structural level, biomechanics plays a functionally critical role.

1.2.1 Organ – Level

The physiological function of the aortic valve occurs mainly at the organ level. At this level, biomechanical studies must be approached in the context of the entire aortic valve and aortic root system. While the valve leaflets are often the focus of discussion, as they generally

exhibit the nidus of tissue-level degeneration and organ-level valve failure, the leaflets are inextricably coupled to the surrounding root and sinuses, both physically and functionally. For example, while coaptation of the valve leaflets ultimately seals the left ventricle during diastole, the leaflets are hinged upon the root along a semilunar line of attachment, and rely upon vortical flow patterns generated in the opposing sinuses to assist in valve closure (Figure 1-10).

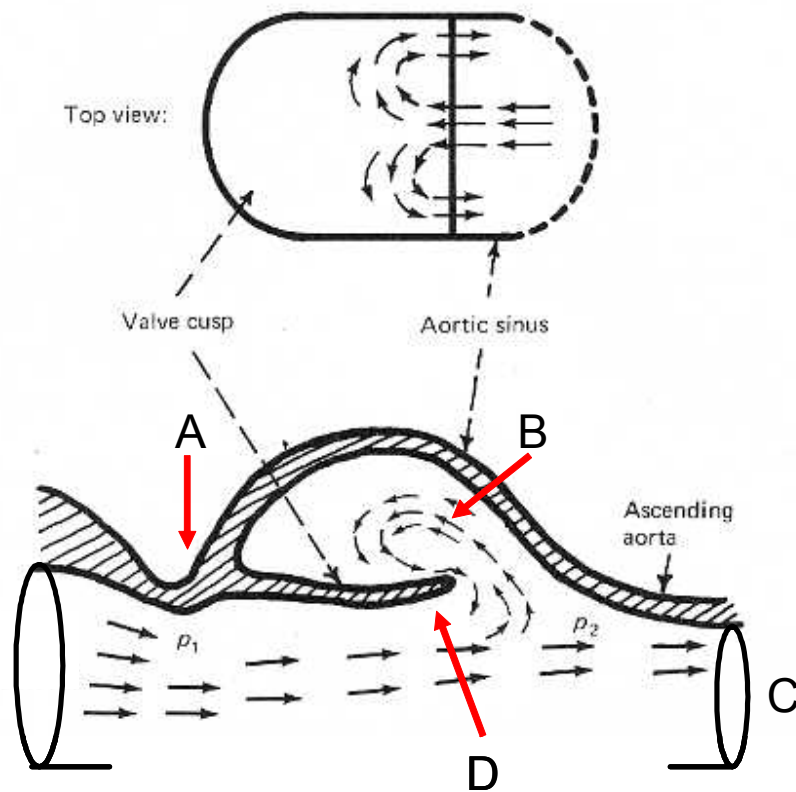


Figure 1-10 Two-dimensional schematic depicting blood flow streamlines in the aortic valve during peak systole. Note the junction between the aortic root, one leaflet, and one sinus (A). The vortical flow patterns generated in the sinus (B) assist in valve closure. Two organ-level structural features of the aortic valve are the circular sinotubular junction (C) and the nodulus (D).

Thus, at the organ level, biomechanical studies of the aortic valve must also consider the solid/fluid interactions. The static and dynamic forces imposed by blood pressure and flow largely dictate the motion and deformation of the leaflets and the root. The valve is generally considered to function passively in response to blood pressure and flow. Thus, it is through the organ-level solid/fluid interactions that mechanical stresses and strains are transduced to the tissue-level, and directly to the cellular-level (in the case of fluid shear stress on the valvular endothelium).

Finally, at the organ level, there exist several distinct regions and structures which are thought to play at least a subtle role in native valve function. For example, between the aorta proper and the aortic root there exists a circular ridge of thickened tissue referred to as the sinotubular junction (Figure 1-10). Another example is the nodule of thickened tissue positioned at the center of the coapting surface of each leaflet (Figure 1-10). The geometric position and structure of these features were described in detail in the previous sections on valve anatomy, however it should be noted here that these features appear to parallel specific functional requirements of the valve. This is yet another example of how the tissue of the aortic valve appears to have been designed to meet the organ level functional requirements.

1.2.2 Tissue – Level

The structure and biomechanical behavior of native valve leaflet tissue is an ongoing area of research. As eluded to previously, organ-level valve failure is almost always secondary to tissue-level degeneration. Likewise, the mechanical response of the valve to blood pressure and flow is ultimately dictated by the tissue properties and their spatial variation. Thus, understanding the normal composition, structure, and mechanical behavior of aortic valve leaflet

tissue is a prerequisite for understanding either normal organ-level function or the progression of pathological tissue degeneration.

For example, acquired aortic valve stenosis—stiffening of the aortic valve leaflets and narrowing of the orifice—often manifests as a clinical problem at the organ-level (e.g., congestive heart failure) long before frank tissue-level failure occurs. However, the origin of valve leaflet stiffening is at the tissue and cellular levels. Thus, studying how changes in the tissue-level properties (e.g., due to calcification) lead to organ-level changes (e.g., increasing systolic pressure gradients) is critical to understanding and ultimately treating the pathology.

Another example is leaflet closure and coaptation. Biaxial mechanical testing, in conjunction with tissue microstructural analysis and histological image analysis, have revealed that the collagen fibers of the native leaflet tissue begin to rotate under relatively low loads, and then straighten out and stiffen (i.e., lose their crimp) at higher loads (Figure 1-11).⁽¹⁹⁾ Interestingly, these microstructural changes in tissue structure appear to parallel the distinct functional requirements of the leaflets during closure and coaptation (i.e., relatively compliant during closure, and becoming stiffer during coaptation), thus demonstrating again the interplay between the organ-level and tissue-level.

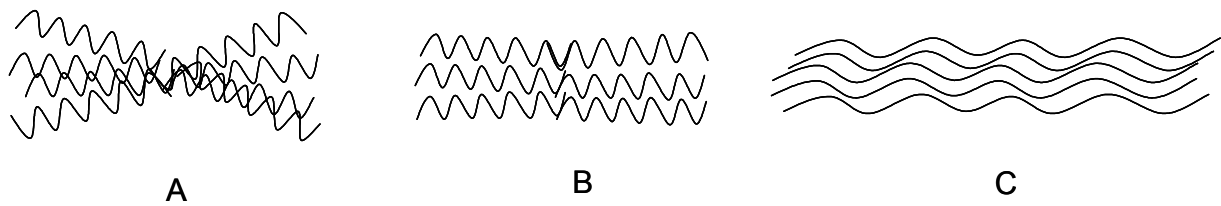


Figure 1-11 Two dimensional schematic depicting collagen fiber rotation (A to B) and un-crimping (B to C) during aortic valve closure and coaptation, respectively.

1.2.3 Cell – Level

In general, the cells of the aortic valve leaflet can be classified as either valvular endothelial cells or VICs as stated in Section 1-1. The valvular endothelial cells form a monolayer over the entire surface of the leaflet and root, continuous with the surrounding endothelium lining the left ventricle and aorta. Thus, the valvular endothelial cells are exposed directly to the complex fluid shear stress patterns generated by pulsatile blood flow through the organ-level geometry. Moreover, it is well known that the ventricular and aortic facing surfaces of the leaflets are exposed to significantly different magnitudes and patterns of fluid shear stress,^(35, 36) and furthermore that valvular endothelial cells on either side can exhibit subtly different phenotypes.⁽³⁷⁾ While no study to date has demonstrated a causal role for fluid shear stresses in specifically governing valvular endothelial cell phenotype, vascular endothelial cells in general are well known to respond to fluid shear stress in a variety of ways.⁽²⁶⁾

As mentioned in Section 1-1, the VICs are found inside the leaflet tissue (i.e., interstitial) and the VICs are a heterogeneous population of cells with properties ranging between smooth muscle-like, myofibroblast-like, and fibroblast-like. As alluded to previously, it has been

hypothesized that a certain fraction of the VICs may contribute toward active modulation of leaflet tissue stiffness during valve operation. While this level of interplay between hierarchal levels has yet to be established, it is clear from the tri-layered leaflet tissue structure that VICs located in different regions of the tissue may be exposed to different stresses and strains during leaflet bending. For example, the tissue-level structural changes observed under increasing load (e.g., collagen fiber rotation and un-crimping, (Figure 1-11) have been hypothesized to transduce concomitant strains to the embedded VICs.

1.3 HEART VALVE DISEASE

1.3.1 General Description and Statistics

Heart valves are very complex structures that can be damaged for a variety of reasons. The following diseases can result in valvular damage:

1. Rheumatic heart disease (Figure 1-12).
2. Inflections of the valves, as seen in bacterial endocarditis.
3. Chronic, or continual long-term wear and tear that leads to calcification and stiffness of the valves.
4. Defects from birth, also known as congenital malformations.

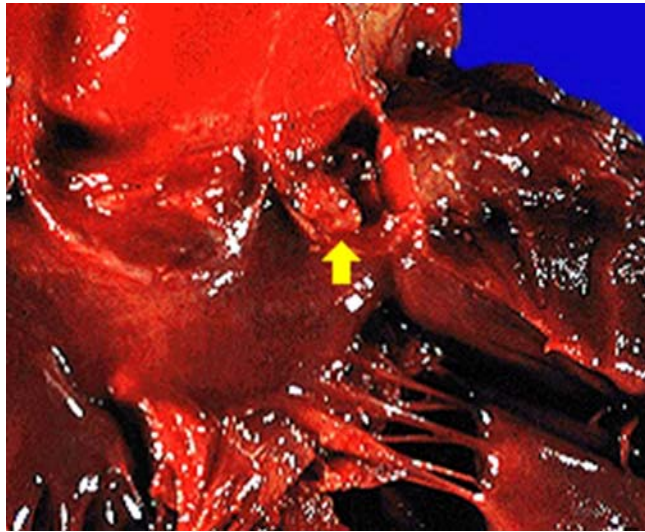


Figure 1-12 Arrow denotes scar tissue due to rheumatic fever (image courtesy of Dr. Richard B. Roberts of Cornell medical school).

These diseases can lead to two possible problems. In the first case the damaged valve can have a smaller opening than the original valve. This is known as “stenosis”. With stenosis, the heart has to work much harder at pushing the blood through. Over time this can cause a lot of strain on the heart and could even lead to death (Figure 1-13). In the second case, the heart valve may allow blood to flow backward, or “insufficiency”. With aortic valve insufficiency, the heart is less efficient at pumping blood to the body. This results in an increased workload, which could cause the heart to fail over time.

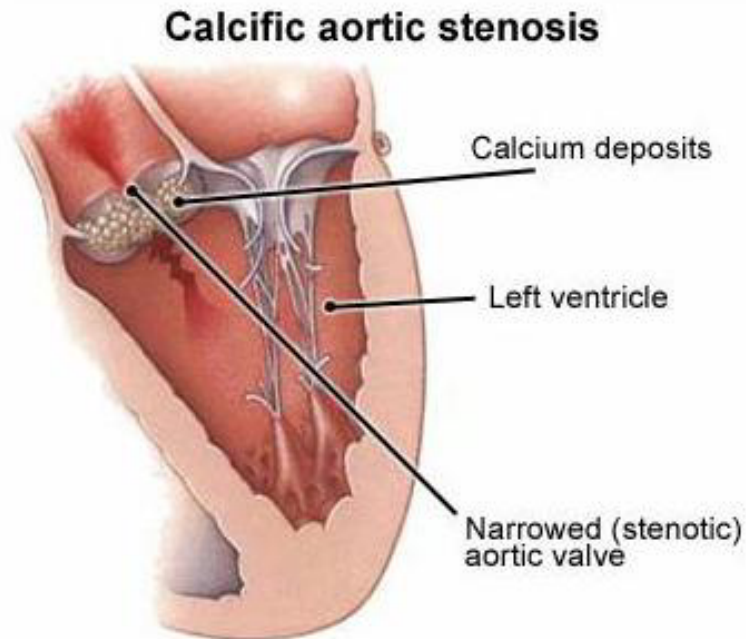


Figure 1-13 A buildup of calcium deposits on the aortic valve may lead to a narrowing of the valve, i.e. calcific aortic stenosis (image courtesy of the Mayo Foundation for Medical Education and Research: <http://www.mayoclinic.com>).

Degenerative aortic valve disease was the most common cause of aortic stenosis in 1990. Among 1870 valves studied between 1965 and 1990, 93% were purely stenotic and 7 % were both stenotic, incompetent, and were regurgitant. Congenitally bicuspid aortic valves were the second most common cause of aortic valve dysfunction among all 1221 valves studied from 1965 to 1990 accounting for 32 %, similar to the finding of the data from 1990 Mayo series alone (28%). Bicuspid valves are most often stenotic (68%), but can become regurgitant (19%) or be both stenotic and regurgitant (13%). They can also be associated with aortic dissection. Furthermore, calcification in the valve leaflets and secondary commissural fusion may all contribute to stenosis. Though incompetent valves are generally not calcified but may

develop leaflet prolapse and annular dilation. Bicuspid valves may also become regurgitant secondary to infective endocarditis. In fact, bicuspid valves were present in 42 % of cases of infective endocarditis cases in the 1221 valve Mayo Clinic series.⁽³⁸⁾

1.3.2 Therapy for Aortic Valve Dysfunction

No good long-term results for repair of aortic stenosis have been reported from several trial series.^(39, 40) Bernal *et al.*⁽⁴¹⁾ investigated the long-term performance of aortic valve repair. The results were obtained in a twenty-two year period in patients who underwent repair of nonsevere rheumatic aortic valve disease. The actual survival curve including hospital mortality was 35.4 % +/- 8.7 % at twenty-two years. According to the data, Bernal *et al.* concluded conservative operations for rheumatic aortic valve disease do not seem appropriate. Conversely, there is growing interest in various repair techniques for aortic insufficiency. However, severe valve damage means that the valve will need to be replaced. Valve replacement is most often used to treat aortic valves and severely damaged mitral valves, and it is also used to treat any valve disease that is life-threatening. Thus, aortic valve replacement is by far the most common treatment for aortic stenosis. In this type of surgery, surgeons remove the narrowed aortic valve and replace it with a mechanical valve or a bioprosthetic valve derived from either porcine, bovine, or human cadaver tissue.

1.4 CURRENTLY AVAILABLE REPLACEMENT HEART VALVES

Prosthetic heart valves were introduced approximately fifty years ago, and are replaced in approximately 285,000 patients each year. Since then their design has gone through

many iterations, although the ideal prosthetic heart valve still remains elusive. The optimal prosthetic valve, according to Harken *et al.*,⁽⁴²⁾ should have:

1. Lasting physical geometric features.
2. Be capable of permanent fixation in the normal anatomic site.
3. It should be chemically inert, non thrombogenic, harmless to blood elements and must not annoy the patient.
4. It must open and close promptly during the appropriate phase of the cardiac cycle.
5. Should offer no resistance to physiological blood flow.

Heart valve prostheses consist of an orifice, through which blood flows, and an occluding mechanism that closes and opens the orifice. There are three classes of heart valve replacements: mechanical prostheses, with rigid, manufactured occluders, tissue valves, with flexible leaflet occluders of animal or human origin, and tissue engineered heart valves.⁽⁵⁾ Each of the heart valve replacements is discussed in the following sections.

1.4.1 Mechanical Valves

1.4.1.1 Overall description Among mechanical valves, ball valves appeared in the early 1960s, disk valves in the early 1970s, and bileaflet valves predominantly during the 1980s. The ball in the ball valves is a silicone rubber polymer, impregnated with barium sulphate for radiopacity, which oscillates in a cage of cobalt-chromium alloy. When the valve is open, blood flows through the circular primary orifice and a secondary orifice between the ball and the housing. In the aortic position, there is a tertiary orifice between the equator of the ball and the aortic wall.⁽⁴³⁾

Improvement on the clinical success of the ball valves was sought by developing designs with reduced height. The first successful low-profile design was the Bjork-Shiley tilting disk valve, introduced in 1969.⁽⁴⁴⁾ It evolved through several design refinements, and about 360,000 valves were implanted. These refinements also introduced a structural failure mode caused by strut fracture in the Convexo-Concave model.

Current development in mechanical valves is based on the bileaflet design, introduced by St. Jude Medical in 1977. Unlike the free-floating occluders in ball and disk valves, the two semicircular leaflets of a bileaflet valve are connected to the orifice housing by a hinge mechanism (Figure 1-14). The leaflets swing apart during opening, creating three flow areas: one central and two peripheral. The St. Jude bileaflet valve has leaflets that open to an angle of 85° from the plane of the orifice and travel from 55° to 60° to the fully closed position, depending on valve size. The original version, whose housing did not rotate within the sewing ring, has been supplemented by a model that does rotate for intraoperative adjustment. It has been used over 600,000 times.



Figure 1-14 Mechanical valve (image courtesy of Edwards Life Sciences: <http://www.edwards.com>).

1.4.1.2 Benefits and drawbacks The principal advantage of the mechanical prostheses is their documented durability and their chief disadvantage is their propensity for thromboembolism. The durability of the currently used mechanical valves is remarkable, given the harsh biological environment in which the valve must perform 40 million cycles per year. For example, the current Starr-Edwards ball valve, now in used for more than 200,000 patients, has had fewer than a dozen structural problems reported to the manufacturer, most of which did not cause clinical problems.

Mechanical valves carry the risk of blood clots forming on or near the valve, and since blood flow through mechanical valve prosthesis must course around the poppet,

mechanical valve prosthesis usually have areas of stasis distal to the orifice. Because the combination of stasis and nonphysiological surface promotes thrombus formation, patients with mechanical valve receive chronic anticoagulation therapy⁽⁴⁵⁾. Even though blood thinners are relatively safe, they do increase the risk of bleeding in the body. If this bleeding occurs in the brain, for example, it could lead to death. In extremely rare circumstances the valve can malfunction and may need to be replaced. A risk of thromboembolism, however, even with satisfactory anticoagulant therapy, continues for at least 15 years after placement of mechanical prosthesis.⁽⁴⁶⁾ In contrast, tissue valves have low rate of serious thromboembolism, and are described below.

1.4.2 Bioprosthetic Heart Valves

1.4.2.1 Overall description BHV, typically derived from either porcine valves or bovine pericardium, currently serve as acceptable substitutes for diseased heart valves. BHV have three leaflets that open and close like a normal human aortic valve. Before insertion, the valve is usually treated with glutaraldehyde to sterilize the valve and to reduce tissue antigenicity and stabilize proteins. The introduction of glutaraldehyde for the fixation of biological tissue by Carpentier and colleagues in 1969 facilitated the use of bioprostheses, both porcine (Figure 1-15) and bovine pericardium, as a satisfactory alternative to mechanical valves. Glutaraldehyde-preserved porcine BHV have been used as cardiac valve substitutes since 1971, and have given patients an excellent quality of life with low rate of thromboembolism, essential lack of thrombosis, and freedom anticoagulant-related hemorrhage.⁽⁴⁷⁾



Figure 1-15 Stented porcine BHV (image courtesy of Edward Life Science: <http://www.edwards.com/> site).

1.4.2.2 Benefits and drawbacks Bioprostheses are considerably less thrombogenic mainly because of the natural properties of the materials used and because of their axial flow properties and leaflet pliability. Furthermore, because most patients are managed without anticoagulation, there is no risk of anticoagulation-related complications, particularly hemorrhage. BHV should probably be confined to the elderly, in whom anticoagulant therapy may have a higher risk, and to potentially childbearing postadolescent women, in whom there is risk of embryopathy and a high frequency of fetal death caused by warfarin.⁽⁴⁵⁾

Rizzoli *et al.*⁽⁴⁸⁾ studied the long-term durability of the aortic valve replacements using Hancock II porcine bioprostheses. After fifteen year follow-up studies, the freedom from valve-related mortality was 84 % +/- 3.5 %, and the percentages for freedom from

thromboembolism, anticoagulant-related hemorrhage were 78.2 % +/- 4 % and 83.5 % +/- 3.6%, respectively. In patients younger than 65 years, actual freedom from structural valve deterioration was less than that seen in older patients (84.5% +/- 3.5% vs. 95% +/- 3.0%). Thus, they concluded heart valve replacement by using Hancock II porcine bioprostheses have excellent durability after fifteen years.

The long-term clinical durability of BHV is currently a major impediment to their usage. In adults, the BHV has a low frequency of deterioration during the first 5 years after implantation; however, there is a significant incidence of tissue failure thereafter.⁽⁴⁹⁾ Before long-term durability data became available, improvement of hemodynamic performance was the focus of development. The clinical introduction of the bovine pericardial valve solved the hemodynamic problem and such valves exhibit hemodynamics better than or equal to some mechanical prostheses.

However, even the most advanced BHV designs continue to suffer from calcific or mechanically induced degeneration after a prolonged period of implantation (10-15 years), resulting in either surgical intervention or mortality. The key to improving the longevity of BHV function is to understand the root causes of their failure.

1.4.2.3 Mechanisms of bioprosthetic valve degeneration Structural failure in the absence of infection is the major cause of dysfunction of the most widely used BHV, providing the indication for approximately three-quarters of reoperations on patients with these valve replacement devices. Three processes accounting for the overwhelming majority of BHV failures are: (1) cuspal mineralization, with or without secondary tearing, (2) design-related cuspal tears,⁽⁵⁰⁾ and (3) non-calcific mechanical failure (i.e., fatigue) of the cuspal structure.

Furthermore, mechanical damage of BHV typically involves one or a combination of the following elements: (1) stress concentration induced by calcification, (2) structural damage induced by calcific depositions, and (3) fatigue effects (unrelated to calcification).

Although the exact mechanism of BHV degeneration remains unclear, one study showed the degenerative failure of the bioprostheses results mainly from calcification and from leaflet tearing at the free edge or at points of leaflet attachment to the leaflet stent.⁽⁵¹⁾ Leaflet deterioration and perforation have also been correlated with regions of highest stress in the tissue.⁽⁵²⁾ Furthermore, other study showed that flexure-induced deterioration may be another major contributing factor of BHV degeneration.⁽⁵³⁾

1.4.2.4 Calcification of porcine bioprosthetic heart valve Calcification of the BHV refers to the buildup of calcium deposits on the valve at the outside of the heart's left ventricle. The BHV failure rates were often enhanced by calcification and this in turn appeared to be associated with stress concentrations. Macroscopic calcification of functioning clinical and experimental BHV begins and is enhanced in areas of leaflet flexion where deformations are maximal; however, the effects on calcification of mechanical deformation are complex.⁽⁴⁶⁾ In the subcutaneous model, enhanced calcification is noted in areas of tissue folds and bends, suggesting that static (as well as dynamic) mechanical deformation potentiates mineralization.⁽⁵⁰⁾

There are two categories of the calcification in BHV: intrinsic and extrinsic. Intrinsic calcification usually occurs within the boundaries of the tissue or biomaterial, involving its original constituents. Intrinsic calcific deposits in BHV are grossly nodular, often friable, yellow-white masses, which predominate at the cuspal commissures and basal attachments, the sites of greatest dynamic mechanical activity during valve function. The earliest deposits in

aortic valves are usually confined to the valvular fibrosa, but later deposits clearly predominate in the spongiosa. Ultrastructural studies of clinical valve tissue demonstrate that calcific deposits are related to cuspal connective tissue cells and their fragments, and collagen.⁽⁵⁰⁾

Extrinsic calcification is associated with elements or tissue not initially present or implanted, such as thrombus, endocarditic with vegetations, or pseudointima. Extrinsic calcific deposits form with thrombi, infected vegetations, or tissue over-growth on bioprosthetic valves. Although intrinsic degenerative mineralization generally requires several years to develop to clinical significance, calcific deposits extrinsic to the leaflets can form rapidly (within several days) in the necrotic inflammatory cells of superficial thrombotic accumulations, or in the vegetations of infective endocarditis.⁽⁵⁰⁾

Evidence points to stiffening by calcification as the primary mechanism responsible for cuspal tearing, as calcific depositions have been implicated in elevating stresses with consequent secondary collagen fiber damage and leaflet tearing. Haziza *et al.*⁽⁵⁴⁾ found pure tear is the results of uneven tissue loading with tearing occurring at sites of maximal stress, and can be related to incorrect mounting or to increase bending stresses in stent-mounted porcine BHV. Some data suggest that the degree of calcification on clinical porcine valves varies according to the pressure differential across the valve during the closed phase of the cardiac cycle, and extensive mechanical deformation during function accelerates calcification of BHV.

1.4.2.5 Non-calcific structural damage The specific contribution to failure of complex mechanisms of non-calcific cuspal damage is likely to be more important in clinical pericardial than in porcine bioprostheses. Cusp perforations and tears frequently cause failure. They are also associated with a commissural suture, which hold leaflets in apposition near the free edge of the

leaflet, adjacent to the stent post.⁽⁴⁶⁾ The alignment stitch is point of leaflet fixation and appears to be a point of considerable mechanical and flexion stress on leaflet material when the valve opens. It is perhaps not surprising that it is at this site that degenerative changes in leaflet material occur. As wear increases the stitch eventually pulls through the leaflet material, allowing the leaflet unusual mobility, and probably potentiating further degenerative changes. Any ability to decrease the incidence of this form of primary valve failure in this or similarly constructed valves may rest on the potential to modify the alignment stitch.⁽⁵⁵⁾

In our laboratory, small angle light scattering (SALS) was used to quantitatively assess changes in porcine BHV fiber architecture (Figure 1-16).⁽²⁾ In brief, a 4 mW HeNe ($\lambda = 632.8$ nm) laser beam was passed through the aortic valve tissue sample. The laser beam was scattered according to the internal planar fiber architecture of the sample, and the resultant angular distribution of scattered light intensity about the laser axis, $I(\Phi)$ versus Φ , was recorded (Figure 1-17). The width of the Φ distribution is indicative of the degree of fiber orientation; highly oriented fiber networks result in a narrow peak, while more randomly distributed fiber networks yield a broader peak. To quantify the degree of fiber orientation, a physically intuitive orientation index (OI) was used. OI was defined as the angle that contains one half of the total area under the Φ distribution, representing 50 % of the total number of fibers.⁽⁵⁶⁾ Thus, a highly oriented fiber network has a low OI value, while a more randomly oriented network has a higher value.

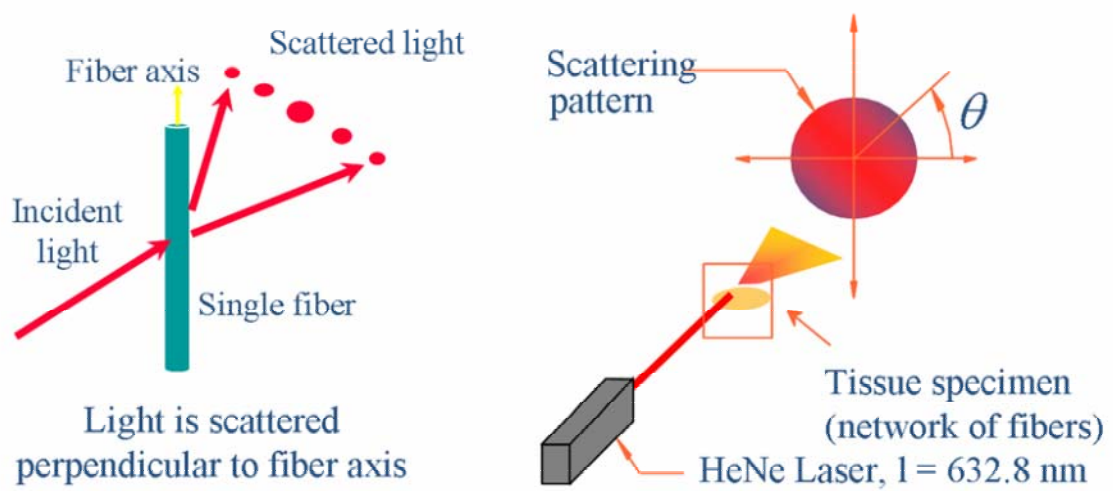


Figure 1-16 SALS device was used to quantitatively assess tissue fiber architecture.

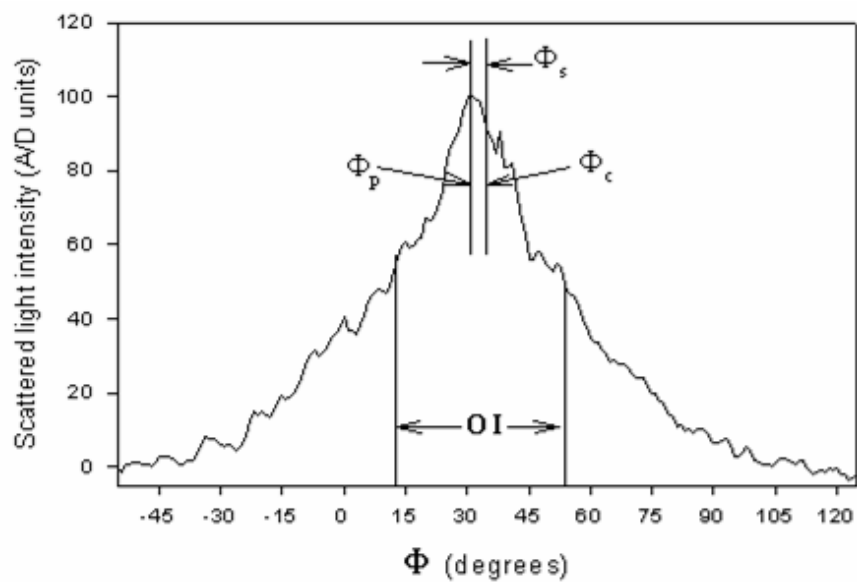


Figure 1-17 A representative resultant angular distribution of scattered light intensity about the laser axis.

Sacks and Schoen⁽²⁾ observed from the x-ray image of the clinically explanted porcine BHV leaflets showing predominant calcification at the basal attachment. The main structural damage regions from the SALS test did not correspond to areas of calcification (Figure 1-18). The region of structural degeneration was observed around nodular compared to the uncycled BHV tissue. Additional, structural damage demonstrated a characteristic spatial distribution surprisingly similar to *in-vitro* fatigues. Authors also found the disruption to the valvular extracellular matrix mediated by mechanical factors independent of calcification accumulates during clinical function of porcine BHV. Such structural damage is largely independent of the amount and distribution of calcification, and occurs in completely non-calcified leaflets. Thus, these results suggested that non-calcific, mechanically induced damaged may play a major role in porcine BHV failure.

OI(deg)

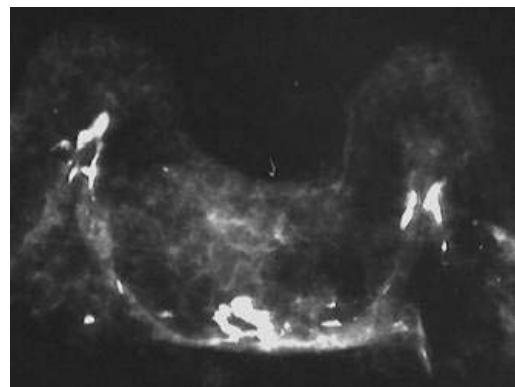
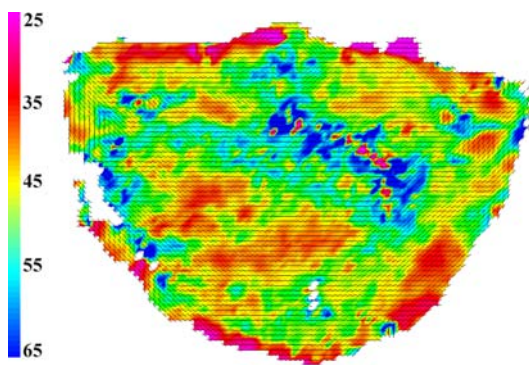


Figure 1-18 SALS image of clinically explanted porcine BHV and x-ray image of calcified BHV.

1.4.2.6 The need to focus on mechanisms of non-calcific structure damage The primary concern with BHV is their limited durability, which has been documented since early 1980s.⁽⁵⁷⁾ Approximately 90 % of all BHV fabricated from porcine aortic valves fail with tearing, and some fail with little or no calcification.⁽⁴⁾ Extensive research on mineralization mechanism has led to prevention strategies, however, the mechanisms and importance of mechanical and chemical deterioration of the valvular extracellular matrix remain uncertain. Moreover, calcific and noncalcific damage may be synergistic, but the mechanisms are unclear. For example, dynamics or static mechanical deformation appear to potentially induce mineralization, internal disruption of structure induced by deformation is probably critical.⁽⁵⁸⁻⁶⁰⁾

Since the long-term durability of a tissue valve is extraordinary dependent on the ongoing quality of its extracellular matrix, few studies have focused specially on the noncalcific damage of loading on the collagen fiber network. Once the mechanism of damage are understood, they can be utilized in the design of novel chemical and mechanical treatment and other conditions of valve fabrication that seek to enhance collagen stability and reduce flexural stresses implicated in degeneration of the collagen matrix.

1.5 MECHANICAL PROPERTIES OF PORCINE BIOPROSTHETIC HEART VALVE

1.5.1 Effects of Chemical Treatment

The basic function of the porcine BHV was reviewed by many groups from an engineering perspective, and it has been suggested that the modifications of mechanical property

were produced in valvular tissue by glutaraldehyde fixation. Chemical reactions of glutaraldehyde with tissue result in the cross-linking of proteins, especially collagen, the most abundant structural protein of porcine aortic valves. In this tissue, Type I collagen predominates, with lesser amounts of type III also present. The chemical interactions of glutaraldehyde with collagen and other proteins involve reactions of the aldehyde functions with protein-bound amines, yielding inter- and intra-molecular cross-links.

The functional and mechanical characteristics of the natural aortic valve and other tissues used in bioprostheses are altered by glutaraldehyde cross-linking procedures. Different follow-up studies have been proposed such as variations of fixation pressures, testing the mechanical property by biaxial techniques and bending device, and fixed tissue has different mechanical properties than native tissue was observed. Those studies were summarized below.

De Biasi *et al.*⁽⁶¹⁾ found that the fixed BHV leaflets have a higher failure load and an increased elastic recovery than that of a native aortic valve. Purinya *et al.*⁽⁶²⁾ studied the mechanical properties of the explanted BHV with 0.625% glutaraldehyde by using the uniaxial loading tests. They concluded that forty-months after implantation, ultimate stress of porcine BHV decreased in the circumferential direction from 4.06 MPa to 1.99 MPa, and the ultimate strain increased from 13 % to 22 %. Vesely⁽⁶³⁾ compared the changes of stiffness before and after the glutaraldehyde fixation of BHV by using the uniaxial tensile tests. The decreasing of valve thickness by 21 % was observed after the fixation due to the action of the hydrophobic glutaraldehyde from the tissue. From the comparisons of native versus glutaraldehyde fixed tissue, glutaraldehyde fixed tissue had a lower stiffness than native tissue at low load, but no difference was found at high load. Vesely concluded the reduction of the stiffness of

glutaraldehyde fixed tissue under low loading condition was due to the cross-linking of the collagen fiber matrix. Courtman *et al.*⁽⁶⁴⁾ studied the viscoelastic characteristics of the native aortic valve and porcine BHV under uniaxial high-strain rate stretching. The higher extensibility and elastic behavior in porcine BHV were observed than the one in native aortic valve. However, it was confirmed to date that uniaxial testing cannot be used to estimate the mechanical behavior accurately due to the presence of mechanical anisotropy of biological soft tissues.⁽²⁴⁾

Lo *et al.*⁽¹⁷⁾ investigated the heterogeneity of the porcine BHV by mapping out the regional variability of the biaxial strain versus pressure relationship. They found the anisotropy is highly variable and greatest in the central region of the leaflets. This study showed that the maximal dispensability is less than 24 % strain in the radial direction and 11 % in the circumferential direction. Adamczyk *et al.*⁽⁶⁵⁾ investigated the role of elastin of porcine BHV before and after the elastase-treatment by using the biaxial mechanical tests. They found the elastin damage led to a considerable increase in the radial dimensions of the tissue, and concluded that damage of the elastin was primarily responsible for changes in the mechanical properties of the valve leaflets.

In our laboratory a three-point bending method was utilized to measure the flexural behavior of native and porcine BHV.⁽⁶⁶⁾ In brief, specimen were removed from the native aortic and porcine BHV leaflets, marked with 5 – 10 small black dots (~ 0.3 mm) along one edge using a permanent marker. The markers were placed along the entire specimen length so that the complete flexure deformation of the specimen could be measured (Figure 1-19). To exam the response of the cuspal layers to tensile or compressive stresses, each specimen was subjected to

bending in both with (WC) and against (AC) the natural curvature of the leaflet (Figure 1-20). When the specimen was flexed in the AC direction, the deformation subjected the fibrosa to tensile loading and the ventricularis to compressive loading, conversely. If layers have different tensile and compressive behaviors, the net tissue response will be a function of bending direction.

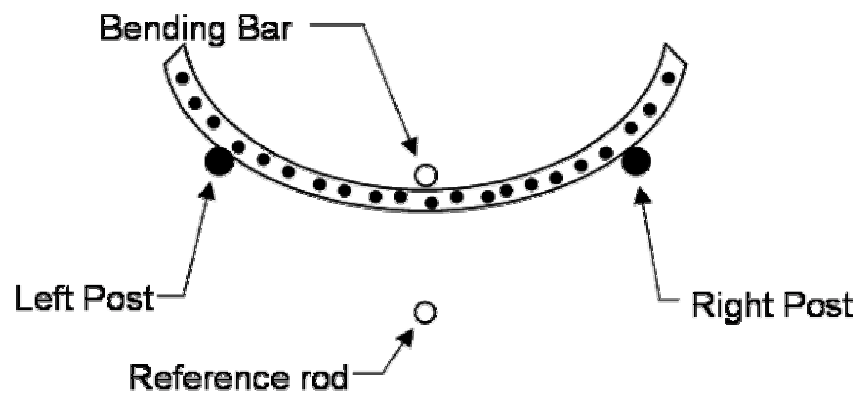


Figure 1-19 Example of the bending experimental set-up. The rectangular (~0.75 mm x ~12 mm) strip of specimen was positioned between two posts and forced into three-point bending at the center.

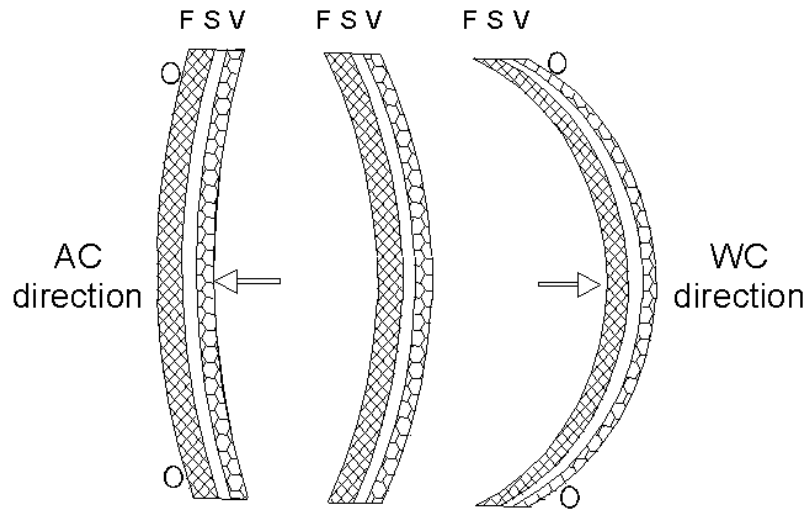


Figure 1-20 Schematic of heart valve tissue bending against (AC) and with (WC) the natural curvature of the leaflet. When the sample was bending in the AC direction, the fibrosa (F) was in tension and the ventricularis (V) was in compression, where S represents spongiosa. When the sample was bending in the WC direction, the ventricularis was in tension and the fibrosa was in compression.

The magnitude of the load, applied at the center of the specimen, was computed from the deflection of the bending bar with respect a reference rod to a resolution of ± 0.112 mg. The data file generated in the tracking steps of the bending testing apparatus in our laboratory was processed using a custom Matlab program. Based on the resolution, post coordinates, load, displacement, and marker coordinates, the program calculated the applied moment, M , and the resulting curvature, κ , of the specimen.

For each time point recorded, the coordinates of the specimen markers were fit to a quadratic equation using least squares regression:

$$y = ax^2 + bx + c \quad (1.1)$$

The curvature, κ , of the specimen at each time point was then calculated from the relation:⁽⁶⁷⁾

$$\kappa = \frac{y''}{(1+(y')^2)^{3/2}} \quad (1.2)$$

In which y' and y'' refer to the first and second derivatives of the quadratic equation, respectively. The applied bending moment M at the center of the specimen was calculated about the left post from the applied load P and the reaction forces at horizontal and vertical direction of the specimen F_x and F_y (Figure 1-21) using

$$M = F_x v + F_y u \quad (1.3)$$

in which the moment arms u and v , represent the horizontal and the vertical distance from the center of the specimen.

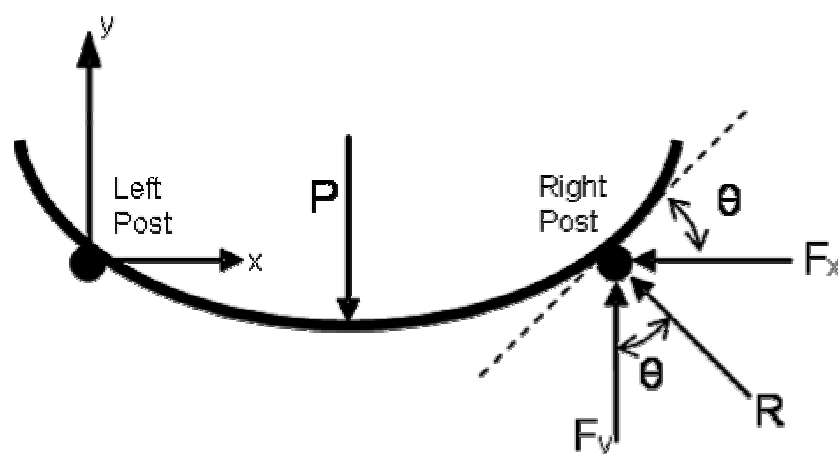


Figure 1-21 Representative force measurement under the three-point bending test.

To compute the effective stiffness, the Bernoulli-Euler moment-curvature relation⁽⁶⁷⁾ was utilized:

$$M = E_{\text{eff}} I \Delta \kappa \quad (1.4)$$

where E_{eff} is the effective stiffness, $\Delta \kappa$ is the change in curvature, computed as the difference between the initial specimen curvature and the deformed curvature. The moment of inertia of the specimen, I , was calculated from the following relation in which w and t are the width and the thickness of the specimen, respectively:

$$I = \frac{1}{12} w t^3 \quad (1.5)$$

The value for E_{eff} for each specimen was reported as the value at the center of specimen where the maximum M occurred. In practice, data was presented as M/I vs. $\Delta \kappa$ so that the slope of the curve is equal to E_{eff} . Due to the specimen structural heterogeneity, the value of E_{eff} represents the effective bending stiffness only for the current bending direction (Figure 1-20).

From the experimental results of bending test for both the native aortic and porcine BHV specimens, Sacks⁽³⁾ observed a nearly perfect response ($r^2 = 0.99$) in native aortic valves over the entire bending curve, with $E_{\text{eff}} = 5.3$ kPa in both flexed in the AC and WC directions (Figure 1-22). In contrast, uncycled porcine BHV demonstrated a bending direction dependent stiffness, with $E_{\text{eff}} = 216$ kPa in AC direction, and $E_{\text{eff}} = 72$ kPa in the WC direction (Figure 1-22). The maximum deflections in the center of specimen were also observed as 2.3 mm in AC

bending direction, and 0.95 mm in WC bending direction, respectively. Furthermore, Sacks observed uncycled porcine BHV demonstrated not only a 20-fold increase in stiffness compared to native tissue, but also an ~3: 1 ratio stiffness in the AC ($E_{\text{eff}} = 216$ kPa): WC ($E_{\text{eff}} = 72$ kPa) directions.

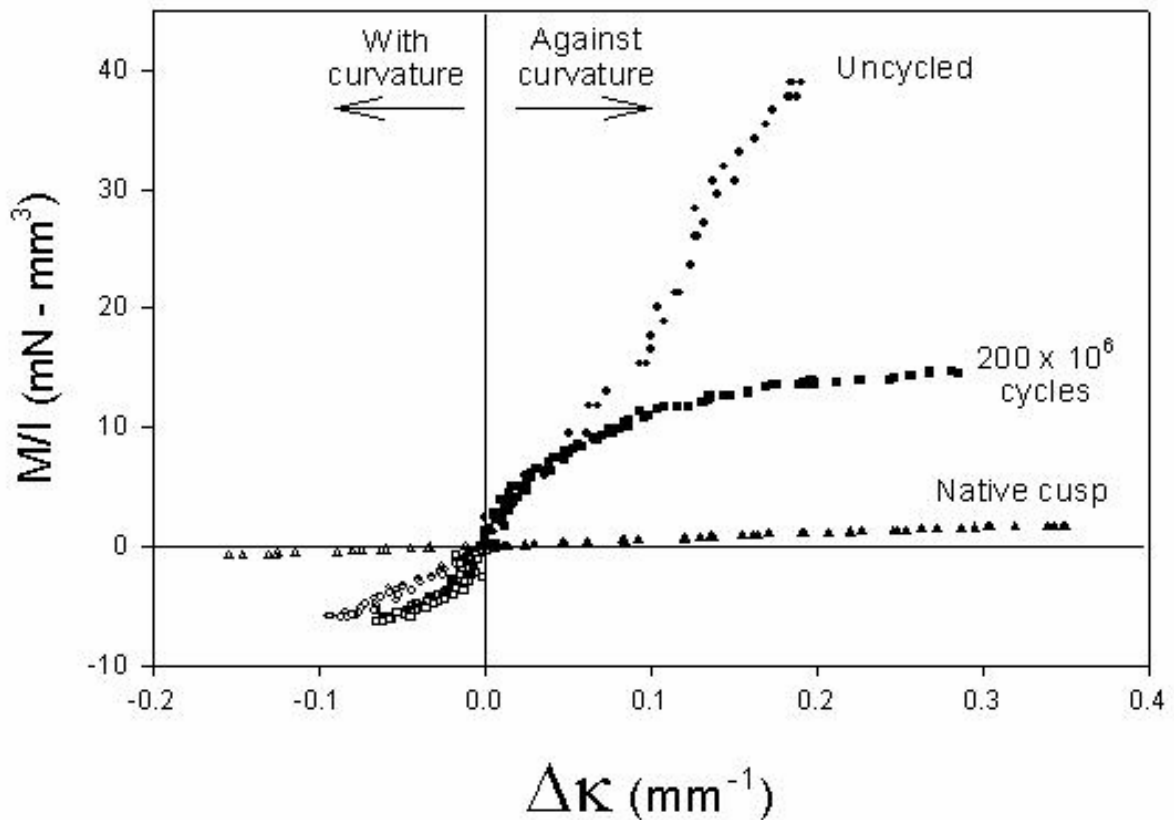


Figure 1-22 A representative M/I vs. $\Delta\kappa$ curve for native aortic valve leaflet demonstrated a linear response over the full range of flexure in both AC and WC directions. In contrast, and uncycled porcine BHV demonstrated a profound bending direction dependent increase in stiffness in AC and WC directions. After 200×10^6 cycles, the AC direction stiffness dropped substantially (adapted from Sacks, *et al.*^(3, 68)).

1.5.2 Effects of Flex Fatigue

Since porcine BHV are intuitively designed devices, they can only be iteratively improved based on results from time-consuming durability testing, animal implantation studies, and clinical trials. Unfortunately, while much research has focused on *in-vivo* testing, relatively little work has been done on understanding the mechanisms underlying BHV degeneration behavior.

In many studies, it has been hypothesized that mechanical fatigue and structural degradation are instrumental to *in vivo* failure. Broom⁽⁶⁹⁾ investigated the mechanical durability of glutaraldehyde preserved bovine and porcine mitral valve tissue in 1977. He showed that there was reduction in the degree of crimping in the fatigued tissue though the finding was from a uniaxial loading testing. This author also concluded that material disruption was not dependent upon the tensile load, but rather the compressive flexure upon unloading. However, the amount and direction of flexure was neither controlled nor quantified, nor were the results correlated to the method of chemical treatment or stress-state during fixation. Vesely *et al.*⁽⁷⁰⁾ studied the viscoelastic behavior of BHV under the accelerated pulse duplicator testing. The difference in stress relaxation was observed at low and high strain-rate stretching. However, the pulse testing subjected the tissue to lower-magnitude cyclic stress than did physiologic loading; the results may either overestimate or underestimate valve durability.

Purinya *et al.*⁽⁶²⁾ found an ~50% reduction in strength in human explanted porcine BHV after only 48 months, this results suggested that the changes in biomechanical properties of the porcine BHV during implantation. Vyavahare *et al.*⁽⁷¹⁾ reported an accelerated fatigue studies (5-500 million cycles) with glutaraldehyde fixed porcine BHV, and the mechanical

function of BHV caused progressive damage to the molecular structure of type I collagen as assessed by Fourier transform IR spectroscopy (FTIR) was observed. The cyclic fatigue caused a progressive loss of helicity of BHV cuspal collagen, which was evident from FTIR spectral changes in the amide I carbonyl stretching region. Furthermore, authors found evidences of BHV fatigue in these studies led to loss of GAGs from the extracellular matrix. They concluded that fatigue-induced damage to type I collagen and loss of GAGs was a major contributing factor to material degeneration in BHV deterioration.

In our laboratory, Gloeckner *et al.*⁽⁶⁶⁾ have studied changes in the flexure properties of porcine BHV subjected to accelerated wear testing under 0-, 50-, 100- and 200-million cycles. Specimens were prepared using previously described valve-preparation⁽⁷²⁾ and flexural experimental methods.⁽³⁾ From the experimental results,⁽⁶⁶⁾ a representative M/I versus $\Delta\kappa$ curve for a 200 million-cycles leaflet demonstrated a non-linear response over the full range of flexure (Figure 1-23). At 200 million accelerated wear testing cycles, bending stiffness decreased in both testing directions (Figure 1-24). Fatigue porcine BHV demonstrated a bending direction dependent stiffness, and an ~1.8: 1 ratio stiffness in the AC: WC bending directions were found, with $E_{\text{eff}} = 174$ kPa in AC direction, and $E_{\text{eff}} = 132$ kPa in the WC direction at early linear portion of M/I versus $\Delta\kappa$ curve (Figure 1-22). The rate of change in the AC direction was greatest, decreasing to about 50 % of the uncycled value at 200 million-cycles with Student's *t* test, $p < 0.05$ (Figure 1-24). There was no statistically significant change occurring in the WC direction (Figure 1-24). The increased occurrence of a non-linear response in the bending direction suggested that it is associated loss of stiffness and fatigue damage (Figure 1-22).

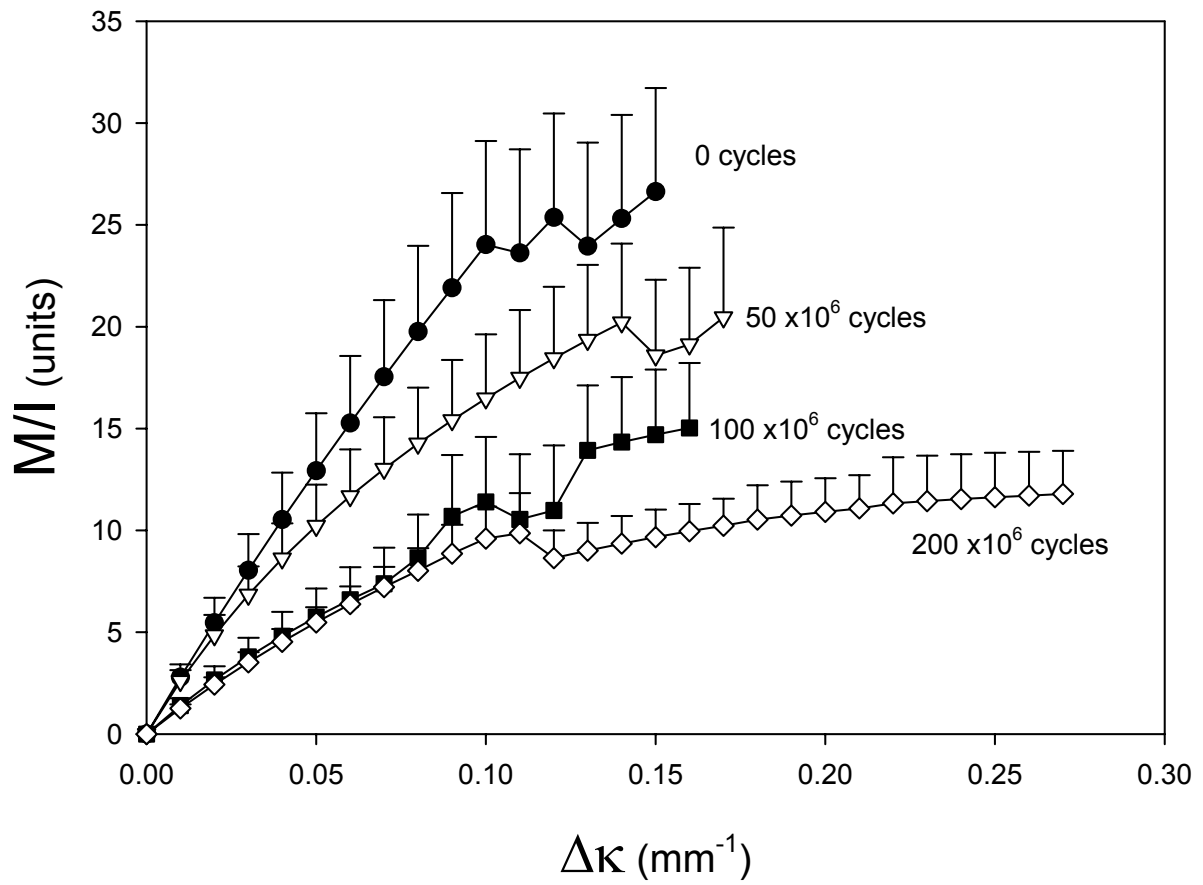


Figure 1-23 M/I versus $\Delta\kappa$ curve have different flexural behaviors at different cycles, and at 200 million-cycles leaflet demonstrated a non-linear response over the full range of flexure.

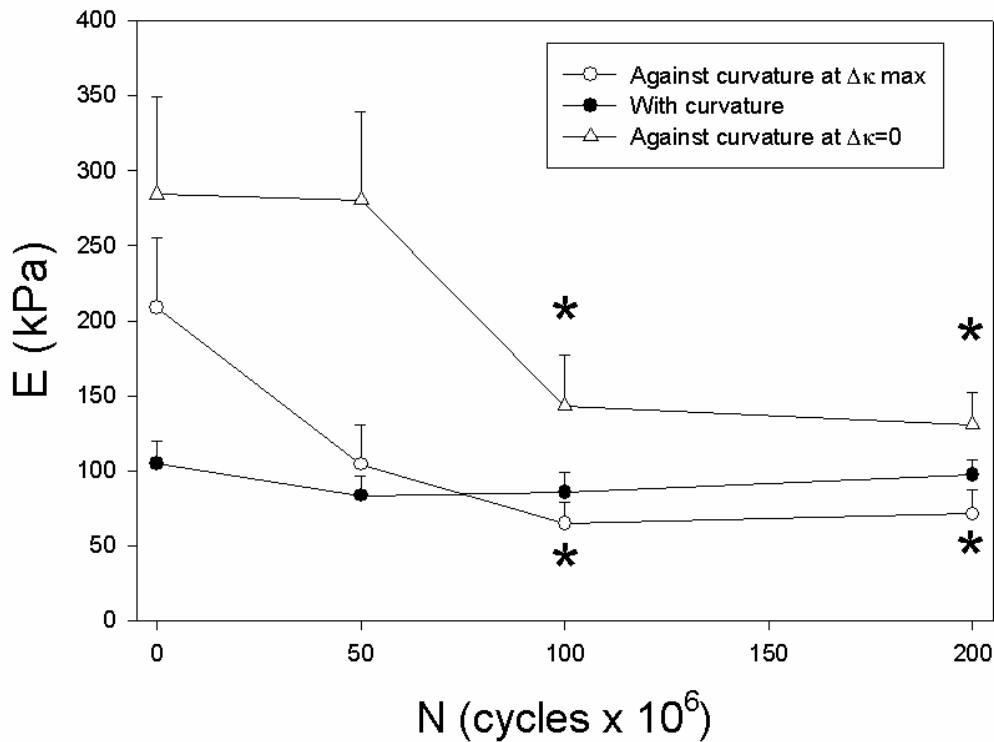


Figure 1-24 Changes in E_{eff} with the number of fatigue cycles (N) in the AC and WC bending direction, * = statistically significant ($p < 0.05$) different from 0 cycles. A substantial drop in stiffness with N was found only in the AC direction, with no statistically significant changes occurring in the WC direction (adapted from Sacks *et al.*⁽⁶⁸⁾).

Observations of the study in our laboratory can be concluded as following: the native tissue demonstrated a nearly perfect linear response over the entire bending curve, with equal slope (E_{eff} values) in both bending directions (Figure 1-22). Uncycled porcine BHV tissue demonstrated a sharply bilinear curve, with the ratio of E_{eff} between the AC and WC bending directions being $\sim 3 : 1$ (Figure 1-22). With progressive cycling at 200 million cycles, specimen demonstrated a non-linear response in the AC direction (Figure 1-22), with the ratio of E_{eff} between the AC and WC bending directions being $\sim 1.8 : 1$ (Figure 1-24). From those flexure

and fatigue testing results, Sacks *et al.*⁽⁶⁸⁾ hypothesized that the larger stiffness drop in the AC bending direction are due to that fibrosa was more effected by fatigue (i.e. large $\Delta\kappa$ value). However, the precise cause for the nonlinear behavior observed in the fatigued tissue M/I vs. $\Delta\kappa$ curves, and the associated increase in occurrence with fatigue, are unknown. Additional micromechanical studies are required to verify and explore these hypotheses in greater depth.

1.5.3 Limitations of Current Knowledge

Biological tissues are complex in their composition and structure. They usually have several different types of atomic bond aligned in different directions and have molecular chains that have a directional orientation. Studies used uniaxial tension loading^(62, 63) allow lateral contraction of the specimen during extension, which can further facilitate axial elongation. Biaxial testing does not permit this process,^(17, 65) and hence a material loaded biaxially with less stretches under the same axial load than one loaded uniaxially.

The complexity of the mechanical properties of the porcine BHV is underscored by the cuspal tri-layered structure (Figure 1-4). Biomechanically, each layer may not only have different intrinsic mechanical properties but are also loaded in tension or compression when the valve flexes during operation. Further, the presence and degree of either tensile or compressive stresses within each layer will change with bending direction. Clearly, how the tensile and compressive layer mechanical properties in flexure change with chemical fixation and especially fatigue due to in-vivo loading is critical to our understanding of poor porcine BHV long-term durability.

1.6 ALTERNATIVELY HEART VALVE REPLACEMENTS: BIOHYBRID AND TISSUE ENGINEERING APPROACHES

The recent focus on developing biohybrid and TEHV reflects the current state of mind in the field of small diameter vascular grafts—that the incorporation of a living cellular component may be essential for long-term biocompatibility and durability.⁽⁷³⁾ As discussed in the previous section, BHV constructed from non-viable, chemically-stabilized soft tissues such as porcine aortic valve and bovine pericardium perform remarkably well in the short-term post-implantation. The absence of an immunologically-recognizable cellular component, native-like mechanical properties, and the high degree of conservation of collagen structure across species are all thought to contribute to the superior biocompatibility of BHV when compared with mechanical valves. On the same token, however, the absence of a living cellular component leaves these tissues with no innate capacity for: (1) physiological collagen turnover, (2) self-repair of accrued fatigue damage, (3) resistance to calcification, (4) active resistance to infection, or (5) growth and remodeling.⁽⁷⁴⁾ While these clinically significant drawbacks have been recognized for a number of years, BHV continue to serve an important role in the treatment of valvular disease; BHV are arguably one of the most successful medical devices ever developed from biologically-derived materials. Their demonstrated reliability, however, has not stopped investigators in their search for the ideal heart valve replacement.

1.6.1 Biohybrid Approaches

The biohybrid concept was first applied to synthetic small diameter vascular grafts in the 1980s, and was later adapted for heart valves in the early 1990s. A biohybrid valve can be described as a combination of either a mechanical or bioprosthetic valve with a living cellular

component — specifically, an endothelium. The governing hypothesis driving the development of such valves is that an ideal prosthetic heart valve may be yielded by combining the durability of the synthetic materials traditionally used in mechanical valves (e.g., pyrolytic carbon) with the thromboresistance afforded by a living endothelium at the blood-biomaterial interface.⁽⁷⁵⁾ In the case of biohybrid valves based on BHV, the hope is that a confluent autologous endothelium may improve calcification resistance and help mask the immunogenicity of the xenogenic tissue.^(76, 77)

In general, the approach to making a biohybrid prosthetic valve has been to surface modify the synthetic materials to support cell attachment,⁽⁷⁸⁾ and subsequently to seed the blood-contacting surfaces of these valves with endothelial cells *in vitro*. Spontaneous endothelialization of BHV and biohybrid valves may occur *in vivo* via transanastomotic ingrowths, however the degree of coverage has been found to be species dependent, with only sporadic endothelialization observed in humans. Attempts to coat mechanical valves with endothelial cells have generally failed due to detachment of the cells upon exposure to fluid shear stress.^(79, 80) While coating BHV with endothelial cells has shown more promise, in particular in BHV fabricated using novel fixation or glutaraldehyde-detoxification schemes, it remains unclear if the presence of an endothelium on a BHV will significantly improve their long-term durability. An endothelium alone is not expected to completely mitigate mechanical fatigue damage, nor would an endothelial cell-lined valve be expected to grow or remodel, as may be required for a permanent pediatric replacement heart valve. In light of the high cost-to-benefit ratio of developing biohybrid heart valves, most of the focus in recent years has shifted to the development of TEHV.

1.6.2 Tissue Engineering Approaches

One of the primary factors motivating the development of tissue engineering technologies is the growing realization that no synthetic material is bioinert. Thus, the permanent implantation of any device constructed from synthetic materials (in particular, blood-contacting devices) will ultimately result in some form of foreign-body reaction. In some cases (e.g., hip replacement) the foreign-body reaction may be self-limiting, with acute inflammation followed by quiescent fibrous tissue encapsulation of the implanted device. In the case of blood-contacting devices, such as vascular grafts or heart valves, the result is generally more dramatic, with a lack of conventional healing consisting of chronic inflammation and/or thrombosis (Tissue Engineering of Vascular Prosthetic Grafts, P Zilla and HP Greisler, RG Landes Co., 1999). Tissue engineered cardiovascular devices aim to reconcile these biocompatibility issues by using biodegradable synthetic or natural materials which are designed to be resorbed and replaced by tissue.

Tissue engineering approaches generally begin with seeding cells onto a porous, three-dimensional substrate (i.e., a scaffold). During the subsequent incubation period, the seeded cells produce an ECM of collagens, proteoglycans, and other factors which imbibe water, thus giving rise to a tissue-like appearance. During the course of *in vitro* incubation the scaffold (e.g., polyglycolic acid (PGA)) degrades and is replaced by the ECM secreted by the cells. Ultimately, the engineered tissue consists of only cells and their secreted ECM, with no residual scaffold material.⁽⁸¹⁾ In the case of TEHV, the majority of the current literature can be roughly divided into two distinct approaches: the Mayer approach and decellularized approaches.

1.6.3 Mayer Approach

In the Mayer approach, TEHV have been fabricated as described above by seeding cells onto biodegradable synthetic scaffolds. Much of this work has been pioneered by Dr. John Mayer's laboratory at Children's Hospital Boston. In the Mayer approach, vascular smooth muscle cells (VSMC) are isolated from an excised blood vessel segment (e.g., from a sheep), expanded *ex vivo*, and seeded onto non-woven synthetic scaffolds, typically composed of PGA, poly-L-lactic acid (PLLA), and/or poly-4-hydroxybutyrate (P4HB; Tephra, Inc., Cambridge, MA).⁽⁸²⁾ The resultant constructs are then incubated for a short period of time (on the order of a few weeks) prior to implantation into the animal which donated the cells (i.e., an autograft). Mechanical conditioning of the TEHV *in vitro* prior to implantation has shown promise in the development of enhanced mechanical properties. It is hypothesized that mechanical stresses or strains directly stimulate the cells of the TEHV to secrete more collagen, thus yielding a stronger tissue.^(83, 84) While these TEHV have been demonstrated to successfully function in the pulmonary circulation of sheep for up to 20 weeks,⁽⁸²⁾ there remain issues to be addressed before such a design would be considered for clinical application.

1.6.4 Decellularized Approaches

The other major approach toward developing a TEHV relies on decellularized porcine valve tissue as the scaffold (e.g., Synergraft; Cryolife, Inc., Atlanta, GA).⁽⁸⁵⁾ Rather than subjecting a porcine aortic valve to glutaraldehyde fixation (as in the case of making a BHV), porcine aortic valves are decellularized by a detergent treatment, leaving the collagen and elastin tissue structure intact. It is hypothesized that these decellularized tissues will promote cellular infiltration following implantation, ultimately becoming completely repopulated with a patient's

own cells, which could then actively repair and remodel the tissue like a native valve. While the native-like mechanical properties and inherent bioactivity of these scaffolds are potentially attractive, there are a number of possible drawbacks to this approach, including the potential for viral transmission, and more fundamentally, the potentially immunogenicity of the unfixed xenogenic tissue. A recent report describes early clinical failures of these valves in pediatric patients, which may have been due to incomplete decellularization of the valve tissue, with a concomitant immune response.⁽⁸⁶⁾ As such, the fate of this branch of TEHV research is currently unclear.

1.6.5 Current Limitations of Tissue Engineered Heart Valve Approaches

Early engineered cardiovascular tissues lacked sufficient mechanical properties for sustaining *in vivo* hemodynamic conditions (blood pressure), and thus required additional mechanical support (e.g., Dacron sleeve).⁽⁸⁷⁾ Advances in our understanding of the factors influencing tissue maintenance and development have led to the implementation of bioreactors and mechanical conditioning regimens as a means of improving the mechanical properties of engineered tissues.⁽⁸⁸⁾ While several of these methodologies have been directly applied to the development of TEHV, the development of suitable and stable mechanical properties remains the single most important limitation of all TEHV approaches.

Specifically related to the current study, it remains unclear how the macroscopic strains imposed on a TEHV during *in vitro* mechanical conditioning are transduced to the cells. Hypothetically, the cyclic deformation (i.e., strain) experienced by a cell in a TEHV would be proportional to some measure of collagen biosynthesis or secretion. As mentioned previously, studies have been conducted to illuminate the role of specific modes of cyclic loading on the

development of TEHV.^(83, 84) While these and other studies have demonstrated relationships between cyclic loading and mechanical properties, the cellular level mechanisms responsible for these changes have yet to be elucidated.

Arguably, the second most important limitation of current TEHV approaches is cell availability. The majority of TEHV studies conducted to date have relied on arterial-derived smooth muscle cells as a surrogate for the valve interstitial cells (VIC).^(30, 34, 89) As will be discussed in a subsequent section on VIC, the phenotypic subtleties of the mixed VIC population are still under investigation, and thus the suitability of arterial smooth muscle cells as a functional substitute for VIC cannot yet be conclusively demonstrated. Moreover, arterial smooth muscle cells must be isolated from an artery; a carotid artery segment is commonly used in sheep studies. Thus, the mere isolation of such cells from a patient could potentially result in significant donor site morbidity. As such, a number of investigators are in the process of evaluating alternative cell sources, such as peripheral blood progenitor cells⁽⁹⁰⁾ and bone-marrow derived stem cells.⁽⁹¹⁾ However, while these cell sources may be attractive from the point of view of availability, once again, the suitability of these cells as a functional substitute for VIC remains to be investigated.

1.7 NEED FOR MICROMECHANICAL MODELING OF THE HEART VALVE TISSUES

In general, micromechanical (multi-scale) simulations aim to mathematically model the relationship between macro-scale and micro-scale material behavior (e.g., organ, tissue, and

cellular level mechanical interactions). In light of the numerical complexity and computational scale of many simulations, they are often implemented via the finite element method, a powerful technique which relies on the superior processing efficiency of a computer to approximate the response of otherwise intractable systems.

There currently exist a number of unresolved problems related to BHV failure and TEHV development in which investigation via micromechanical simulations might yield important, and otherwise undiscoverable, insights. In this section, two prototypical examples of such applications—one applied, and one basic—will be introduced for the purpose of illustrating the potential of micromechanical simulations in addressing multi-scale aortic valve biomechanics problems.

A fundamental unresolved issue in BHV failure is the mechanism of non-calcific (fatigue-related) tissue degeneration.⁽²⁾ Recent studies have demonstrated changes in the mechanical properties of BHV tissue with accelerated fatigue, including microstructural changes in the collagen fiber network, however the mechanism by which these changes occur, and moreover, the layer-specific changes, are as of yet unknown.⁽⁹²⁾ In light of the tri-layered structure of the aortic valve tissue used in fabricating BHV, micromechanical simulations in which the mechanical interaction between the three layers is modeled and related to the overall tissue behavior may be useful in elucidating the contribution of the individual layers to non-calcific tissue degeneration.

A more applied example is found in the *in vitro* mechanical conditioning of TEHV. As will be discussed in subsequent sections, TEHV fabricated by seeding vascular-derived cells onto synthetic scaffolds have demonstrated augmented tissue development in an *in vitro* pulsatile

flow environment.⁽⁸²⁾ While recent studies have proceeded to investigate the independent effects of the relevant modes of loading present in such an environment,^(83, 84, 93) micromechanical simulations of mechanotransduction from the tissue-level to the cellular-level could potentially yield a more fundamental, substrate-independent, basis for mechanical conditioning protocols. For example, studies involving two-dimensional cell culture on elastomeric membranes have demonstrated correlations between cyclic strain and collagen biosynthesis in smooth muscle cells.⁽⁹⁴⁾ Hypothetically, the cyclic deformation (i.e., strain) experienced by a cell in a three-dimensional TEHV would stimulate a proportional change in collagen biosynthesis, and thus, potentially, contribute toward the development of engineered tissue mechanical properties.

In conclusion, while the physiological function of the aortic valve occurs primarily at the organ-level, understanding native valve pathologies, BHV degeneration, and TEHV development uniformly call for a multi-scale appreciation of aortic valve mechanical behavior. Furthermore, the multi-scale mechanical interactions between the organ, tissue, and cellular level of the aortic valve may be particularly well-suited for investigation via micromechanical simulations.

1.8 CURRENT STATE OF BIOMECHANICAL STUDIES OF EXTRACELLULAR MATRIX

1.8.1 Interaction of Extracellular Matrix and Cell

Recently researchers have employed finite element methods to study the interactions of ECM and cells. These models typically involve mapping solutions between macroscopic and

microscopic domains. Based on different assumptions and finite element methods, validities of numerical models are restricted in their interactions. For example, attempts to develop computer simulations of collagenous tissues based on macroscopic property descriptions have often been limited in application by simplicity of the model; simulations based on microscopic descriptions have numerical limitations imposed by the size of mathematical problems.

For example, Baer and Guilak, *et al.*⁽⁹⁵⁻⁹⁸⁾ established a macro-micro finite element model to study the intervertebral disc (IVD) (Figure 1-25), and the macroscopic finite element solution was used to determine boundary conditions for a microstructural model. It was assumed that cells do not contribute to the mechanical properties of the tissue. The transversely isotropic material property was used in the IVD and the chondrocyte, which were listed in Table 1-1. The strain magnitudes observed in both the cell and the matrix were large compared to the far-field strain and exceeded the limits of infinitesimal strain theory (when the displacements and displacements gradients are small, second order terms were neglected in the displacement gradients; for infinitesimal deformation, one can differentiate displacements with respect to the current coordinates or the referential coordinates to evaluate the infinitesimal strain tensor).

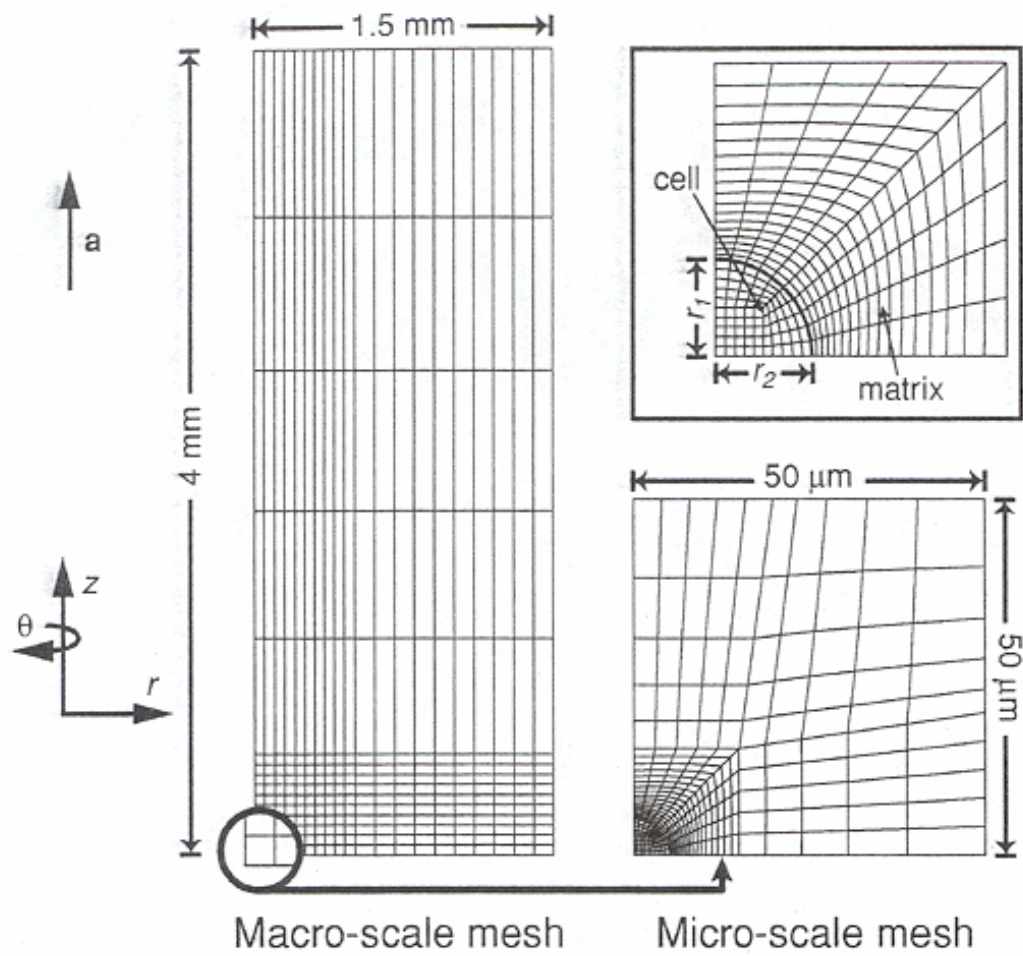


Figure 1-25 The multi-scale and axisymmetric finite element mesh (adapted from Baer, *et al.*⁽⁹⁹⁾).

Table 1-1 Material properties of the studies in the interaction of microscopic and microscopic models, in Which E represents elastic moduli, G represents shear moduli, and ν is Poisson's ratio.

Authors	Macroscopic tissue	Tissue property	Microscopic cell / fiber	Cell property
Baer <i>et al.</i> (2000)	Intervertebral disc cell (IVD)	Transversely isotropic: E = 0.25 MPa G = 0.1 MPa $\nu = 0.25$	Chondrocyte	Transversely isotropic: E = 9×10^{-4} MPa G = 4×10^{-4} MPa $\nu = 0.25$
Agoram <i>et al.</i> (2001)	N/A	N/A	Collagen gel	E = 150 MPa
Breul <i>et al.</i> (2002)	Muscle tissue	Neo-Hookean: E = 0.028 MPa G = 0.01 MPa $\nu = 0.45$	Myoblasts	Neo-Hookean: E = 2.8×10^{-3} MPa G = 1×10^{-3} MPa $\nu = 0.45$

Kouznetsova and Bouten *et al.*^(100, 101) adapted the representative volume element (RVE) as a microscopic domain (Figure 1-26), original introduced by Hill.⁽¹⁰²⁾ RVE was defined by Kanit *et al.* as:⁽¹⁰³⁾ “The RVE is usually regarded as a volume of heterogeneous material that is sufficiently large to be statistically representative of the composite: i.e., to effectively include a sampling of microstructural heterogeneities that occur in the composites. This is generally the principle adopted, and it leads to the fact that the RVE must include a large number of the composite micro-heterogeneities (grains, inclusions, voids and fibers, etc.). It must however remain small enough to be considered as a volume element of continuum mechanics.” However in the study by Kouznetsova and Bouten *et al.*,^(100, 101) these direct micro-macro approaches do not lead to an overall material description valid for the whole macroscopic piece of material, but

estimate the relevant stress-strain relationship at a macroscopic point by performing separate calculations on the RVE, i.e., microstructure, assigned to that macroscopic point. They assumed cells are firmly attached to the matrix and local cell deformations are determined by non-linear finite element analysis of the heterogeneous microstructure. The simulation showed that the heterogeneity in the microstructure has a profound impact on the resulting cell deformation.

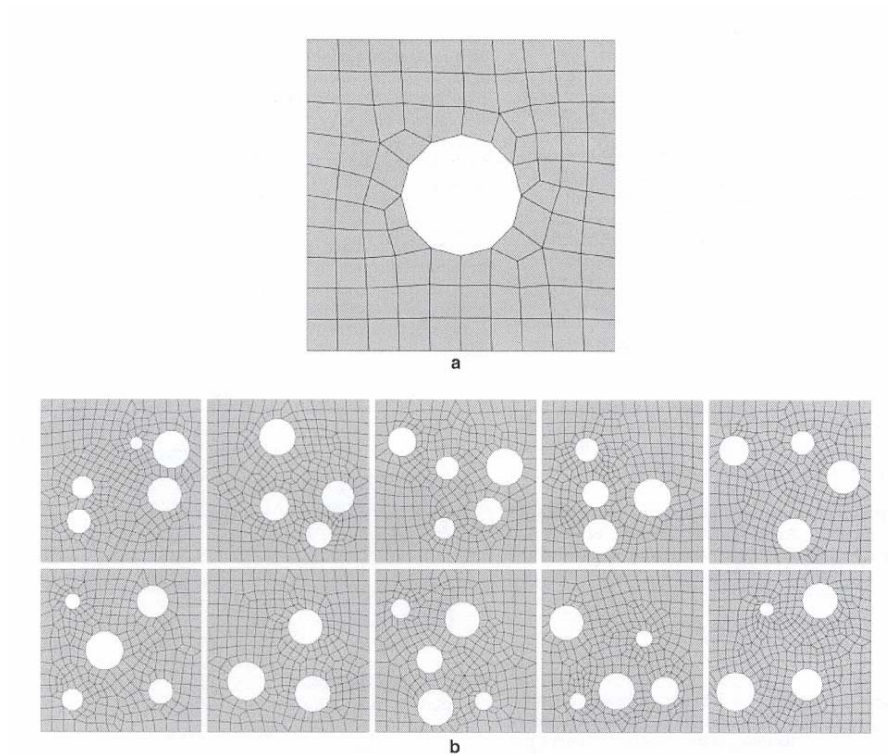


Figure 1-26 (a) RVE with one hole, representing a regular structure, and (b) ten random RVEs (adapted from Kouznetsova *et al.*⁽¹⁰⁰⁾).

Agoram, and Barocas *et al.*⁽¹⁰⁴⁻¹⁰⁶⁾ used an anisotropic biphasic theory to describe the mechanics of tissue equivalents (TE). Due to the assumptions that the macroscopic domain is

divided into finite elements and each element contains a microscopic scale network (Figure 1-27). Instead of stress constitutive equation, the macroscopic problem is distributed over the microscopic scale network and solved in each element to satisfy the formulation of Cauchy's stress continuity equation over the macroscopic domain. They assumed network fibrils (fibril segment between elements) reorient according to the local (macroscopic) deformation of the network, and cells reorient and migrate preferentially with the preferred fiber direction, and with cell alignment and migration measured in magnetically aligned networks. The material property of TE was listed in Table 1-1.

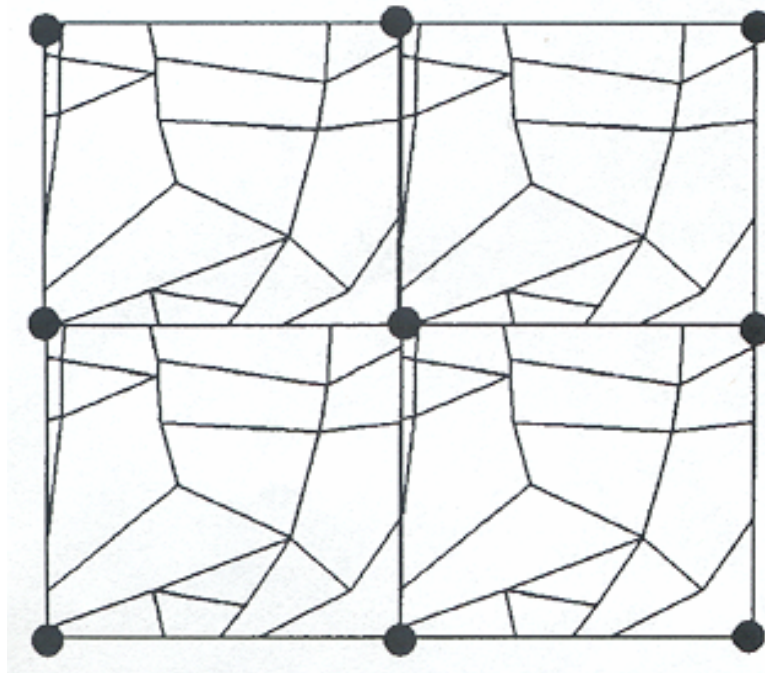


Figure 1-27 TE microscopic model was showed above, and macroscopic nodes were shown by solid circles.⁽¹⁰⁴⁾

Breuls *et al.*⁽¹⁰⁷⁾ used the multilevel finite element approach to predict local cell deformation in engineered tissue constructs (Figure 1-28). Cell deformations were predicted from the nonlinear finite element analysis of the microstructure, consisting of an arrangement of cells embedded in matrix material, so-called RVE. Effective macroscopic tissue behavior was derived by a computational homogenization procedure. Neo-Hookean material property was used in the muscle tissue of the macroscopic model and the myoblasts in the microscopic model, where engineering constants were listed in Table 1-1. Authors simulated the compression of a skeletal muscle tissue construct and studied the influence of microstructural heterogeneity on local cell deformations. The results showed that heterogeneity has a profound impact on local cell deformations, which highly exceed macroscopic deformations. Moreover, authors observed the microstructural heterogeneity and the presence of neighboring cells led to complex cell shapes and causes non-uniform deformations within a cell. However, this model cannot describe the bending mode, since the edges on opposite sides of the RVE deform in a similar way.

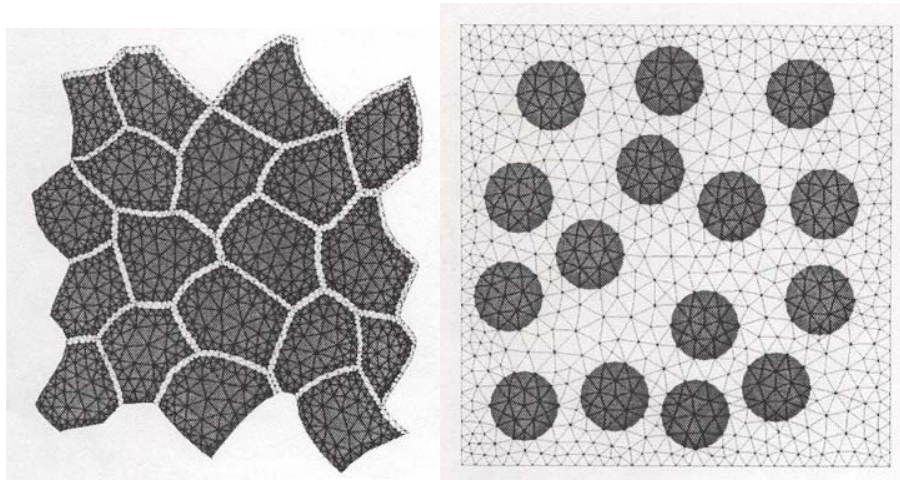


Figure 1-28 Finite element models of muscle tissue (left panel) and myoblasts (right panel).⁽¹⁰⁸⁾

Wakatsuki et al.^(109, 110) derive an integral constitutive relation for bio-artificial tissue models in terms of its cellular and matrix components to understand how the cells and matrix that comprise a tissue determine its mechanical properties. They translated the anisotropy of the microscopic cell distribution into anisotropic mechanical behavior of the macroscopic tissue. They assumed cells do not migrate within the matrix, and cells do not remodel in response to the mechanical stresses. However, this method only can be used in finite deformation stress analysis. Zahalak *et al.*⁽¹¹⁰⁾ used a combination of continuum and statistical mechanics to derive a constitutive equation for bio-artificial tissue, relating stress to deformation history, which makes explicit the separate contributions of cells and matrix. For a given matrix constitutive relation to deduce the mechanical properties of the cells from measurements on the tissue or, alternatively, knowing the mechanical properties of individual cells, authors predicted the mechanical behavior of the composite tissue. However, several assumptions authors had to

make, such as, (a) the small-strain tensor is adequate to describe the tissue deformation, (b) the cells deform with the continuum, and (c) the cells can be characterized mechanically by a Hill muscle model. Those assumptions led the cell contribution to the total tissue stiffness is somewhat higher relative to the matrix contribution, and release the assumptions could only led to the complexity of the problem.

1.8.2 Constitutive Models of Soft Tissues

Studies have used three-dimensional plane-stress constitutive equations to study the stress-strain relationship of soft tissues. The mechanical properties of tissues can be described by those constitutive equations, and must satisfy certain restrictions. Lanir⁽¹¹¹⁾ first proposed a structural theory for the homogeneous biaxial stress-strain relationship in two-dimensional flat tissues. These constitutive equations only applied for isotropic soft tissue in finite static deformation.⁽¹¹²⁾ After that, constitutive equation for fibrous connective tissues derived from the strain-energy function was proposed in 1983.⁽¹¹³⁾ In this study, Lanir considered general cases in which the fibers are elastic and the matrix hydrostatic pressure is a unique function of the strain. Several assumptions were made regarding the tissue's structure leading to a mathematical form:

1. Each fiber is thin and perfectly flexible. It has no compressive strength and if contracted will buckle under zero load.
2. The effect of the matrix flow during deformation is that of a hydrostatic pressure.
3. Each fiber is subjected to a uniaxial strain, which is the tensorial transformation of the overall strain in the fiber's direction.

1.8.3 Constitutive Model of the Heart Valve Tissue

For general form of linear equations of motion in three-dimensional, Horowitz, *et al.* ⁽¹¹⁴⁾ developed a constitutive law for the myocardium. This constitutive equation was derived from the divergence of Cauchy stresses that requires the sum of the external tractions applied on the tissues plus the hydrostatic pressure p . In order to incorporate the histological data into the material laws, several basic assumptions regarding the mechanical behavior of the myocardium precede the formulation itself:

1. The myocardium may be treated as a hyperelastic material, i.e., there exists a strain energy function from which the stresses are derived.
2. The fibers that comprise the myocardium are thin and extensible, but do not resist compression.
3. The fluid matrix carries only hydrostatic pressure, which in turn is affected by length and configuration changes of the fibers.

In our laboratory, Sun *et al.* ⁽²³⁾ developed an appropriate constitutive model to predict the mechanical behavior under generalized loading states. An interpolation technique for the pseudo-elastic response to guide modification of the final model form was utilized. A seven parameter modified Fung model utilizing additional quadratic terms was developed to perform rigorous experimentation involving all functional deformations. This constitutive model included high in-plane shear stresses using glutaraldehyde treated bovine pericardium as the representative BHV biomaterial.

Few studies have focused specifically on developing constitutive models to describe the material behavior of native aortic valves. Driessen *et al.*⁽¹¹⁵⁾ developed a constitutive model to relate the fiber configuration to the tissue stress within the aortic valves. The constitutive model was extended with a structural parameter, the fiber volume fraction, to account for the amount of fiber present within the material. The authors hypothesized that collagen fiber reorientation was induced by macroscopic deformations and the amount of collagen fibers was assumed to increase with the mean fiber stretch. The results showed the computed preferred fiber orientation runs from commissure to commissure and resembles the fiber direction in the native aortic valve.

In our laboratory, Billiar and Sacks^(19, 116) extended upon the work of Lanir^(111-113, 117, 118) by developing constitutive models specific to native aortic valve and its material property can be described by only three parameters.^(19, 116) This model was able to fully simulate the highly anisotropic and nonlinear in-plane biaxial mechanical behavior and account for the effects of small misalignments in the leaflet specimens with respect to the biaxial test axes that increased the accuracy of the model material parameters (Figure 1-29). This structural model which incorporating fiber orientation data⁽¹¹⁹⁾ for native tissue, it is assumed that the tissue behaves as a hyperelastic material, where, the tissue stress is the sum of a matrix stress and a cell stress where cells follow the deformation of the surrounded tissue continuum.

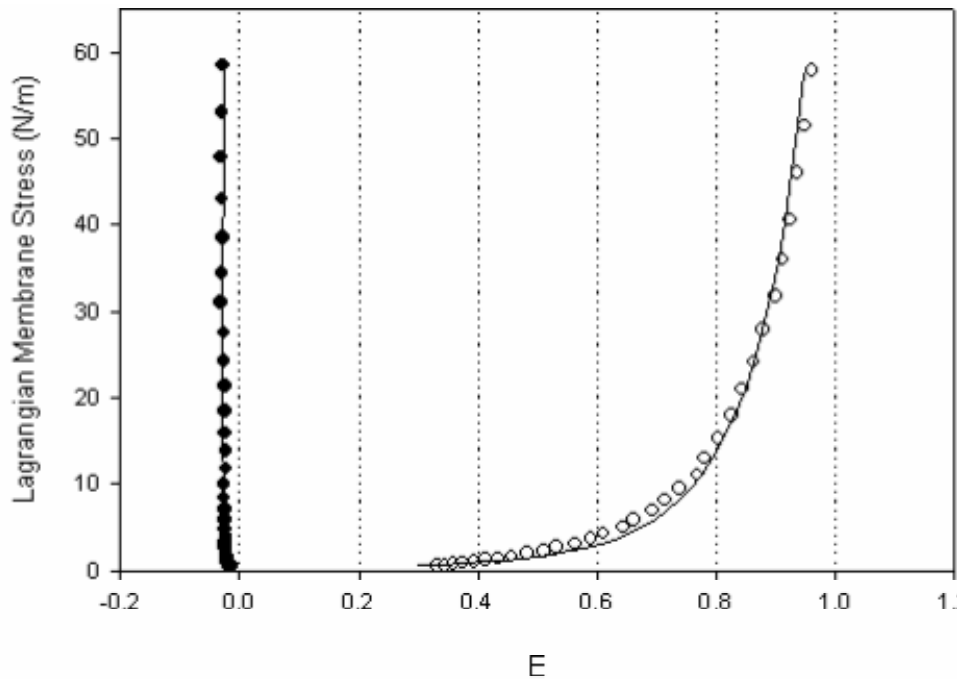


Figure 1-29 The structural model is able to fully simulate the highly anisotropic and nonlinear in-plane biaxial mechanical behavior.^(19, 116)

1.8.4 Numerical Studies of the Heart Valve Tissues

Many computer-based models of native heart valves were studied focusing on the leaflet morphology to the requirements of proper valve functions. Simulations of the aortic valve incompetence by varying the tissue thickness and anisotropic elastic moduli which are increasing with age and Marfan syndrome were studied.⁽¹²⁰⁻¹²⁴⁾ Reduction of leaflet deformation and restriction of coaptation were found in the studies. Grande-Allen *et al.*⁽¹²⁰⁻¹²⁴⁾ found stresses varied across the valve due to the inherent morphologic asymmetry and stress sharing. They concluded these findings could be utilized to evaluate the root-valve relationship in the BHV.

Gnyaneshwar *et al.*⁽¹²⁵⁾ studied the stresses developed during the cardiac cycle in aortic valve. Three-dimensional dynamic finite element model was used to exam the equivalent stress (von-Mises) during the closing and opening phases. Pressure patterns during the cardiac cycle were given in to the simulation and linear elastic model was assumed for the material. Authors observed an increase in stress at the coaptation surface during closure, and an increase in stress as the point of attachment of the leaflet to the root is approached from the free surface.

Hart *et al.*⁽¹²⁶⁾ studied the fluid-structure interaction in the aortic valve by using the finite element method to address the importance of systolic operation on the valve's functionality. The results showed that during systole the leaflets of the stented valve appear to be moving with the fluid in a kinematical process governed by the fluid motion. However, the parameters (material properties) in the model didn't attain a physiological correct behavior, and the sources of the parameters were not referenced. Thus, the development of valve models that more closely resemble the physiological situation with an anisotropic material behavior was under the investigations in their laboratory.

Shear effects in the native aortic and porcine BHV tissue have been studied by using Fung's quasi-linear viscoelastic theory.⁽¹²⁷⁾ The experimental data was implemented in to the quasi-linear viscoelastic theory and seven parameters were obtained from the fitting. The results of shear showed the huge differences between native and porcine BHV, whereas little or no difference was observed when the same tissues tested uniaxially. Chew *et al.*⁽¹²⁸⁾ simulated the failure mode in a porcine BHV. Hyperelastic material property was used for all three symmetrical leaflets. Progressive damage was observed in the model at the location where tears have been found *in vivo*.

Finite element bileaflet pericardial BHV have been studied by many groups to investigate the flexural stresses distribution. Krucinski *et al.*⁽¹²⁹⁾ simulated flexure patterns in three-dimensions during complete valve opening, and the stress distributions indicated flexural stresses induced near the commissures and within the free margin. A linear isotropic material of the leaflets was assumed in the model. This finding supported that an important mode of mechanical failure of tissue valves in flexural damage induced during valve opening. Three-dimensional stress analysis of Sheffield pericardial bicuspid valve has been studied by Thornton *et al.*⁽¹³⁰⁾ The leaflets with linear elastic materials were modeled during closure, and with subsequent pressurization conditions. The highest stress was observed at the top of the stent posts in the regions of commissures. Patterson *et al.*⁽¹³¹⁾ compared the results of linear and nonlinear simulations of the leaflets in a bicuspid bovine pericardium BHV. The results showed that the nonlinear model was more responsive to the time-varying pressure wave, and deformed into more complex shapes during the cardiac cycle, which induced lower compressive but higher tensile stresses in the leaflets.

Burriesci *et al.*⁽¹³²⁾ studied influence of anisotropy on the mechanical behavior of mitral valve. The results showed that even a small amount of anisotropy can significant affects the mechanical behavior of the valve, and that an appropriate orientation of the fibers can contribute to optimizing the stress distribution in the leaflets. Dynamic finite element implementation of mitral valves was studied by using hyperelastic finite strain, non-linear strain-energy function.⁽¹³³⁾ The constitutive equations were developed based on the reduced Hughes-Liu shell, which was suitable for relating Cauchy stress to the rate of deformation. This method was validated by an analytic solution and compared with a non-linear transversely isotropic

inflation problem. They concluded this study provided a method to model biologic membranes with an experimentally driven strain-energy function.

1.8.5 Limitations

The macro-micro finite element model from the studies of Baer and Gulik *et al.* (Table 1-2),⁽⁹⁵⁻⁹⁸⁾ a large intervertebral disc ECM within a cell in the center was created. Only the macroscopic model was simulated since the assumption of cells do not contribute to the mechanical properties of the ECM. Thus, the results were restricted to equilibrium deformation states, since many important transient phenomena that occur in the local cellular environment could not be explicitly studied. Furthermore, certain matrix properties and cell geometries led to strains that exceeded the limits of infinitesimal strain theory due to the size of the model.

Agoram, and Barocas *et al.*⁽¹⁰⁴⁻¹⁰⁶⁾ used an anisotropic biphasic theory to describe the mechanics of tissue equivalents (Table 1-2). But this model over-predicted experimentally observed forces for an anisotropic tissue equivalents parallel to the direction of alignment due to the model assumed that every crossover point in a scanning electron micrograph is a crosslink. Furthermore the density of crosslink is overestimated because the assumption, which contributes to the discrepancy between the model predictions and the observed data. Since fictional segments connect the ends of fiber segments introduced bending and for an anisotropic mesh stretched in the direction of alignment, the fictional segments experience little deformation of load, thus, the fictional segments do not undergo large-scale deformation. Thus, the nature of the microscopic network is limited in this study.

Table 1-2 Micromechanical studies by other researchers: (a) Intervertebral disc (IVD),⁽⁹⁵⁻⁹⁸⁾ (b) tissue equivalents (TEs),⁽¹⁰⁴⁻¹⁰⁶⁾ (c) representative volume element (RVE).^(100, 101, 107)

Authors	Tissue	Finite element mapping method	Assumptions	Results	Limitations
Baer <i>et al.</i> (2000)	Intervertebral disc (IVD)	Macro – Micro	Cells do not contribute to the mechanical property of the tissue; Finite deformation	Elongated cells lower the strain distributions proximal to the cell	Lack of applications in microscopic modeling
Agoram <i>et al.</i> (2001)	Tissue equivalents (TEs)	Micro – Macro	Cells deform with the continuum; Large deformation	Over-predict forces for the TE on the preferred direction	Lack of strength consideration in macroscopic model
Breul <i>et al.</i> (2002)	Representative volume element (RVE)	Micro – Macro	Cells deform with the continuum; Large deformation	Macroscopic mechanical property depends on cell density	Can not describe bending mode

Breuls *et al.*⁽¹⁰⁷⁾ proposed a direct micro-macro method (Table 1-2). The results of macroscopic deformations varied strongly throughout the macroscopic body. Thus, also the imposed RVE deformations were highly dependent on the location in the macroscopic body. The heterogeneity of the microstructure results in a range of averaged strain energy densities per cell within a RVE. Depending on the architecture of the microstructure and location of the RVE this averaged cell strain energy density range can be large, indicating that individual cells can experience deformations which highly exceed the macroscopic deformation. The micro-macro strategy from the study of Kouznetsova⁽¹⁰⁰⁾ provided an approach to determine the macroscopic response of heterogeneous materials with microstructural characteristics (Table 1-2). However, when this method was applied, macroscopic constitutive behavior was left out; large deformations can not be calculated accurately.

1.9 MOTIVATION AND SPECIFIC CONTRIBUTION OF PRESENT STUDY

Heart valves are replaced in approximately 285,000 patients each year, with tissue valve replacement accounting for approximately 40%.⁽³⁾ As the number of the BHV implanted for over fifteen years increased, deficiencies in long-term durability became the paramount problem. Recent studies of clinical explants, including comparisons of the localization of collagen fiber disruption to regions of calcification, have revealed prominent and diffuse structural damage independent of calcification.⁽²⁾ Previous experimental results generated in our laboratory on the porcine BHV leaflet indicated that fatigue results in a dramatic loss in flexural stiffness. However, the mechanism underlying this non-linear flexural behavior has yet to be explained.

Furthermore, evidence showed that ECM and cell phenotype in TEHV prepared *in vitro* and implanted *in vivo* can undergo remodeling, and eventually have cellular and matrix features resembling the native valve.⁽⁴⁾ These observations, coupled with the growing interest of the tissue engineering community in understanding the mechanical interactions of cells with ECM, led us to hypothesize that numerical simulations of cell deformations might provide key insight into a broad spectrum of questions related to cell/ECM interactions, including but not limited to: mechanisms of native aortic valve degeneration, TEHV development, and native heart valve homeostasis.

The goal of the current study is using micromechanical approach to model the BHV flexural behavior and quantify the cellular-level VIC nuclei deformation response to the mechanical stimulations in the ECM. Specifically, the aims of this study are:

1. We hypothesize that the changes reported in the effective porcine BHV leaflet flexural stiffness are layer specific. This study is focused on (a) determining how changes in the individual layer properties due to chemical fixation in the porcine BHV through the finite element simulations. (b) We hypothesize that the occurrence of non-linearity in the flexural response arises from the fatigue. (c) The study also focuses on simulating how changes in the individual layer properties in the porcine BHV leaflet change with fatigue.

2. We propose to quantify the deformation of VIC nuclei under various physiologically relevant levels of transvalvular pressure. (a) We hypothesize that a relationship may exist between the valve tissue layer and the deformation experience by VIC nuclei under applied pressure. (b) We also aim to quantify the distribution of the VIC nuclei deformation across the thickness of the tri-layer aortic valve leaflet. (c) We aim to model the effect of transvalvular pressure on the VIC nuclei deformations in the native tissue by finite element method and investigate the mechanocytes of the VIC nuclei. The results of the deformation and local mechanical environment of VIC nuclei can guide to develop an understanding of VIC / ECM mechanical interactions.

2.0 MODELING THE FLEXURAL BEHAVIOR OF THE NATIVE AORTIC AND THE PORCINE BIOPROSTHETIC HEART VALVE LEAFLET

In this chapter, we sought to establish a more quantitative understanding of the individual layer flexural behavior of native aortic, uncycled, and fatigued porcine bioprosthetic heart valve (BHV) leaflet. A finite element approach was used to void the kinematic restrictions inherent in beam approximations to solve for the flexural stress-strain as a full three-dimensional problem. Parametric studies were conducted by using finite element simulations in order to optimize the appropriate model to previously reported data on the flexural response of native aortic, chemically treated, and fatigued porcine BHV leaflet.^(3, 66, 68)

2.1 OVERVIEW OF THE FINITE ELEMENT IMPLEMENTATION

Beam theory is a one-dimensional approximation of a three-dimensional continuum mechanics due to the slenderness assumptions: the dimensions of the cross-section are small compared to typical dimensions along the axis of the beam. The main advantage of beam elements is that they are geometrically simple and have few degrees of freedom. This simplicity is achieved by assuming that the member's deformation can be estimated entirely from variables

that are functions of position along the beam axis only. However, beam element was not used in this study due to its certain assumptions that may not apply to our further analysis and applications. Furthermore, since analytical approach with kinematics limitations to a three-dimensional non-linear flexural problem in soft tissues requires rigorous formulations, finite element modeling was chosen in this study.

2.1.1 Nonlinear Finite Element Modeling of Heart Valve Tissue Leaflet Flexural Behavior

In the native aortic and porcine BHV leaflets bending simulations, the modeling approach utilized non-linear continuum mechanics to describe the experimentally measured flexural behavior. In the nonlinear finite element analysis the solutions cannot be calculated by solving a single system of linear equations, therefore, Newton's method is used for finite element program. Detailed non-linear finite element solution procedure by Newton's method was presented in Appendix A.

This study focused on the transmural strain distributions of aortic and porcine BHV leaflets under flexure, three-dimensional continuum element was required. However, the fully integrated isoparametric continuum elements, in both two and three dimensions, are too stiff in modeling the simple flexural deformation of a beam. Although full-order integration elements can represent strain and displacement fields exactly, they tend to "lock" in bending problems because a disproportionately large shear-related strain energy arises, which greatly increases the flexural rigidity of the model.

Second-order reduced-integration isoparametric elements can reproduce quadratic displacement fields, and in the evaluation of the element strain energy eliminates the shear-

locking phenomenon, thus enabling the elements to model a pure bending response without any shear strains. In this case multiple elements through the thickness (transversal direction) are required to model the bending response accurately. However, reduced-integration element has a serious drawback if there are too few kinematic boundary conditions, which it can result in mesh instability, commonly referred to as "hour-glassing." Flanagan and Belytschko (1981) and Belytschko *et al.* (1984) described a control technique and this method involves the construction of generalized hourglass strains that are orthogonal to the rigid body modes. Hourglass stresses are related to the hourglass strains through stiffness parameters. These stiffness coefficients are relatively small when compared with the actual stiffness of the material. Based on these considerations, second-order reduced-integration isoparametric elements, hexahedra, incorporating hour-glassing control were used in the flexural behavior simulations.

2.1.2 User-Defined Material Properties

To capture the layer moduli, i.e., tensile and compressive material properties in different layer of native aortic and porcine BHV leaflets, different material properties were required. However, the available built-in material properties in many commercial finite element programs were restricted to characterize biomaterial behaviors, most numeric simulations started to be realized via custom code.⁽¹³⁴⁾

To incorporate a user-defined material property into a commercial available code, one generally needs to follow the procedure in Figure 2-1. ABAQUS (ABAQUS, Pawtucket, RI) was used as a platform for numerical implementation; utility-routine and solution-dependent variable coded by Fortran (Digital Equipment Co., Nashua, NH) were incorporated into ABAQUS through its user subroutines user-defined field. This code was generated for adjusting

the material property matrix based on the finite element method calculated bending stresses at each time increment in each element.

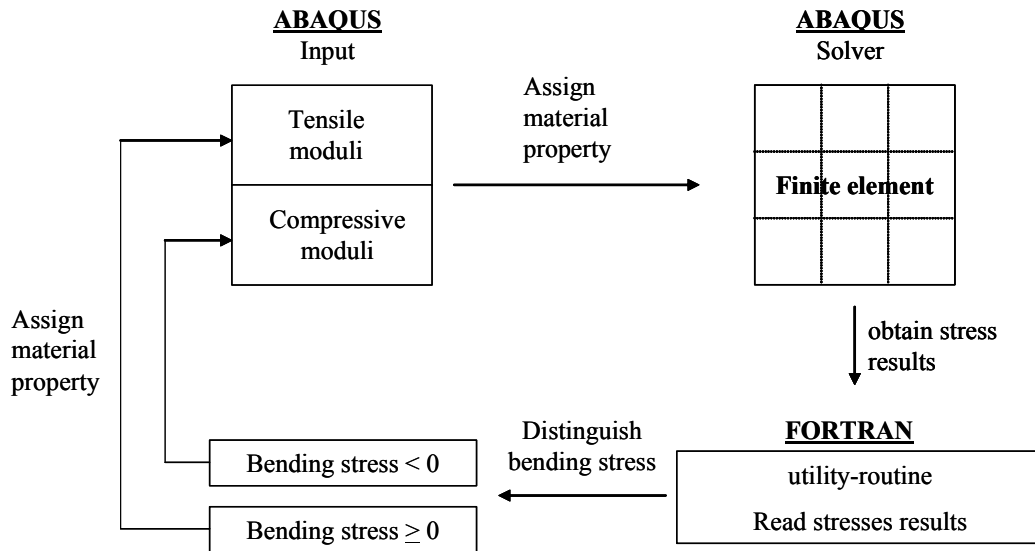


Figure 2-1 A flow chart for finite element implementation of solution-dependent variables.

General steps of incorporating the user-defined field to simulate the bending test as following:

1. During the finite element modeling, assign tensile moduli to the elements would be subjected to tensile loading and assign compressive moduli to the elements would be subjected to compressive loading during finite element bending simulation.
2. Custom utility-routine coded by Fortran accesses integration points and obtains resultant bending stresses at current time-increment in each element.

3. Custom user-defined field coded by Fortran distinguish positive and negative bending stresses.
4. Custom solution-dependent variable assigns tensile moduli or compressive moduli to the elements with appropriate moduli for next time-increment bending simulation.
5. Follow step 2 to step 4 until the solution of bending simulation converges based on the Newton's method algorithm in ABAQUS.

2.2 METHODS

The composite beam model needs to describe the essential micromechanics of the tissue, but avoids the need for a detailed description of tissue structure. It is known that the valve leaflets consist of three layers: the ventricularis, spongiosa, and fibrosa (Section 1.1.4), since the spongiosa is rich in glycosaminoglycans and low in collagen and elastin, it was thought to be structurally unable to support significant tensile or compressive loads.⁽¹³⁵⁾ Furthermore, it was likely that a significant degree of bonding occurs between these layers, as they have been shown to interact mechanically with enough force to induce residual stresses in the native leaflet.⁽¹³⁶⁾ Sacks, *et al.*⁽⁶⁸⁾ found no evidence of strain discontinuity across the layer boundaries in either the against (AC) or with (WC) the natural curvature bending directions (Figure 1-20) for both native and chemically-treated tissues, as would be expected if there was sufficient layer slip occurred. Collectively, these findings suggest that the fibrosa and ventricularis layers are sufficiently bonded that slip between the layers was negligible. Based on these considerations, a bi-layer

composite beam model was developed for the native aortic and porcine BHV leaflets in flexure, representing the major load bearing layers: the fibrosa and ventricularis.

2.2.1 Composite Model Development

Two-layered composite beam models were generated using a commercial finite element pre- and post-processing program Altair® Hypermesh® (Altair, Troy, MI), with overall model dimensions of 10 mm x 0.75 mm x 0.3 mm according to the specimen geometry from the three-point bending experimental set-up.⁽⁶⁶⁾ Equal thickness of each layer was incorporated, and local x, y, z Cartesian coordinates were used among the elements of the models, where x represents the longitudinal direction, y represents the transversal direction, and z represents tangential direction (Figure 2-2). The experimental three-point bending test was conducted by applying the deflection of the bending bar with respect a reference rod as mentioned in Section 1.5, and since our studies focused on reproducing the bending behavior of the experiments,⁽⁶⁶⁾ deflections were then applied on the center of the composite beam models.

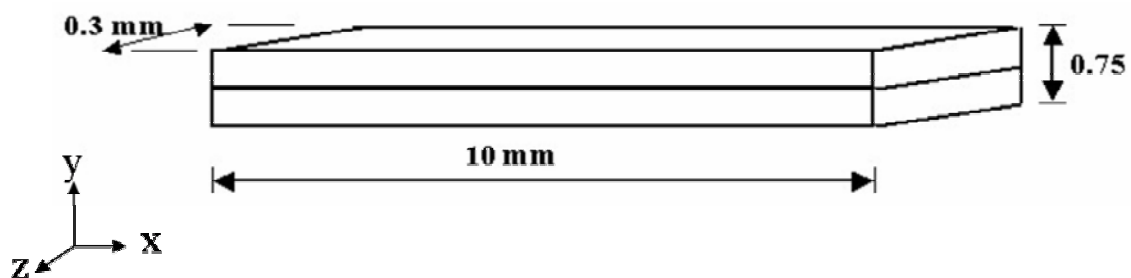


Figure 2-2 Schematic diagram of the Cartesian coordinate representation of a two-layer porcine BHV specimen composite beam model.

The boundary conditions of our composite beam models was using standard three-point bending test method, described in Section 1.5,⁽⁶⁶⁾ where the translational degrees of freedom at the left hand side of the model was constrained, out-of-plane and transversal motions at the right hand side of model were also constrained, and the model was free to slide in the longitudinal direction at the right hand side (Figure 2-3). Furthermore, to simulate the three-point bending experiments performed in our laboratory as mentioned in Section 1.5,⁽⁶⁶⁾ composite beam models were required to deflect 2.3 mm on the center of the beam in the AC bending direction and 0.95 mm in the WC bending direction (Figure 2-4).

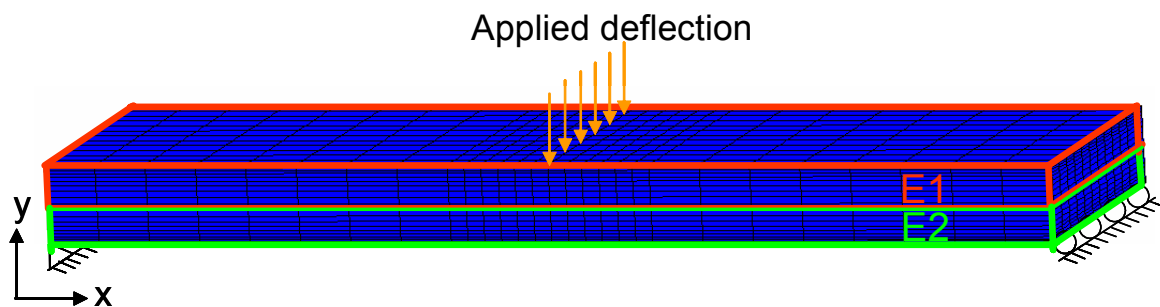


Figure 2-3 Boundary conditions for the bi-layer composite beam model required to simulate the flexural behavior under three point bending, in which E1 and E2 represent different linear, or non-linear layer moduli.

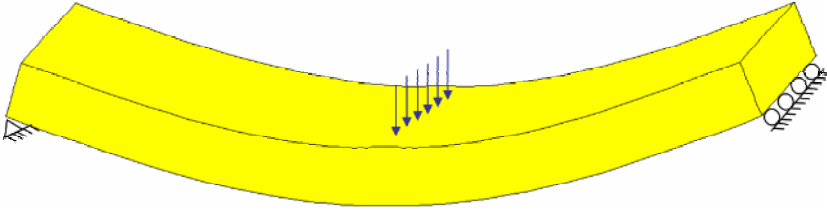
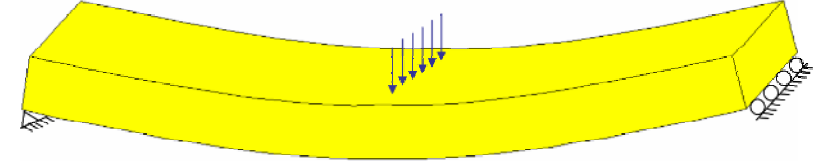
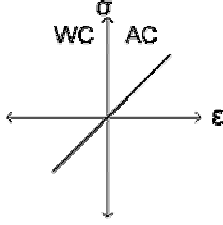
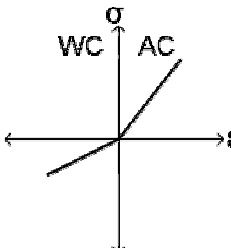
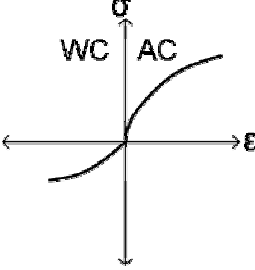
Bending direction	Three-point bending simulation	Applied deflection (mm)
AC		2.3
WC		0.95

Figure 2-4 The boundary conditions of the composite beam models were required to deflect 2.3 mm on the center of the beam in the AC bending direction and 0.95 mm in the WC bending direction based on the previous experiments.⁽⁶⁶⁾

An incompressible isotropic material was used over all models based on the available data suggesting that the native aortic and porcine BHV tissue contain mostly water.⁽¹³⁷⁾ Since the experimental setup could only measure the effective stiffness (E_{eff}) of the whole specimen structure (Section 1.5), and it was unable to yield information on the individual layer property, parametric study was required. Furthermore, native aortic valve leaflet was found with same tensile and compressive moduli, the uncycled porcine BHV leaflet was found with different linear tensile and compressive moduli, and fatigued porcine BHV leaflet was found of

consisting different non-linear tensile and compressive moduli (Figure 1-22),^(3, 68) three different classes material property of the composite beam models were studied (Table 2-1).

Table 2-1 Three different classes material property of the composite beam models based on the previous experimental findings (Figure 1-22).⁽⁶⁶⁾

Tissue	Material Property
Class 1: native aortic valve (Uni-modular: $AC = WC$)	
Class 2: chemical-treated uncycled BHV (Linear bi-modular: $AC \neq WC$)	
Class 3: fatigued BHV (Non-linear bi-modular: $AC \neq WC$)	

In addition, according to the study by Yu *et al.*,⁽¹³⁸⁾ if a model is prismatic and made of a homogeneous Hookean material, the centroidal axis is the neutral axis. If the material of the

model is heterogeneous but layered, with each layer having a different stress-strain relationship, the neutral axis does not coincide with the centroidal axis, and shifts toward to the stiffer layer.⁽¹³⁹⁾ Since porcine BHV tissue is not homogeneous and likely has different tensile and compressive mechanical properties,^(3, 68) the location of the neutral axis is required to be tracked throughout the finite element simulations in order to determine the appropriate stress-strain relationship.

To compute E_{eff} in both the AC and WC bending directions from the finite element results, the Bernoulli-Euler moment-curvature relation was utilized (equation 1-4). The coordinates in the transversal direction (y) of each time-increment along the longitudinal (x) direction were directly generated from the finite element solver-ABAQUS. Data file was processed using a custom program written in Mathematica (Wolfram Research, Inc., Champaign, IL) and analyzed followed the procedures of three-point bending experiments mentioned in Section 1-5.

In brief, for each time-increment, the longitudinal coordinates of the interface of the fibrosa and ventricularis layers in the composite beam model were fit to a quadratic equation (equation 1-1). The curvature of the deformed composite beam model at each time-increment was then calculated from equation 1-2. Change in curvature was then computed as the difference between the initial model curvature (initial model curvature equals to zero in the finite element simulations) and the deformed curvature. The longitudinal and transversal components of the reaction forces of the fixed nodes at the left hand side of the composite beam model were generated from the finite element solver. Furthermore, solver output the longitudinal and the transversal distance from the center to the left hand side fixed nodes of the composite beam

model. Based on these data, the custom program calculated the moment applied to the composite beam model at each time-increment from equation 1-3. The value of predicted effective stiffness for each node along the transversal direction at the center of the composite beam model (Figure 2-3) was then calculated through equation 1-4.

2.2.2 Flexural Mechanical Behavior of Native Aortic Valve Leaflet

From our laboratory experimental data as mentioned in Section 1-5,^(3, 68) a linear response of the E_{eff} in native aortic valve leaflet was observed in both flexed in the AC and WC directions (Figure 1-22). To reproduce the bending behavior of native aortic valve specimen from the experiments, two distinct models were considered. In the first model, a linear composite beam model was created to mimic the *in vitro* native aortic heart valve specimen under three-point bending experiment. This composite beam model had identical moduli in tension and compression, $E^T = E^C$, and it was classified as a uni-modular, uni-layer model (class 1, model A) (Figure 2-5: A), in which E is the layer moduli, and superscripts T and C represent tensile and compressive moduli, respectively.

In the second model the fibrosa and ventricularis layer had different linear moduli. To simulate the tensile and compressive material properties in the fibrosa and ventricular layers, $E_F^T = E_F^C$, $E_V^T = E_V^C$, but $E_F \neq E_V$ were assigned, and it was classified as a uni-modular, bi-layer model (class 1, model B) (Figure 2-5: B), in which subscripts F and V represent the fibrosa and the ventricularis layer, respectively. Different linear material properties were used through the custom coded user-defined material properties in the models.

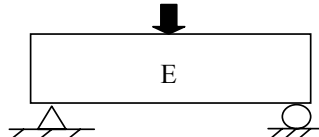
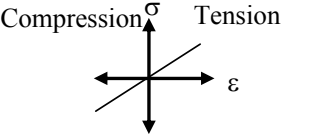
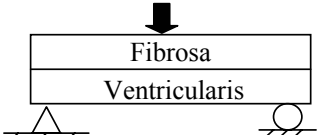
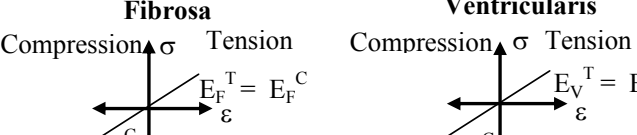
Class 1 material model		Layer moduli assumptions
A. Uni-modular, uni-layer	Schematic analysis method	
		$E^T = E^C$
B. Uni-modular; bi-Layer	Schematic analysis method	
		$E_F \neq E_V$ $E_F^T = E_F^C$ $E_V^T = E_V^C$

Figure 2-5 Class 1: The schematic analysis method for uni-modular, uni-layer and bi-layer composite beam models of native aortic valve leaflet under three-point bending in WC direction. Uni-modular, uni-layer and bi-layer composite beams under three-point bending in AC direction were simulated but not shown in this figure.

2.2.3 Flexural Mechanical Behavior of Porcine Bioprosthetic Heart Valve Leaflet

As described in Section 1-5, porcine BHV leaflet is heterogeneous but layered, thus, when the leaflet was flexed in the AC direction, the deformation subjected the fibrosa to tensile loading and the ventricularis to compressive loading, and when the leaflet was flexed in the WC direction, the deformation subjected the fibrosa to compressive loading and the ventricularis to tensile loading (Figure 1-20). Furthermore, from previous laboratory three-point bending experimental results, Sacks *et al.*^(3, 68) observed the AC:WC layer moduli with a ratio ~3:1 for uncycled porcine BHV (Figure 1-22). This result suggested that the degree of flexural stiffness differences in both bending directions, in either tension or compression, may vary between individual layers.

To reproduce the flexural behavior of uncycled porcine BHV from the three-point bending experiments in Section 1-5,⁽⁶⁶⁾ three distinct models were considered. In the first model, a linear bi-modular uni-layer composite beam model was created to mimic the *in vitro* uncycled porcine BHV specimen using three-point bending test. The model was also utilized to verify the custom coded user-defined material properties into the finite element solver. This composite beam model had different tensile and compressive moduli, with a ratio of 3:1, $E^T = 3 E^C$, and was classified as class 2, model A (Figure 2-6: A).

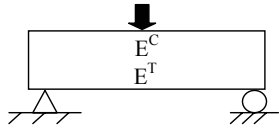
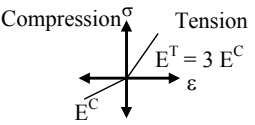
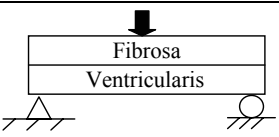
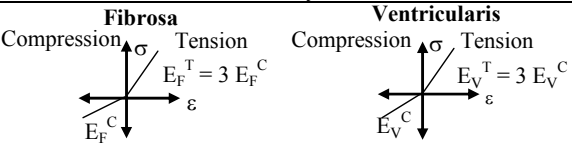
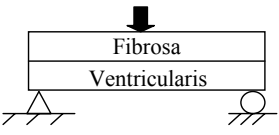
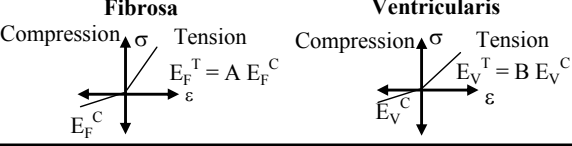
Class 2 material model: linear bi-modular (uncycled porcine BHV)		Layer moduli assumptions
A. Linear bi-modular; uni-layer	Schematic analysis method	
		$E^T = 3 E^C$
B. Linear bi-modular; bi-layer (I)	Schematic analysis method	
		$E_F^T \neq E_V^T$ $E_F^T = 3 E_F^C$ $E_V^T = 3 E_V^C$
C. Linear bi-modular; bi-layer (II): $E_F^T = 3 E_V^T$	Schematic analysis method	
		$E_F^T = 3 E_V^T$ $E_F^T = A E_F^C$ $E_V^T = B E_V^C$

Figure 2-6 Class 2: The schematic analysis method for linear bi-modular, uni-layer and bi-layer composite beam models of porcine BHV leaflets under three-point bending in WC direction. Linear bi-modular, uni-layer and bi-layer composite beam under three-point bending in AC direction were simulated but not shown in this figure.

In the second model the fibrosa and ventricularis layer had different tensile and compressive moduli⁽¹⁴⁰⁾ with a ratio of 3:1, $E_F^T = 3 E_F^C$, $E_V^T = 3 E_V^C$, and the tensile moduli in the fibrosa layer is different from the tensile moduli in the ventricularis layer $E_F^T \neq E_V^T$ (class 2, model B) (Figure 2-6: B). The third model considered a ratio of tensile and compressive moduli in both the fibrosa and ventricularis layers, in which a ratio of 3 was incorporated to mimic the experimental finding of an ~3:1 ratio stiffness in the AC:WC directions (Figure 1-22).^(3, 68) As mentioned earlier, when the leaflet was flexed in the AC direction, the deformation subjected the fibrosa to tensile loading and the ventricularis to compressive loading, conversely. Stiffness in the AC bending direction was assumed and mimicked as tensile material property for the fibrosa layer, and stiffness in the WC bending direction was assumed and treated as ventricularis tensile material property. According to our laboratory experimental results from Sacks,^(3, 68) the ~3:1 ratio stiffness was observed in the AC:WC bending direction of uncycled porcine BHV, the material property was then assumed and assigned as $E_F^T = 3 E_V^T$ through the custom coded user-defined material properties (class 2, model C) (Figure 2-6: C). In this case, parametric study was performed to characterize individual layer moduli of uncycled porcine BHV leaflet. The moduli were assigned in to the composite beam model as $E_F^T = A E_F^C$, $E_V^T = B E_V^C$, in which A is the ratio of the tensile moduli to the compressive moduli in the fibrosa layer, and B is the ratio of the tensile moduli to the compressive moduli in the ventricularis layer (Figure 2-6: C). Furthermore, Sacks *et al.* found^(3, 68) uncycled porcine BHV demonstrated a bending direction dependent stiffness with $E_{\text{eff}} = 216$ kPa in the AC bending direction, and $E_{\text{eff}} = 72$ kPa in the WC bending direction (Figure 1-22), parametric study of the different combinations of the ratios A and B were illustrated in Table 2-2:

Table 2-2 Parametric study of chemical-treated uncycled porcine BHV leaflet flexural behavior.

1. From the measured $E_{\text{eff}} = 216$ kPa in the AC bending direction, the average material property was calculated as:

$$\frac{1}{2}(E_V^C + E_F^T) = 216 \text{ kPa} \quad (2.1)$$

2. From the measured $E_{\text{eff}} = 72$ kPa in the WC bending direction, the average material property was calculated as:

$$\frac{1}{2}(E_F^C + E_V^T) = 72 \text{ kPa} \quad (2.2)$$

3. When the leaflet was flexed in the AC direction, the deformation subjected the fibrosa to tensile loading and the ventricularis to compressive loading, conversely, the relationship of the tensile property in the fibrosa and ventricularis layer was expressed as:

$$E_F^T = 3 E_V^T \quad (2.3)$$

4. A is the ratio of the tensile moduli to the compressive moduli in the fibrosa layer, and the relationship of tensile and compressive material properties in the fibrosa layer was expressed as:

$$E_F^T = A E_F^C \quad (2.4)$$

5. B is the ratio of the tensile moduli to the compressive moduli in the ventricularis layer, and the relationship of tensile and compressive material properties in the ventricular layer was expressed as:

$$E_V^T = B E_V^C \quad (2.5)$$

The five equations above were then used to generate permissible combinations of A and B. Different combinations of tensile to compressive moduli for the fibrosa and ventricularis

layers were summarized in Table 2-3, which provided ratios of tensile to compressive moduli for the fibrosa and ventricularis layers of uncycled porcine BHV leaflet.

Table 2-3 Parametric study of different combinations of tensile and compressive moduli in AC and WC bending directions for uncycled flexural models. E represents the layer moduli, superscripts T and C represent tensile and compressive moduli, subscripts F and V represent the fibrosa and the ventricularis layer, A is the ratio of the tensile moduli to the compressive moduli in the fibrosa layer, and B is the ratio of the tensile moduli to the compressive moduli in the ventricularis layer, respectively.

A	B	$E_{\text{eff}}^{\text{AC}} = 216$ (in kPa) $E_{\text{eff}}^{\text{WC}} = 72$			
		E_F^T	E_F^C	E_V^T	E_V^C
1	1 / 9	108	108	36	324
2	1 / 4.5	172.8	86.4	57.6	259.2
3	1 / 3	216	72	72	216
4	1 / 2.25	246.8	61.7	82.3	185.2
5	1 / 1.8	270	54	90	162
9	1	324	36	108	108
18.2	2	370.3	20.3	123.4	61.7
27	3	388.8	14.4	129.6	43.2
36	4	398.77	11.08	132.92	33.23
45	5	405	9	135	27

2.2.4 Changes in the Flexural Behavior of the Porcine Bioprosthetic Heart Valve with Fatigue

As stated in Section 1-5, a representative M/I vs. $\Delta\kappa$ for a 200 million-cycles leaflet demonstrated a non-linear response over the full range of flexure using an accelerated wear testing (Figure 1-22).^(3, 68) An ~1.8: 1 ratio stiffness in the AC:WC directions was found (Figure

1-22),^(3, 68) and the published M/I vs. $\Delta\kappa$ function of 200 million-cycles was expressed in the exponential form:

$$M/I = \tilde{C}_0 (1 - e^{-\tilde{C}_1 \Delta\kappa}) \quad (2.6)$$

in which parameters \tilde{C}_0 and \tilde{C}_1 in the AC and WC bending directions (Table 2-4):

Table 2-4 The M/I vs. $\Delta\kappa$ relationship of 200 million-cycles in AC and WC bending directions of fatigued porcine BHV.^(3, 68)

	\tilde{C}_0	\tilde{C}_1
AC bending direction	14.17	12.7
WC bending direction	15.15	6.6

Since E_{eff} was calculated from the Bernoulli-Euler moment-curvature relation equation (1-4), one can differentiate this relation with respect to $\Delta\kappa$ and represented as:

$$\frac{d(M/I)}{d(\Delta\kappa)} = E_{\text{eff}} \quad (2.7)$$

As mentioned in Section 1-5, experimental data was presented as M/I vs. $\Delta\kappa$ so that the slope of the curve is equal to E_{eff} . It suggested that E_{eff} declines non-linearly and is as function of strain. Thus, moment-curvature equations were then rewritten as in equation (2.8), and was differentiating in two different bending directions as showed in equation (2.9) and (2.10)

:

$$E(\varepsilon) = \frac{d(M/I)}{d(\Delta\kappa)} = \tilde{C}_0 \tilde{C}_1 (e^{-\tilde{C}_1 \varepsilon}) \quad (2.8)$$

$$E^{AC}(\varepsilon) = C_1 (e^{-C_2 \varepsilon}) \quad (2.9)$$

$$E^{WC}(\varepsilon) = C_3 (e^{-C_4 \varepsilon}) \quad (2.10)$$

in which parameters C_1 , C_2 , C_3 and C_4 in the AC and WC bending directions were showed in Table 2-5.

Table 2-5 The material constants of the stiffness in the AC and BC bending directions of fatigued porcine BHV leaflet.

AC bending direction	C_1	180
	C_2	12.7
WC bending direction	C_3	100
	C_4	6.6

Though the mechanism of decreasing in flexural rigidity is still unclear, from comparing results of flexural behaviors among the native aortic, uncycled porcine BHV and the fatigued porcine BHV leaflets, we hypothesize these non-linear behaviors as described as following:

1. Compressive and tensile strengths decrease non-linearly after cyclic loading in both the fibrosa and ventricular layers.

2. Compressive strength decreases non-linearly after cyclic loading but tensile strength remains constant in both the fibrosa and ventricular layers.
3. Tensile strength decreases non-linearly after cyclic loading but compressive strength remains constant in both the fibrosa and ventricular layers.

From our hypotheses, three distinct models with nonlinear bi-modular material properties were considered to reproduce the flexural behavior of *in vitro* fatigued porcine BHV leaflet from the three-point bending experiments.^(3, 66, 68) Parametric study was required to identify individual layer moduli of fatigued porcine BHV leaflet (Table 2-6).

Table 2-6 Parametric study of fatigued porcine BHV leaflet flexural behavior.

1. We assumed tensile material property dominates the flexural behavior with 1.8:1 ratio stiffness found experimentally (Figure 1-22):^(3, 68)

$$E_F^T = 1.8 E_V^T \quad (2.11)$$

2. A is the ratio is the ratio of the tensile moduli to the compressive moduli in the fibrosa layer, and the relationship of tensile and compressive material properties of the fibrosa layer was expressed as:

$$E_F^T = \underline{A} E_F^C \quad (2.12)$$

3. B is the ratio of the tensile moduli to the compressive moduli in the ventricularis layer, and the relationship of tensile and compressive material properties of the ventricularis layer was expressed as:

$$E_V^T = \underline{B} E_V^C \quad (2.13)$$

Equations (2.11) - (2.13) were then used to generate permissible combinations of A and B. In the first model, a nonlinear bi-modular material in which the moduli were functions of the strains was considered (class3, model A) (Figure 2-7: A). This composite beam model had different non-linear tensile and compressive moduli in both the fibrosa and ventricularis layers, and followed equations (2.9) - (2.13). The moduli were assigned into the composite beam model through the custom coded user-defined material properties, where C_1 , C_2 , C_3 , and C_4 were optimized by comparing the M/I vs. $\Delta\kappa$ response to the experimental measured M/I vs. $\Delta\kappa$ response.

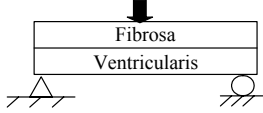
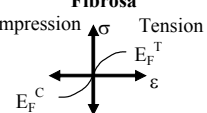
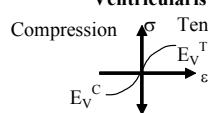
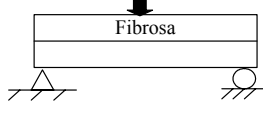
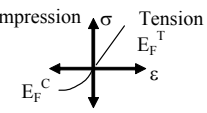
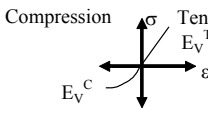
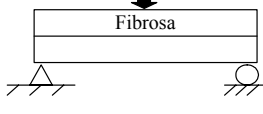
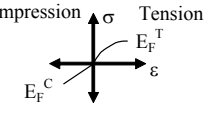
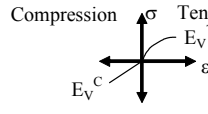
Class 3 material model: non-linear; bi-modular; bi-layer (fatigued porcine BHV)		Layer moduli assumption
A. Non-linear tension; non-linear compression	Schematic analysis method	Equations (2.9) - (2.13)
	<div style="display: flex; justify-content: space-around;"> <div style="text-align: center;"> <p>Fibrosa</p>  </div> <div style="text-align: center;"> <p>Ventricularis</p>  </div> </div>	
B. Linear tension; non-linear compression	Schematic analysis method	
	<div style="display: flex; justify-content: space-around;"> <div style="text-align: center;"> <p>Fibrosa</p>  </div> <div style="text-align: center;"> <p>Ventricularis</p>  </div> </div>	
C. Non-linear tension; linear compression	Schematic analysis method	
	<div style="display: flex; justify-content: space-around;"> <div style="text-align: center;"> <p>Fibrosa</p>  </div> <div style="text-align: center;"> <p>Ventricularis</p>  </div> </div>	

Figure 2-7 Class 3: The schematic analysis method for non-linear bi-modular bi-layer composite beam models of fatigued porcine BHV leaflet under WC three-point bending direction. Non-linear bi-modular bi-layer composite beam under AC bending direction were simulated but not shown in this figure.

In the second model, a linear tensile but non-linear compressive material property was incorporated into the composite beam model to mimic the *in vitro* fatigued porcine BHV leaflet. The composite beam model had different linear tensile and non-linear compressive moduli in both the fibrosa and ventricularis layers (class3, model B) (Figure 2-7: B). Parametric study was also performed to characterize individual layer moduli of fatigued porcine BHV leaflet. The moduli were assigned into the composite beam models through the custom coded user-defined material properties as $E^{AC} = \text{constant}$ and equations (2.10) - (2.13).

In the third model, a nonlinear tensile but linear compressive material property was incorporated into the composite beam model. The composite beam model had different non-linear tensile and linear compressive moduli in both the fibrosa and ventricularis layers (class 3, model C) (Figure 2-7: C). The moduli were assigned into the composite beam models through the custom coded user-defined material properties as $E^{WC} = \text{constant}$, equation (2.9), and equations (2.11) - (2.13).

2.3 RESULTS

2.3.1 Validation of User-Defined Material Properties

To reproduce the flexural behavior of uncycled porcine BHV from the three-point bending experiments,⁽⁶⁶⁾ finite element method was used. A custom code of material property was incorporated into the finite element solver due to its limited applications in biomechanics. To ensure that bending stress update and custom material properties were properly implemented into the solver, a linear bi-modular uni-layer model was created for verification. A material property relation of $E^T = 3E^C$, $E^T = 216 \text{ kPa}$ and $E^C = 72 \text{ kPa}$ were assigned through the Fortran

coded user-defined field as described previously (Figure 2-6: A). The result of stress-strain relationship along the transversal direction at the center of the composite beam generated the specific layer moduli as showed in Figure 2-8. The calculated stiffness from the finite element results (described in Section 2.2) corresponded well to the assigned material property of the individual layer, indicating the custom codes function appropriately.

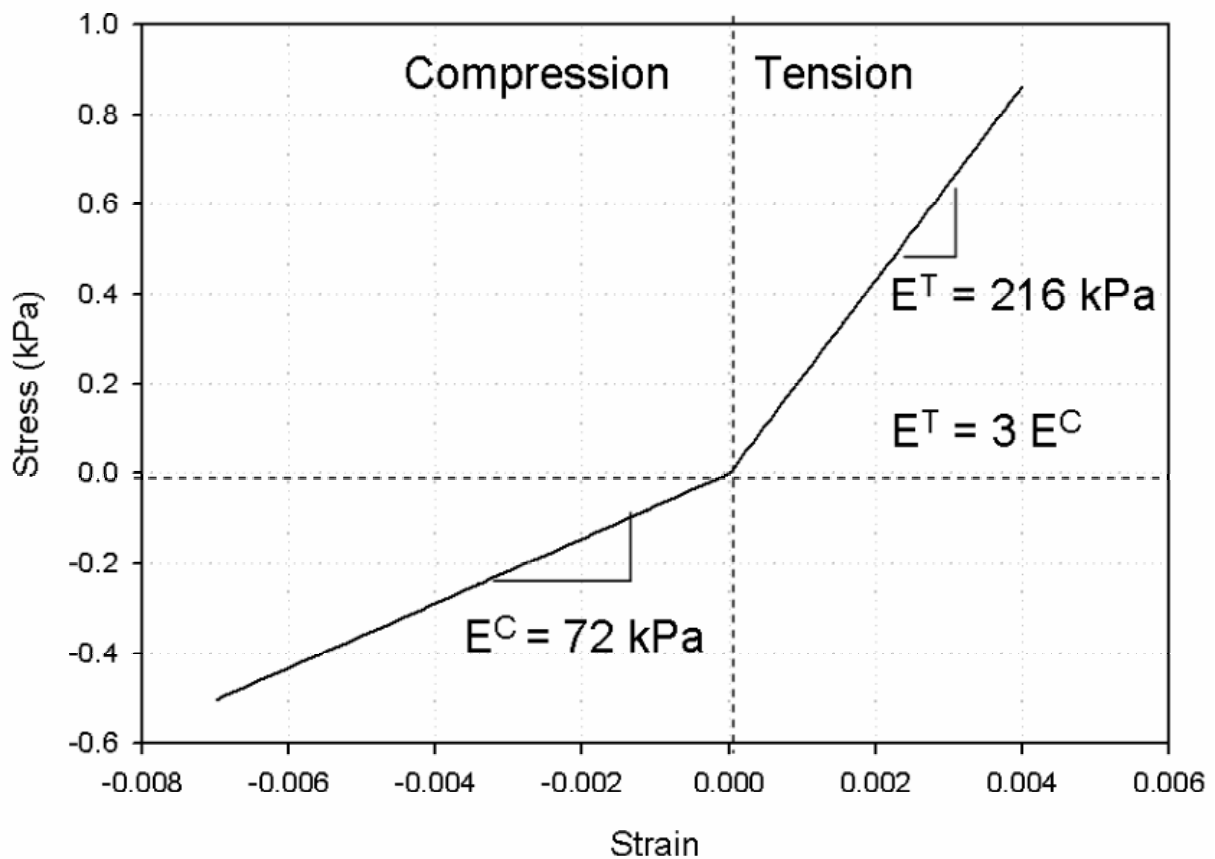


Figure 2-8 Custom code validation: the stress-strain relationship in a linear bi-modular composite beam model (Figure 2-6: A). The result of stress-strain relationship generated from the finite element solver verified custom coded material property ($E^T = 216 \text{ kPa}$, $E^C = 72 \text{ kPa}$, and $E^T = 3E^C$).

2.3.2 Flexural Behavior of the Porcine Bioprosthetic Heart Valve

A ratio of fibrosa tensile to ventricularis tensile moduli of 3 was incorporated to mimic the experimental finding of an ~ 3: 1 ratio of E_{eff} measured in the AC:WC directions.^(3, 68) The experimental measured effective stiffness in the AC and WC bending directions were $E^{\text{AC}} = 216$ kPa and $E^{\text{WC}} = 72$ kPa, respectively (1-17). The following combination of moduli from the finite element simulations agreed with the experimental measured values: $E_{\text{F}}^{\text{T}} = 370$ kPa, $E_{\text{F}}^{\text{C}} = 20.3$ kPa, $E_{\text{V}}^{\text{T}} = 123.4$ kPa and $E_{\text{V}}^{\text{C}} = 61.7$ kPa in both AC and WC bending directions, and in this combination, $E_{\text{F}}^{\text{T}} = 3E_{\text{V}}^{\text{T}}$, $A = 18$, and $B = 2$, which are tabulated in Table 2-7. M/I vs. $\Delta\kappa$ results of finite element simulations compared to the experimental findings was showed in Figure 2-9, with $r^2 = 0.962$ in AC bending direction and $r^2 = 0.967$ in WC bending direction.

Table 2-7 A comparison of experimental effective stiffness to the individual layer moduli finite element results of the uncycled porcine BHV.

Experimental results: Effective stiffness (kPa)		Finite element results: Individual layer moduli (kPa)	
AC	216	E_{F}^{T}	370
		E_{F}^{C}	20.3
WC	72	E_{V}^{T}	123.4
		E_{V}^{C}	61.7

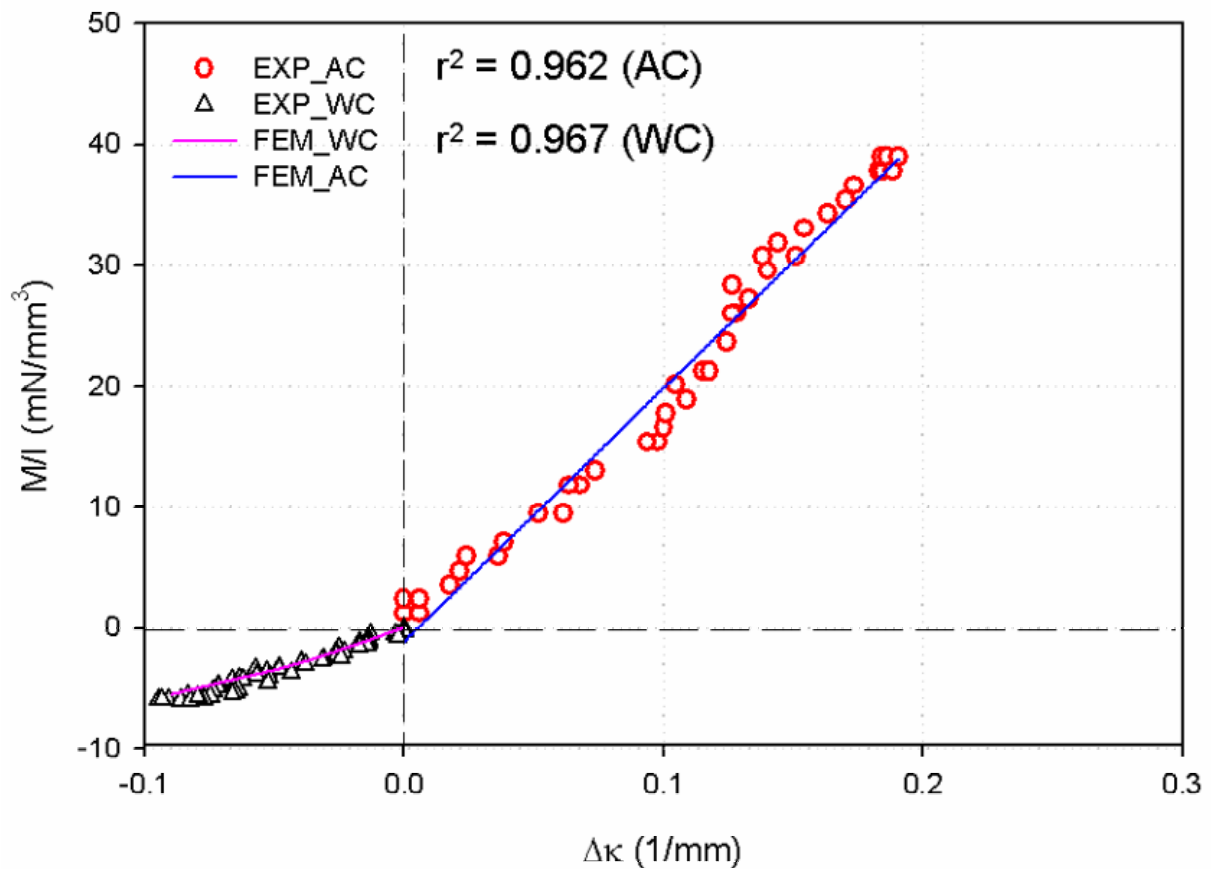


Figure 2-9 A comparison of the M/I vs. $\Delta\kappa$ curves from experimental data^(3, 68) to the finite element results of the uncycled porcine BHV in both WC and AC bending directions ($r^2 = 0.962$ in AC bending direction and $r^2 = 0.96$ in WC bending direction).

As mention in Section 1-5, since porcine BHV tissue is not homogeneous and has different tensile and compressive flexural behavior,^(3, 68) the location of the neutral axis does not coincide with the centroidal axis. A normalized thickness ranging from 0 to 1 was used in experimental testing due to various thicknesses of the test specimens, where 0 demarcates the ventricular surface and 1 demarcates the aortic surface. Since the neutral axis falls at the location when axial strains equal to zero,⁽¹⁴¹⁾ neutral axis locations was tracked from all finite

element results in order to compare the experimental measured neutral axis shift. A detailed experimental measured neutral axis location was presented in Appendix B. The bi-layer composite beam models were created with equal thickness in each layer, and the neutral axis of the models before bending simulations is located at the interface of the model with the 0.5 coordinate in the transversal direction. The neutral axis shift predicted by the composite beam model was 0.5 to 0.74 in the AC bending direction (Figure 2-10), and 0.5 to 0.57 in the WC bending direction (Figure 2-11). The corresponding transmural strain distributions in the AC and WC bending directions were also illustrated in Figure 2-10, and Figure 2-11, respectively.

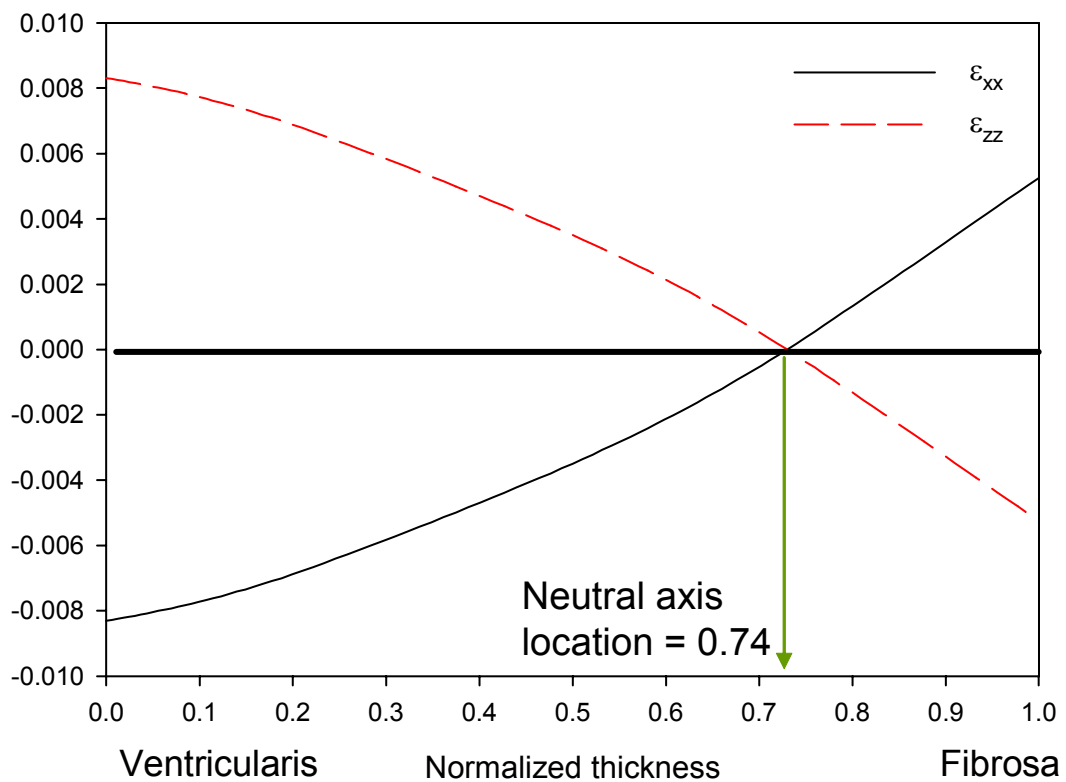


Figure 2-10 The neutral axis shift for the composite beam model was from 0.5 to 0.74 in the AC bending direction, and the corresponding transmural strain distributions were showed above.

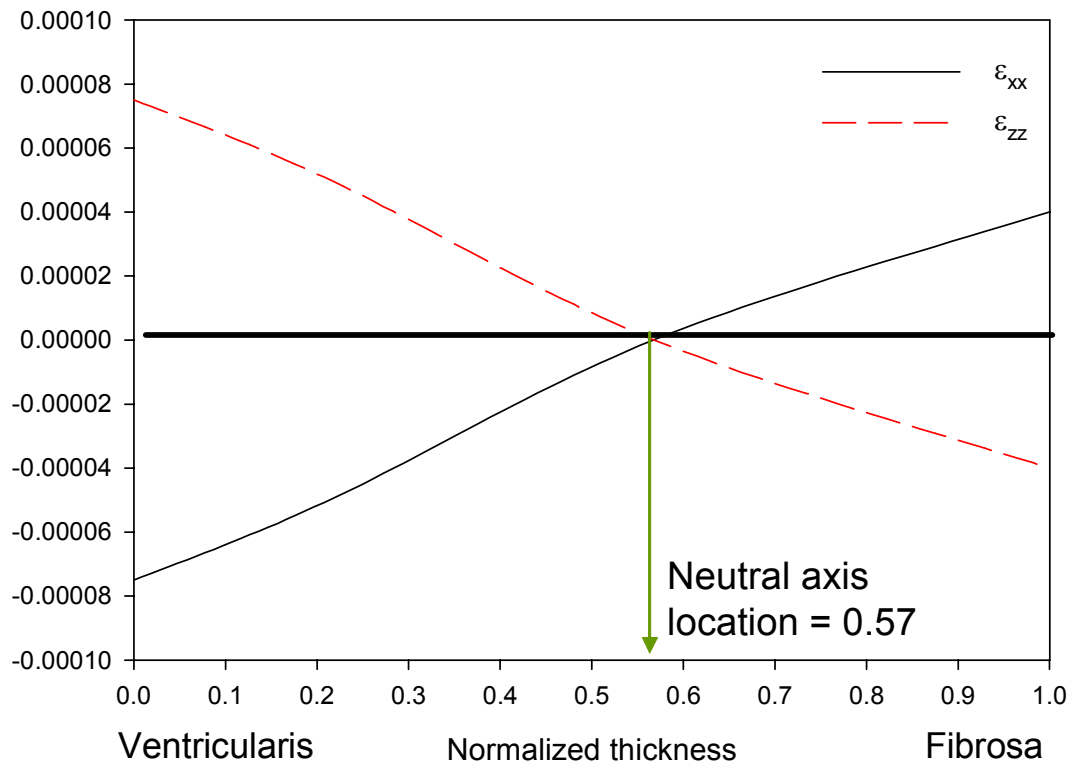


Figure 2-11 The neutral axis shift for the composite beam model was from 0.5 to 0.57 in the WC bending direction, and the corresponding transmural strain distributions were showed above.

From the experimental data in our laboratory (presented in Appendix B), the neutral axis was located at 0.54 normalized thickness for the native aortic valve tissue (sample size n = 1). However, for uncycled porcine BHV, the neutral axis location was observed at 0.64 normalized thickness in the WC bending direction (sample size n = 1), and at 0.84 normalized thickness in the AC bending direction (sample size n = 1) (Figure 2-12). The neutral axis shift predicted by the composite beam model was 0.5 to 0.57 in the WC bending direction, and 0.5 to 0.74 in the AC bending direction (Figure 2-12).

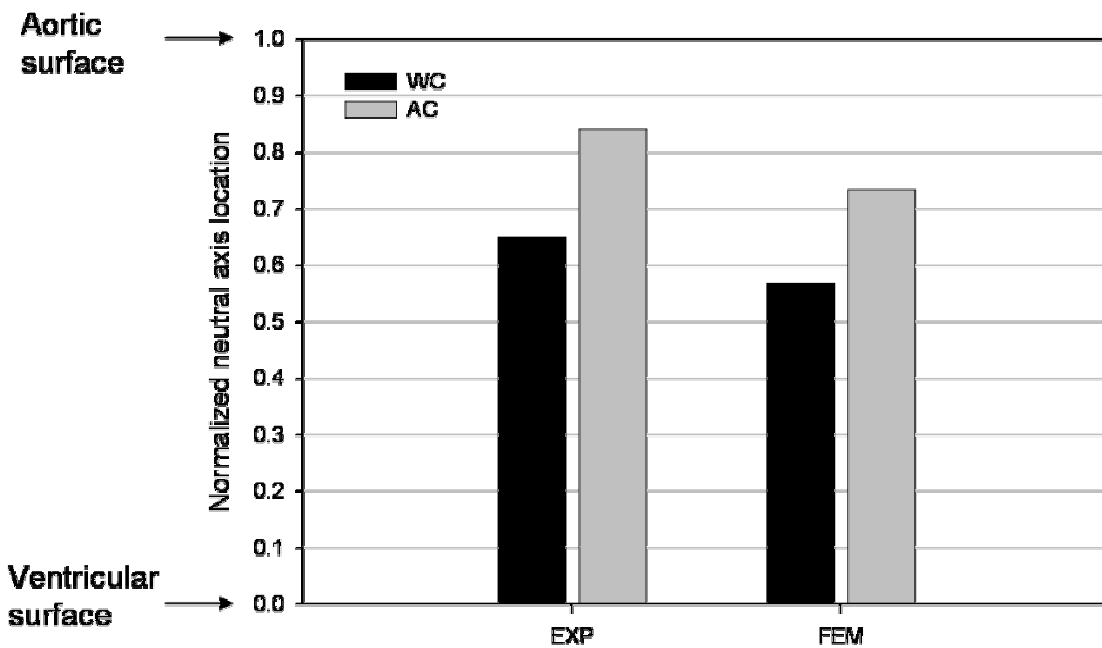


Figure 2-12 From the experimental data, the neutral axis shifted from 0.54 to 0.64 in WC direction and from 0.54 to 0.84 in AC direction (sample size n = 1). The neutral axis shift for the composite beam models were from 0.5 to 0.57 in the WC direction, and from 0.5 to 0.74 in the AC direction (sample size n = 1).

2.3.3 Flexural Behavior of the Porcine Bioprosthetic Heart Valve with Fatigue

Parametric studies were conducted in order to optimize the appropriate model to previously reported data on the flexural response of fatigued porcine BHV tissue (Figure 1-22).⁽³⁾

⁶⁸⁾ Validation of the optimized models was conducted by comparing the predicted moment-curvature response to existing experimental data generated in our laboratory using three-point bending. From Table 2-4, the effective stiffness of fatigued porcine BHV found experimentally were expressed in equation (2.9) and (2.10). In our finite element parametric study as mention in Section 2.2.4, we modulated C_1 , C_2 , C_3 and C_4 to fit the experimental results. The combination of moduli from the finite element simulations agreed with the experimental $M/I-\Delta\kappa$ curve in both

AC and WC bending directions was tabulated in Table 2-8. In this combination, $\underline{A} = 15$, and $\underline{B} = 1.8$, and $M/I-\Delta\kappa$ results of the finite element simulations compared to the experimental findings in AC and WC bending directions were showed in and Figure 2-13 and Figure 2-14, respectively.

Table 2-8 A comparison of effective stiffness of experimental results from equation (2.9) and (2.10) to the individual layer moduli finite element results of the fatigued porcine BHV at 200 million-cycles.

	Experimental results					Finite element results			
Parameters	C_1	C_2	C_3	C_4	Parameters	C_1	C_2	C_3	C_4
Effective stiffness of whole structure:	180	12.7	100	6.6	Fibrosa layer:	180	-30	12	-30
					Ventricularis layer:	132	-60	73.3	-60

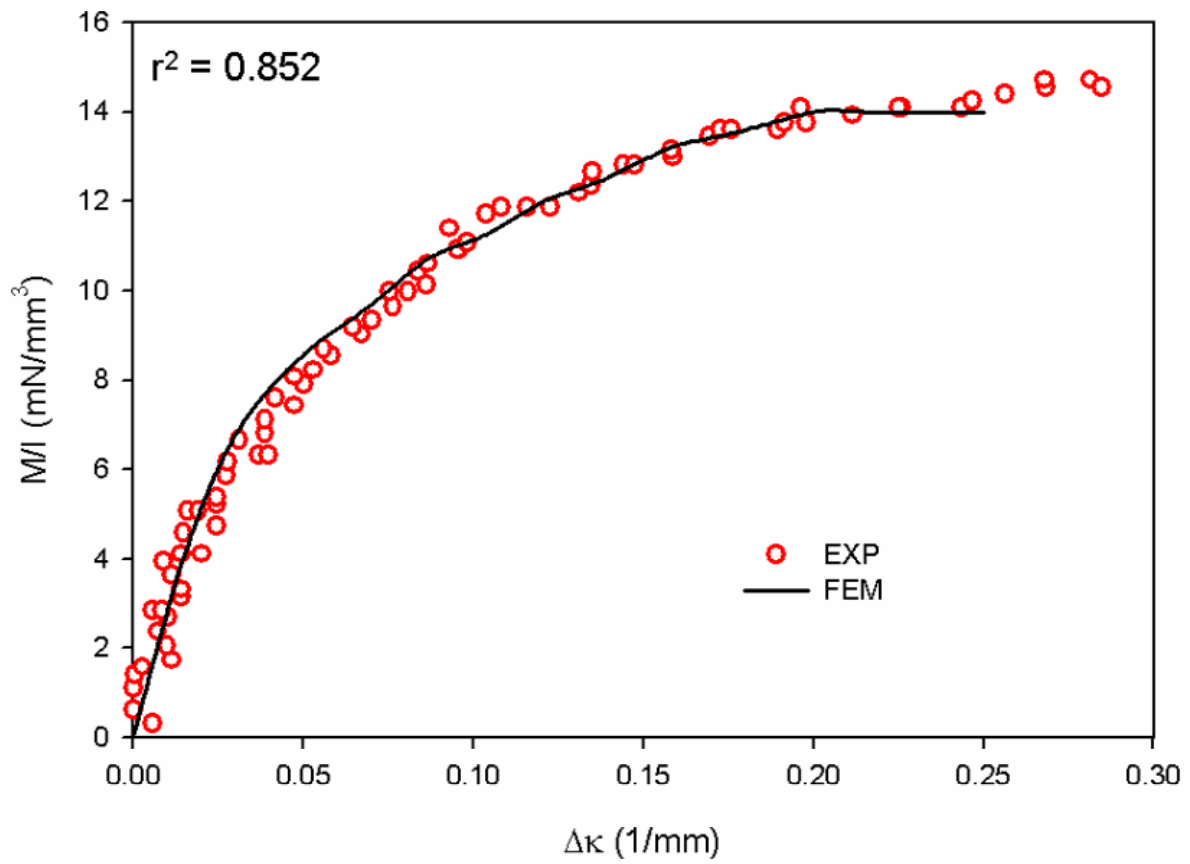


Figure 2-13 Comparison of the M/I vs. $\Delta\kappa$ curves from experimental data^(3, 68) to the finite element results of the fatigued porcine BHV in the AC bending direction ($r^2 = 0.852$) at 200-million cycles.

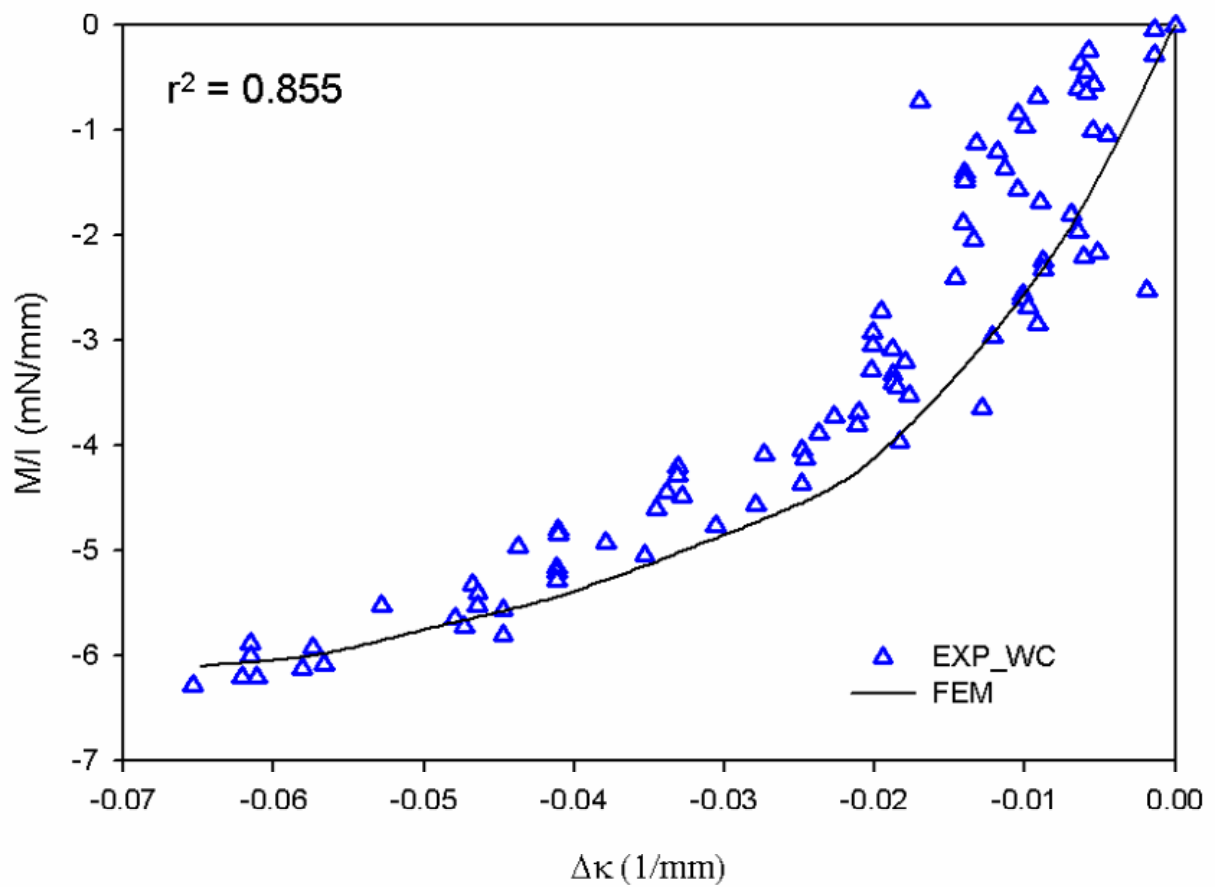


Figure 2-14 Comparison of the M/I vs. $\Delta\kappa$ curves from experimental data^(3, 68) to the finite element results of the fatigued porcine BHV in the WC bending direction ($r^2 = 0.855$) at 200 million cycles.

In the previous experimental studies,^(3, 68) a substantial decrease in stiffness was measured in the AC direction with increasing number of fatigue cycles (Figure 1-23). No statistically significant changes were found in the WC direction. A 50 % decrease in stiffness in AC bending direction was found after 200×10^6 cycles.⁽⁶⁸⁾ From finite element results, a direct comparison of the linear layer moduli (uncycled porcine BHV) with the nonlinear model (fatigued porcine BHV) was not possible, however, under the assumption described previously

that E^{AC} was dominated by the E_F^T and E^{WC} was dominated by E_V^T , we compared the values of the nonlinear models in the small strain region to the layer moduli, and calculated the drop of the moduli in fatigued models to the uncycled models. From our finite element results, the nonlinear model predicted an approximately 50 % drop in AC bending direction (370 kPa to 180 kPa), with no substantial change in the WC bending direction (123.4 kPa to 132 kPa) (Table 2-9).

Table 2-9 Finite element results of layer moduli: the fatigued porcine BHV model (200 million cycles) predicted an approximately 50 % drop in AC bending direction (370 kPa to 180 kPa), with no substantial change in the WC bending direction (123.4 kPa to 132 kPa).

Bending direction	Layer moduli of uncycled BHV leaflet (kPa)	Layer moduli of fatigued BHV leaflet (kPa)	differences of layer moduli
AC	E_F^T	E_F^T	~50 %
	370	180	
WC	E_V^T	E_V^T	No substantial difference
	123.4	132	

2.4 SUMMARY

This study focused on developing composite beam models to simulate the flexural behavior of native aortic valve, uncycled, and fatigued BHV tissues. In developing the composite beam models, it was assumed that there exists a significant degree of bonding

between the fibrosa and ventricularis layers such that the spongiosa layer could be neglected. The modeling approach utilized non-linear continuum mechanics to describe the highly non-linear material characteristics to the porcine BHV leaflets and the large deformation that occur during leaflets flex.

Two-layered composite beam models were created, and the three-point bending method was utilized by applying displacement at the center of the beam, with appropriate constraints on the right and left-hand sides of the beam. Linear, non-linear bi-modular moduli were incorporated through the custom coded material properties into the finite element solver such that these models were used to simulate the flexural behavior of native aortic valve, uncycled BHV, and fatigued BHV tissues. In addition, a variety of information, including deflections, reaction forces, local coordinates of interested material points were generated, allowing for calculating moments and change in curvatures so that these finite element predictions were compared with experimental data.⁽⁶⁶⁾

The individual layer tensile and compressive properties were found in both the AC and WC bending directions in the uncycled and fatigued porcine BHV composite beam models. Results of the moment-curvature relationship for the predicted moduli demonstrated a very good fit in both the AC ($r^2 = 0.962$ for chemical-treated and $r^2 = 0.852$ for fatigued porcine BHV) and WC ($r^2 = 0.967$ for chemical-treated and $r^2 = 0.855$ for fatigued porcine BHV) directions compared to the experimental finding (Figure 2-9, Figure 2-11 and Figure 2-12).^(3, 66, 68) Results of change in the layer moduli due to fatigue effect were compared to the experimental data. A 50 % drop of stiffness in the AC direction and no substantial differences in stiffness in the WC direction were verified (Figure 1-23 and Figure 2-13). A summary of individual layer moduli of

uncycled, and fatigued BHV was tabulated in Table 2-10. In the uncycled porcine BHV composite beam model, corresponding neutral axis shift was compared to the neutral axis shift found experimentally (Figure 2-10), and no significant differences were found in both the AC and WC bending directions. The study of the changes in flexural properties of the fibrosa and ventricularis layers enhances the understanding of the degradative mechanisms of porcine BHV.

Table 2-10 A summary of finite element results of individual layer moduli and addition information were presented in Table 2-7, Table 2-8, equations (2.9) and (2.10). Linear bi-modular stress-strain relationship was presented in black for uncycled BHV, and non-linear bi-modular stress-strain relationship was presented in red for fatigued BHV.

Stress-strain	Fibrosa		Ventricularis	
	σ	ϵ	σ	ϵ
Uncycled BHV	E_F^T	370	E_V^T	123.4
	E_F^C	20.3	E_V^C	61.7
Fatigued BHV	C1	180	C1	132
	C2	-30	C2	-60
	C3	12	C3	73.3
	C4	-30	C4	-60

3.0 GEOMETRIC CHANGES IN HEART VALVE INTERSTITIAL CELL NUCLEI DUE TO TRANSVALVULAR PRESSURE

Valve interstitial cell (VIC) and biological characteristics have been studied.^(30, 32-34, 89, 142-144) However less attention has been given to the local mechanical environment of VIC in the native aortic valve tissue. Thus quantitative knowledge of how the VIC response to loading (mechanocytes) translated from the tissue-level stress is necessary. It has been hypothesized that a certain fraction of the VICs may contribute toward modulation of leaflet tissue stiffness during valve operation,^(30, 32-34) and Taylor *et al.*⁽³⁴⁾ found VICs are responsible for maintaining the extracellular matrix (ECM) scaffold that provides the mechanical characteristics vital for sustaining the unique dynamic behavior of the valve, and these cells exhibit a profile which may allude to their role in valve function. Furthermore, recent interest in the development of tissue engineered heart valve (TEHV)^(73, 83) suggests that knowledge of how the native aortic valve's microstructure adjusts to strain is essential in the development of a TEHV. In investigating the mechanism of native aortic valve function and to accurately construct TEHV prostheses, a complete understanding of the native aortic VIC is required.

In the present study, we aimed to investigate the relationship of tissue-level ECM strains and the cellular-level VIC nuclei deformation, thus, quantification the deformation of aortic VIC nuclei under various physiologically relevant levels of tissue stress induced by transvalvular pressure

was conducted. The geometry of deformed VIC nuclei under various pressures were measured experimentally from photomicrographs histology sections of native tissue. Furthermore, as stated in Chapter 1, since fibrosa, spongiosa and ventricularis consist different structural components, varies tissue layer stresses exist. Based on this information, we hypothesized that a relationship may exist between the valve tissue layer and the deformation experienced by VIC nuclei under an applied transvalvular pressure. Therefore we also aimed to quantify the distribution of VIC nucleus deformation for each layer.

3.1 METHODS

3.1.1 Database and Specimen Preparation

All tissue sections were taken from previous study by Sacks *et al.*⁽²⁹⁾ In brief, fresh porcine heart valves were shipped in chilled physiological saline, and the aortic root / valve complex was removed immediately upon arrival. Care was taken to remove as much of surrounding myocardium as possible from the root area, and the coronary arteries were closed with sutures. After dissection the valves were mounted onto a tank that is part of a device that allow for a steady pressure head while the valves are fixed. The tank was filled with room temperature physiological buffer solution, and the device was activated to establish a preset pressure head. Pairs of valves were fixed at pressures of 1, 2, 4, 60 and 90 mmHg yielding a total of six leaflets per pressure level.

The leaflets were then sending to the laboratory, sectioned for histology. Circumferential, transmural, and radial directions were used for the local coordinates in all

specimen, in which, circumferential direction represents the aligned fiber direction, and transmural direction represent the direction across the tissue thickness, and the radial direction is orthogonal to the circumferential and transmural directions. A three-dimensional native aortic valve tissue was quantified with two different two-dimensional cross-sections, in which circumferential-transmural and radial-transmural cross-sections were prepared for examining(Figure 3-1). The specimens were stained by Hematoxylin and Eosin (H & E) or Masson methods and those two methods stained she VIC nuclei all in black and collagen in pink and blue, respectively (Figure 3-2).

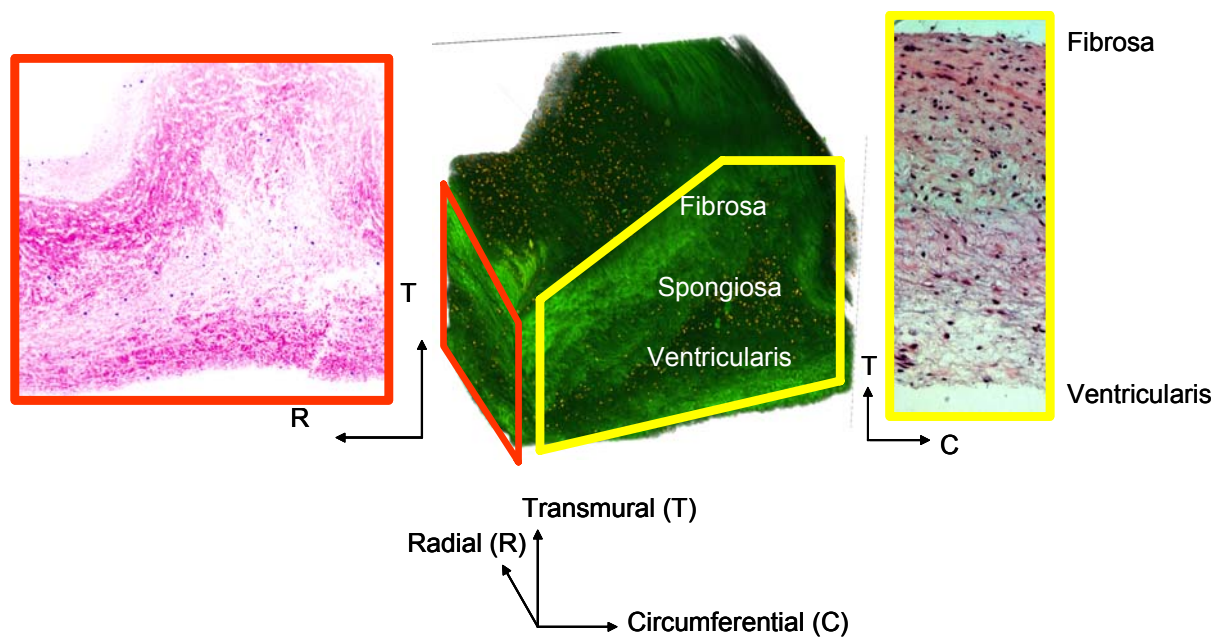
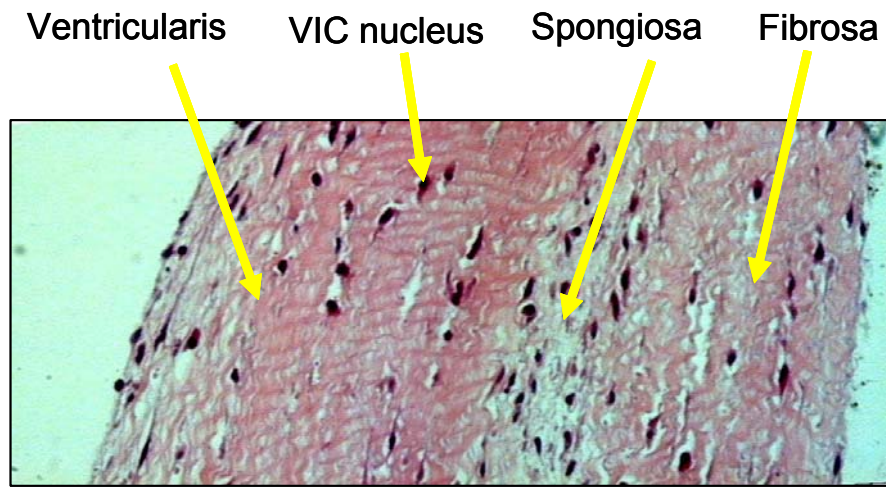
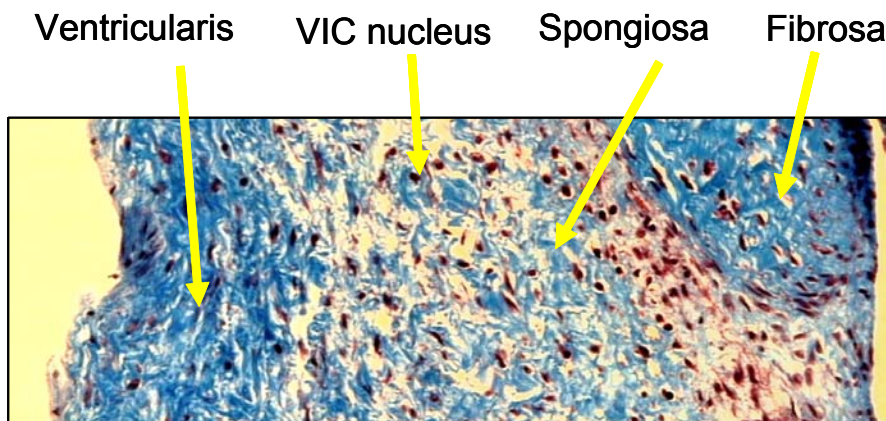


Figure 3-1 Three-dimensional native aortic valve tissue was prepared for two different cross-sectional specimens (center panel). In the left panel, radial-transmural cross-section was used, and in the right panel, circumferential-transmural cross-section was used for measuring the geometry of the VIC nuclei.



0 mmHg: Hematoxylin and Eosin



0 mmHg: Masson

Figure 3-2 Hematoxylin and Eosin (H & E) and Masson stained the VIC nuclei all in black, and collagen in pink and blue, respectively.

Whole series of histology sections in the circumferential-radial directions were quantified. A total of forty-eight slides of native aortic valve leaflets were available, covering 0,

1, 2, 4, 60, 90 mmHg transvalvular pressure levels (Figure 3-3). Each slide contains three sections, and five photomicrographs were digitized circumferentially for each section, and each image covered three layers of the aortic leaflet: fibrosa, spongiosa, and ventricularis (Figure 3-4). Summary the histological specimen database was tabulated in Table 3-1, and from simple calculation total 720 images with total 142560 cells was required to be quantified. In addition, one representative slide on the radial-transmural cross-section under 0 mmHg was quantified and provided supplementary information for further three-dimensional quantification of cellular geometry.

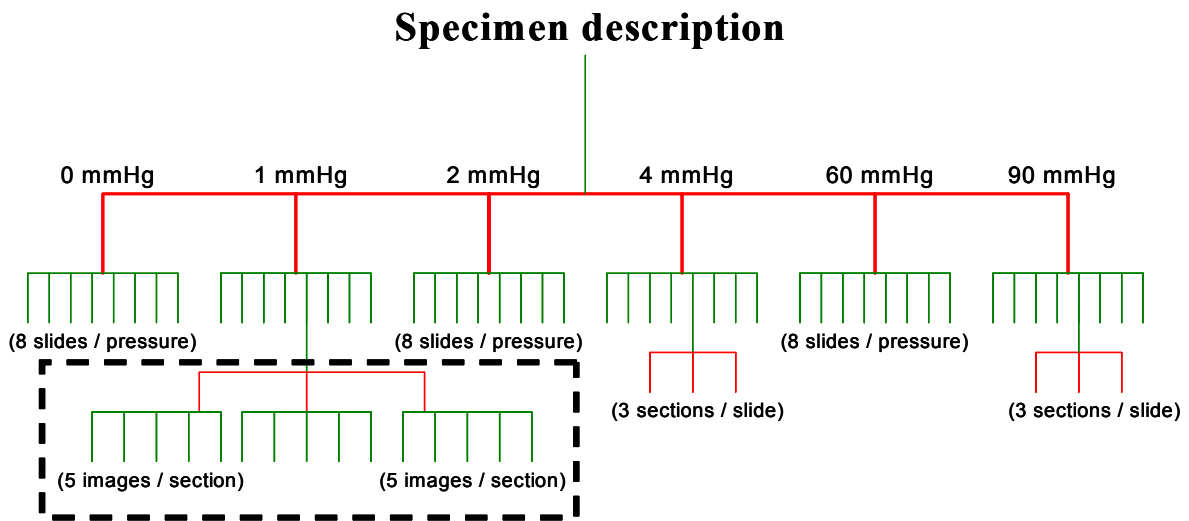


Figure 3-3 A total of forty-eight slides of native aortic valve leaflets were prepared, covering 0, 1, 2, 4, 60, 90 mmHg transvalvular pressure levels. Each pressure level included eight slides, and each slide contained three sections (all sections prepared but not showed in the figure above), and five photomicrographs of histology sections were digitized for each section (all images for each section were digitized as shown in the dash-box).

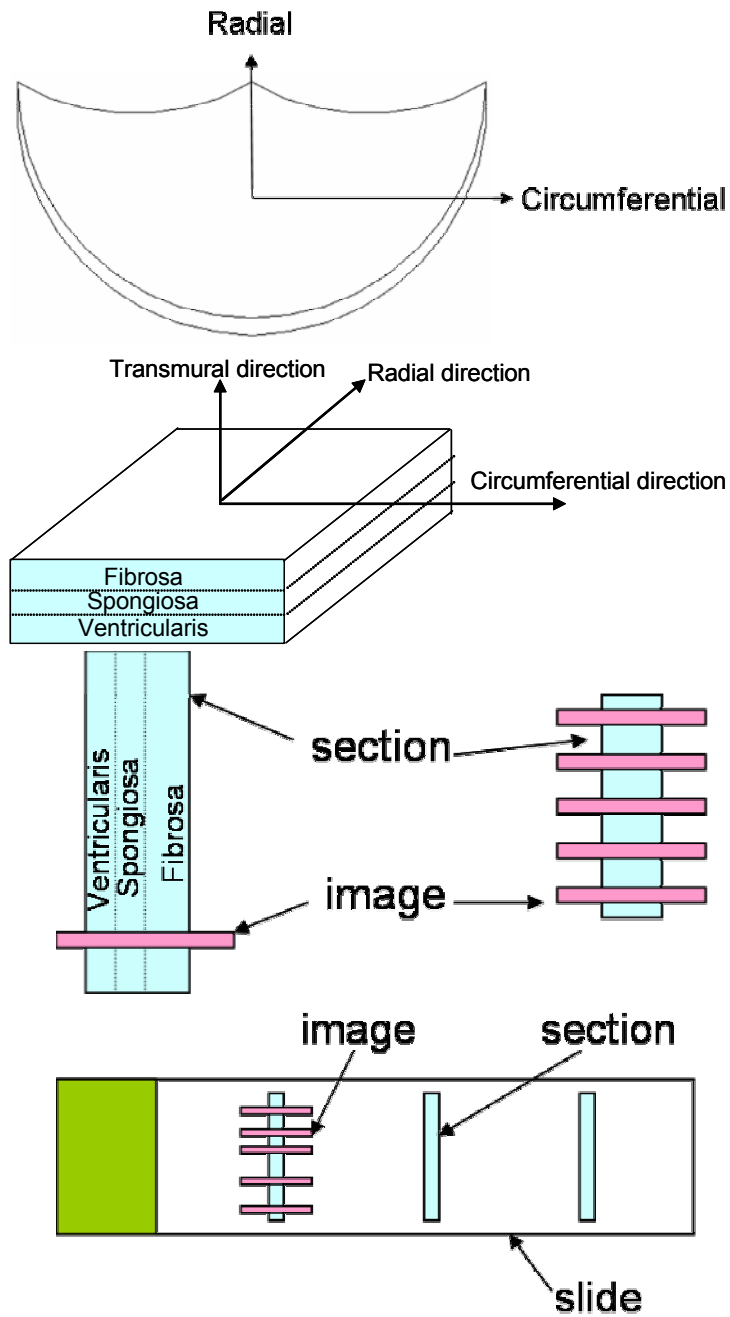


Figure 3-4 Section was prepared including three layers of the aortic leaflet: fibrosa, spongiosa, and ventricularis transmurally. Five photomicrographs were digitized circumferentially for each section, and each image covered all three layers of the aortic valve.

Table 3-1 Summary of histological specimen database.

							Total
Pressure level	0 mmHg	1 mmHg	2 mmHg	4 mmHg	60mmHg	90 mmHg	6 pressure levels
Number of slides per pressure	8	8	8	8	8	8	48 slides
Number of sections per slide	3	3	3	3	3	3	144 sections
Number of images per section	5	5	5	5	5	5	720 images
Number of cells per image	152	245	133	175	224	259	142560 cells

3.1.2 Image Processing

All VIC nuclei were quantified in photomicrographs along the transmural direction in order to cover all three layers, and digital images were acquired at 400X magnification. Since the view-range of the microscopy was limited, a panoramic image was required to cover all three layers. The panoramic image was created by 4-5 over-lapped photomicrographs to cover all three layers along the transmural direction (Figure 3-5). In order to achieve the best quality of the panorama image, 50-70% range of over-lapping was required. Since total 720 panoramic photomicrographs were required based on our specimen database (Table 3-1), $720 \times 5 = 3600$ digital images were acquired for this study. Sample of five panoramic photomicrographs in 0 mmHg along the circumferential and transmural directions for a section were shown in Figure 3-6, and additional panoramic photomicrographs under different transvalvular pressures are presented in Appendix C.

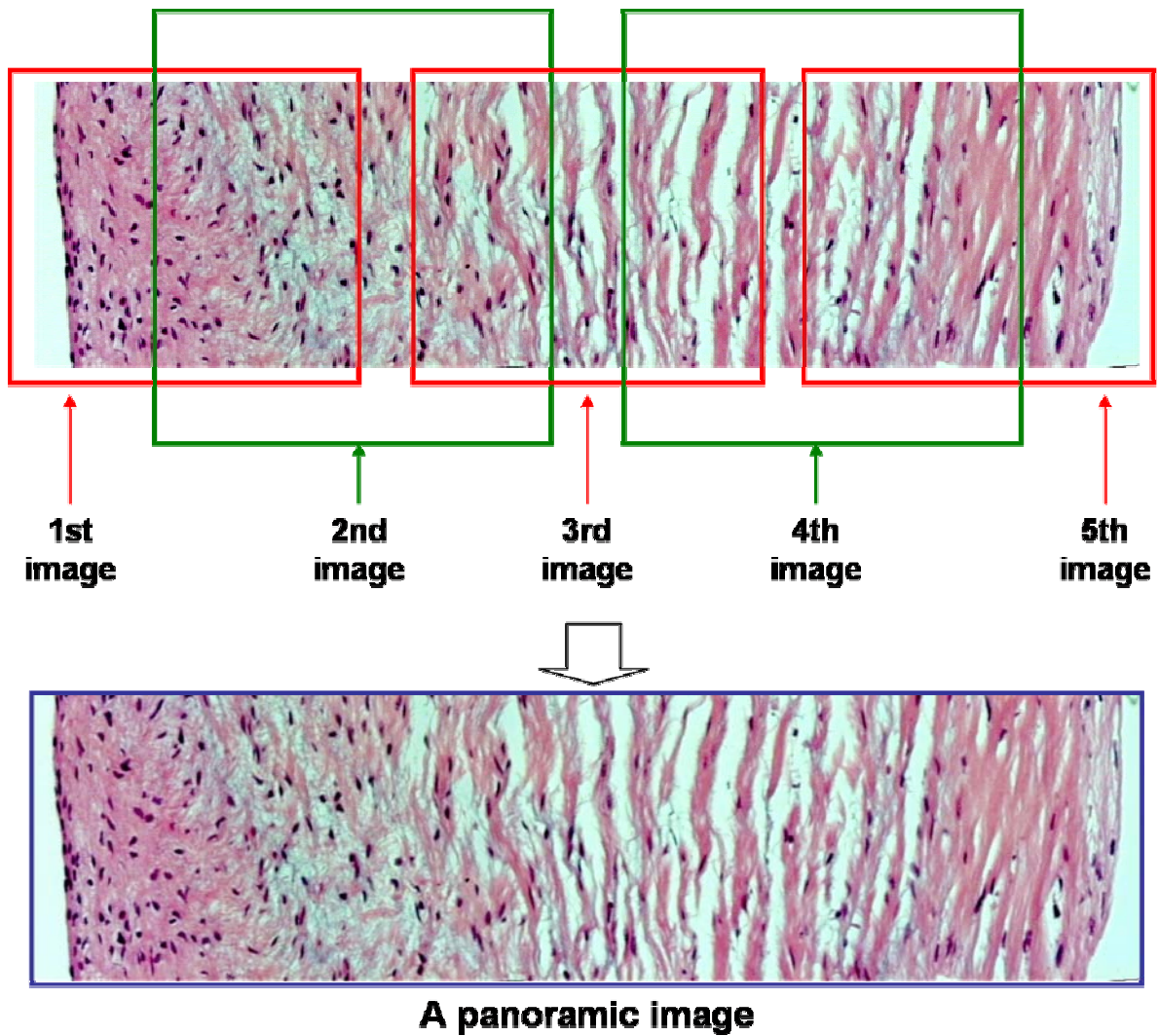
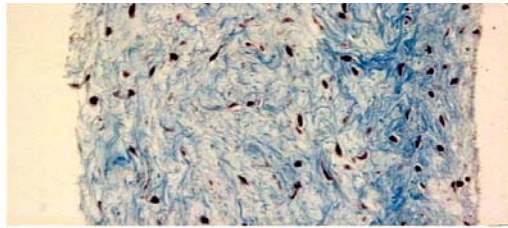
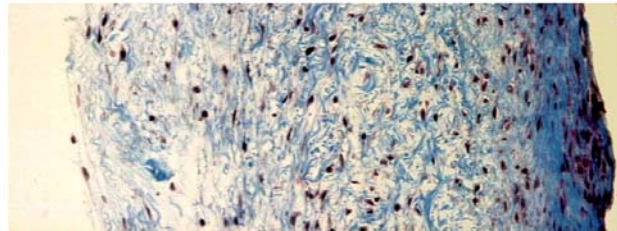


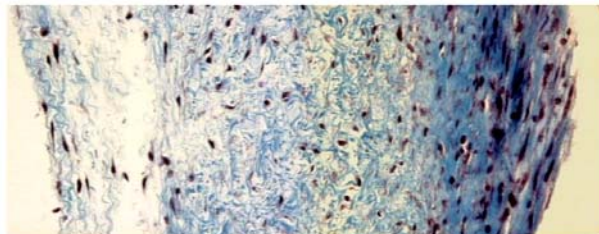
Figure 3-5 A panoramic image was created by 4-5 over lapped images to cover all three layers transmurally. In order to achieve the best quality of the panoramic image, 50-70% range of over-lapping was required.



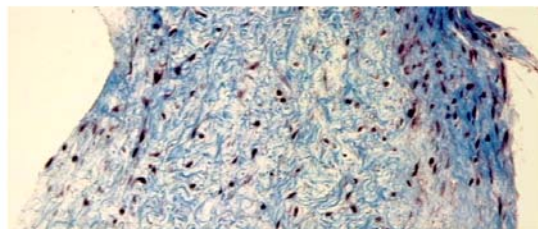
0 mmHg; Masson; Slide B; Section 1(X); Cross-section location 1



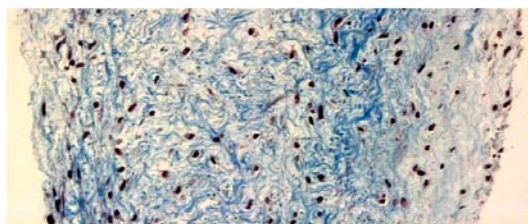
0 mmHg; Masson; Slide B; Section 1(X); Cross-section location 2



0 mmHg; Masson; Slide B; Section 1(X); Cross-section location 3



0 mmHg; Masson; Slide B; Section 1(X); Cross-section location 4



0 mmHg; Masson; Slide B; Section 1(X); Cross-section location 5

Figure 3-6 Sample of five panoramic photomicrographs in 0 mmHg along circumferential direction for one section.

Deformed VIC nucleus aspect ratio was chosen as a two-dimensional measurement of nucleus “shape” rather than the uni-dimensional values of absolute nucleus length and width alone. Analysis of the deformation of VIC nuclei under various transvalvular pressures required a rigorous statistical treatment, and thus was facilitated by using a single parameter to describe the overall VIC nucleus deformation. Furthermore, the VIC nuclei appearing in histological sections were sliced offset from their centroid, and thus the absolute VIC nucleus length or width observed in a histological section are only apparent values. Based on the available VIC nuclei shapes visualized in the circumferential-transmural cross-sections, elliptic VIC nuclei were observed. Thus, we assumed the axes of the elliptic VIC nucleus parallel to the circumferential and transmural directions. However, the nucleus aspect ratio of elliptical sections taken orthogonal to the long axis is equal; thus nucleus aspect ratio represents a more dependable measure of VIC nucleus deformation. The aspect ratio of VIC nucleus was defined as following:

$$\text{Aspect ratio} = \frac{a}{b} \quad (3.1)$$

in which major axis length = 2a, and minor axis length = 2b in the panoramic images. The major and minor axis lengths in pixels of the deformed VIC nuclei were quantified using SigmaScan (SPSS, Inc. Chicago, IL.) (Figure 3-7).

In order to correlate the relationship between the valve tissue layer and the deformation experienced by VIC nuclei under an applied transvalvular pressure, the local coordinates in transmural and circumferential directions of deformed VIC nuclei were also quantified. The x – axis was defined parallel to the transmural direction, and y axis was defined perpendicular to the x – axis (Figure 3-7). To demonstrate the tendency of VIC nucleus

deformation in the tri-layered aortic leaflet, local coordinates was conducted for calculating the thickness of the sample along the transmural direction (x). In this study, normalized thickness was used due to the various thicknesses in samples, in which 0 indicates the ventricularis layer in the ventricular surface, and 1 indicates the fibrosa layer in the aortic surface (Figure 3-8). Images were calibrated using a calibration slide in which the dimension of 1 – pixel was found to be equal to 0.4 μm , thus all the data generated from the imaging software converted to unit in μm . A representative length of 10 μm in the tissue was shown in Figure 3-8.

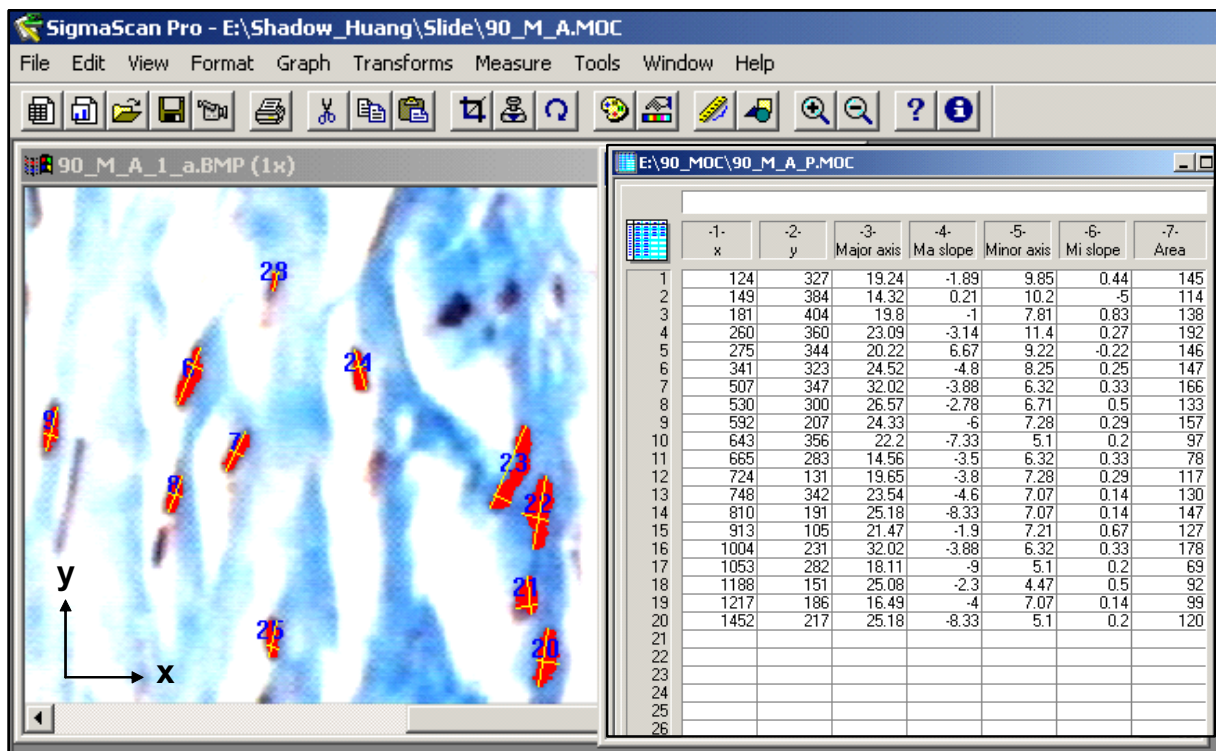


Figure 3-7 A sample image of VIC nuclei inside the tissue under 90 mmHg was digitized by SigmaScan (SPSS, Inc. Chicago, IL). Local coordinates, the major-, minor-axis lengths, slope, area of deformed VICs were generated by the imaging software.

90 mmHg

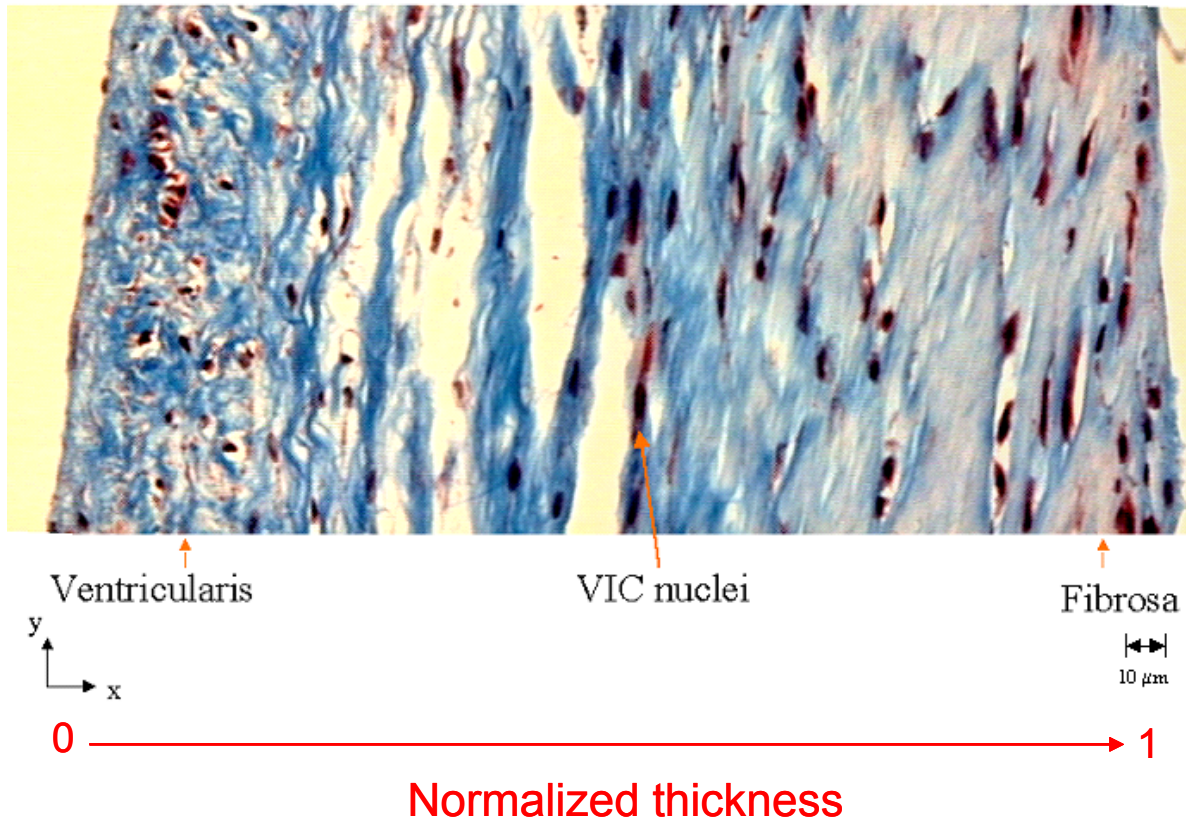


Figure 3-8 One sample image of VIC nuclei inside the tissue under 90mmHg transvalvular pressure and was prepared including three layers of the aortic leaflet: fibrosa, spongiosa, and ventricularis. Local coordinates were used for calculating the normalized thickness from ventricularis layer to fibrosa layer. A representative length of 10 μm was also shown above.

Based on the available VIC nucleus aspect ratio data visualized and measured in the circumferential-transmural and radial-transmural cross-sections, Figure 3-9 provided a hypothesized prolate ellipsoidal cellular geometry from our laboratory in which a, b, and c are the major axis length in the circumferential, radial, and transmural directions. The prolate elliptic cell sits in the circumferential, radial, and transmural directions, in which each colored hatched plane corresponds to its color-coded normal direction. For example, transmural

direction is the normal direction of blue hatched plane which is also the circumferential – radial cross-section.

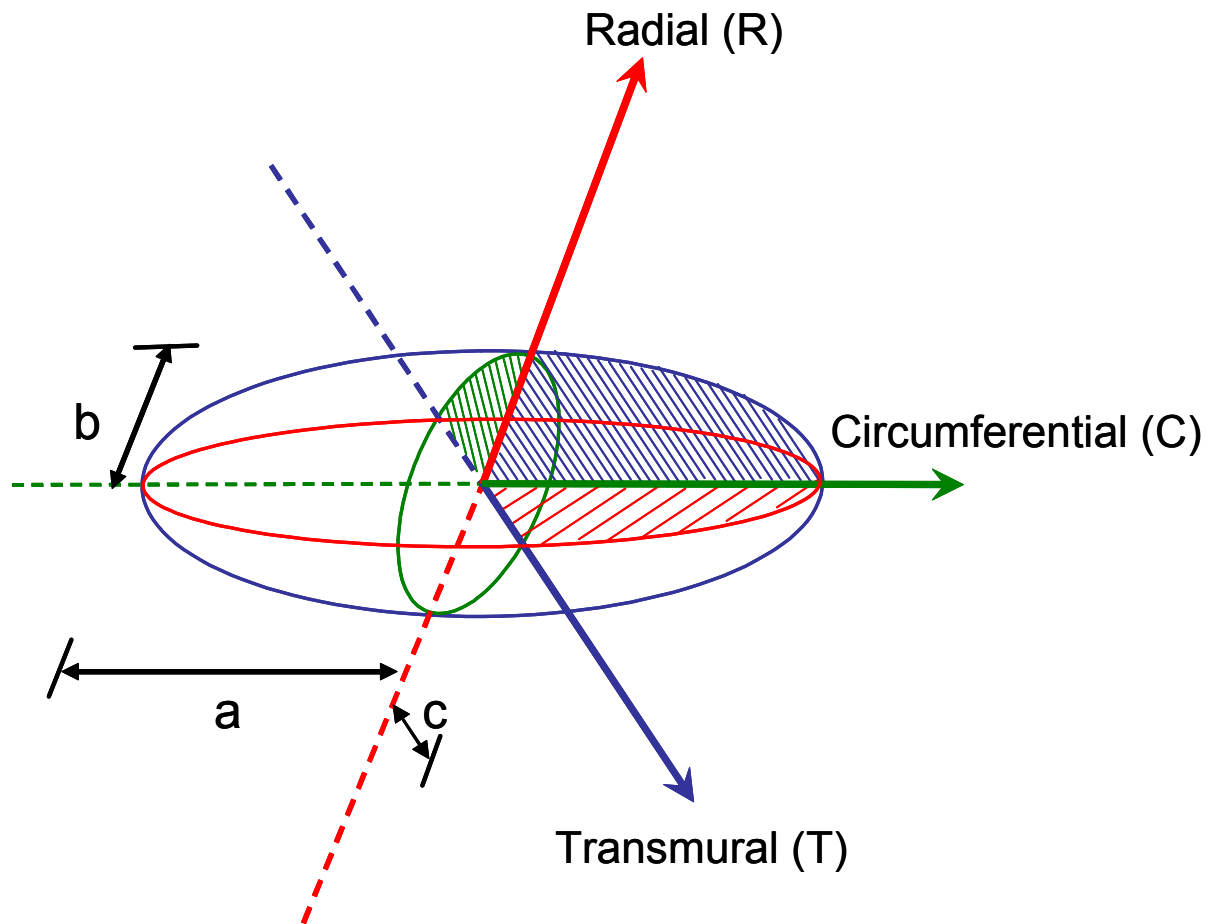


Figure 3-9 A schematic of a hypothesized prolate ellipsoidal cellular geometry in circumferential, radial, and transmural directions.

A schematic of deformed VIC nucleus in the circumferential-radial directions was illustrated in Figure 3-10 (a), in which major axis length = $2a$, and minor axis length = $2b$ (Figure 3-10 (b)). From the given data, the moments of inertia of the deformed VIC nucleus were

calculated by using equations (3.2) and (3.3), and the area of an elliptic VIC nucleus was calculated by equation (3.4).⁽¹⁴⁵⁾

$$I_1 = \frac{\pi}{4} a b^3 \quad (3.2)$$

$$I_2 = \frac{\pi}{4} b a^3 \quad (3.3)$$

$$\text{Area} = a \times b \times \pi \quad (3.4)$$

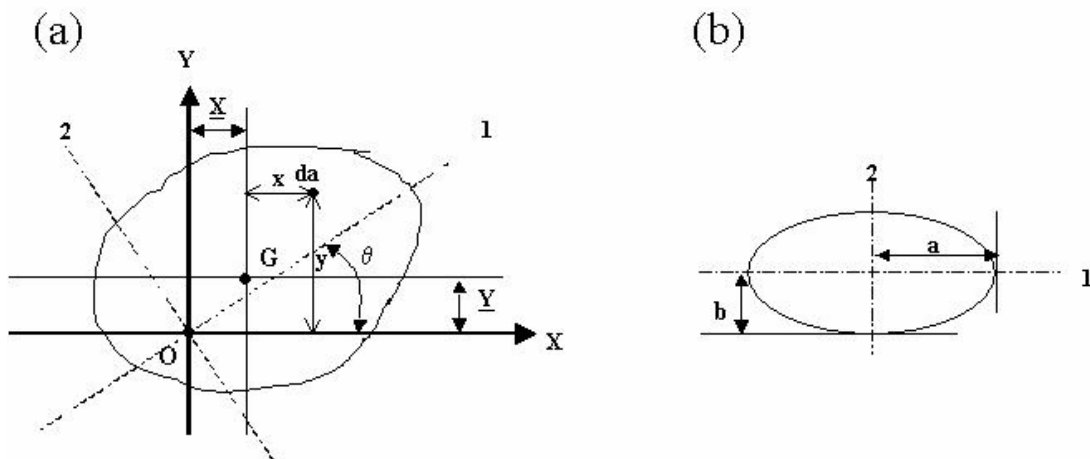


Figure 3-10 A schematic of a deformed VIC nucleus where major axis length = 2a, and minor axis length = 2b. From the given data, the moment of inertia of the deformed VIC nucleus was then calculated.⁽¹⁴⁵⁾

3.1.3 Statistical Analyses

In our experimental design, in order to demonstrate statistically significant differences ($p < 0.05$) in VIC nuclei aspect ratio, we anticipated 3 sections per slide. In addition, it was not known if there would be intra-section variability, therefore we performed 5 images for each section to establish if there were statistically significant differences between images in the same section. In order to get a sufficient distribution density, the number of cell nucleus (n) was calculated from the formula:

$$n = \frac{p \times q}{(SE)^2} \quad (3.5)$$

in which p was the proportion of population, $q = 1 - p$, SE was standard error of the proportion.⁽¹⁴⁶⁾ For 95% of confidence level, and $SE = \frac{0.05}{1.96} = 0.03 = 3\%$, and by assuming 50% of the population was valid for the test ($p = 50\%$, and $q = 50\%$), which gave us the number of cellular nucleus $n = \frac{p \times q}{(SE)^2} = \frac{50\% \times 50\%}{(3\%)^2} \approx 280$. Thus, for each slide, 95 cell nuclei per section ($280/3 = 95$), in which at least 19 cellular nuclei per image ($95/5 = 19$) were required for measurements in regions of the histological section. In this study, we anticipated measuring all the cellular nuclei for the analysis.

Five statistical studies were performed to correlate the effects of transvalvular pressure on VIC nuclei geometry from the available specimen mentioned in Figure 3-3 and Table 3-1: (1) Study the intra-image variability, (2) study the intra-section variability, (3) study the intra-slide variability, (4) study the intra-pressure variability, and (5) study the inter-pressure

variability. Summary of statistical study listed in Table 3-2 performed to correlate the effects of transvalvular pressure on VIC nuclei dimensions from the available histological specimen database.

Table 3-2 Summary of statistical study performed to correlate the effects of transvalvular pressure on VIC nuclei dimensions from the available histological specimen database (Table 3-1). Study (1): the intra-image variability, study (2) the intra-section variability, study (3) the intra-slide variability, study (4) the intra-pressure variability, and study (5) the inter-pressure variability.

	Image	Section	Slide	Pressure
Cellular nuclei	Study (1): Intra-image variability			
Image		Study (2): Intra-section variability		
Section	Inter-image variability (same as study (2))		Study (3): Intra-slide variability	
Slide		Inter-section variability (same as study (3))		Study (4): Intra-pressure variability
Pressure			Inter-slide variability (same as study (4))	
				Study (5): Inter-pressure variability

From the database mentioned previously, five panoramic images were in the same section, three sections were in the same slide, and each pressure level covered eight slides (Figure 3-3), thus traditional statistical method (experiments with two or three factors) was unable to perform the accurate statistical analysis.⁽¹⁴⁷⁾ Since the factor “section” was nested

under the factor “slide”, and the factor “slide” was nested under factor “pressure”, nested designs were performed to establish the statistically significant differences between pressure levels (Figure 3-3).⁽¹⁴⁸⁾ All statistical data analysis was performed by SYSTAT (SYSTAT 10, SPSS, Inc. Chicago, IL.).

A two-sample t test was under the assumption that two populations have equal variance conditions, $\sigma_1^2 = \sigma_2^2$. From our specimen database, we were interested in comparing a variance of population, σ_1^2 , to another variance of population, σ_2^2 , F-distribution was required.⁽¹⁴⁹⁾ We assumed that cells in different pressure levels, slides and sections have independent normal distributions, thus, the sizes of random samples have been independently drawn from two normal distribution populations. The ratio showed below

$$\frac{\frac{s_1^2}{\sigma_1^2}}{\frac{s_2^2}{\sigma_2^2}} = \frac{\frac{S_1^2}{\sigma_1^2}}{\frac{S_2^2}{\sigma_2^2}} \quad (3.6)$$

possesses a probability distribution in repeated sampling referred to as an F–distribution, where s^2 represents the sample variance, and σ^2 represents the population variance. Two parameters were required in F-distribution, namely the number of degrees of freedom (DF), were then obtained from the sample size.⁽¹⁴⁹⁾

3.1.3.1 Intra-section and intra-slide variability Aspect ratio and area of cellular nuclei were measured and compared. From the analyzed cellular nuclei data sets and based on the nested design, we assumed that slide and sections were two independent normal distributions with independent variances σ_{slide}^2 and $\sigma_{\text{section}}^2$. We calculated the number of degrees of freedom of

slide ($DF_{\text{slide}} = 7$, the number of degrees of freedom of section (slide) ($DF_{\text{section (slide)}} = 16$, and the number of degrees of freedom of error ($DF_{\text{error}} = 432$ from the sample size, which were tabulated in Table 3-3.⁽¹⁴⁸⁾ The F-distribution was used under 95% confidence intervals (tail probabilities $\alpha = 0.025$), to demonstrate the statistical intra-image, intra-slide, and intra-slide variability, and F-values were referred to Hogg and Johannes (1992).⁽¹⁴⁸⁾

Table 3-3 Calculated number of degrees of freedom of slide (DF_{slide}), the number of degrees of freedom of section (slide) ($DF_{\text{section(slide)}}$), and the number of degrees of freedom of error (DF_{error}) from the specimen database.

DF_{slide}	= number of slide -1	= 8 - 1 = 7
$DF_{\text{section (slide)}}$	= number of slide x (number of section -1)	= 8 x (3-1) = 16
DF_{error}	= number of slide x number of section x (number of cell -1)	= 8 x 3 x (19 -1) = 432

3.1.3.2 Intra-pressure and inter-pressure variability From the analyzed cellular nuclei data under different pressure levels, we assumed that pressure, slide, and sections were independent normal distributions with independent variances $\sigma_{\text{pressure}}^2$, σ_{slide}^2 , and $\sigma_{\text{section}}^2$. We calculated the number of degrees of freedom of pressure ($DF_{\text{pressure}} = 5$, the number of degrees of freedom of slide (pressure) ($DF_{\text{slide(pressure)}} = 42$, the number of degrees of freedom of section (slide) ($DF_{\text{section(slide)}} = 96$, and the number of degrees of freedom of error ($DF_{\text{error}} = 2592$, which were tabulated in Table 3-4.⁽¹⁴⁸⁾ As mentioned previously, the F-distribution was used under 95% confidence intervals (tail probabilities $\alpha = 0.025$), to demonstrate the statistical intra-slide, intra-pressure,

and inter-pressure variability, and F-values at different pressure-level were referred to Hogg and Johannes (1992).⁽¹⁴⁸⁾

Table 3-4 Calculated DF_{pressure} , $DF_{\text{slide}(\text{pressure})}$, $DF_{\text{section}(\text{slide})}$, and DF_{error} from the specimen database.

DF_{pressure}	= number of pressure -1	= 6 - 1 = 5
$DF_{\text{slide}(\text{pressure})}$	= number of pressure x (number of slide -1)	= 6 x (8-1) = 42
$DF_{\text{section}(\text{slide})}$	= number of pressure x number of slide x (number of section -1)	= 6 x 8 x (3 -1) = 96
DF_{error}	= number of pressure x number of slide x number of section x (number of cell -1)	= 6 x 8 x 3 x (19 -1) = 2592

3.2 RESULTS

3.2.1 Aspect Ratio of Valve Interstitial Cell Nuclei

Results are presented for whole serious available forty-eight slides. The results of the average aspect ratio of cellular nuclei in the circumferential–transmural cross-section under different pressure levels were illustrated in Figure 3-11. Statistical program was incorporated to analyze the five studies to correlate the effects of transvalvular pressure on VIC nuclei geometry from the available specimen mentioned in Table 3-2. Among six transvalvular pressure levels, aspect ratio of VIC nuclei in the tissue demonstrated three data groups as 1.8:1, 2.6:1, and 4.5:1 nuclei aspect ratios in 0 and 1 mmHg, 2 and 4 mmHg, and 60 and 90 mmHg, respectively. Significant inter-pressure variability was found everywhere except 0- and 1-mmHg, 2- and 4-mmHg, and 60- and 90-mmHg (ANOVA, $p < 0.001$) (Figure 3-11). In addition, the average VIC nuclei aspect ratios measured in the radial-transmural direction under 0 mmHg was 1.35 and this value provided reference information for further finite element simulations.

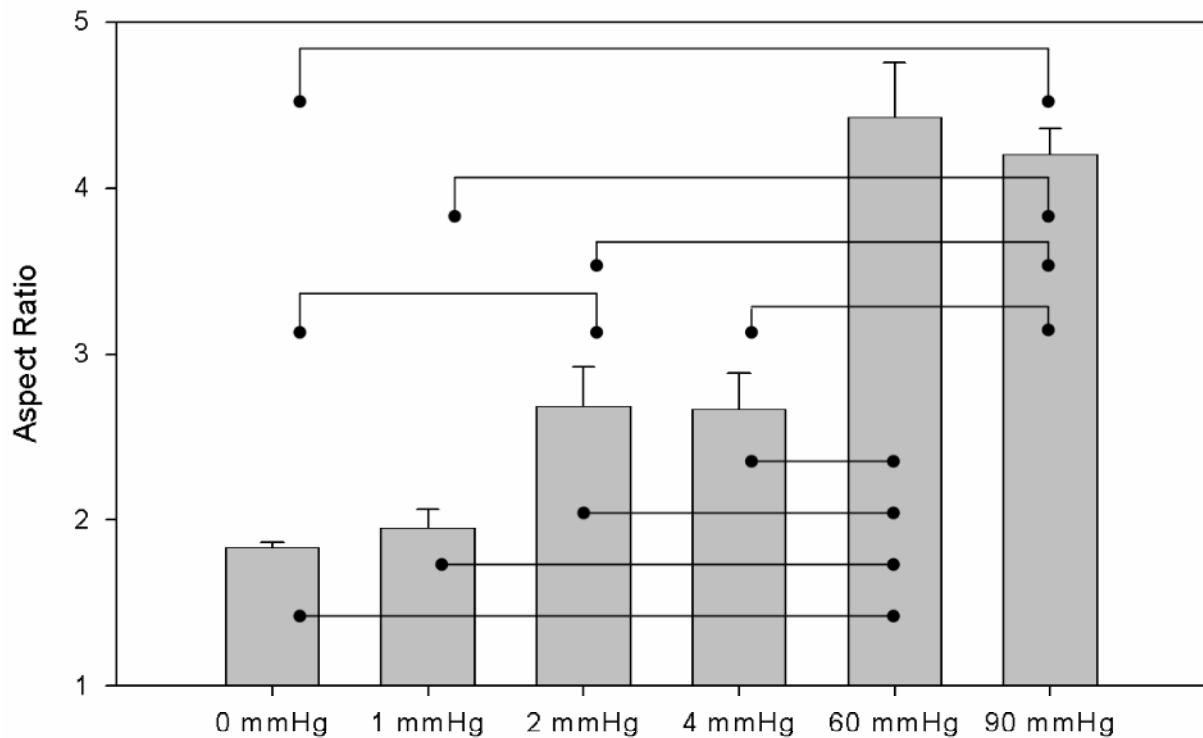


Figure 3-11 A comparison of the VIC nuclei aspect ratios under six pressure levels. The barbells (●—●) indicate inter-pressure statistical differences, which were found everywhere except 0- and 1-mmHg, 2- and 4-mmHg, and 60- and 90-mmHg (ANOVA, $p < 0.001$).

3.2.2 Intra-Section and Intra-Slide Variability

A representative results of cellular nuclei aspect ratio study of intra-slide variability in 0 mmHg pressure level was shown in Figure 3-12, and additional results of the intra-slide variability under different transvalvular pressure levels were presented in Appendix D. Degrees of freedom were calculated to obtain the F-values and the analysis of variance (ANOVA) was generated by the statistical program. The resultant ANOVA table was tabulated in Table 3-5 for 0, 1, 2, 4, 60, and 90 mmHg transvalvular pressure levels. The ANOVA value for factor “slide” indicates the ANOVA value for slide, represents the variability of slides under the same pressure

level. The ANOVA value for factor “section (slide)” indicates the ANOVA value for section, represents the variability of section in the same slide under the same pressure level. As calculated previously, $DF_{\text{slide}} = 7$, $DF_{\text{section}(\text{slide})} = 16$, and $DF_{\text{error}} = 432$. For example, under 0 mmHg pressure level, the ANOVA value of the slide = 4.661, and the ANOVA value of the section = 1.562 (Table 3-5).

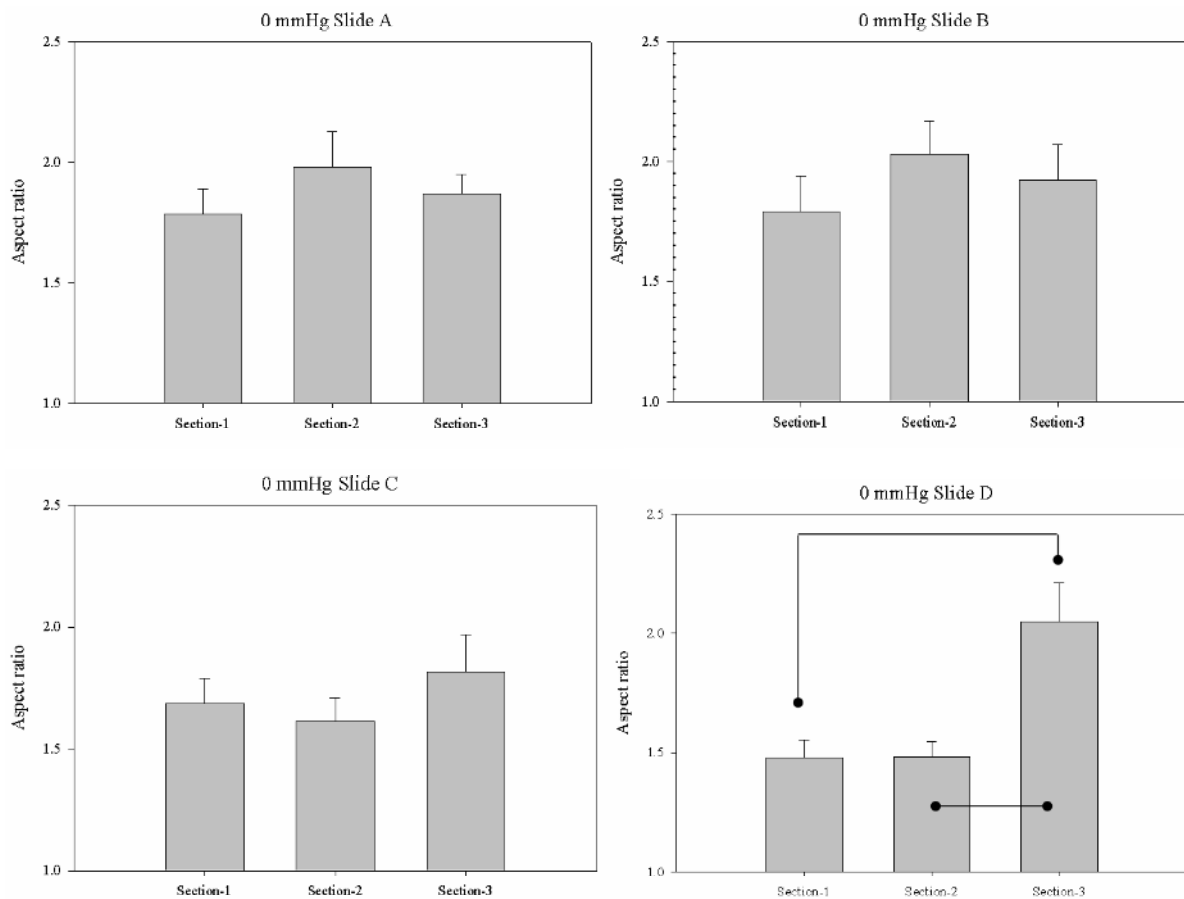


Figure 3-12 A representative results of cellular nuclei aspect ratio study of intra-slide variability under 0 mmHg pressure level, and the barbells (●—●) indicates statistical differences ($p < 0.05$).

Table 3-5 Statistical results of ANOVA table for intra-slide and intra-section variability.

Analysis of variance				
0 mmHg				
Factor	Sum-of-squares	Degrees of freedom	Mean square	ANOVA
Slide	9.478	7	1.354	4.661
Section (slide)	7.26	16	0.454	1.562
Error	125.488	432	0.29	
1 mmHg				
Factor	Sum-of-squares	Degrees of freedom	Mean square	ANOVA
Slide	39.315	7	5.616	8.638
Section (slide)	10.832	16	0.677	1.041
Error	280.888	432	0.65	
2 mmHg				
Factor	Sum-of-squares	Degrees of freedom	Mean square	ANOVA
Slide	170.903	7	24.415	17.007
Section (slide)	60.384	16	3.774	2.629
Error	620.174	432	1.436	
4 mmHg				
Factor	Sum-of-squares	Degrees of freedom	Mean square	ANOVA
Slide	142.426	7	20.347	15.260
Section (slide)	29.839	16	1.865	1.399
Error	575.987	432	1.333	
60 mmHg				
Factor	Sum-of-squares	Degrees of freedom	Mean square	ANOVA
Slide	313.963	7	44.852	11.518
Section (slide)	233.215	16	14.576	3.743
Error	1682.204	432	3.894	
90 mmHg				
Factor	Sum-of-squares	Degrees of freedom	Mean square	ANOVA
Slide	95.102	7	13.586	3.988
Section (slide)	75.743	16	4.734	1.390
Error	1471.671	432	3.407	

F-values, $F(\alpha, DF_{\text{slide}}, DF_{\text{section (slide)}})$ and $F(\alpha, DF_{\text{section (slide)}}, DF_{\text{error}})$, were referred to Hogg and Johannes (1992).⁽¹⁴⁸⁾ In which F-distribution was used under 95% confidence intervals (tail probabilities $\alpha = 0.025$), DF_{slide} represents degrees of freedom of slide, $DF_{\text{section(slide)}}$ represents degrees of freedom of section (slide) and DF_{error} represents of degrees of freedom of error (Table 3-6).

Table 3-6 Results from the ANOVA table and F-table for intra-slide and intra-pressure variability.

	Factor	ANOVA	F-value	Results
0 mmHg	Slide	4.661	$F(0.025, 7, 16) = 3.2194$	Significant variability exists between slides
	Section (slide)	1.562	$F(0.025, 16, 243) = 1.8$	No significant variability exists between sections
1 mmHg	Slide	8.638	$F(0.025, 7, 16) = 3.2194$	Significant variability exists between slides
	Section (slide)	1.041	$F(0.025, 16, 243) = 1.8$	No significant variability exists between sections
2 mmHg	Slide	17.007	$F(0.025, 7, 16) = 3.2194$	Significant variability exists between slides
	Section (slide)	2.629	$F(0.025, 16, 243) = 1.8$	Significant variability exists between sections
4 mmHg	Slide	15.26	$F(0.025, 7, 16) = 3.2194$	Significant variability exists between slides
	Section (slide)	1.399	$F(0.025, 16, 243) = 1.8$	No significant variability exists between sections
60 mmHg	Slide	11.518	$F(0.025, 7, 16) = 3.2194$	Significant variability exists between slides
	Section (slide)	3.743	$F(0.025, 16, 243) = 1.8$	Significant variability exists between sections
90 mmHg	Slide	3.988	$F(0.025, 7, 16) = 3.2194$	Significant variability exists between slides
	Section (slide)	1.39	$F(0.025, 16, 243) = 1.8$	No significant variability exists between sections

Statistically significant differences were defined as the value of ANOVA is greater than the F-value. The results of the ANOVA tables (Table 3-5) compared with F-table (Table 3-6) were summarized as following:

1. Intra-section variability: Statistically significant differences were found in 2, 60 mmHg transvalvular pressure level due to intra-image variability.
2. Intra-slide variability: Statistically significant differences were found in all transvalvular pressure levels due to intra-section variability.
3. No intra-section variability was found in 90 mmHg transvalvular pressure level, however, intra-slide variability was observed.

3.2.3 Results of Intra-Pressure and Inter-Pressure Variability

A representative results of cellular nuclei aspect ratio of intra-pressure variability under 0 mmHg pressure level was shown in Figure 3-13, and additional results of intra-pressure variability under different transvalvular pressure levels were presented in Appendix D. To demonstrate the statistical intra-pressure and inter-pressure variability in our nested experimental design (Figure 3-3), F-values were required. Degrees of freedom were calculated as mentioned previously, and the ANOVA value was generated from statistical program. The resultant ANOVA table was tabulated in Table 3-7, in which the ANOVA value for factor “pressure” indicates the ANOVA value for pressure, and the ANOVA value for factor “slide (pressure)” indicates the ANOVA value for slide, represents the variability of slides under the same pressure level. The ANOVA value for factor “section (slide)” indicates the ANOVA value for section, represents the variability of the section in the same slide and under the same pressure level. As

calculated in previously section, $DF_{\text{pressure}} = 5$, $DF_{\text{slide}(\text{pressure})} = 42$, $DF_{\text{section}(\text{slide})} = 96$, and $DF_{\text{error}} = 2592$. In Table 3-7, the ANOVA value of the pressure = 389.219, the ANOVA value of the slide = 10.006, and the ANOVA value of the section = 2.369.

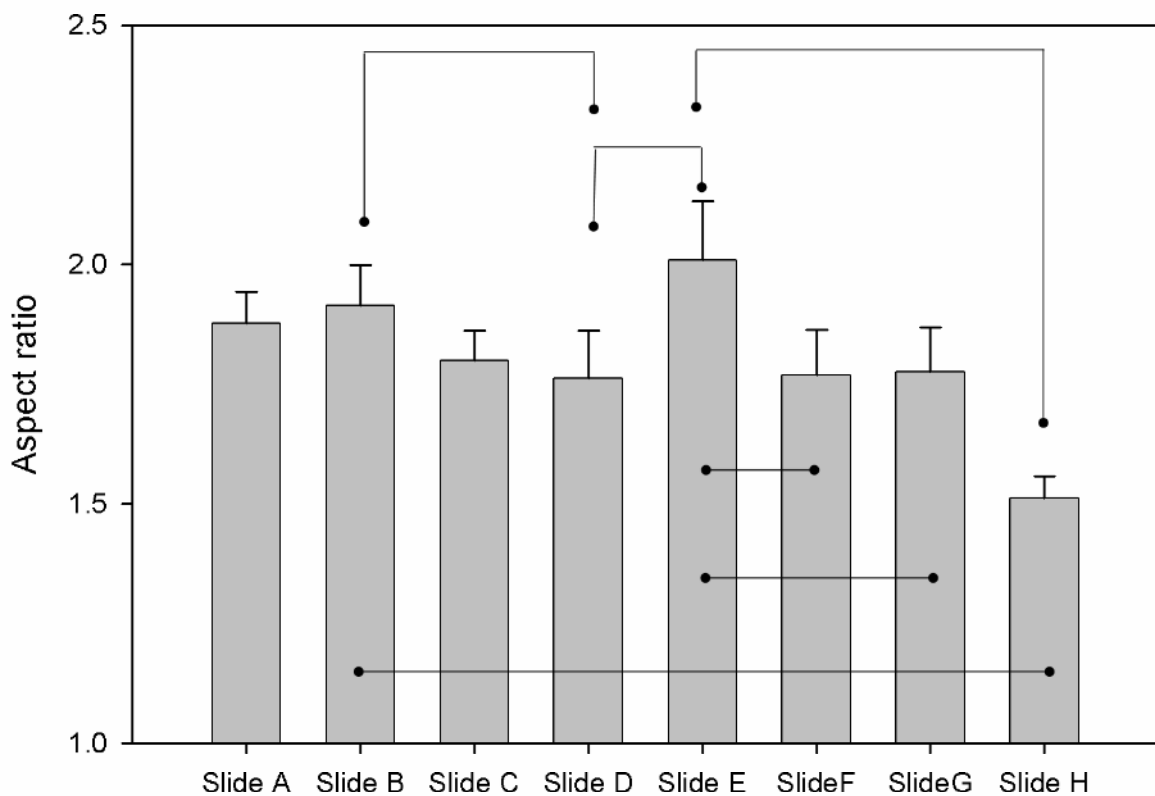


Figure 3-13 A representative results of cellular nuclei aspect ratios study of intra-pressure variability under 0 mmHg pressure level, and the barbells (●—●) indicates statistical differences ($p < 0.05$).

Table 3-7 Statistical results of ANOVA table for inter-pressure variability.

Analysis of variance				
Factor	Sum-of-squares	Degrees of freedom	Mean squares	ANOVA
Pressure	3571.55	5	714.231	389.219
Slide (pressure)	771.186	42	18.362	10.006
Section (slide)	417.273	96	4.347	2.369
Error	4756.713	2592	1.835	

F-values, $F(\alpha, DF_{\text{pressure}}, DF_{\text{slide}(\text{pressure})})$, $F(\alpha, DF_{\text{slide}(\text{pressure})}, DF_{\text{section}(\text{slide})})$, and $F(\alpha, DF_{\text{section}(\text{slide})}, DF_{\text{error}})$, were referred to Hogg and Johannes (1992)⁽¹⁴⁸⁾ In which F-distribution was used under 95% confidence intervals (tail probabilities $\alpha = 0.025$), DF_{pressure} represents the degrees of freedom of pressure, $DF_{\text{slide}(\text{pressure})}$ represents the degrees of freedom of slide, $DF_{\text{section}(\text{slide})}$ represents the degrees of freedom of section, and DF_{error} represents the degrees of freedom of error.

Table 3-8 Results from ANOVA table and F-table for inter-pressure variability.

Factor	ANOVA	F-value	Results
Pressure	389.219	$F(0.025, 5, 42) = 2.89$	Significant variability exists between pressure levels due to slide-variability.
Slide (pressure)	10.006	$F(0.025, 42, 96) = 1.657$	Significant variability exists between slides due to section-variability.
Section (slide)	2.369	$F(0.025, 96, 2592) = 1.316$	Significant variability exists between sections

The ANOVA tables (Table 3-6) compared with F-table (Figure 3-12) were summarized as following:

1. Statistically significant intra-section variability was found among all databases.
2. Statistically significant intra-slide variability was found due to intra-section variability.
3. Statistically significant intra-pressure variability was found due to intra-slide and intra-section variability.

3.2.4 Distribution of Nuclei Aspect Ratio

From our unpublished laboratory results, the thickness of the ventricular layer was estimated as 25-30% of the total thickness, and the thickness of the fibrosa layer was estimated as 25-30% of the total thickness in the native aortic valve leaflet. Aspect ratio of cellular nuclei vs. normalized thickness of the tissue showed in Figure 3-14 indicated that under zero- and low-transvalvular pressure (0 and 4 mmHg), the deformation of VIC nuclei reached an almost constant level toward to the ventricularis layer (normalized thickness = 0 ~ 0.3). 11 % change in nuclei aspect ratio was observed at normalized thickness location 0.25. However, around the fibrosa layer (normalized thickness = 0.7 ~ 1), aspect ratio of cellular nuclei under 4 mmHg slightly increased, while there were no detectable changes of the aspect ratio of cellular nuclei under 0 mmHg. 40 % and 51 % changes in nuclei aspect ratio were observed at normalized thickness locations 0.65 and 0.85, respectively. Under high transvalvular pressure (90 mmHg), the aspect ratios of VIC nuclei were greater than those under the zero- and low-pressure levels with 54 %, 76 % and 49 % changes in nuclei aspect ratio at the normalized thickness location

0.25, 0.65, and 0.85, respectively. A clear trend of increased aspect ratio of cellular nuclei for 90 mmHg was found toward to the fibrosa layer. Statistically significant differences were found everywhere by comparing the VIC nuclei aspect ratios at 90mmHg to those at 0 mmHg pressure levels ($p < 0.05$). Statistically significant different were found by comparing the VIC nuclei aspect ratios at 4 mmHg to those at 90 mmHg.

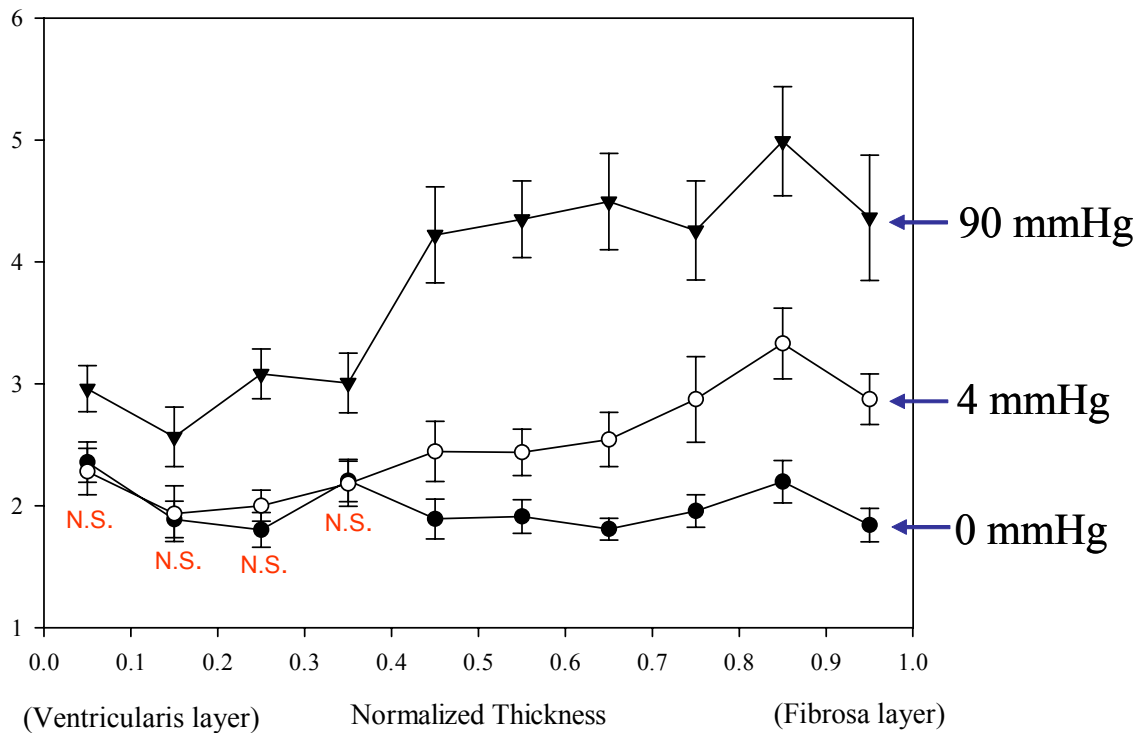


Figure 3-14 Aspect ratios of cellular nuclei vs. normalized thickness for all the cellular nuclei data at zero-, low- and high-pressure levels. Statistically significant differences were found everywhere by comparing the VIC nuclei aspect ratios at 4 and 90 mmHg to those at 0 mmHg pressure levels. Statistically significant different were found everywhere by comparing the VIC nuclei aspect ratios at 4 mmHg to those at 90 mmHg. “N.S.” indicates no statistically significant differences ($p < 0.05$).

Area of cellular nuclei vs. normalized thickness of the sample under zero-, low-, and high-transvalvular pressure (0, 4 mmHg, 90 mmHg) was shown in Figure 3-15. The area of VIC nuclei remained relatively consistent level from the ventricularis layer (normalized thickness = 0 ~ 0.3) to the fibrosa layer (normalized thickness = 0.7 ~ 1). 39 % and 38 % changes in the area of VIC nuclei were observed among 0 mmHg and 4 mmHg at normalized location 0.5, and 0.55, respectively. At location 0.75, change in area of VIC nuclei increased to 71 %, and significant differences was observed at 4 mmHg pressure level at locations 0.15 and 0.75. At the normalized thickness location 0.95, little change in area was observed (6 %). Compare the change in area of VIC nuclei with 0 mmHg and 90 mmHg, 39 % at location 0.1 and 30 % at location 0.95 were observed, and no substantial differences were found along the thickness. In conclusion, the aspect ratio of cellular nuclei vs. normalized thickness changed within the increasing transvalvular pressure was observed (Figure 3-14), however, in the area of cellular nuclei vs. normalized thickness studies, little or few increasing or decreasing of area of cellular nuclei was found (Figure 3-15), indicating most of the VIC nuclei appearing in the histological sections were sliced from their centroid, and the axes of the VIC nuclei parallel to the circumferential and transmural directions.

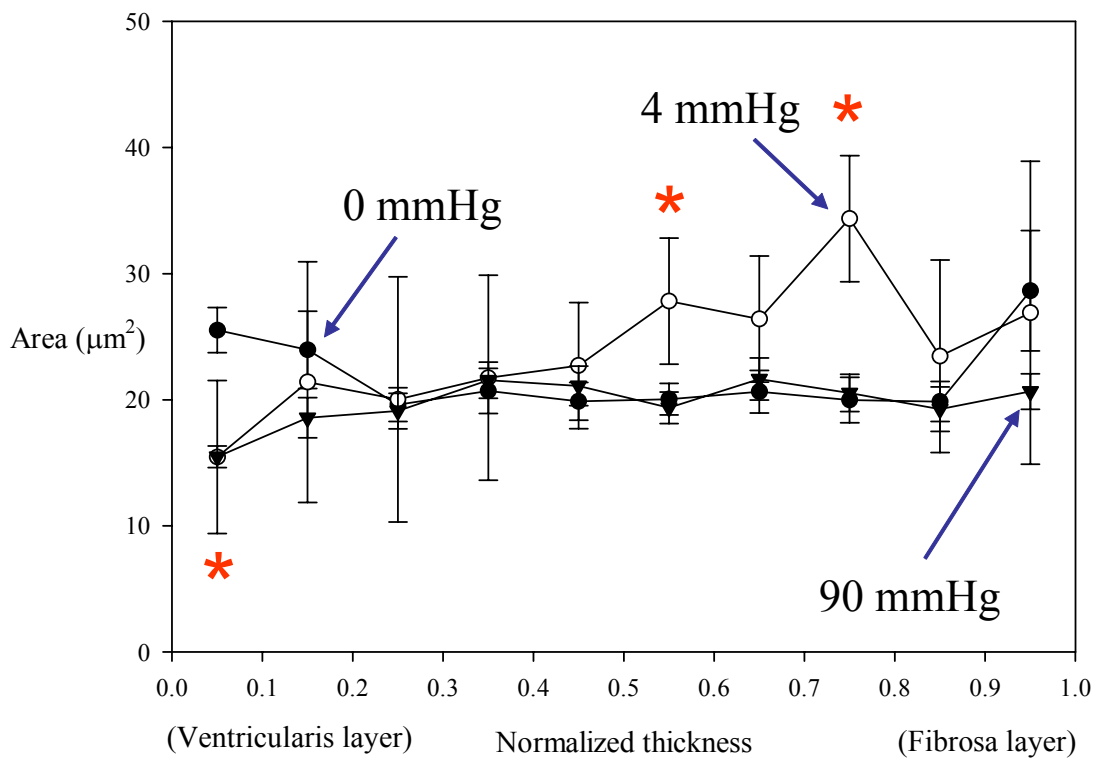


Figure 3-15 Area of cellular nuclei vs. normalized thickness for all the cellular nuclei data for zero-, low- and high-pressure levels, in which (*) indicates statistically significant differences were found by comparing the VIC nuclei areas under 4 and 90 mmHg to those under 0 mmHg ($p < 0.05$).

The average aspect ratio of cellular nuclei at 0.25 normalized thicknesses was 1.75 under 0 mmHg transvalvular pressure, and the average aspect ratio of cellular nuclei at 0.85 normalized thickness under 0 mmHg was 2.25 (Figure 3-14). The average area of cellular nuclei at 0.25 normalized thickness under 0 mmHg was $18.5 \mu\text{m}^2$, and the average area of cellular nuclei at 0.85 normalized thickness under 0 mmHg was $18.1 \mu\text{m}^2$. For those given data, Table 3-9 provided the calculated nuclei aspect ratio and its corresponding area of VIC nuclei, in which

if $a_1 = 3.2$ (long axis of the ellipse at 0.25 normalized thickness), $b_1 = 1.83$ (short axis of the ellipse at 0.25 normalized thickness), the aspect ratio cellular nuclei was 1.75 (Figure 3-14), and the area of cellular nuclei was $18.5 \mu\text{m}^2$ (Figure 3-15). If $a_2 = 3.6$ (long axis of the ellipse at 0.85 normalized thickness), and $b_2 = 1.6$ (short axis of the ellipse at 0.85 normalized thickness), the cellular nuclei aspect ratio was 2.25 (Figure 3-14), and the area of cellular nuclei was $18.1 \mu\text{m}^2$ (Figure 3-15). A schematic cellular deformation as shown in Figure 3-16, which indicated that under the same pressure level, elongation of the cellular nuclei along the normalized thickness was found without increasing the area of the cellular nuclei.

Table 3-9 Calculation the VIC nuclei aspect ratio and its corresponding area under 0 mmHg

0 mmHg	Normalized thickness location	Major axis length (a)	Minor axis length (b)	Aspect ratio (a / b)	Area (a x b x π)
Location 1	0.25	3.2	1.83	1.75	18.5
Location 2	0.85	3.6	1.6	2.25	18.1

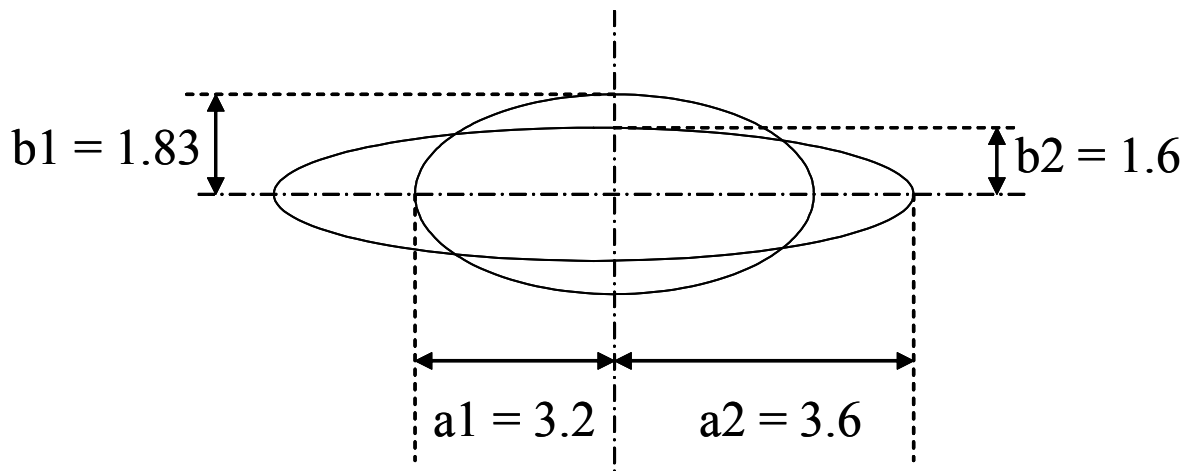


Figure 3-16 An schematic cellular deformation indicated that under the 0 mmHg pressure level, elongation of the cellular nuclei (aspect ratio from 1.75 to 2.25) along the normalized thickness (from 0.25 to 0.85) was found while the area of the cellular nuclei remained constant (area $\approx 18 \mu\text{m}^2$).

Under 4 mmHg transvalvular pressure level, the average aspect ratio of cellular nuclei at 0.15 normalized thicknesses was 1.8, and the average aspect ratio of cellular nuclei at 0.85 normalized thickness under 4 mmHg was 3.4 (Figure 3-14). The average area of cellular nuclei at 0.15 normalized thickness under 4 mmHg was $20.18 \mu\text{m}^2$, and the average area of cellular nuclei at 0.85 normalized thickness under 4 mmHg was $20.67 \mu\text{m}^2$. For those given data, Table 3-10 provided the calculated nuclei aspect ratio and its corresponding area of VIC nuclei, in which if $a_1 = 3.4$ (long axis of the ellipse at 0.15 normalized thickness), $b_1 = 1.8$ (short axis of the ellipse at 0.15 normalized thickness). The aspect ratio cellular nuclei was 1.89 (Figure 3-14), and the area of cellular nuclei was $20.18 \mu\text{m}^2$ (Figure 3-15). If $a_2 = 4.7$ (long axis of the ellipse at 0.85 normalized thickness), and $b_2 = 1.4$ (short axis of the ellipse at 0.85 normalized

thickness). The aspect ratio cellular nuclei was 3.35 (Figure 3-14), and the area of cellular nuclei was $20.67 \mu\text{m}^2$ (Figure 3-15).

Table 3-10 Calculation the VIC nuclei aspect ratio and the corresponding areas under 4 mmHg and 90 mmHg pressure levels.

4 mmHg	Normalized thickness location	Major axis length (a)	Minor axis length (b)	Aspect ratio (a / b)	Area (a x b x π)
Location 1	0.15	3.4	1.8	1.89	20.18
Location 2	0.85	4.7	1.4	3.35	20.67
90 mmHg	Normalized thickness location	Major axis length (a)	Minor axis length (b)	Aspect ratio (a / b)	Area (a x b x π)
Location 1	0.15	4	1.6	2.5	20.01
Location 2	0.75	5.04	1.26	4	19.95

Under 90 mmHg transvalvular pressure, the average aspect ratio of cellular nuclei at 0.15 normalized thicknesses was 2.5, and the average aspect ratio of cellular nuclei at 0.75 normalized thickness under 90 mmHg was 4 (Figure 3-14). The average area of cellular nuclei at 0.15 normalized thickness under 90 mmHg was $20.01 \mu\text{m}^2$, and the average area of cellular nuclei at 0.75 normalized thickness under 90 mmHg was $19.95 \mu\text{m}^2$. For those given data, Table 3-10 provided the calculated nuclei aspect ratio and its corresponding area of VIC nuclei, in which if $a_1 = 4$ (long axis of the ellipse at 0.15 normalized thickness), $b_1 = 1.6$ (short axis of the ellipse at 0.15 normalized thickness). The cellular nuclei aspect ratio was 2.5 (Figure 3-14), and

the area of cellular nuclei was $20 \mu\text{m}^2$ (Figure 3-15). If $a_2 = 5.04$ (long axis of the ellipse at 0.75 normalized thickness), and $b_2 = 1.26$ (short axis of the ellipse at 0.75 normalized thickness). The aspect ratio cellular nuclei was 4 (Figure 3-14), and the area of cellular nuclei was $19.95 \mu\text{m}^2$ (Figure 3-15). Based on these considerations, three-dimensional net-volume of VIC nuclei was investigated under different transvalvular pressure levels in the further finite element simulations.

3.2.5 The Relationship of Nuclei Aspect Ratio and Collagen Fiber Architecture

As indicated in the previous section, a positive trend was found between the measured VIC nuclei aspect ratio and the applied transvalvular pressure in specimen of the native aortic valves (Figure 3-11). As highlighted by the histological sections analyzed in this study, the VIC nuclei are in intimate contact with their surrounding collagenous extracellular matrix (ECM), and thus a change in VIC nuclei aspect ratio under applied transvalvular pressure is likely concomitant to deformation of the ECM. As stated in Section 1.4, to quantify the degree of fiber orientation, an orientation index (OI) was used by small angle light scattering technique and a highly oriented fiber network has a low OI value, while a more randomly oriented network has a higher value. Figure 3-17 depicts the effects of increasing transvalvular pressure on collagen fiber alignment (panel A) and VIC nuclei aspect ratio (panel B) for comparison (Figure 3-17).

Gross visual comparison of the two plots in Figure 3-17 yielded three distinct regions: a region of steep change between 0 and 1 mmHg, a transition region between 1 and 4 mmHg, and a region of asymptotic behavior between 4 and 60 mmHg. In the previous study, it was hypothesized that the large decreases in OI (increases in alignment) from 0 to 1 mmHg are due predominantly to large fiber alignment, while the more subtle increases in fiber rotations from 1

to 60 mmHg are due to changes in collagen crimp and collagen fiber compaction. The fact that VIC nuclei aspect ratio changes appeared to parallel the changes in collagen fiber alignment is not surprising given the intimate relationship between the VIC nuclei and the collagenous ECM.

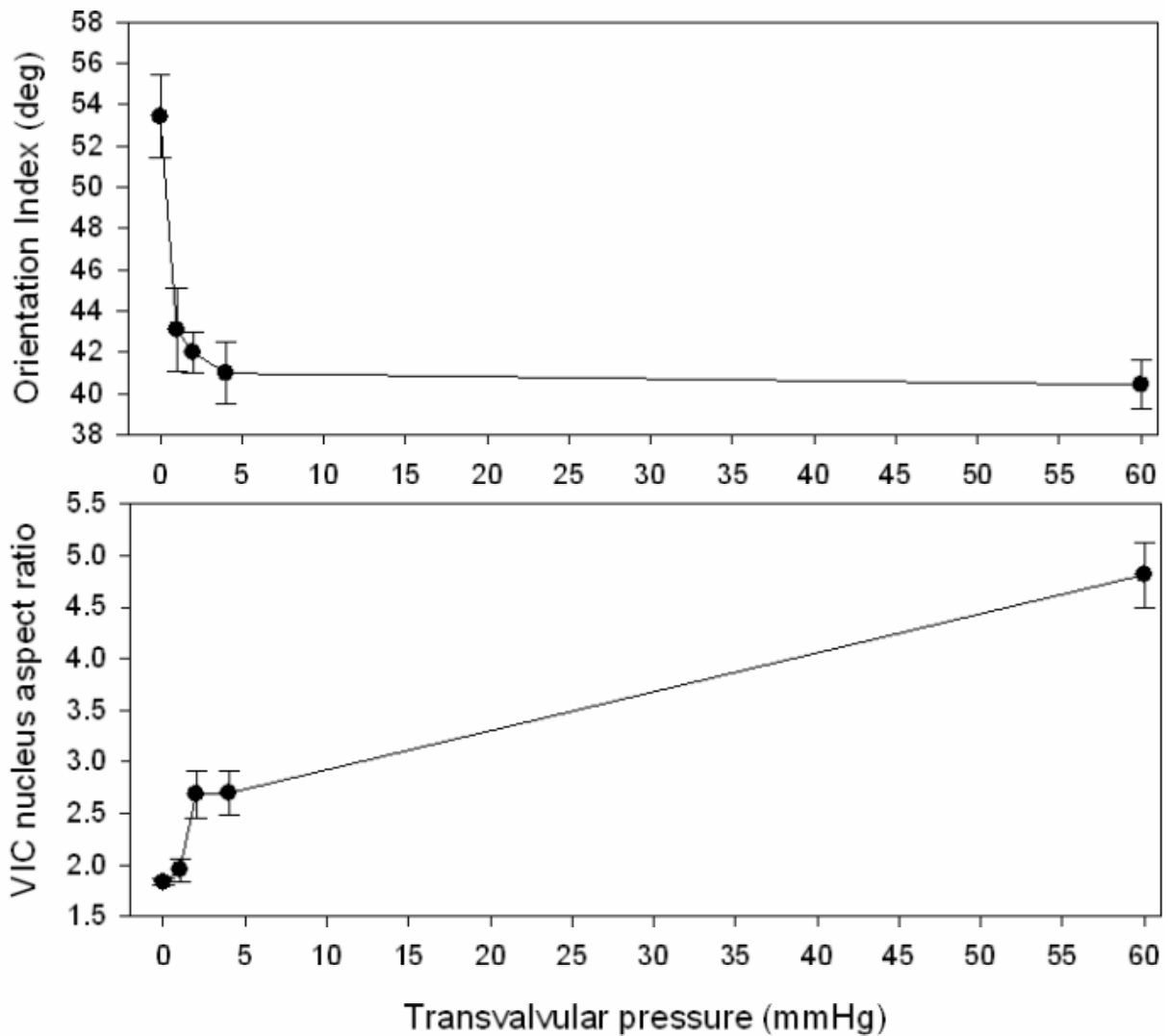


Figure 3-17 Orientation Index vs. transvalvular pressure, and VIC nuclei aspect ratio vs. transvalvular pressure. A trend was found associated with the fiber orientation and the deformed VIC nuclei aspect ratio.

In Figure 3-18 the VIC nuclei aspect ratio in the ventricularis layer is plotted versus the OI for 0, 1, 2, 4, and 60 mmHg transvalvular pressure gradients. In Figure 3-19, the VIC nuclei aspect ratio in the fibrosa layer is plotted versus the OI. Changes in the VIC nuclei aspect ratio in the ventricularis and fibrosa layer were qualitatively similar. Interestingly, the increase in VIC nuclei aspect ratio from 0 to 1 mmHg was higher in the fibrosa layer than in the ventricularis layer. Considering that the 0 mmHg aspect ratio of VIC nuclei in the fibrosa and ventricularis are approximately equal, and that the 0 mmHg OI of the fibrosa layer is significantly less than the ventricularis layer (~ 48.5 versus 58), these data suggest a higher degree of coupling between the VIC nuclei and the collagen fibers in the fibrosa compared with the ventricularis. This could potentially be explained by the high elastin content of the ventricularis, which may serve to dampen the coupling between the VIC nuclei and the collagen fibers. Furthermore, the ultimate VIC nuclei aspect ratio observed under 60 mmHg was significantly higher in the fibrosa compared with the ventricularis (~ 5 versus 4). Interestingly, these maximum aspect ratios occur around an OI of 39 in both layers, suggesting that other factors (such as collagen fiber diameter or density) may be acting, in addition to overall collagen fiber network alignment.

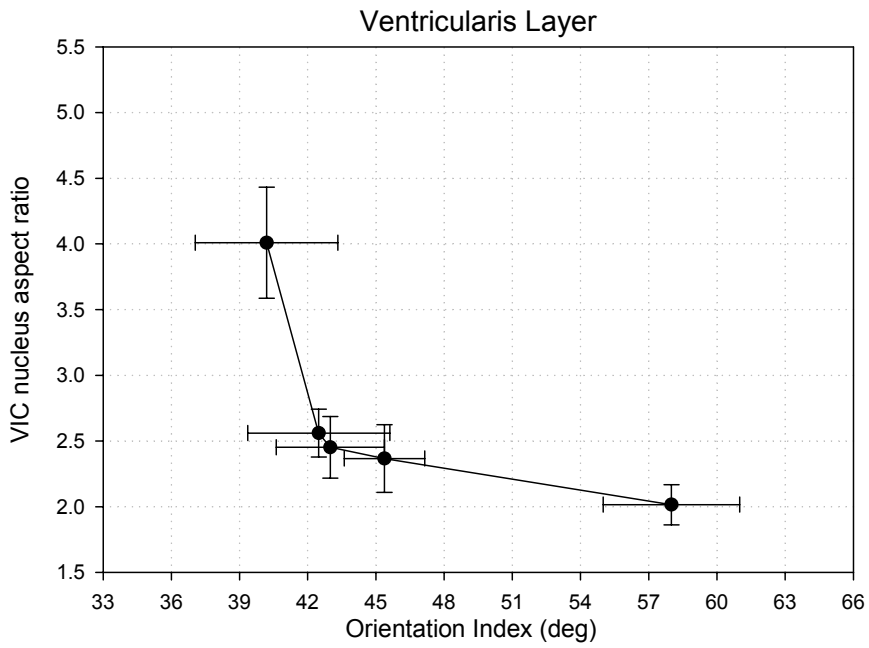


Figure 3-18 VIC nuclei aspect ratio vs. OI in the ventricular layer.

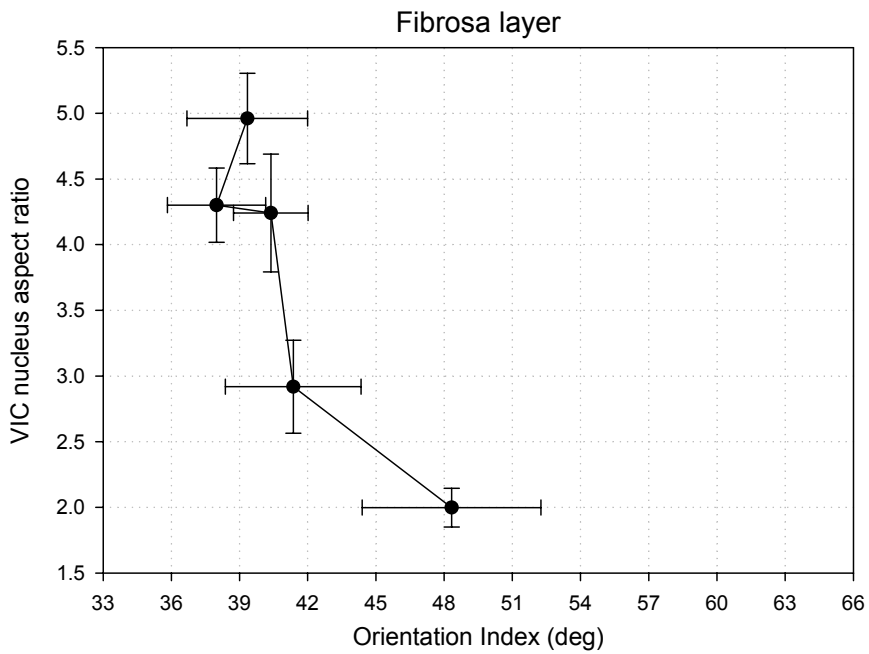


Figure 3-19 VIC nuclei aspect ratio vs. OI in the fibrosa layer.

3.3 SUMMARY

Five studies were conducted to correlate the effects of transvalvular pressure on VIC nuclei geometry from the available specimen (Table 3-1 and Figure 3-3). In the present study, the deformation of aortic VICs under various physiologically relevant levels of transvalvular pressure was quantified. The elongated aspect ratios of VICs were calculated by dividing the major axis to the minor axis under various pressures measured experimentally from photomicrographs of native aortic valve leaflets. From the measurements of VIC nuclei aspect ratio in two different cross-sections: circumferential-transmural, and radial-transmural directions, a prolate ellipsoidal cellular geometry was hypothesized in our laboratory (Figure 3-9).

However, under six different transvalvular pressure levels, three distinct averaged VIC nuclei aspect ratio were found: from 0 – 1 mmHg, the averaged VIC nuclei aspect ratio was 1.8, from 2 – 4 mmHg, the averaged VIC nuclei aspect ratio was 2.6, and under 60 – 90 mmHg, the averaged VIC nuclei aspect ratio was 4.5. Furthermore, different VIC nuclei aspect ratios in different valve tissue layer were observed, where in the fibrosa layer, VIC nuclei aspect ratio is higher than one found in the ventricularis layer (Figure 3-14). Area of VIC nuclei were also measured, no substantial differences were found either in the different layers or different pressure levels (Figure 3-15). Thus, the relationship of physiological transvalvular pressure measured *in vivo* and the corresponding VIC nuclei aspect ratios at a specific time point during valve operation was represented in Figure 3-20, where VIC nuclei aspect ratios with consistent areas increased with the increasing transvalvular pressure.

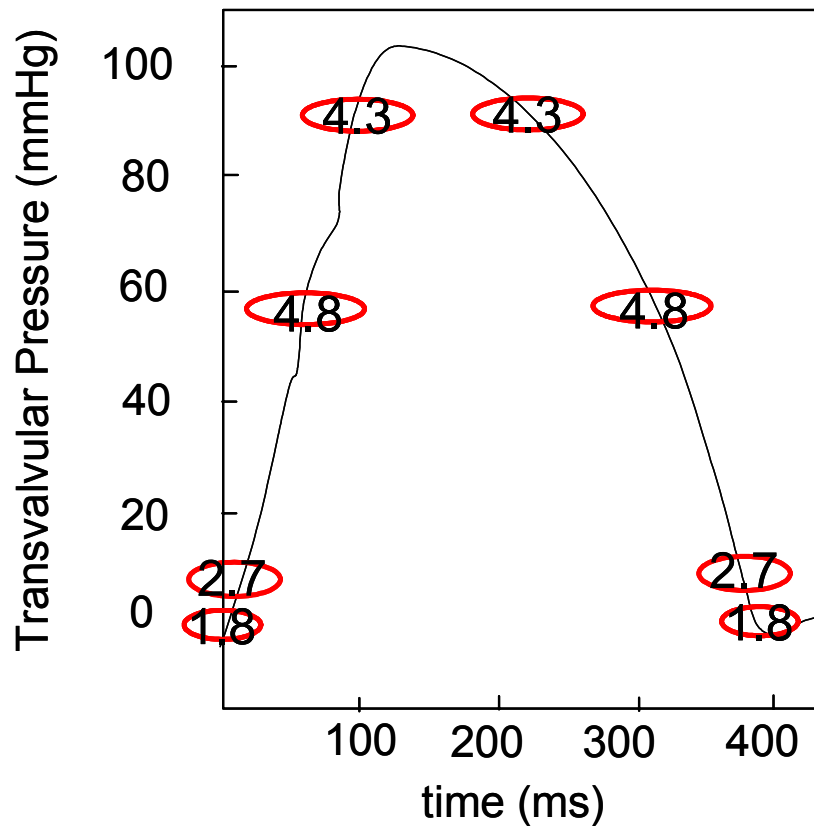


Figure 3-20 The relationship of physiological transvalvular pressure measured *in vivo* and the corresponding VIC nuclei aspect ratios at a specific time point during valve operation. The VIC nuclei aspect ratios with consistent areas increased with the increasing transvalvular pressure.

Since the VIC nuclei are in contact with the surrounding ECM and a change in VIC nuclei aspect ratio under applied transvalvular pressure is related to deformation of the ECM, VIC nuclei aspect ratios were compared to the OI measured previously (Figure 3-17).⁽²⁹⁾ Three distinct zones were observed: from 0 – 1 mmHg, large decreased OI value (large increased in the fiber alignment), but little changes in the VIC nuclei aspect ratio were found, suggesting fiber alignment did not alter the deformation of VIC nuclei under low-pressure level. However, from 1 – 4 mmHg, VIC nuclei aspect ratio increased with little changes in the OI. In our laboratory, it

has been hypothesized fiber rotation induced by the radial force did not have strong influences on the fiber alignment, but have potential effects on the deformation of VIC nuclei. From our previous experimental data,⁽²⁹⁾ by 4 mmHg most, but not all, of the crimp either had been increasingly diminished or completely removed. Thus, under 4 – 60 mmHg pressure level, consistent OI with significant increased VIC nuclei aspect ratio observed in this study, indicating that other factors present between the fiber network and VIC nuclei deformation. In our laboratory, it has been hypothesized that under higher-pressure level, compacting of the fiber may induce the compression in the fiber network and elongates the VIC nuclei.

In conclusion, the deformation of VIC nuclei under various transvalvular pressures was quantified, and a relationship was found between the valve tissue layers. Furthermore, a coupling exit between the VIC nuclei and fiber network response to the transvalvular pressure were observed. This information forms the basis of an interaction of VIC nuclei and ECM and leads to an understanding of VIC nuclei capable of responding to mechanical stimulation.

4.0 SIMULATION THE EFFECT OF TRANSVALVULAR PRESSURE ON THE VALVE INTERSTITIAL CELL NUCLEI GEOMETRY

In Chapter 3 the VIC nucleus aspect ratio (i.e., a measure of the changes in overall cellular geometry) was quantified with respect to applied transvalvular pressure. In this chapter, a two-dimensional microscopic model of the aortic valve leaflet tissue was developed to investigate how mechanical stresses are transmitted from the leaflet ECM to the VIC nucleus. In order to apply simulated loads to the microscopic model, transvalvular pressures ranging from 0 mmHg to 90 mmHg were transformed into biaxial tension states. Furthermore, the results of Chapter 3 suggested a possible relationship between VIC nucleus aspect ratio and collagen fiber architectures under applied transvalvular pressure. Thus we used a constitutive model to describe the anisotropic ECM component in the microscopic model. Microscopic models of tissue incorporating cell / ECM interaction may represent a key next step in understanding the mechanical behavior of native aortic valve leaflet tissues.

4.1 MODEL DEVELOPMENT I: STRESS STATE OF HEART VALVE LEAFLET

The heart valve leaflet is considered to be a thin-walled membrane shell. The heart valve leaflet was assumed to be static equilibrium, and that the only loading on the tissue is due

to the transvalvular pressure. Thus quasi – static loading state due to the transvalvular pressures applied to the heart valve leaflet simulated the *in vivo* diastolic state, i.e., valve is in closed position.

The heart valve leaflet has a “double-curved” surface.⁽¹⁵⁰⁾ Since the circumferential and radial directions in the aortic heart valve leaflet are perpendicular to each other in the central belly region,⁽⁵⁶⁾ and the out-of plane axis is orthogonal to the leaflet surface, a set of rectangular Cartesian coordinates (x, y, and z) was used, with circumferential (x), radial (y), and transmural directions (z) (Figure 4-1). A small section of leaflet from the central belly region was assumed to be circular, thus $r_x = r_y = r$,⁽¹⁵⁰⁾ in which r_x and r_y are the natural curvatures in the circumferential and radial directions.

The tissue was loaded by the transvalvular pressure in the negative transmural direction such that the tissue must generate the resistant loads to balance out the transvalvular pressure. We assumed the heart valve leaflets are subjected to a uniform tension at the edge and a uniform lateral pressure as shown in Figure 4-1. If p is the pressure per unit area of the membrane and T is the uniform traction per unit length of its boundary, the tensile forces acting on the circumferential direction of an infinitesimal element give the resultant in the upward

direction $-T\left(\frac{\partial^2 z}{\partial x^2}\right)dx dy$, and the tensile forces acting on the radial direction of the element give

the resultant: $-T\left(\frac{\partial^2 z}{\partial y^2}\right)dx dy$. The equation of equilibrium of the element was represented as

shown in equation (4.1),

$$-p \, dx \, dy + T \frac{\partial^2 z}{\partial x^2} dx \, dy + T \frac{\partial^2 z}{\partial y^2} dx \, dy = 0 \quad (4.1)$$

equation (4.1) was arranged and represented as

$$\frac{\partial^2 z}{\partial x^2} + \frac{\partial^2 z}{\partial y^2} = \frac{p}{T} \quad (4.2)$$

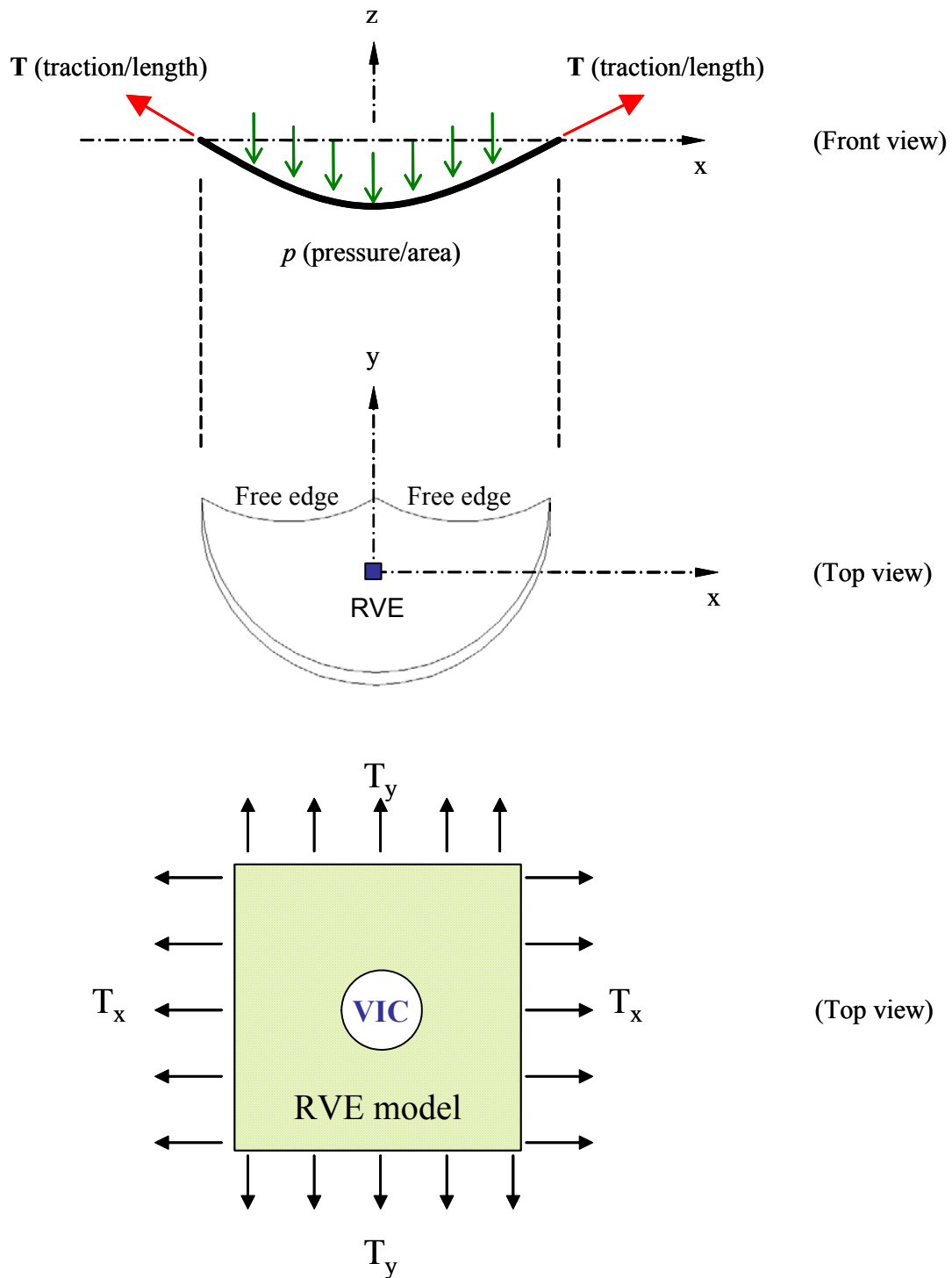


Figure 4-1 The heart valve leaflets are subjected to a uniform tension at the edge and a uniform lateral pressure. p represents the pressure per unit area of the membrane and T represents the uniform traction per unit length of its boundary.

If the unit vector n is the exterior unit normal vector of tissue, the in-plane traction vectors can be expressed as T_x and T_y in the circumferential and radial direction, respectively.⁽¹³⁹⁾

Since an infinitesimal element of tissue was modeled, the equation of the tissue surface was

written as $z = \frac{x^2}{2r_x} + \frac{y^2}{2r_y}$, and since $\frac{\partial z}{\partial x} \approx 1$ and $\frac{\partial z}{\partial y} \approx 1$ for a thin tissue, the curvature is equal to

$\frac{\partial^2 z}{\partial x^2} = \frac{1}{r_x}$ and $\frac{\partial^2 z}{\partial y^2} = \frac{1}{r_y}$.⁽¹⁵¹⁾ Equation (4.2) was expressed as

$$\frac{T_x}{r_x} + \frac{T_y}{r_y} = p \quad (4.3)$$

We assumed $r_x = r_y = r$ and $T_x = T_y = T$ from the assumption that the geometry at the central belly region of the heart valve is circular, equation (4.3) was rewritten as

$$2 \frac{T}{r} = p \quad (4.4)$$

Equation (4.4) is the Laplace law for a thin membrane, $T = \frac{pr}{2}$, which leads that leaflet in-plane traction is directly related to the curvature of the leaflet at various transvalvular pressure loading. By using the Laplace law derived above, the transvalvular pressure was then transformed into tensions in the circumferential and radial directions for the investigation via micromechanical simulations.

4.2 FINITE ELEMENT MICROSCOPIC MODEL FORMULATION

4.2.1 Multi-Scale Modeling Considerations

In formulating our multi-scale model for simulating the interactions of ECM and VIC, three distinct models were generated in different length scales: a macroscopic ECM model (scale: mm) and two microscopic models (scale: μm). The macroscopic ECM model was conducted to verify the proper constitutive model implementation. The geometry of macroscopic ECM model was 10 mm x 10 mm x 0.5 mm according to the specimen prepared in the experiments setup in our laboratory.⁽²⁹⁾ 8-node quadrilateral, reduced-integration plane-stress elements were used in this ECM model with number of 100 elements. Loading applied at the edges of the macroscopic ECM model was calculated by Laplace law for transforming transvalvular pressure to equal-biaxial tension as described above.

As stated in Chapter 3, VIC nuclei deformation (aspect ratio) are the only information we have available. Since VIC nuclei are a large portion of the volume of the VIC, only the nuclei were modeled in this study. Thus, the two microscopic models were generated to simulate the effect of transvalvular pressure. As mentioned in Chapter 3, two difference cross-sections were extracted for measuring the aspect ratio experimentally. In our finite element simulation, circumferential-radial cross-section was used due to experimental data availability for the microscopic model. Two distinct models of circular and elliptic VIC nuclei embedded into the ECM were considered.

In the first model, a circular VIC nuclei microscopic model was adapted from Baer *et al.*⁽⁹⁹⁾ by assuming VIC nuclei has equal radius in the circumferential and radial directions.

Though leaflet ECM is composed of multiple layers, for simplicity one layer of the leaflet was assumed in our microscopic model. Furthermore, we assumed the size of the microscopic model^(100, 103) is relatively small such that model contains only one VIC nucleus and surrounded by the ECM. The boundary of the VIC nucleus and ECM was assumed perfectly bonded together, i.e., displacements are continuous over the edge of the VIC nucleus. Since little is known of the interface of VIC nucleus and ECM, this assumption is a reasonable guess as the first step of our study. The dimension of the microscopic model is $100\ \mu\text{m} \times 100\ \mu\text{m} \times 1\ \mu\text{m}$ ECM and includes a radius $7.5\ \mu\text{m}$ circular VIC nucleus in the circumferential and radial directions (Figure 4-2).⁽¹⁵²⁾ In this two-dimensional finite element simulation, $1\ \mu\text{m}$ thickness was chosen arbitrary into the model for our convenience. 8-node quadrilateral, reduced-integration plane-stress elements were used in this microscopic model with number of 2560 elements.

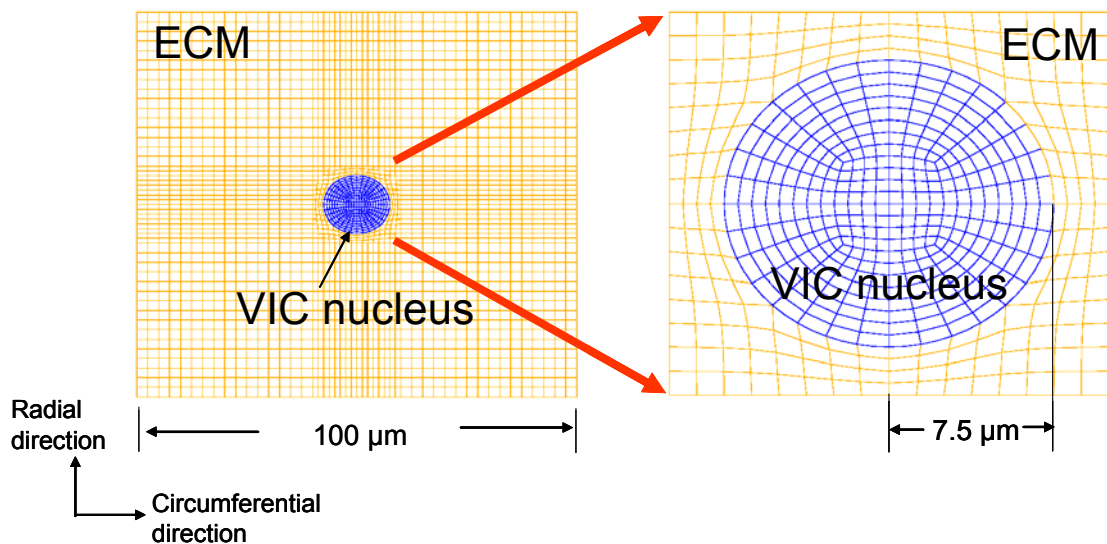


Figure 4-2 Finite element microscopic model of one circular VIC nucleus within its ECM.

From Chapter 3, a prolate ellipsoidal cellular geometry was hypothesized in our laboratory (Figure 3-9), and from the previous experimental results, the average aspect ratio 1.8 was observed in the circumferential-transmural cross-section, and aspect ratio 1.35 was observed in the radial-transmural cross-section under 0 mmHg transvalvular pressure. Thus one can estimate the aspect ratio in the circumferential-radial cross-section as described in equations (4.5) – (4.7).

$$\frac{a}{c}=1.8 \quad (4.5)$$

$$\frac{b}{c}=1.35 \quad (4.6)$$

$$\frac{a}{b}=\frac{a}{c} \times \frac{c}{b}=1.8 \times \frac{1}{1.35}=1.3 \quad (4.7)$$

in which, a, b, c are the major axis lengths in the circumferential, radial and transmural directions, respectively. Based on these considerations, in the second microscopic model, an elliptic VIC nucleus was considered. 7.5 μm in the radial direction was assumed and set as a reference length, thus, 9.75 μm was calculated in the circumferential direction from equation (4.7). The microscopic model with elliptic VIC nucleus was showed in Figure 4-3. 8-node quadrilateral, and 6-node triangle reduced-integration plane-stress elements were used in this microscopic models with number of 1674 elements.

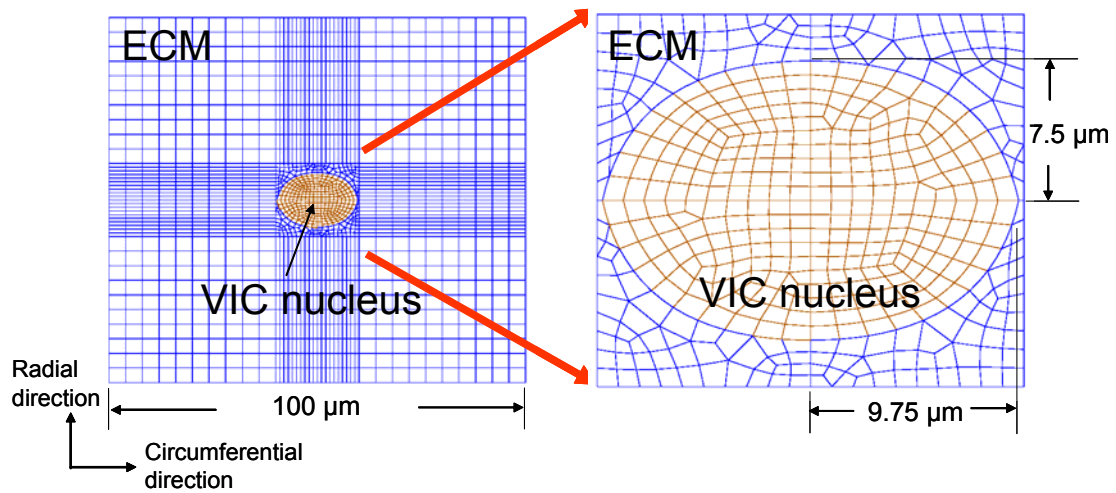


Figure 4-3 The finite element microscopic model with elliptic VIC nucleus was showed above.

4.2.2 Finite Element Simulations of the Interactions of Extracellular Matrix and Valve Interstitial Cell Nucleus

Laplace law was used by converting the transvalvular pressure into a membrane tension as described in the previous section. Transvalvular pressure (mmHg) was transferred to stress (Pa) through the formula: $1 \text{ mmHg} \approx 133 \text{ Pa}$. Thus the unit of pressure was alternately represented in Pa. For example, at 90 mmHg transvalvular pressure level, equivalent stress was calculated as

$$90 \times 133 \approx 12000 \text{ Pa} = 12,000 \text{ N/m}^2 \quad (4.8)$$

Using Laplace law in equation (4.4), and our published laboratory data,⁽¹⁵³⁾ $r = 10 \text{ mm} = 0.01 \text{ m}$, membrane tension at 90 mmHg transvalvular pressure was calculated as

$$T = (12000 \text{ N/m}^2 \times 0.01\text{m}) / 2 = 60 \text{ N/m} \quad (4.9)$$

This value corresponded to the peak physiological tissue stress of 120 kPa in the belly region, assuming a thickness of 0.5 mm.^(19, 154) Equibiaxial loading was applied at the boundaries of the macroscopic ECM model, in which loading (F) was calculated through the membrane tension multiply by the length of the model:

$$F = T \times L = 60 \text{ N/m} \times 10 \text{ mm} = 0.6 \text{ N} \quad (4.10)$$

Detailed results of all calculations under all transvalvular pressure levels were tabulated in Table 4-1.

Table 4-1 Loading conditions for finite element simulations under all transvalvular pressure levels.

	1 mmHg	2 mmHg	4 mmHg	60 mmHg	90 mmHg
Equivalent stress (Pa)	133	266	533	8,000	12,000
Laplace law-tension (N/m)	0.667	1.33	2.67	40	60
Tissue stress (MPa)	1.33×10^{-3}	2.67×10^{-3}	5.3×10^{-3}	0.08	0.12
Loading (N)	6.67×10^{-3}	1.33×10^{-2}	2.67×10^{-2}	0.4	0.6

4.2.3 Material Moduli for the Valve Interstitial Cell and Extracellular Matrix

In this study, the VIC nuclei were modeled as circular and elliptic inclusions with incompressible linearly elastic homogenous isotropic (LEHI) material and a Neo-Hookean hyperelastic material.⁽⁹⁵⁻⁹⁷⁾ Parametric studies were conducted by varying the VIC nucleus elastic moduli two orders higher and two orders lower of the referenced moduli,⁽⁹⁷⁾ (Table 1-1) which were tabulated in Table 4-2.

Table 4-2 Material property of the VIC nucleus, in which E represents elastic moduli in MPa, G represents shear moduli in MPa, and ν represents Poisson ratio.

	LEHI	Neo-Hookean Hyper-elastic	LEHI Parametric study 1	LEHI Parametric study 2
Material constants	$E = 9 \times 10^{-4}$ (MPa) $\nu = 0.45$	$G = 4 \times 10^{-4}$ (MPa)	$E = 9 \times 10^{-2}$ (MPa) $\nu = 0.45$	$E = 9 \times 10^{-6}$ (MPa) $\nu = 0.45$

Deformations of VIC nuclei with different material properties were compared under 1, 2, 4, 60, and 90 mmHg transvalvular pressure levels. The ECM was modeled using a published Fung elastic constitutive model from our laboratory^(23, 155) for simulating planar anisotropic biological materials in the study. In brief, it is assumed that native valve tissues behave as hyperelastic materials following the concept of pseudoelasticity.⁽¹³⁷⁾ The second Piola-Kirchhoff stress was derived from a two-dimensional strain energy with incompressibility assumption:

$$\mathbf{S} = \frac{\partial W}{\partial \mathbf{E}} \quad (4.11)$$

in which W represents the strain energy, \mathbf{S} represents the second Piola-Kirchhoff stress tensor, and \mathbf{E} represents the Green strain tensor. A non-linear Fung elastic constitutive model:

$$W = \frac{c}{2} (e^Q - 1) \quad (4.12)$$

was utilized,^(23, 24, 155) and the energy function was incorporated with full expansion of quadratic terms of Q :

$$Q = A_1 E_{11}^2 + A_2 E_{22}^2 + 2A_3 E_{11} E_{22} + A_4 E_{12}^2 + 2A_5 E_{11} E_{12} + 2A_6 E_{12} E_{22} \quad (4.13)$$

in which c and A_i are material constants, and subscripts of E 's represent the circumferential, radial and shear strains. Furthermore, Sun *et al.*^(23, 24, 155) observed the importance of convexity conditions of constitutive model derived from the energy function. To ensure the stability of numerical simulation, they proposed for planar biaxial loading of biological materials, restrictions of parameters in the constitutive model were required:^(23, 24, 155)

$$c > 0,$$

$$A_1 > |A_3|, A_2 > |A_3| \quad (4.14)$$

$$A_1 A_2 A_4 + 2A_3 A_6 A_5 - A_5^2 A_2 - A_6^2 A_1 - A_3^2 A_4 > 0$$

Parameters c and A 's were obtained from fitting the experimental data from Billiar and Sacks⁽¹⁹⁾ to the non-linear Fung elastic constitutive model through a nonlinear optimization software package such as Microsoft[®] Excel Solver (Frontline Systems Inc. Incline Village, NV).

The Fung elastic constitutive model was generated and converted to a user-defined material (UMAT) user subroutines.⁽¹⁵⁵⁾ The stiffness matrix \mathbf{C} was derived and was defined as

$$\mathbf{C} = \frac{1}{J} \frac{\partial \boldsymbol{\sigma}}{\partial \mathbf{E}} \quad (4.15)$$

in which J is the determinant of deformation gradient, $\det |\mathbf{F}|$, $\boldsymbol{\sigma}$ is the Cauchy stress. Since the 2nd Piola-Kirchhoff stress, \mathbf{S} , was used in the Fung elastic constitutive model, equation (4.15) was represented as⁽¹⁵⁶⁾

$$\mathbf{C} = \frac{1}{J} \frac{\partial (\mathbf{F} \mathbf{S} \mathbf{F}^T)}{\partial \mathbf{E}} \quad (4.16)$$

During the finite element analysis, the material property of ECM was defined as the stiffness \mathbf{C} through the custom code derived by Sun *et al.*⁽¹⁵⁵⁾ and the procedure of incorporating a UMAT mode into a commercial available code was conducted.⁽¹⁵⁵⁾ In brief, firstly, fitting the experimental data^(19, 116) to the constitutive modeling through a nonlinear optimization software package to obtain the parameters estimates for the constitutive model. In this study, data set from one representative specimen was chosen, and 5 out of 7 different loading protocols of the experimental results were selected which contained only positive strain behaviors, due to the limitation of the Fung elastic constitutive model. Secondly, code the constitutive model into finite element platform, such as ABAQUS / UMAT by Fortran software. Thirdly, conduct a

single element test to test the correctness of UMAT coding. Lastly, perform the complex multi-element simulations.

4.2.4 Predicted Aspect Ratios of Valve Interstitial Cell Nuclei

The final displacements in the circumferential and radial directions of the deformed VIC nuclei under 1, 2, 4, 60, and 90 mmHg were generated from the finite element solver. One can calculate the final major axis lengths from the local coordinates at the interface of the VIC nucleus and ECM (Figure 4-4), in which A, B, C, and D are the local coordinates at the interface of the VIC nucleus and ECM. Circumferential and radial stretches, λ_1 and λ_2 , were calculated from the final major axis lengths divided by the original major axis lengths, and λ_3 was calculated by using the incompressibility assumption, $\lambda_3 = 1/(\lambda_1\lambda_2)$. Thus, one can obtain the final major axis length in the transmural direction. The predicted VIC nucleus aspect ratio in the circumferential- transmural directions was then calculated by a/c , in which a and c are the major axis lengths in the circumferential and transmural directions, respectively.

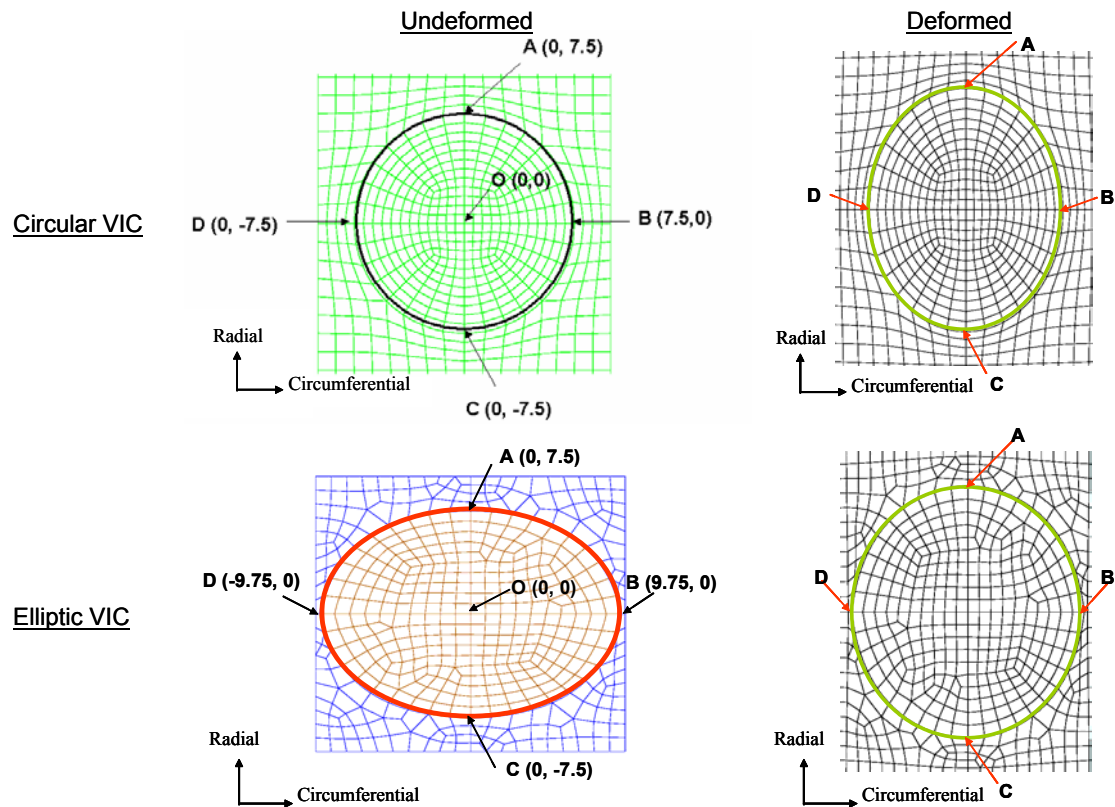


Figure 4-4 A representative undeformed, deformed circular and elliptic VIC nuclei finite element models, in which A, B, C, and D are the local coordinates at the interface of the VIC nuclei and ECM.

In Chapter 3, elongations of VIC nucleus with consistent areas under various transvalvular pressure levels were observed. To investigate the relationship of the aspect ratio and volume of the VIC nucleus under different transvalvular pressure levels, one can calculate the volume V from the three major axis lengths by equation (4.17), in which a , b , and c are the major axis lengths in the circumferential, radial and transmural directions, respectively.

$$V = \frac{4}{3} \pi (a b c) \quad (4.17)$$

4.3 RESULTS

4.3.1 Parameter Values and Single Element Test

Nonlinear regression results for the Fung elastic constitutive model, parameters c and A 's with convexity constraint were listed in Table 4-3. Five different loading protocols were incorporated in which circumferential loading : radial loading are 1:1, 1.5:1, 2:1, 2.5:1, and 3:1.⁽¹⁹⁾ The predicted 2nd Piola-Kirchhoff stress versus Green strain incorporated with the parameters, were illustrated in Figure 4-5 – Figure 4-9, and agreements were observed in the circumferential and radial directions under different loading conditions. Under five different loading conditions, the predicted 2nd Piola-Kirchhoff stress versus Green strain incorporated with the parameters, were illustrated in Figure 4-10.

Table 4-3 Seven parameters of the Fung elastic constitutive model with convexity constraint: $c > 0$, $A_1 > |A_3|$, $A_2 > |A_3|$ and $A_1A_2A_4 + 2A_3A_6A_5 - A_5^2A_2 - A_6^2A_1 - A_3^2A_4 > 0$.

Parameters	c	A_1	A_2	A_3	A_4	A_5	A_6
With convexity constraint	0.0097	49.558	5.2871	-3.124	16.031	-0.004	-0.02

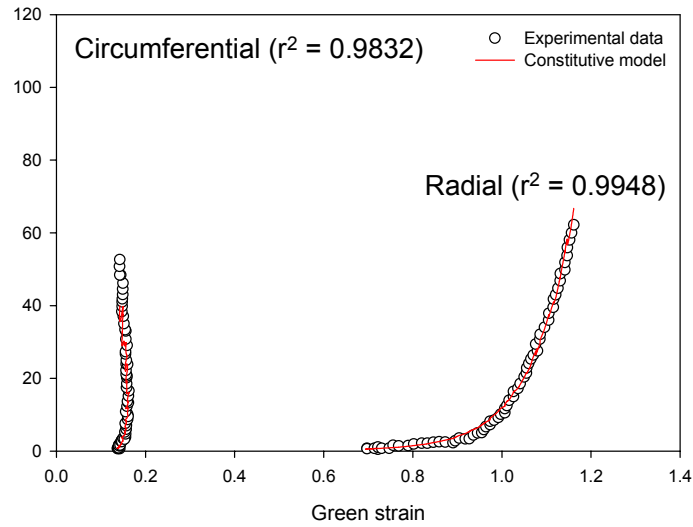


Figure 4-5 Results of the Fung elastic constitutive model with seven parameters under equal biaxial loading conditions (circumferential loading : radial loading = 1:1) and agreements were observed in the circumferential ($r^2 = 0.9832$) and radial directions ($r^2 = 0.9948$).

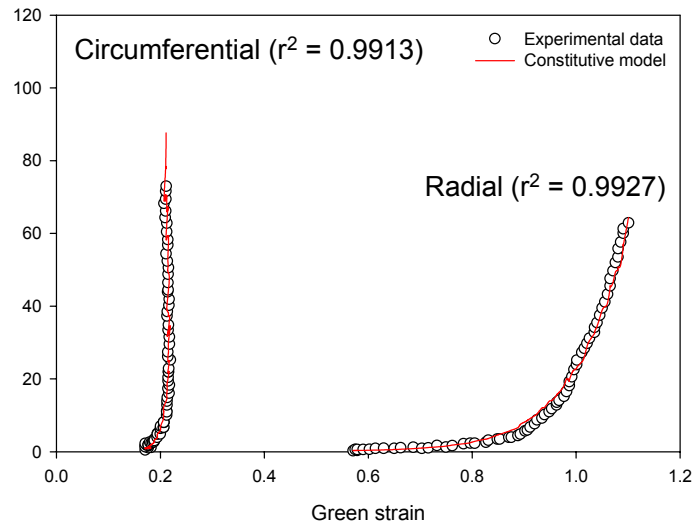


Figure 4-6 Results of the Fung elastic constitutive model with seven parameters under loading conditions of circumferential loading : radial loading = 1.5:1. Agreements were observed in the circumferential ($r^2 = 0.9913$) and radial directions ($r^2 = 0.9927$).

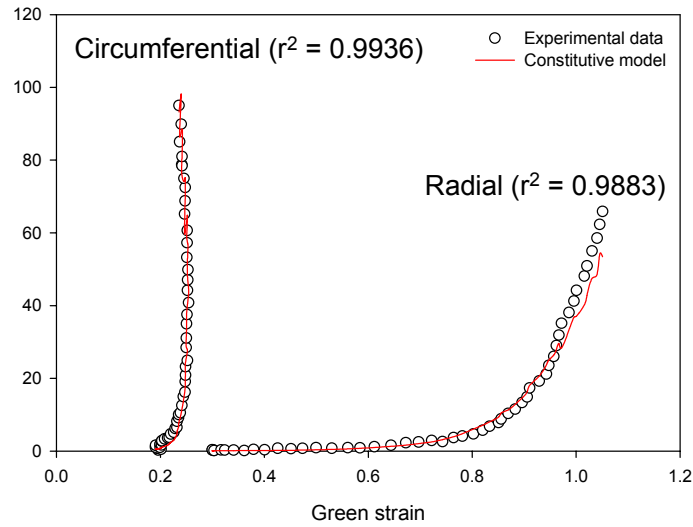


Figure 4-7 Results of the Fung elastic constitutive model with seven parameters under loading conditions of circumferential loading : radial loading = 2:1. Agreements were observed in the circumferential ($r^2 = 0.9936$) and radial directions ($r^2 = 0.9883$).

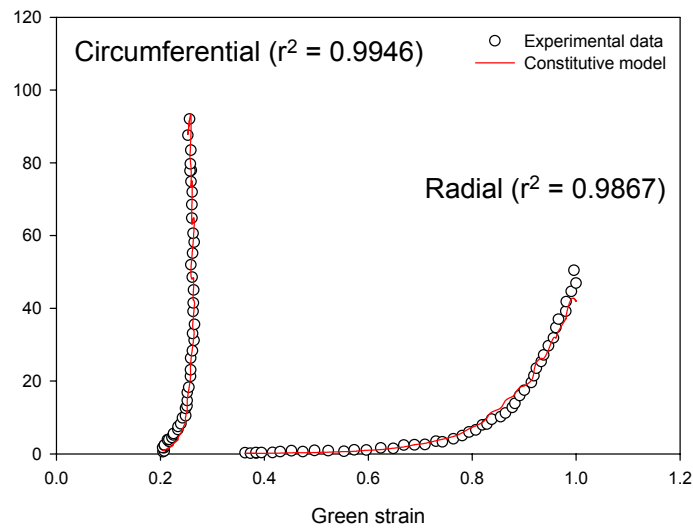


Figure 4-8 Results of the Fung elastic constitutive model with seven parameters under loading conditions of circumferential loading : radial loading = 2.5:1. Agreements were observed in the circumferential ($r^2 = 0.9946$) and radial directions ($r^2 = 0.9867$).

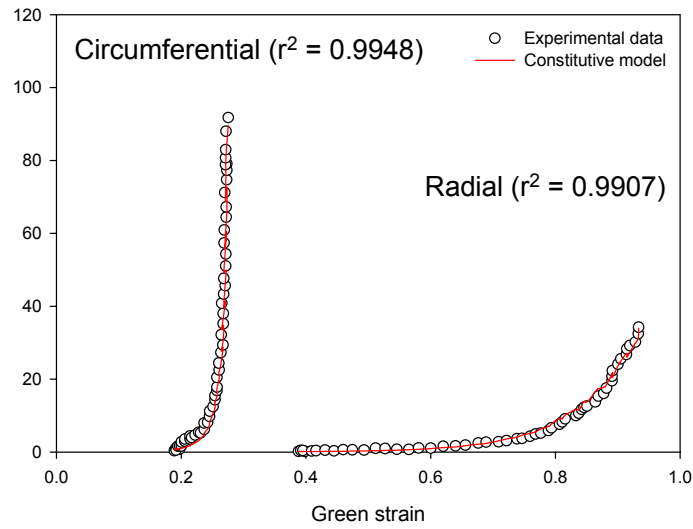


Figure 4-9 Results of the Fung elastic constitutive model with seven parameters under loading conditions of circumferential loading : radial loading = 3:1. Agreements were observed in the circumferential ($r^2 = 0.9948$) and radial directions ($r^2 = 0.9907$).

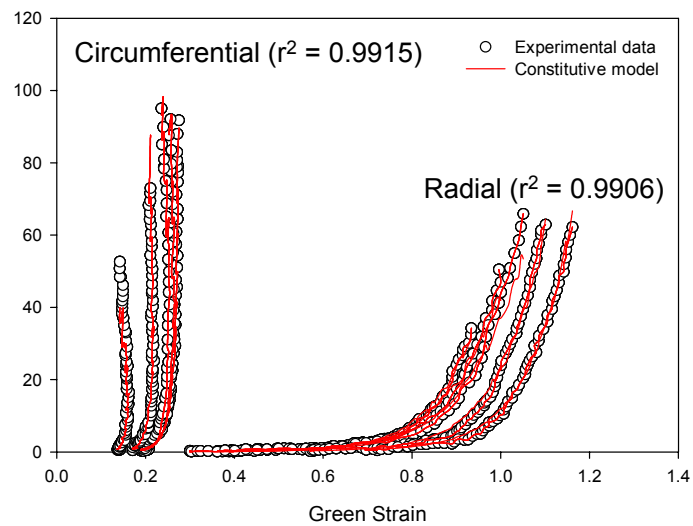


Figure 4-10 Results of the Fung elastic constitutive model with seven parameters under different biaxial loading conditions and agreements were observed in the circumferential ($r^2 = 0.9915$) and radial directions ($r^2 = 0.9906$) under different loading conditions.

The seven parameters were input into finite element solver and a single element simulation was conducted. A representative stress-strain relationship of single element test results under the equibiaxial loading condition comparing to the experimental data and the Fung elastic constitutive model was illustrated in Figure 4-11 ($r^2 = 0.71$ and $r^2 = 0.72$ in the circumferential and radial directions, respectively). It indicated that the material model was incorporated into the finite element analysis appropriately.

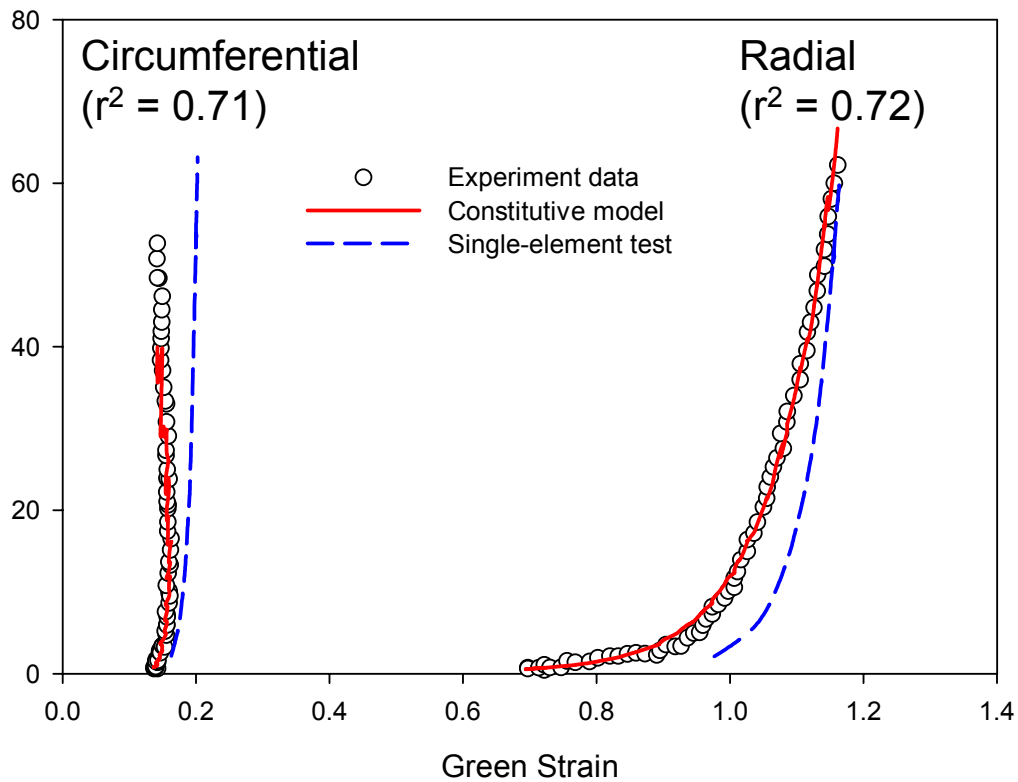


Figure 4-11 A representative stress-strain relationship of single element test results under the equibiaxial loading condition comparing to the experimental data and the constitutive model ($r^2 = 0.71$ and $r^2 = 0.72$ in the circumferential and radial directions, respectively).

4.3.2 Effects of Valve Interstitial Cell Nucleus Material Property

As mentioned in Section 4-2, the circular VIC nucleus microscopic model was created with equal radius in the circumferential and radial directions, with an aspect ratio 1 under initial zero loading condition. However, from the previously experimental measurements under 0 mmHg transvalvular pressure, aspect ratio was 1.834 ± 0.0902 in the circumferential-transmural directions. All the finite element results in circumferential-radial directions were required further data analysis to obtain the aspect ratios in the circumferential-transmural directions. Furthermore, direct comparisons from the predicted aspect ratios of VIC nuclei to the experimental measured aspect ratios of VIC nuclei are not possible; percent change in the aspect ratio (%) was conducted for comparison the predicted values to the experimental measured values.

Parametric studies of various VIC nuclei material properties were conducted (Table 4-2). Calculations of the VIC nuclei aspect ratios, and percent change in the aspect ratio (%) of the LEHI circular VIC nucleus microscopic model were tabulated in Table 4-4, and detailed results of parametric studies were presented in Appendix E. By varying the VIC nuclei material properties, a comparison of percent change in the aspect ratio (%) versus different pressure levels was illustrated in Figure 4-12. The LEHI circular VIC nuclei microscopic model with elastic moduli = 9×10^{-4} MPa and hyperelastic Neo-Hookean material property exhibited similar behavior, however, the other two models showed slightly different responses. Thus, LEHI material property (9×10^{-4} MPa) of VIC nucleus was chosen as a base-line in this study.

Table 4-4 LEHI circular VIC nucleus microscopic model: results of the major axis lengths in the circumferential, radial, and transmural directions, calculation of aspect ratio and percent change in aspect ratio under 6 different pressure levels.

	1 mmHg	2 mmHg	4 mmHg	60 mmHg	90 mmHg
a	7.538	7.579	7.667	8.575	8.718
b	7.852	8.158	8.644	11.133	11.432
c	7.128	8.644	6.366	4.419	4.233
Aspect ratio	1.06	1.112	1.2	1.94	2.06
Percent change in aspect ratio	6%	11.12%	20%	94%	106%

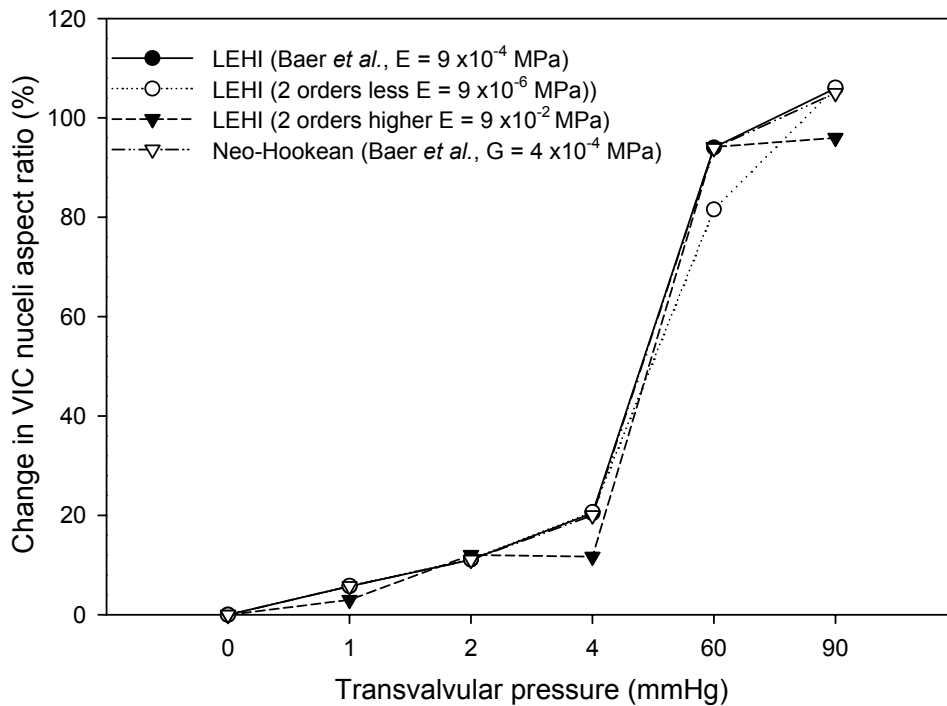


Figure 4-12 Parametric studies of varying the VIC nuclei material properties, and a comparison of percent change in the aspect ratio (%) versus different pressure levels was showed above.

4.3.3 Effects of Valve Interstitial Cell Nucleus Initial Geometry

The circular and elliptic VIC nuclei with LEHI material property ($E = 9 \times 10^{-4}$ MPa) in the microscopic models were created with aspect ratio of 1 and 1.3 in the circumferential-radial directions, respectively. Calculation of the aspect ratio and percent change in aspect ratio (%) of elliptic VIC nucleus microscopic model under all pressure levels were listed in Table 4-5. Predicted VIC nucleus aspect ratios in two microscopic models and VIC nucleus aspect ratios measured experimentally versus the transvalvular pressure were illustrated in Figure 4-13. From Figure 4-13, the predicted VIC nucleus aspect ratios of elliptic VIC nucleus microscopic model were closer to the measured VIC nucleus aspect ratios at all pressure levels, suggesting the elliptic VIC nucleus microscopic model was plausible to predict the deformations of the VIC nuclei.

Table 4-5 LEHI elliptic VIC nucleus microscopic model: results of the major axis lengths in the circumferential, radial, and transmural directions, calculation of aspect ratio and percent change in aspect ratio under 6 different pressure levels.

	1 mmHg	2 mmHg	4 mmHg	60 mmHg	90 mmHg
a	9.673	9.636	9.634	10.303	10.427
b	8.266	8.863	9.668	12.48	12.775
c	4.948	4.632	4.247	3.077	2.97
Aspect ratio	1.955	2.08	2.268	3.349	3.51
Percent change in aspect ratio	8.474 %	15.414 %	25.86 %	85.80 %	94.81 %

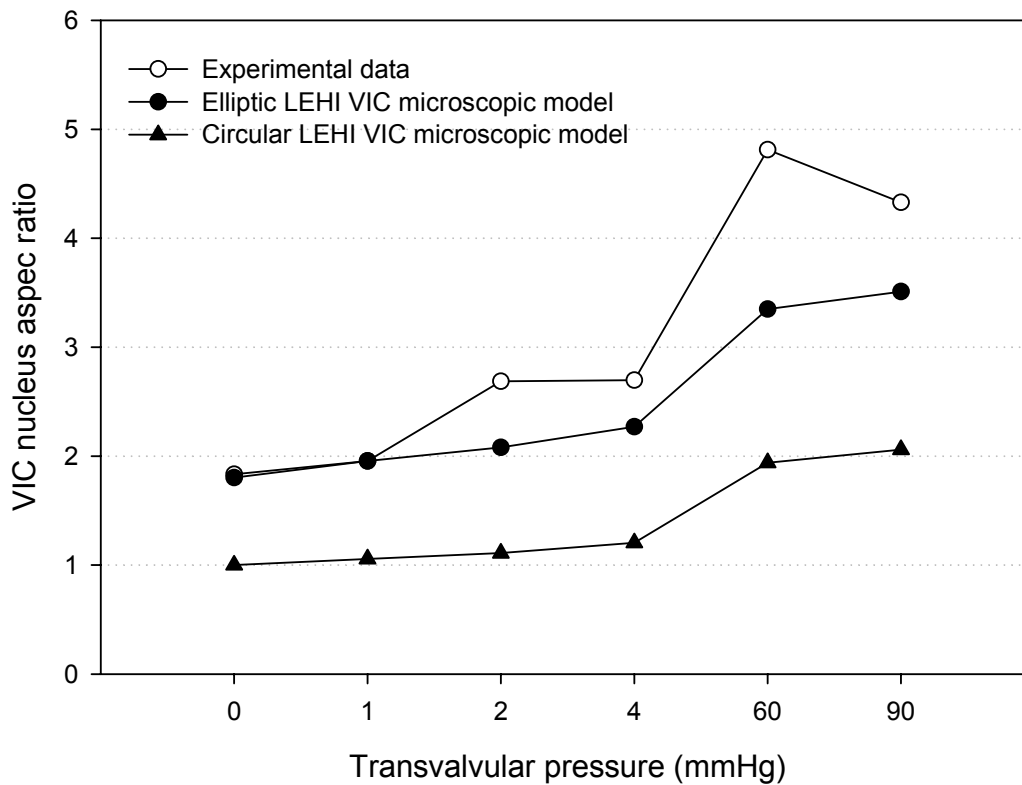


Figure 4-13 A comparison of VIC nucleus aspect ratios measured experimentally and calculated from the finite element simulations.

Calculated percent change in the VIC nucleus aspect ratio data (Table 4-4 and Table 4-5) versus the transvalvular pressures was represented in Figure 4-14, and from Figure 4-14, the elliptic and circular VIC nucleus microscopic models have similar percent change in aspect ratio (%) compared to the experimental data. Furthermore, in Figure 4-14, the predicted percent change in aspect ratio (%) followed the trend of the percent change in aspect ratio (%) found experimentally. Base on the calculated data from Table 4-4 and Table 4-5, one can calculate the differences of the percent change in aspect ratio (%) from the elliptic and circular VIC

nucleus microscopic models to the experimental measured VIC nucleus percent change in aspect ratio (%) (Table 4-6). Three distinct zones were observed in Figure 4-14 and Table 4-6: at 0 and 1 mmHg pressure levels, percent changes in aspect ratio (%) of the predicted values corresponded well to the one of experimental measurements. At 2 and 4 mmHg transvalvular pressure levels, the differences between the percent changes in aspect ratio (%) from predicted values to the measured values were 66% and 45% of the elliptic VIC nucleus microscopic model, and 76%, and 56% of the circular VIC nucleus microscopic model, respectively. However, at 60 and 90 mmHg pressure levels, the differences between the percent change in aspect ratio (%) from predicted values to the measured values decreased, they were 47% and 30% of the elliptic nucleus microscopic model, and 42%, and 22% of the circular VIC nucleus microscopic model, respectively (Table 4-6).

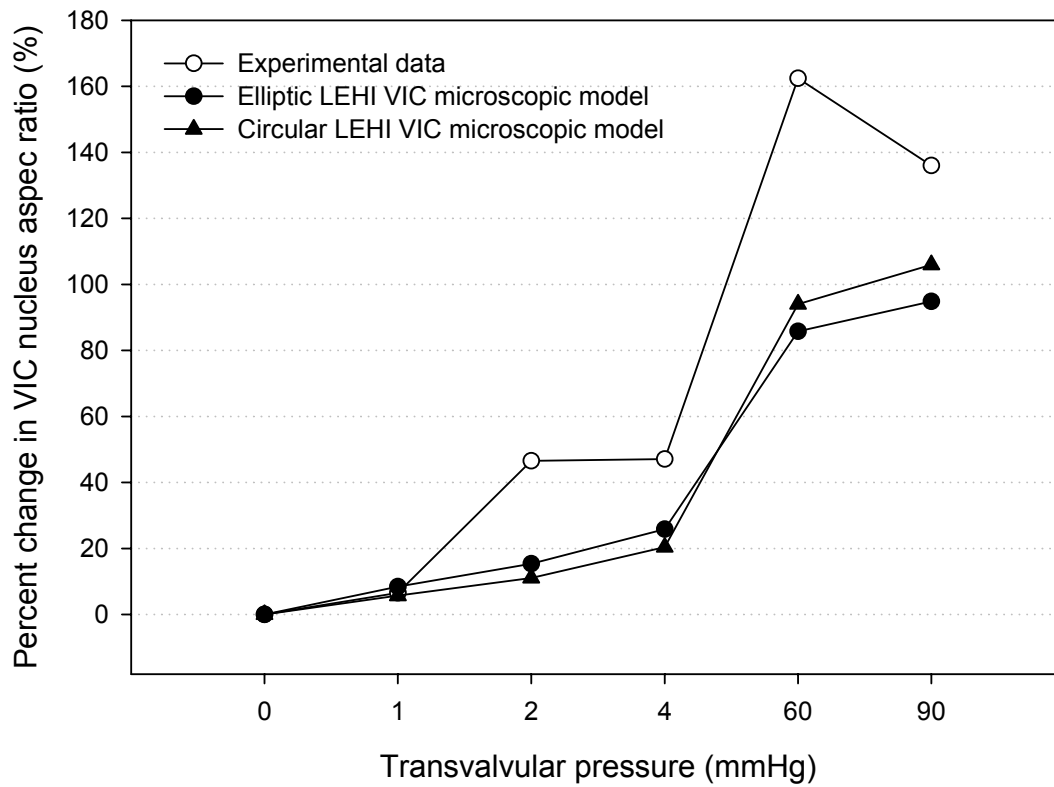


Figure 4-14 A comparison of percent change in aspect ratio (%) measured experimentally and calculated from the finite element simulations.

Table 4-6 The differences of the percent change in aspect ratio (%) from the elliptic and circular VIC nucleus microscopic models to the experimental measured VIC nucleus percent change in aspect ratio.

	0 mmHg	1 mmHg	2mmHg	4 mmHg	60 mmHg	90 mmHg
Elliptic	0 %	28 %	66 %	45 %	47 %	30 %
Circular	0 %	12.8 %	76 %	56 %	42 %	22 %

As stated in Section 4.2.4, the volumes of VIC nucleus under different transvalvular pressure levels were studied. One can calculate the volumes of circular and elliptic VIC nuclei from the data provided in Table 4-4 and Table 4-5 by equation (4.17). For example, the circular VIC nucleus microscopic model (radius = 7.5 μm) under 1 mmHg with $a = 7.5375$ (μm), $b = 7.8527$ (μm), $\lambda_3 = 0.948$, and one can calculate $c = \lambda_3 \times 7.5 = 7.11$ (μm). Detailed volume calculations were provided in Table 4-7, in which consistent volume was observed while VIC nucleus aspect ratios increased with increased transvalvular pressure in both the circular and elliptic VIC nucleus microscopic models. Interestingly, the calculated volumes have slightly higher values in the circular VIC nucleus microscopic models than ones in the elliptic VIC nucleus microscopic models, but have no substantial differences from the circular and elliptic VIC nucleus microscopic models.

Table 4-7 Calculations of volume of two microscopic models under different pressure levels, in which all units in μm .

	Circular VIC microscopic Model				Elliptic VIC microscopic Model			
Pressure level	a (μm)	b (μm)	c (μm)	Volume (μm^3)	a (μm)	b (μm)	c (μm)	Volume (μm^3)
0 mmHg	7.5	7.5	7.5	1767.14	9.75	7.5	5.4	1657.1
1 mmHg	7.5375	7.8527	7.1275	1767.14	9.673	8.266	4.948	1657.1
2 mmHg	7.579	8.1583	6.8229	1767.14	9.635	8.863	4.632	1657.1
4 mmHg	7.6672	8.644	6.3655	1767.14	9.634	9.668	4.247	1657.1
60 mmHg	8.575	11.133	4.419	1767.14	10.30	12.48	3.076	1657.1
90 mmHg	8.718	11.432	4.233	1767.14	10.423	12.775	2.969	1657.1

4.3.4 Local Mechanical Environment of Valve Interstitial Cell Nucleus

From the results of the circular VIC nucleus with LEHI material property (elastic moduli = 9×10^{-4} MPa) microscopic model, a peak stress = 0.12 MPa in the circumferential and radial directions were found at the boundary of the microscopic model under 90 mmHg transvalvular pressure (Figure 4-15). Furthermore, corresponding Logarithmic strain distributions in both the circumferential and radial directions were illustrated in Figure 4-16. Higher strain was observed inside the circular VIC nucleus due to its low moduli, and local strain distribution increased toward to the boundary of the microscopic model (propagation). In the circumferential direction, simple continuum model predicted the strain field propagation up to 41 μm away from the center of the VIC nucleus, but only 26.7 μm away from the center of the VIC nucleus propagation was observed in the radial direction.

Higher stress concentrations was observed in the elliptic VIC nucleus microscopic model than the one in the circular VIC nucleus microscopic model, suggesting the cellular local mechanical environment was influenced by the cellular geometry (Figure 4-15 and Figure 4-17). The corresponding Logarithmic strain distributions in both the circumferential and radial directions of the elliptic VIC nucleus microscopic models were showed in Figure 4-18. Different strain distributions were observed in the circumferential direction compared to the one observed in the radial direction, and the local strain distribution did not have the similar propagation as one observed in the circular VIC nucleus microscopic models. At 4 mmHg pressure level, stress and strain distributions were illustrated in Figure 4-19 and Figure 4-20, and from Figure 4-20, strain field propagation was observed only at the radial direction. Based on these observations, it

is suggested the local mechanical environment was strongly influenced by the VIC nucleus geometry.

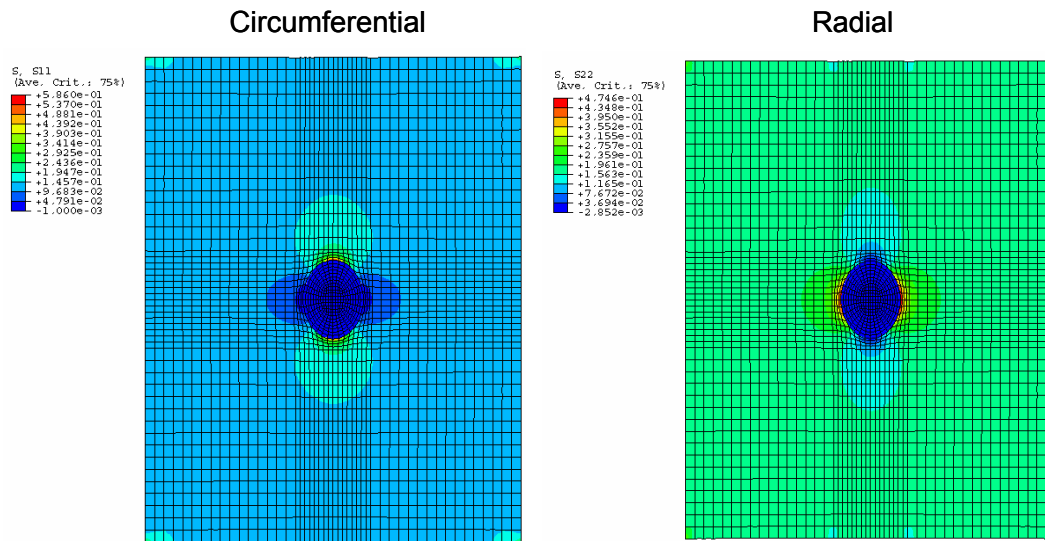


Figure 4-15 Stress distributions in the circumferential and radial directions of the circular VIC nucleus microscopic model under 90 mmHg transvalvular pressure were showed above.

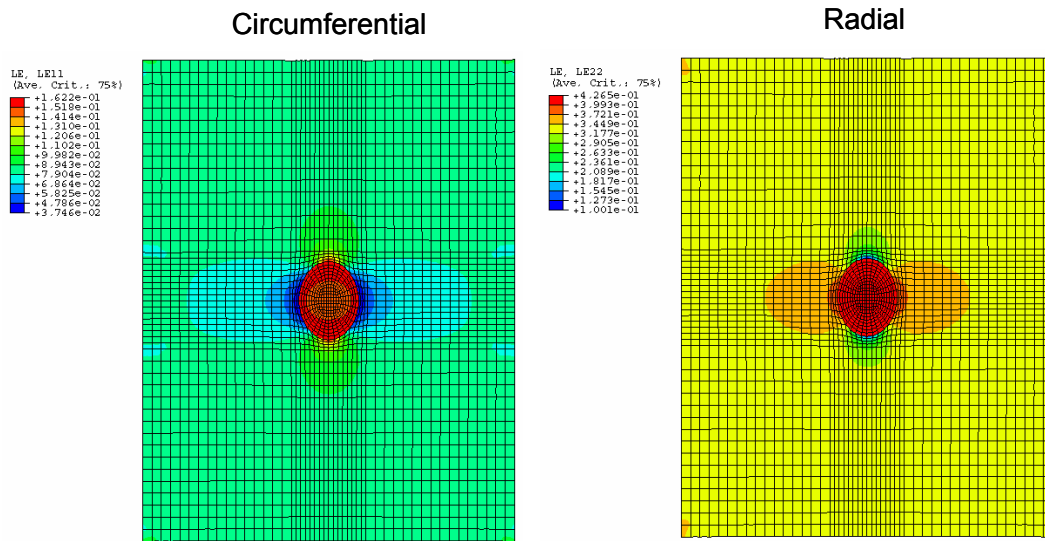


Figure 4-16 Strain distributions in the circumferential and radial directions of the circular VIC nucleus microscopic model under 90 mmHg transvalvular pressure were showed above.

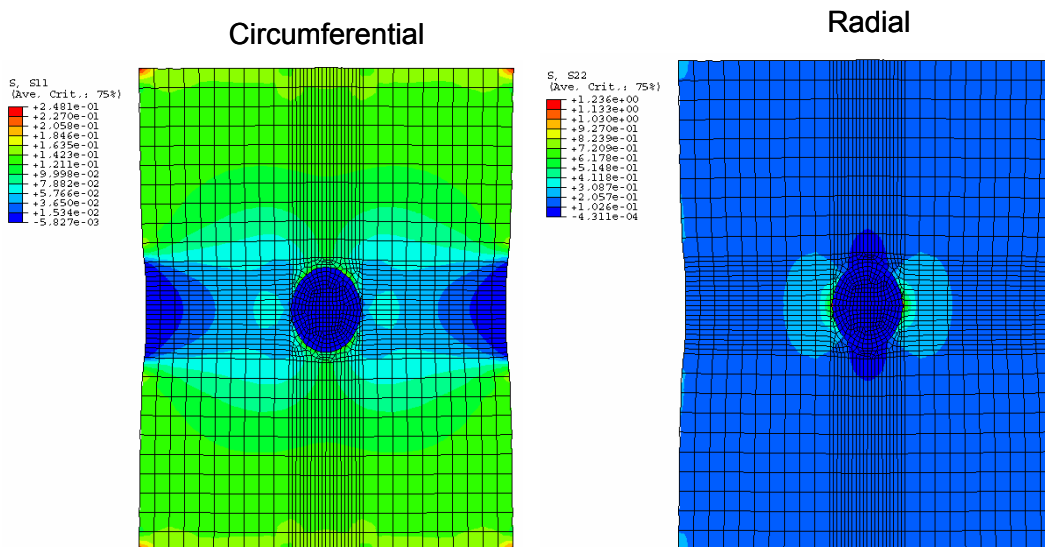


Figure 4-17 Stress distributions in the circumferential and radial directions of the elliptic VIC nucleus microscopic model under 90 mmHg transvalvular pressure were showed above.

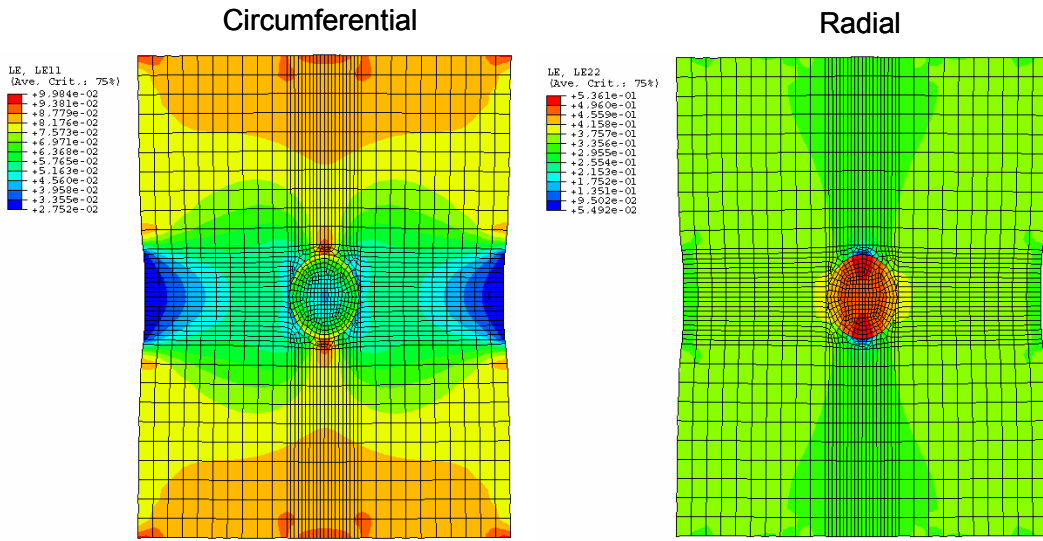


Figure 4-18 Strain distributions in the circumferential and radial directions of the elliptic VIC nucleus microscopic model under 90 mmHg transvalvular pressure were showed above.

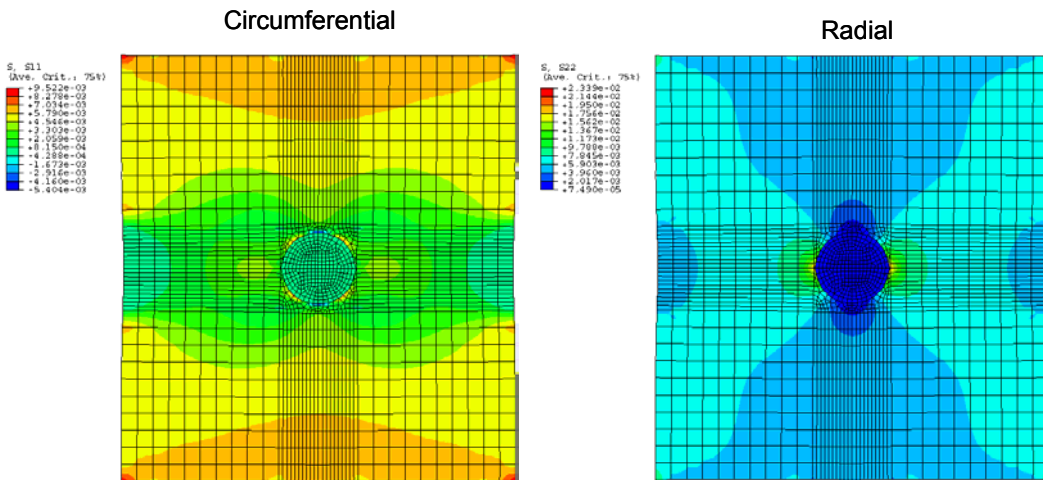


Figure 4-19 Stress distributions in the circumferential and radial directions of the elliptic VIC nucleus microscopic model at 4 mmHg transvalvular pressure level were showed above.

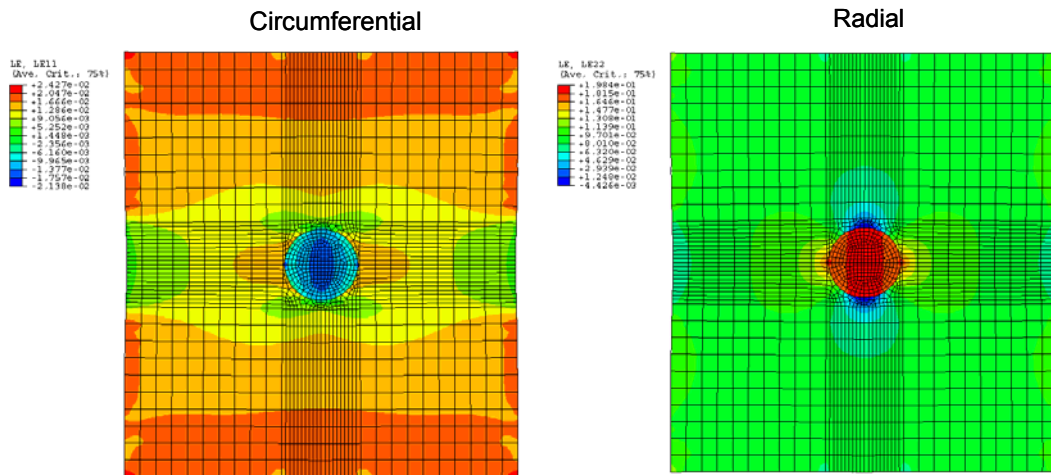


Figure 4-20 Strain distributions in the circumferential and radial directions of the elliptic VIC nucleus microscopic model at 4 mmHg transvalvular pressure level were showed above.

4.4 SUMMARY

The law of Laplace was utilized for transferring the transvalvular pressure into in-plane tensions applied on the native aortic valve tissue. Microscopic model was created that contains only one VIC nucleus embedded in the surrounding ECM in the circumferential and radial directions. A Fung elastic constitutive model was conducted into the finite element simulation, represents the ECM material property. The predicted VIC nucleus aspect ratios were compared to the measured aspect ratios from photomicrographs of histological sections of the native tissues. The VIC nucleus aspect ratios in the circumferential-transmural directions were calculated under the incompressibility assumption. Finite element results of percent change in VIC nucleus aspect ratio (%) followed the trend which was found experimentally. Three distinct zones were found while comparing the percent change in aspect ratio (%) in both the simulations and measurements.

In conclusion, from the parametric studies, the LEHI material property was chosen for the VIC nucleus material property, which provided a basic index for the simulation of the interaction of cell / ECM. Furthermore, the elliptic VIC nucleus microscopic model presented closer actual values in the VIC nucleus aspect ratios while compared to the experimental findings. Local mechanical environments of VIC nuclei were investigated, and the strain field propagation was observed in the circular VIC nucleus microscopic model. However, strain field propagation was not observed in the elliptic VIC nucleus microscopic model, suggesting the local mechanical environments of VIC nucleus exceeded the limited size of the microscopic model. Furthermore, the stress concentration was observed with the higher values in the circular VIC microscopic model than the one in the circular VIC microscopic model (Figure 4-21), suggesting the cellular local mechanical environment was strongly influenced by the cellular geometry, thus, and further investigation was required.

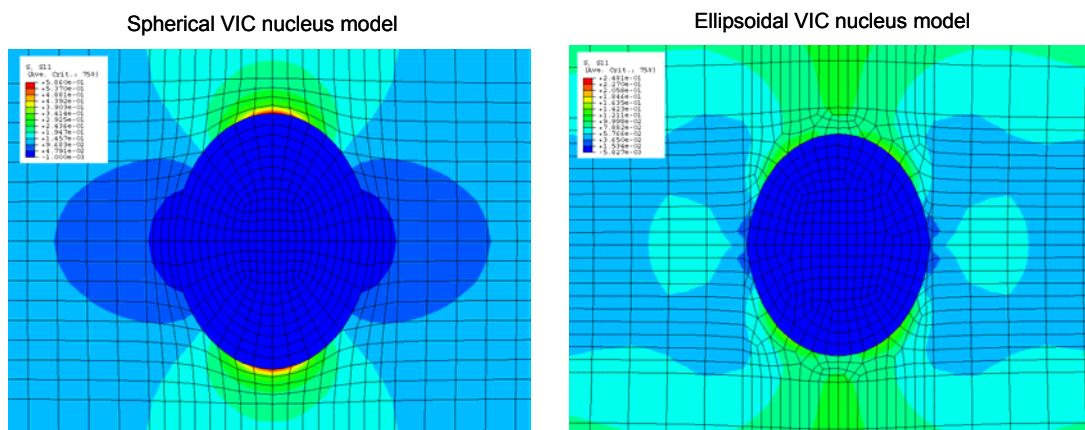


Figure 4-21 Local circumferential stress states of circular VIC nucleus (left panel) and elliptic VIC nucleus (right panel) at 90 mmHg transvalvular pressure (Note: different legend scales were used in those two models)

In addition, we compared the stretches at the interface of the VIC nucleus / ECM to the stretches at the boundary of the elliptic microscopic model, in which stretch was calculated by the final length divided by the original length. Larger stretches at the interface of the VIC nucleus / ECM were observed in both the circumferential and radial directions (Table 4-8), suggesting that the VIC nucleus does not simply follow the deformation of the tissue.

Table 4-8 Stretches at the interface of the VIC nucleus and ECM and the stretches at the boundary of the elliptic microscopic model at 90mmHg pressure levels.

	Interface of the VIC nucleus / ECM	Boundary of the elliptic model
Circumferential	1.0525	1.0139
Radial	1.6548	1.4898

5.0 CONCLUSIONS AND FUTURE STUDIES

The micromechanical simulations of heart valve leaflet presented herein yield fresh insight into the biomechanical behavior of native and porcine BHV heart valve tissues, from the effect of organ-level transvalvular pressures on cellular-level VIC nucleus deformation in the native porcine aortic valve, to the layer-specific changes in mechanical properties incurred by valve leaflet tissues with mechanical fatigue. In this final chapter a summary of the modeling procedures, analysis techniques, and major results are presented. In addition, while the potential impact of these studies on future heart valve research is difficult to predict, here we discuss several avenues of exploration which we feel warrant further investigation.

5.1 MODELING THE FLEXURAL BEHAVIOR OF PORCINE BHV TISSUES

5.1.1 Summary

The goals of this study were to estimate the effective moduli of the individual load-bearing layers (i.e., fibrosa and ventricularis) of porcine BHV tissues, and to furthermore investigate whether porcine BHV incur layer-specific changes in effective mechanical properties with fatigue. To achieve these goals, we developed a composite beam model to simulate

experimental three-point bending tests of uncycled and fatigued porcine BHV leaflet tissues.⁽⁶⁶⁾ Rectangular samples of tissue were modeled as two-layer, three-dimensional finite element composite beam. The specimen flexural behavior was modeled using either linear or non-linear bi-modular material properties for the individual layers. Best-fit estimates of the individual layer tensile and compressive moduli were determined from parametric studies in which the finite element model output was matched to the overall effective modulus of the tissue measured in both the AC and WC bending directions. The simulated M/I vs. $\Delta\kappa$ results demonstrated good agreement with the experimental data for both the uncycled and fatigued BHV leaflet tissues. No significant differences were found between the predicted and experimental neutral axis shift in either the AC and WC bending directions, thus providing further evidence for the validity of our modeling approach. The most important finding of this study was that porcine BHV incur an approximately 50% decrease in the estimated effective tensile modulus (i.e., slope of the M/I vs. $\Delta\kappa$ plot in the small strain region) of the fibrosa layer by 200-million cycles of accelerated wear testing. Furthermore, the predicted neutral axis shift was compared to the experimentally measured neutral axis shift for the uncycled porcine BHV tissue.

5.1.2 Relation to Other Studies

Vesely *et al.*⁽⁵³⁾ previously reported estimates of the elastic material properties of the individual layers based on uniaxial tensile testing data. The fibrosa layer was reported to be stiffer than the ventricularis; however this study was limited only to circumferentially-oriented samples of the native tissue. In a separate study, Vesely and Boughner⁽¹⁸⁾ reported leaflet bending moduli in the AC and WC bending directions using simple beam theory, however the individual layer bending moduli were not estimated. The neutral axis location was also

presented in their study, however an isotropic model with a single elastic modulus was used to predict this neutral axis location.⁽¹⁸⁾ Such an analysis would not be expected to provide reliable information on the position of the neutral axis, as the aortic valve leaflet tissue is well known to consist of three distinct layers, with each layer exhibiting a unique structure and biochemical composition of collagens, elastin, and/or glycosaminoglycans. Thus, it would be expected to yield different mechanical properties for the layers and a different neutral axis location under flexural. In conclusion, to the best of our knowledge, the results presented herein in our study represent the first computationally rigorous estimates of the layer-specific mechanical properties of porcine BHV tissues.

5.1.3 Recommendations for Future Studies

The finite element simulations conducted as part of our flexure studies suggest that the collagen-rich fibrosa incurs the brunt of mechanical fatigue, predicting significant decreases in the effective modulus of the fibrosa layer by 200 million accelerated cycles (16 Hz, 0 to 80 mm Hg).⁽⁶⁶⁾ This is important finding, as a number of academic and industrial research groups are currently investigating novel fixatives and fixation methods which may have the capability of specifically targeting the individual layers of the valve leaflet tissue.^(157, 158) For example, it has previously been demonstrated that mechanical fatigue induces loss of glycosaminoglycans (10 million cycles; primarily found in the spongiosa layer) prior to denaturation of collagen fibers (50 million cycles; primarily in the fibrosa layer) in porcine BHV.⁽⁷¹⁾ Moreover, periodate-mediated stabilization of glycosaminoglycans in the central spongiosa layer has recently been demonstrated,⁽¹⁵⁸⁾ with concomitant reductions in valvular calcification. While these results are interesting, a practical future study might evaluate and compare the overall flexural mechanical

properties of GAG-stabilized BHV to standard BHV. Furthermore, the finite element models developed in the current flexure studies could be applied directly to ascertain whether the effective modulus of the fibrosa layer was preserved in GAG-stabilized BHV. It may well be that the mechanism by which this novel fixation technique mitigates fatigue of the overall BHV flexural properties is by preserving the hypothesized shear-stress dampening properties of the spongiosa,^(71, 159) and thus mitigating fatigue of the fibrosa layer.

5.2 GEOMETRIC CHANGES IN HEART VALVE INTERSTITIAL CELL NUCLEUS

5.2.1 Summary

Changes in VIC nucleus aspect ratios with increasing transvalvular pressure were simulated. Major and minor lengths of VIC nucleus were computed from histological sections. Local coordinates of VIC nucleus inside the tissue were recorded to quantify the distribution of the VIC nucleus deformation for each layer. Three distinct groups of VIC nucleus aspect ratios in zero –, low –, and high – pressure levels were observed, however no statistically significant differences were observed in the VIC nucleus area measurements at different pressure levels.

A continuum mechanics based finite element simulations were constructed to investigate how global tissue stress translates to local mechanical VIC nucleus environment. Change in the nucleus aspect ratio was calculated for comparing the predicted values to the experimental findings, where predicted percent change in the nucleus aspect ratio follows the trend of experimental percent change in the nucleus aspect ratio. Parametric studies were

conducted to investigate the effect of VIC nucleus material properties and initial modeling geometry. The nucleus aspect ratio results from LEHI elliptic VIC nucleus microscopic model was observed closer to the experimental findings. High strain concentrations were observed in the microscopic models due to lower magnitude of the moduli, and this finding consistent to the study by Baer et al.⁽⁹⁹⁾

In our circular VIC microscopic model, the strain field propagation was observed up to 41 μm away from the center of the VIC nucleus and 26.7 μm away from the center of the VIC nucleus in the circumferential and radial directions, respectively. It indicated the size of the microscopic model is appropriate such that the propagation occurred inside the model. However, strain field propagation was not observed in the circular VIC microscopic model, suggesting the local mechanical environments of VIC nucleus exceeded the limited size of the microscopic model. Furthermore, the stress concentration was observed with the higher values in the circular VIC microscopic model than the one in the elliptic VIC microscopic model, suggesting the cellular local mechanical environment was strongly influenced by the cellular geometry. In addition, we compared the displacements at the interface of the VIC nucleus and ECM to the displacements at the boundary of the elliptic microscopic model, larger deformations at the interface of the VIC nucleus / ECM were observed in both the circumferential and radial directions, suggesting that the VIC nucleus does not simply follow the deformation of the tissue.

Furthermore, the volumes of the VIC nucleus were calculated, and higher volume of the circular VIC nucleus was observed than the elliptic VIC nucleus, however the volume are consistent with the increased transvalvular pressures in both the circular and elliptic VIC nucleus microscopic models. Baer et al.⁽⁹⁹⁾ used the three-dimensional reconstruction to determine the

average radii of an elliptic annulus fibrosus, the average volume value was calculated however, with incorrect formula. The higher volume data was also reported in their circular finite element model of the annulus fibrosus. Although they claimed that the elongated cell predicted by the finite element model influenced higher cell micromechanical environment, no experimental data was provided for validation.

5.2.2 Implications

As mentioned in Chapter 1, orientation index (OI) relates to the fiber network orientation, and from the previously experimental measured VIC nucleus aspect ratio results (Figure 3-17 – Figure 3-19), significant decreasing OI with little change in VIC nucleus aspect ratios was observed. It suggested under the 0 – 1 mmHg transvalvular pressures, fiber straightening occurred in the tissue, inducing a decrease OI value but little influence on the VIC nucleus deformations (Figure 5-1). Furthermore, our predicted VIC nucleus aspect ratio corresponded well to the measured VIC nucleus aspect ratio (Figure 4-9), indicating the constitutive model from our laboratory⁽¹⁵⁵⁾ is adequate to describe the interaction of ECM and VIC nucleus under the 0 – 1 mmHg pressure levels.

At the 1 – 2 mmHg pressure levels, little changes in OI with increased measured VIC nucleus aspect ratios were observed (Figure 3-17 – Figure 3-19) and at the 2 – 4 mmHg pressure levels, little changes in OI and measured VIC nucleus aspect ratios were found. The data suggested other fiber coupling takes effects, which did not detect by the OI value from the small angle lighting scattering (SALS) technique at the 1 – 4 mmHg pressure levels. From the results at the 2 – 4 mmHg pressure levels showed in Figure 4-9, the differences of nucleus aspect ratio from the predicted values to the measured values were 22 % and 16 % in the elliptic VIC

microscopic models (Figure 5-1), indicating finite element simulation did not replicate the interaction of ECM / cell appropriately at these pressure levels, suggesting further investigation is required to understand this subtle effect to the deformations of VIC nucleus.

Under the 4 – 90 mmHg pressure levels, little changes in OI was observed but increased measured nucleus aspect ratios were found (Figure 3-17 – Figure 3-19). We hypothesized the elongation of VIC nucleus due to fiber compaction effects, and thus this phenomenon could not be detect by the OI values from SALS measurement but was observed in the increasing VIC nucleus aspect ratios. The differences of the nucleus aspect ratio from the predicted values to the measured values was 18% (at 90mmHg pressure level in Figure 5-1), which was lower than the one found at the 2 mmHg, but higher than the one found at 4 mmHg (Figure 5-1). It is suggested though our Fung's elastic constitutive model did not include the effect of fiber straightening or compaction alone, combined effects such as fiber straightening with compaction have more influences to alter the simulation accuracy at the pressure level 2 – 4 mmHg.

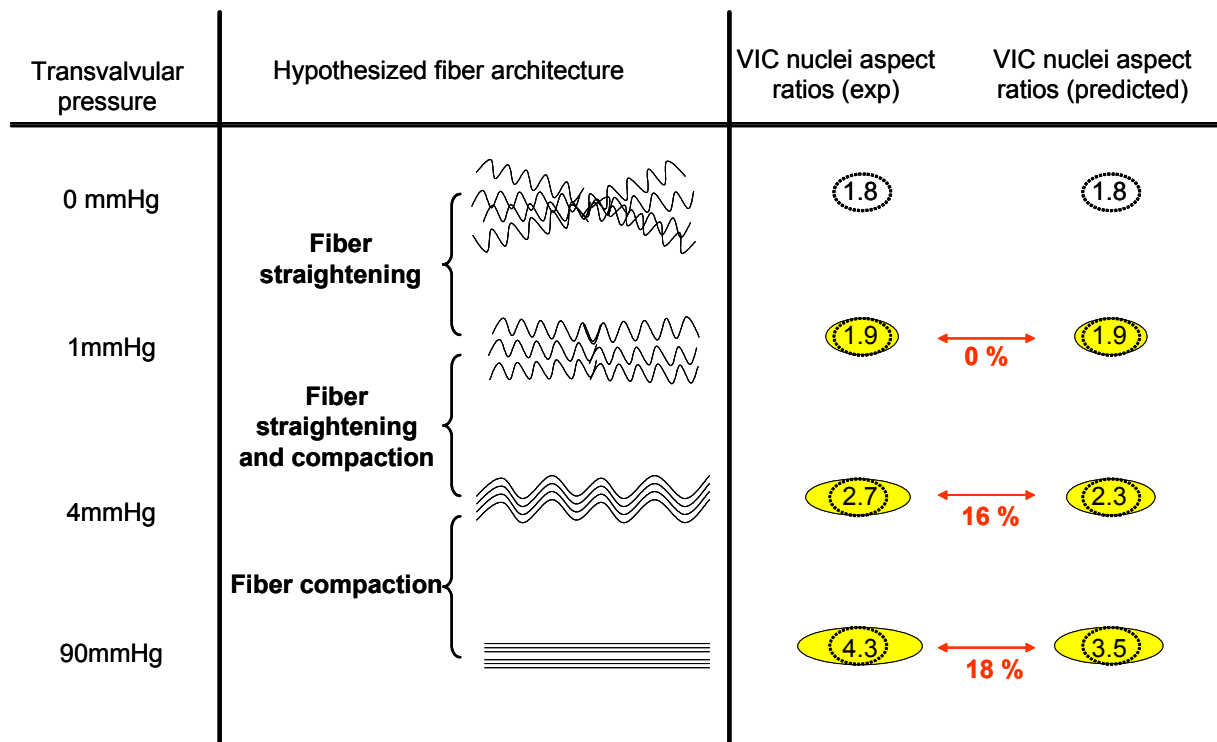


Figure 5-1 Two dimensional schematic depicting fiber straightening and compaction with corresponding VIC nucleus deformation induced from the ECM.

Furthermore, since we are unable to simulate the fiber micromechanical events due to the increasing of transvalvular pressure, underestimated finite element results appears to confirm these factors (fiber compaction). The predicted VIC nucleus aspect ratio followed the trend of measured VIC nucleus aspect ratio and did not overestimate the experimental results (Figure 4-9), indicating VIC nucleus deformation parallels the deformation of the tissue, and suggesting the VIC nuclei were sufficiently coupled to the surrounding ECM. Thus, the perfectly bonded assumption at the interface of the VIC nucleus and ECM used in the finite element simulations appears to be supported by our study. In conclusion, a continuum mechanics based finite element method and the Fung's elastic constitutive model form our laboratory described basic

response but was not able to capture all of it; additional mechanisms of the cell/ECM were required to be investigated, and a rigorous study is necessary either conducting by experimental design or complex numerical modeling development.

5.2.3 Recommendations for Future Studies

It has been hypothesized that cellular contraction can lead to deformation of the fiber network.^(104, 106) Under certain conditions, such as mechanical constraint, inhomogeneous cell distribution can result in inhomogeneous deformation and consequent fiber alignment, thereby affecting the subsequent deformation.^(104, 106) Currently, studies conducted in our laboratory have demonstrated a significant increase in the effective stiffness under flexure due to the coordinated contraction of VIC nucleus.⁽¹⁶⁰⁾ The contractile ability of VICs may contribute to valve function, suggesting continued research on the investigating VIC nucleus mechanism may elucidate the role of VIC nucleus for sustaining the unique dynamic behavior of the valve.

In the present study, a prolate elliptic cellular geometry was hypothesized, and with the available measured VIC nucleus aspect ratio data, a three-dimensional finite element model may aid the understanding of the deformation and mechanocytes of VIC nucleus in the native aortic valve tissues. Furthermore, a plausible structural constitutive model developed in our laboratory⁽¹¹⁶⁾ was able to overcome the limitation of Fung's model, e.g., fiber coupling considerations. However, incorporating the structural model into finite element solver resulted in the numerical convergence problems, which was stated by Sun.⁽¹⁵⁵⁾ This is due to the restriction of modifying convergence criteria in the current commercial finite element package, thus, switching to another solver or developing a custom codes with user-defined interface might offer more accuracy in predicting local mechanical environments of VIC nucleus.

In the multi-scale studies we report the first quantitative information on the deformation of VIC nucleus (i.e., VIC) in native porcine aortic valves subjected to various physiological transvalvular pressures. While it may ultimately prove impossible to conclusively demonstrate *in vivo*, these histological data tentatively suggest that the VIC nuclei undergo layer-specific deformations with each cardiac cycle, and thus suggest that cyclic VIC nucleus deformation may be innate to valvular homeostasis. These findings could prove to be critically important, not only in understanding the progression of certain valvular diseases in the native valves, but also in the development of living, tissue engineered heart valves (TEHV), in which cyclic mechanical conditioning *in vitro* has already demonstrated considerable utility.⁽⁸²⁾

With respect to native valvular disease, the progression of human aortic valve stenosis (i.e., a disruption of valvular homeostasis) has been shown to be associated with expression of the extracellular matrix glycoprotein tenascin-C.⁽¹⁶¹⁾ Furthermore, it has been shown that expression of matrix metalloproteinase-2 (MMP-2) is co-localized with tenascin-C in calcific aortic stenosis,⁽¹⁶²⁾ and that inhibition of MMP activity can attenuate tenascin-C production and concomitant calcification in an *in vivo* model.⁽¹⁶³⁾ Interestingly, the expression of MMPs, including MMP-2, have been shown to be modulated by static and cyclic mechanical loading (e.g., tensile strain) in vascular smooth muscle cells and endothelial cells in both 2D tissue culture systems,^(164, 165) as well as in 3D tissue engineering settings,^(166, 167) These findings warrant investigation of the possible effects of static or cyclic VIC nuclei deformation on MMP expression in the native aortic valve. For example, explanted porcine aortic valves could be maintained in organ culture under conditions of either static or cyclic transvalvular pressure in a pulsatile flow bioreactor, and MMP expression could be assessed by northern and western blotting for MMP mRNA and protein, respectively. It may be that deviations from normal VIC

nuclei deformation (perhaps due to calcific stiffening or fatigue-associated degeneration of the leaflet tissue ECM) lead to deviations in the expression of MMPs from that of native valves,⁽¹⁶⁸⁾ with concomitant effects on tenascin-C expression and valvular calcification. Similar studies could also be undertaken in tissue engineered heart valves (TEHV), as MMPs are known to be involved in the remodeling of such engineered cardiovascular tissues.⁽¹⁶⁹⁾

APPENDIX A: NONLINEAR FINITE ELEMENT SOLUTION PROCEDURE

As a brief introduction of the basic concepts, in the finite element method one seeks to divide the domain of interest into a finite number of non-overlapping but contiguous sub domains, called elements and thus, a boundary value problem or initial value problem is reduced to a system of equations of the form:

$$[\mathbf{K}]\{\mathbf{u}\}=\{\mathbf{F}\} \quad (\text{A.1})$$

where $[\mathbf{K}]$ is the (structural) stiffness matrix, $\{\mathbf{u}\}$ the vector of unknowns (such as displacements) and $\{\mathbf{F}\}$ the boundary loads. When $[\mathbf{K}]$ depends on $\{\mathbf{u}\}$, the system of equations is *nonlinear* and thereby requires special consideration for solution (e.g. Newton-Raphson method).

Finite element simulations of soft tissues are in general nonlinear and a finite element model can involve from a few to many variables. In terms of these variables the equilibrium equations obtained by discretizing the virtual work equation can be written symbolically as

$$F^N(\mu^M) = 0 \quad (\text{A.2})$$

where F^N is the force component conjugate to the N^{th} variable in the problem and μ^M is the value of the M^{th} variable. The basic problem is to solve equation (A.2) for the μ^M throughout the history of interest.

Many of the problems are time or history-dependent, so the solution must be developed by a series of "small" increments. Two issues arise: how the discrete equilibrium statement equation (A.2) is to be solved at each increment, and how the increment size is chosen.

Generally Newton's method is used as a numerical technique for solving the nonlinear equilibrium equations. The motivation for this choice is primarily the quadratic convergence rate obtained by using Newton's method compared to the convergence rates exhibited by alternate methods (usually modified Newton or quasi-Newton methods) for the nonlinear problems. The basic formalism of Newton's method is as follows ⁽¹⁷⁰⁾. Assume that, after iteration i , an approximation μ_i^M , to the solution has been obtained. Let \mathbf{c}_{i+1}^M be the difference between this solution and the exact solution to the discrete equilibrium equation (A.2). This means that

$$\mathbf{F}^N(\mu_i^M + \mathbf{c}_{i+1}^M) = 0 \quad (\text{A.3})$$

Expanding the left-hand side of this equation in a Taylor series about the approximate solution μ_i^M then gives

$$\mathbf{F}^N(\mu_i^M) + \frac{\partial \mathbf{F}^N}{\partial \mu^P}(\mu_i^M) \mathbf{c}_{i+1}^P + \frac{\partial^2 \mathbf{F}^N}{\partial \mu^P \partial \mu^Q}(\mu_i^M) \mathbf{c}_{i+1}^P \mathbf{c}_{i+1}^Q + \dots = 0 \quad (\text{A.4})$$

If μ_i^M is a close approximation to the solution, the magnitude of each \mathbf{c}_{i+1}^M will be small, and so all but the first two terms above can be neglected giving a linear system of equations:

$$\frac{\partial \mathbf{F}^N}{\partial \mu^P}(\mu_i^M) \mathbf{c}_{i+1}^P = -\mathbf{F}^N(\mu_i^M) \quad (\text{A.5})$$

The next approximation to the solution is then and the iteration continues.

$$\mu_{i+1}^M = \mu_i^M + \mathbf{c}_{i+1}^M \quad (\text{A.6})$$

Convergence of Newton's method is best measured by ensuring that all entries in F_i^N and all entries in c_{i+1}^M are sufficiently small. Both these criteria are checked by default in a finite element code, for example, ABAQUS.

Even though many finite element codes are commercially available, frequently they are misused in biomechanics, and one is cautioned to understand, or at least appreciate, the underlying mechanics prior to implementation. Therefore, most significant contributions continue to be realized via custom codes.

APPENDIX B: TRANSMURAL SURFACE STRAIN DURING BENDING

A critical experimental ability in evaluating the micromechanics of porcine BHV flexure is determination of the transmural strain field in the porcine BHV flexure specimens. Transmural strains are required to determine the location of the neutral axis, where the strains and stress are zero. In a homogeneous beam, the neutral axis will be located at the centroid of the cross-section (e.g. in the center of a beam with a rectangular cross-section). However, in a beam made up of two or more dissimilar materials, the neutral axis will shift toward the stiffer material.⁽¹⁷¹⁾ Thus, finding the neutral axis location can determine if differences exist in the porcine BHV layer mechanical properties.

In our laboratory, we have recently developed a technique to quantify the transmural strain distribution of porcine BHV cuspal specimens under flexural loading. This was accomplished using small India ink particles (25~50 μ m diameter) applied to the upper side of the bending specimens using an air brush (Figure B-1). We were consistently able to identify 90 or more markers over the entire cuspal surface and track their displacements during flexure (Figure B-1 (b)). The optical system of our bending device was also modified to use a high magnification macro lens capable imaging a 1 mm x 1 mm area, and with the use of our 1K x 1K digital camera, we were able to obtain a net spatial resolution of ~1 μ m/pixel. SigmaScan (Jandel Sci) was used to auto digitize marker position.

To determine the neutral axis, porcine BHV flexure specimens were prepared as above and subjected to flexure in both the AC and WC directions. An area of the specimen was identified towards the middle to get near maximum moment but also away from the force rod to avoid local stress effects (boxed region in Figure B-1 (a)). 94 small India ink markers over the

entire transmural surface were identified and tracked referenced to a local x-y coordinate system, whose origin is on the ventricularis side and with the x axis oriented parallel to the local specimen edge (Figure B-1 (b)). Marker displacements were determined, with u defined as the displacement in the x direction and v the displacement in the y direction. To compute the strains, the displacement gradients were determined by fitting the displacement fields to:

$$\begin{aligned} u &= a_0 + a_1x + a_2y + a_3xy + a_4x^2 + a_5y^2 \\ v &= b_0 + b_1x + b_2y + b_3xy + b_4x^2 + b_5y^2 \end{aligned} \quad (\text{B-1})$$

Equation (B-1) fit the u, v displacement data very well, with $r^2 \geq 0.98$. Thus, we computed the 2D Finite Green's strain tensor (E_{ij}) using formulas found in:⁽¹⁷²⁾

$$E_{xx} = u_x + \frac{1}{2} [u_x^2 + v_x^2] \quad E_{xy} = \frac{1}{2} [u_y + v_x + u_x u_y + v_x v_y] \quad E_{yy} = v_y + \frac{1}{2} [u_y^2 + v_y^2] \quad (\text{B-2})$$

where $u_x = \partial u / \partial x = a_1 + a_3y + 2a_4x$, etc. From E_{ij} , the stretch ratios λ in the x and y directions were computed using $\lambda_x = \sqrt{2E_{xx} + 1}$ and $\lambda_y = \sqrt{2E_{yy} + 1}$. The neutral axis location is determined where $\lambda_x = 1$.

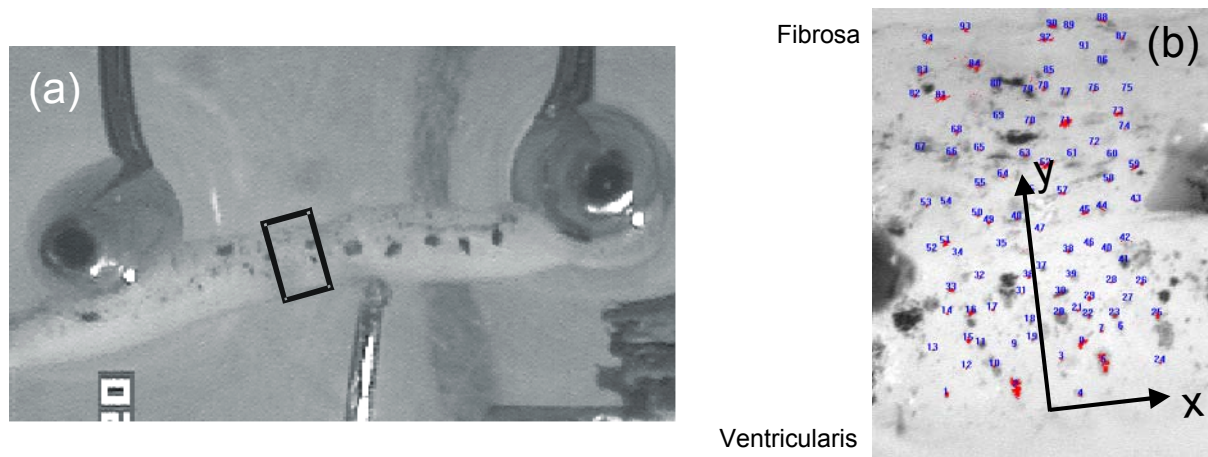


Figure B-1 (a) A porcine BHV specimen mounted in the flexural testing device, showing the graphite particles used for curvature measurements, and the rectangular box delimiting the area where the transmural strains were computed. (b) Close up image of the rectangular region in (a) showing the locations and identification numbers of the 94 markers used to determine the transmural displacement field, along with the location of the local x-y axes. The two large markers on the left and right side of the image are the graphite markers used for curvature measurements shown in (a).

In all cases the shear component E_{12} was small so that its effect can be ignored. Results for λ_x for a fresh and fixed porcine BHV leaflet specimen flexed in the AC direction are shown in Figure B-2. Interestingly, the λ_x transmural distribution was very linear for both specimens. Porcine BHV stretch distributions were found to be linear for both λ_x and λ_y (due to space limitations only λ_x is shown). More importantly, chemical fixation shifted the neutral axis from 0.54 (about halfway) to 0.84. When the fixed specimen was flexed in the WC direction, the location of the neutral axis shifted to 0.64 (Figure B-3 (a)). Finally, while the location of the neutral axis depended on bending direction, it did not depend on the amount of bending deflection (Figure B-3 (b)).

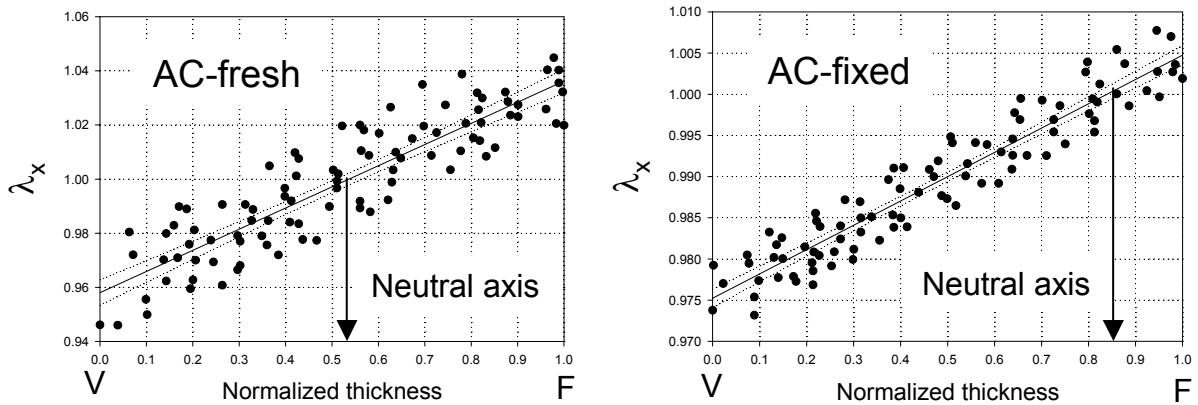


Figure B-2 λ_x transmurial distribution for the region shown in Fig. 6-a in the AC direction for a fresh and fixed specimen, with thickness normalized from 0 (V=ventricularis) to 1 (F=Fibrosa). Both distributions are very linear. While the neutral axis was located at 0.5 for the fresh tissue, it shifted to 0.84 for the fixed, suggesting different layer stiffnesses.

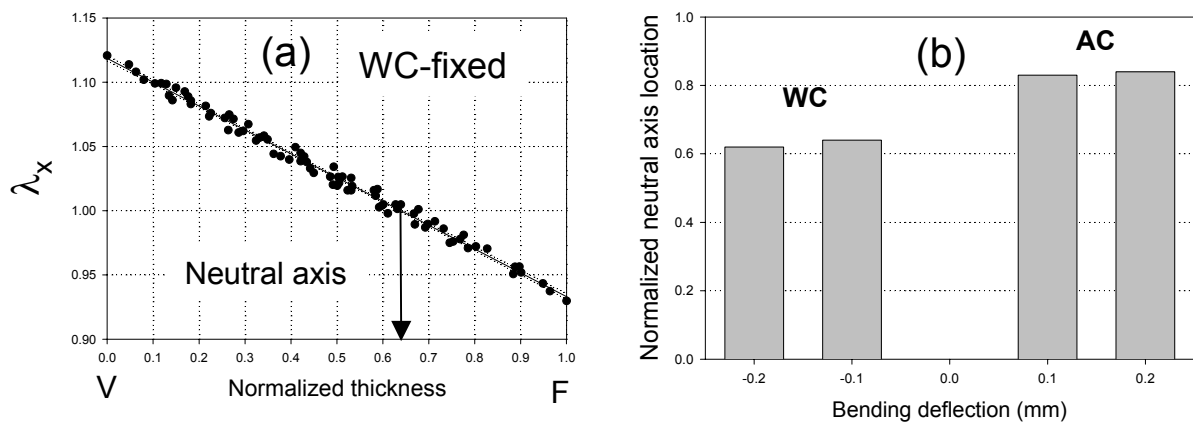
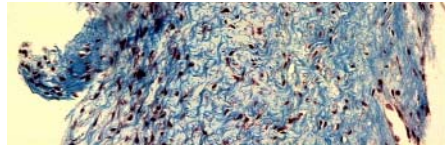


Figure B-3 (a) λ_x transmurial distribution for the same fixed specimen as in Fig. 7 but flexed in the WC direction. Again, the distribution was linear. More importantly, the neutral axis shifted from 0.84 to 0.64, suggesting a change in layer stiffnesses in tension and compression. (b) Normalized location of the neutral axis location as a function of bending direction and amount of specimen deflection for two deflection levels each. Although the neutral axis location depended on bending direction, it did not depend on the amount of bending deflection within each direction.

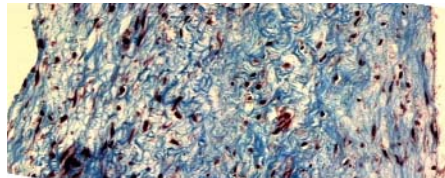
These important results indicate that: The porcine BHV cuspal layers exhibit different mechanical stiffnesses. Because the ventricularis and fibrosa layers are alternately subjected to compression and tension when flexed in the AC and WC directions, the existence of different neutral axis locations in the two bending directions implies that each layer has different stiffnesses in tension and compression. Since the M/I vs. $\Delta\kappa$ relationship was linear, and that the neutral axis location did not depend on the amount of bending deflection within each bending direction, it is likely that each layer has a linear stress-strain response in flexure (i.e. low strain region).

APPENDIX C: PHOTOMICROGRAPH OF HISTOLOGY SECTIONS

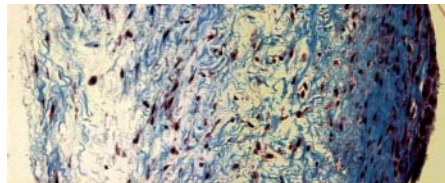
1. 0 mmHg (slide A, section 1) with Masson stained



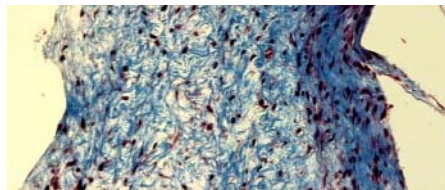
0 mmHg; Masson; Slide A; Section 1; Cross-section location 1



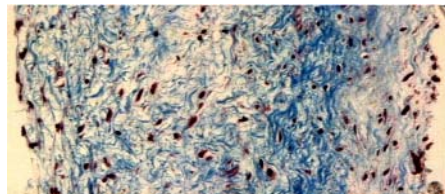
0 mmHg; Masson; Slide A; Section 1; Cross-section location 2



0 mmHg; Masson; Slide A; Section 1; Cross-section location 3



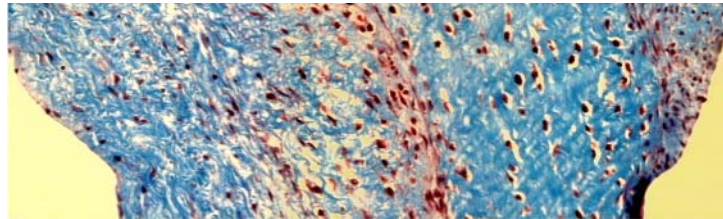
0 mmHg; Masson; Slide A; Section 1; Cross-section location 4



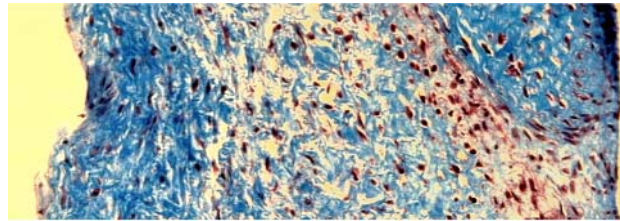
0 mmHg; Masson; Slide A; Section 1; Cross-section location 5

Figure C-1 Sample of five panoramic photomicrographs in 0 mmHg (slide A, section 1) with Masson stained.

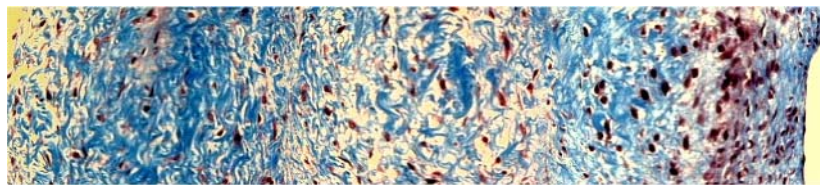
2. 0 mmHg (slide A, section 2) with Masson stained



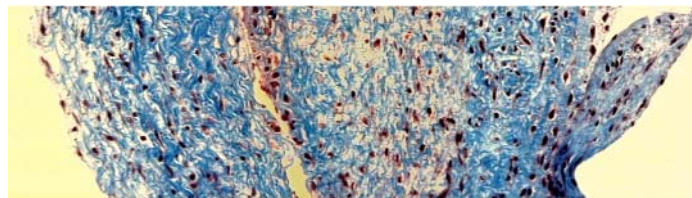
0 mmHg; Masson; Slide A; Section 2(Y); Cross-section location 1



0 mmHg; Masson; Slide A; Section 2(Y); Cross-section location 2



0 mmHg; Masson; Slide A; Section 2(Y); Cross-section location 3



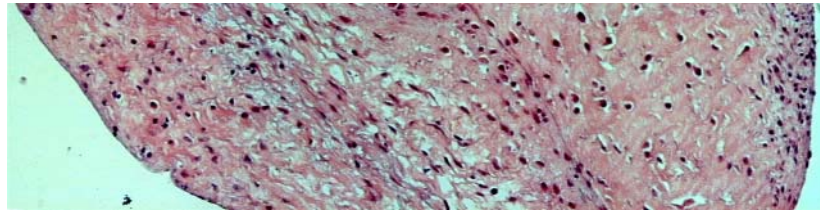
0 mmHg; Masson; Slide A; Section 2(Y); Cross-section location 4



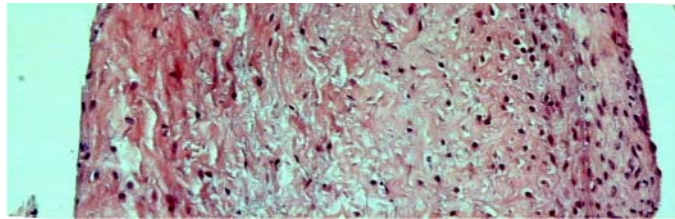
0 mmHg; Masson; Slide A; Section 2(Y); Cross-section location 5

Figure C-2 Sample of five panoramic photomicrographs in 0 mmHg (slide A, section 2) with Masson stained.

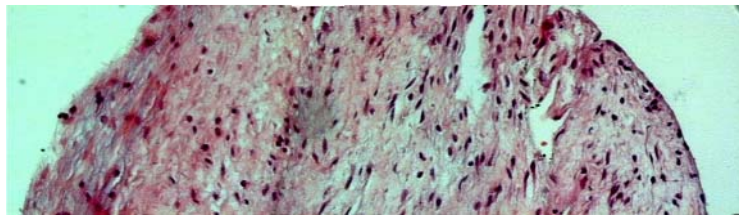
3. 0 mmHg (slide C, section 1) with H & E stained



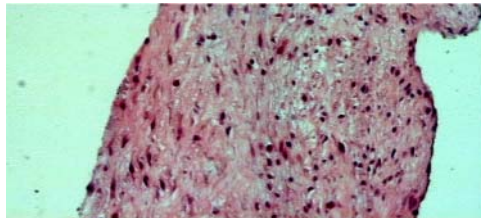
0 mmHg; H & E; Slide C; Section 1(X); Cross-section location 1



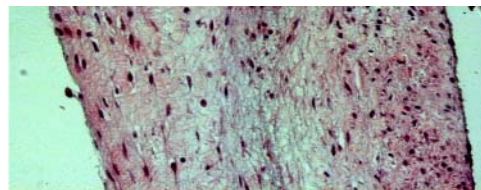
0 mmHg; H & E; Slide C; Section 1(X); Cross-section location 2



0 mmHg; H & E; Slide C; Section 1(X); Cross-section location 3



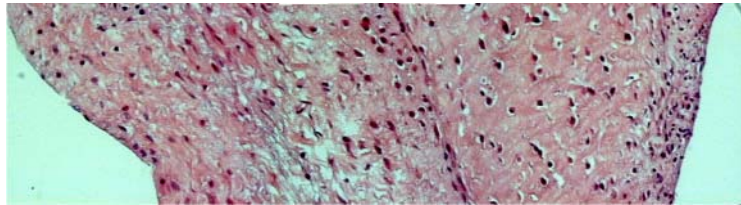
0 mmHg; H & E; Slide C; Section 1(X); Cross-section location 4



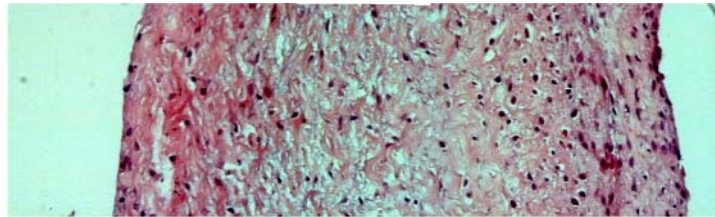
0 mmHg; H & E; Slide C; Section 1(X); Cross-section location 5

Figure C-3 Sample of five panoramic photomicrographs in 0 mmHg (slide C, section 1) with H & E stained.

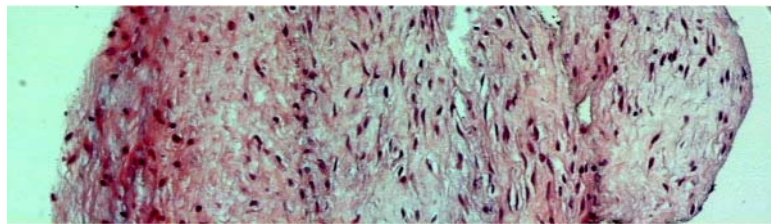
4. 0 mmHg (slide C, section 2) with H & E stained



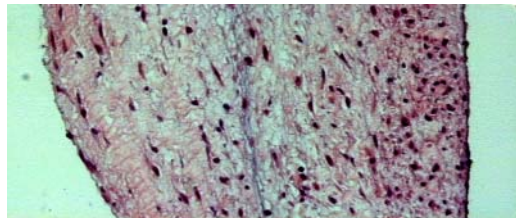
0 mmHg; H & E; Slide C; Section 2(Y); Cross-section location 1



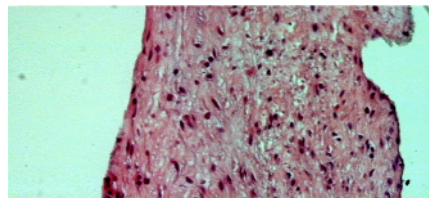
0 mmHg; H & E; Slide C; Section 2(Y); Cross-section location 2



0 mmHg; H & E; Slide C; Section 2(Y); Cross-section location 3



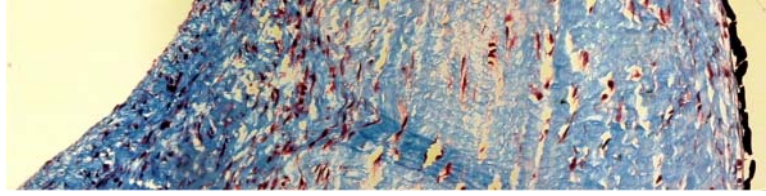
0 mmHg; H & E; Slide C; Section 2(Y); Cross-section location 4



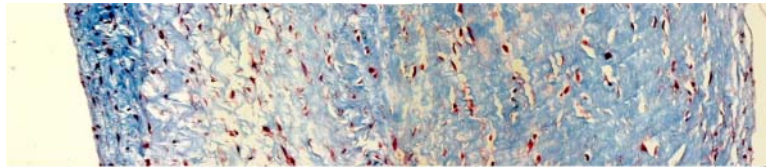
0 mmHg; H & E; Slide C; Section 2(Y); Cross-section location 5

Figure C-4 Sample of five panoramic photomicrographs in 0 mmHg (slide C, section 2) with H & E stained.

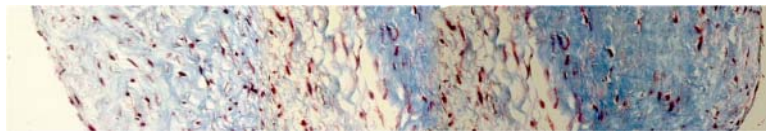
5. 1 mmHg (slide A, section 1) with Masson stained



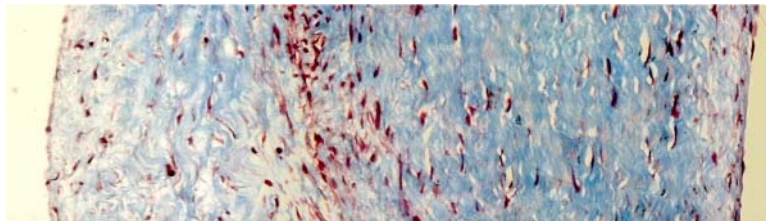
1 mmHg; Masson; Slide A; Section 1(X); Cross-section location 1



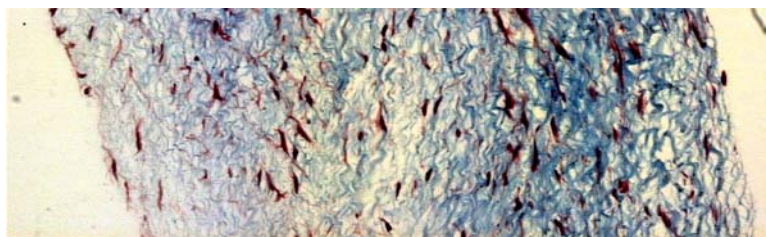
1 mmHg; Masson; Slide A; Section 1(X); Cross-section location 2



1 mmHg; Masson; Slide A; Section 1(X); Cross-section location 3



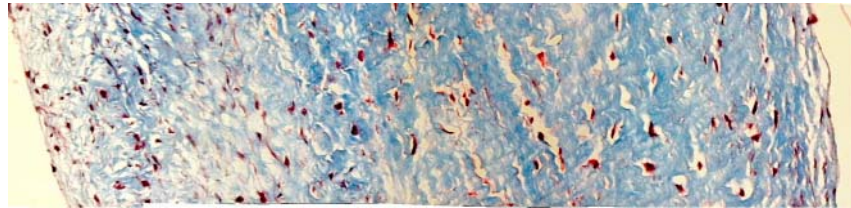
1 mmHg; Masson; Slide A; Section 1(X); Cross-section location 4



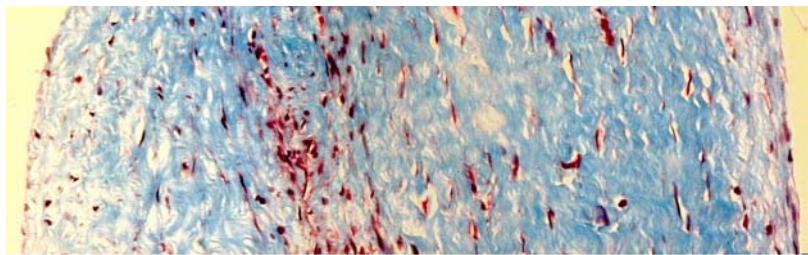
1 mmHg; Masson; Slide A; Section 1(X); Cross-section location 5

Figure C-5 Sample of five panoramic photomicrographs in 1 mmHg (slide A, section 1) with Masson stained.

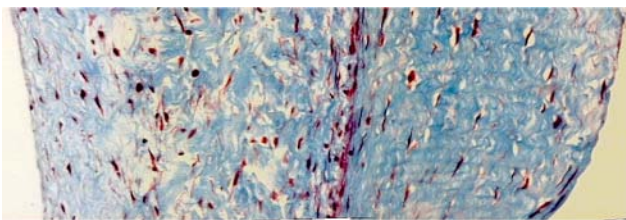
6. 1 mmHg (slide A, section 2) with Masson stained



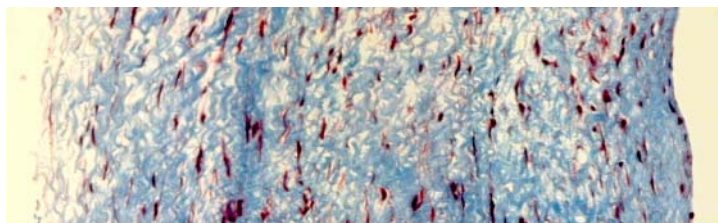
1 mmHg; Masson; Slide A; Section 2(Y); Cross-section location 1



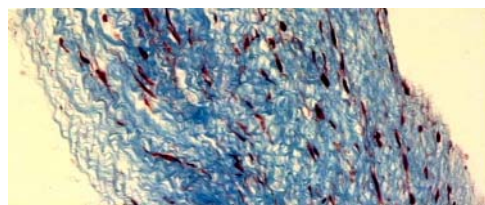
1 mmHg; Masson; Slide A; Section 2(Y); Cross-section location 2



1 mmHg; Masson; Slide A; Section 2(Y); Cross-section location 3



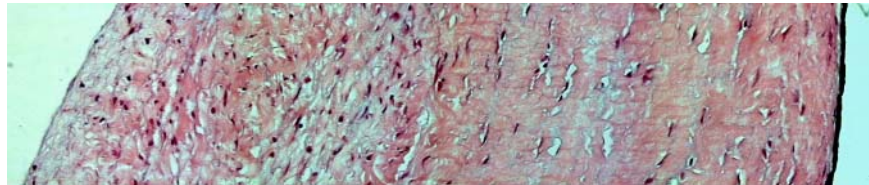
1 mmHg; Masson; Slide A; Section 2(Y); Cross-section location 4



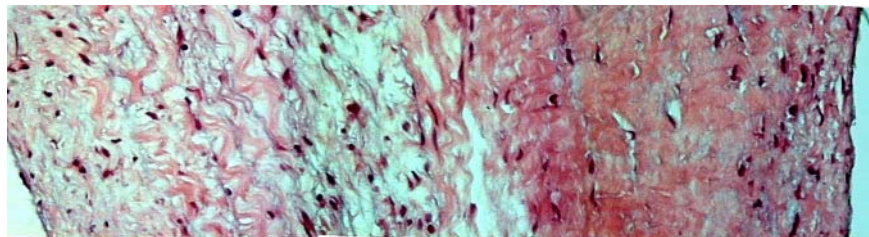
1 mmHg; Masson; Slide A; Section 2(Y); Cross-section location 5

Figure C-6 Sample of five panoramic photomicrographs in 1 mmHg (slide A, section 2) with Masson stained.

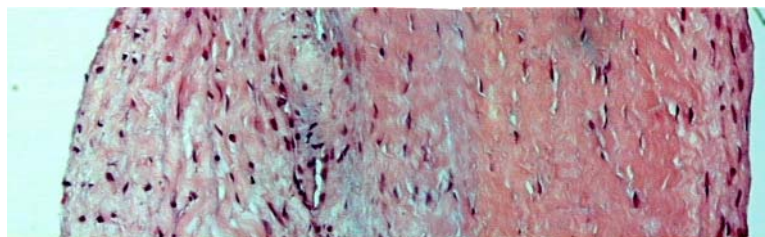
7. 1 mmHg (slide A, section 1) with H & E stained



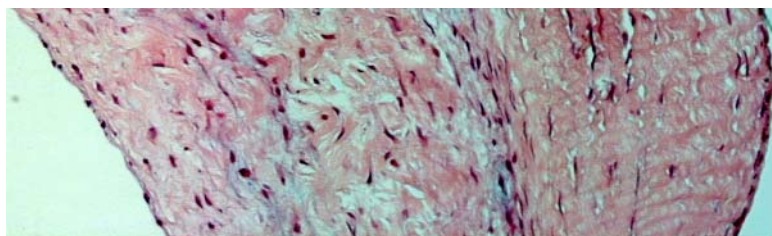
1 mmHg; H & E; Slide A; Section 1(X); Cross-section location 1



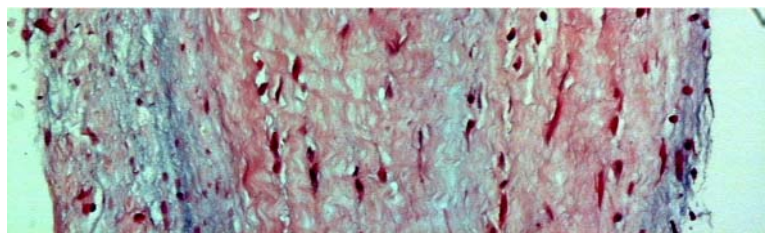
1 mmHg; H & E; Slide A; Section 1(X); Cross-section location 2



1 mmHg; H & E; Slide A; Section 1(X); Cross-section location 3



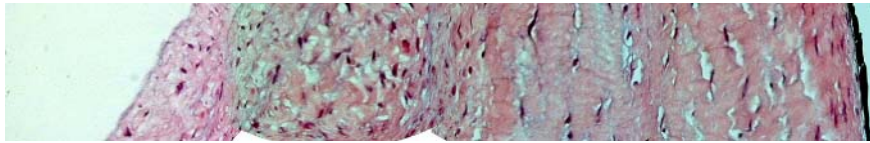
1 mmHg; H & E; Slide A; Section 1(X); Cross-section location 4



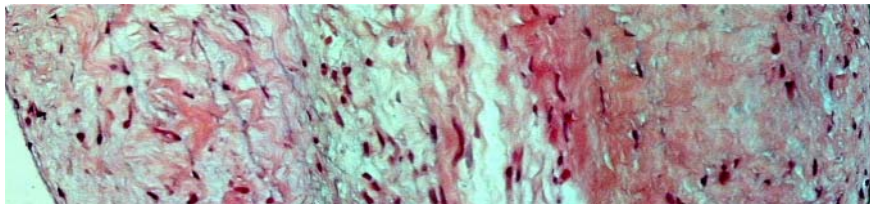
1 mmHg; H & E; Slide A; Section 1(X); Cross-section location 5

Figure C-7 Sample of five panoramic photomicrographs in 1 mmHg (slide A, section 1) with H & E stained.

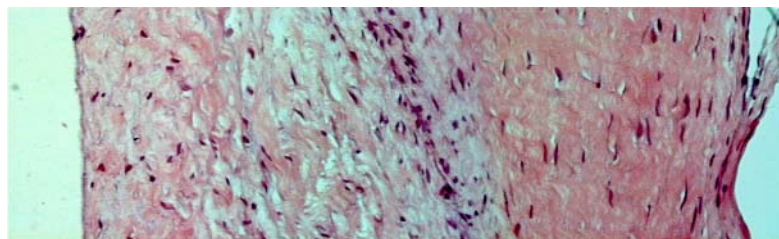
8. 1 mmHg (slide A, section 2) with H & E stained



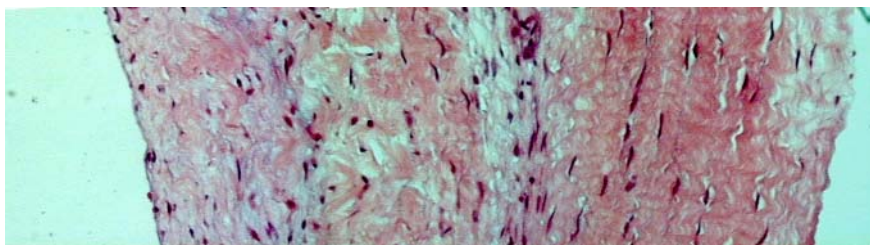
1 mmHg; H & E; Slide A; Section 2(Y); Cross-section location 1



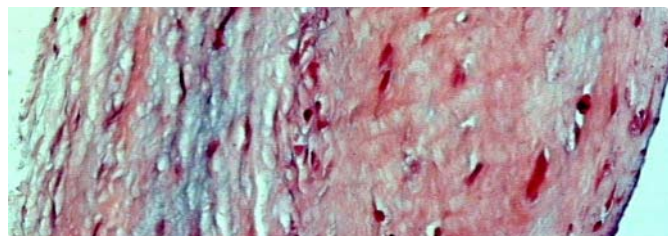
1 mmHg; H & E; Slide A; Section 2(Y); Cross-section location 2



1 mmHg; H & E; Slide A; Section 2(Y); Cross-section location 3



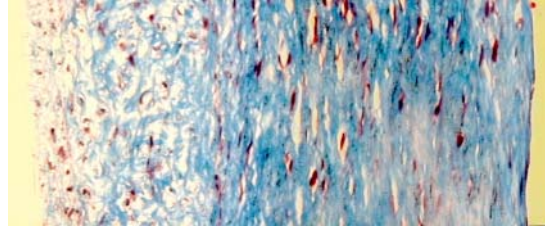
1 mmHg; H & E; Slide A; Section 2(Y); Cross-section location 4



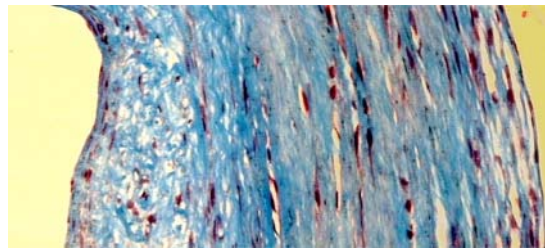
1 mmHg; H & E; Slide A; Section 2(Y); Cross-section location 5

Figure C-8 Sample of five panoramic photomicrographs in 1 mmHg (slide A, section 2) with H & E stained.

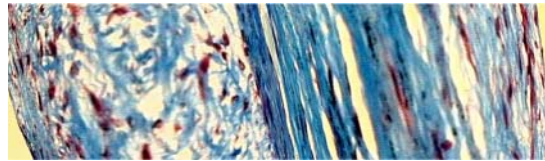
9. 2 mmHg (slide A, section 1) with Masson stained



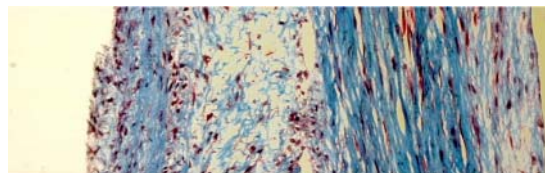
2 mmHg; Masson; Slide A; Section 1; Cross-section location 1



2 mmHg; Masson; Slide A; Section 1; Cross-section location 2



2 mmHg; Masson; Slide A; Section 1; Cross-section location 3



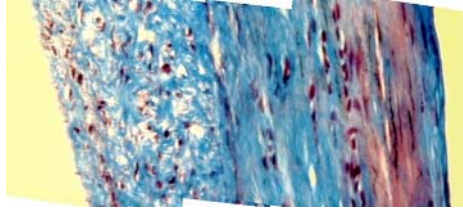
2 mmHg; Masson; Slide A; Section 1; Cross-section location 4



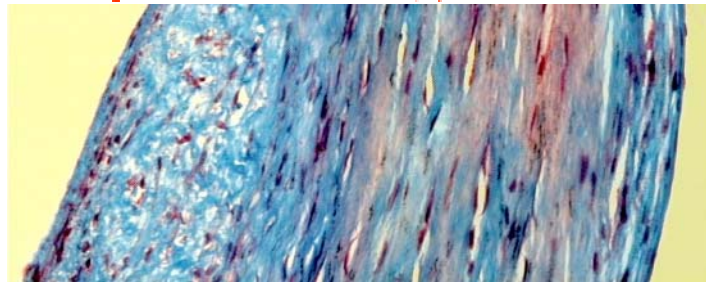
2 mmHg; Masson; Slide A; Section 1; Cross-section location 5

Figure C-9 Sample of five panoramic photomicrographs in 2 mmHg (slide A, section 1) with Masson stained.

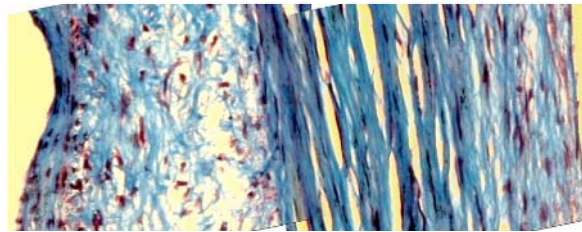
10. 2 mmHg (slide A, section 2) with Masson stained



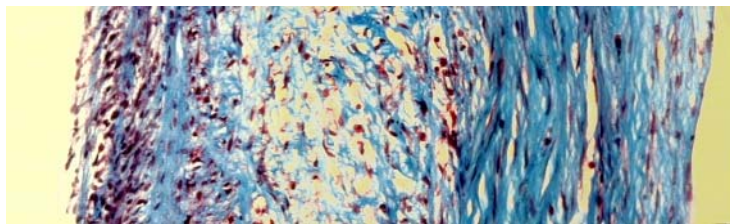
2 mmHg; Masson; Slide A; Section 2(Y); Cross-section location 1



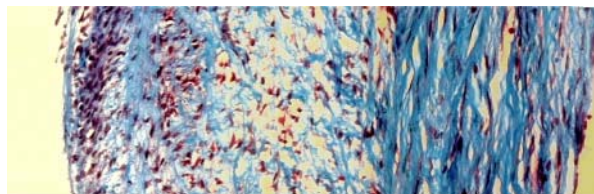
2 mmHg; Masson; Slide A; Section 2(Y); Cross-section location 2



2 mmHg; Masson; Slide A; Section 2(Y); Cross-section location 3



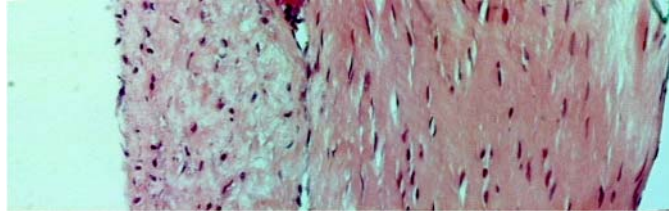
2 mmHg; Masson; Slide A; Section 2(Y); Cross-section location 4



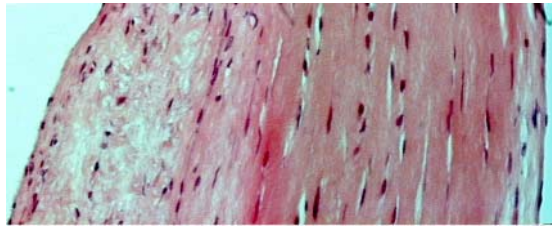
2 mmHg; Masson; Slide A; Section 2(Y); Cross-section location 5

Figure C-10 Sample of five panoramic photomicrographs in 2 mmHg (slide A, section 2) with Masson stained.

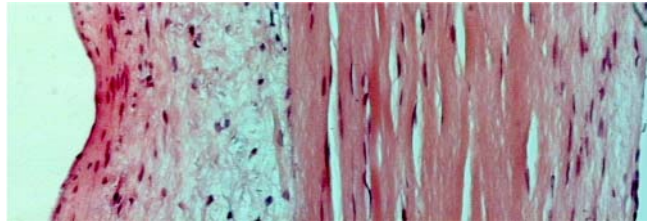
11. 2 mmHg (slide A, section 1) with H & E stained



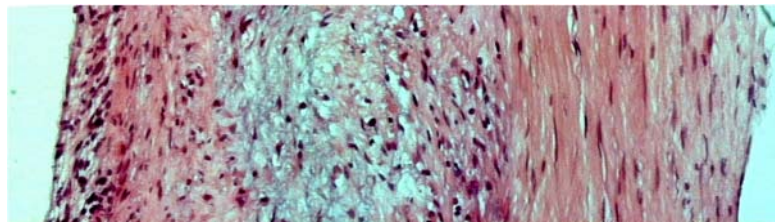
2 mmHg; H & E; Slide A; Section 1(X); Cross-section location 1



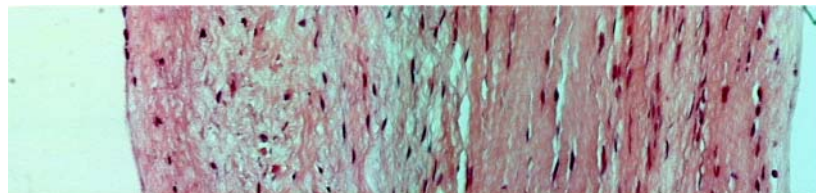
2 mmHg; H & E; Slide A; Section 1(X); Cross-section location 2



2 mmHg; H & E; Slide A; Section 1(X); Cross-section location 3



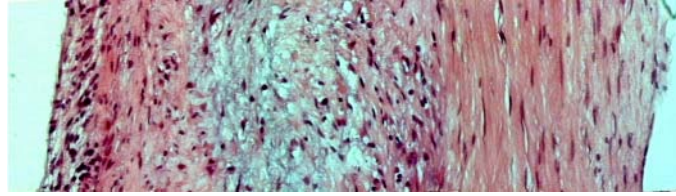
2 mmHg; H & E; Slide A; Section 1(X); Cross-section location 4



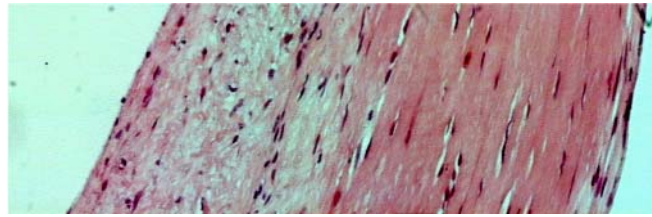
2 mmHg; H & E; Slide A; Section 1(X); Cross-section location 5

Figure C-11 Sample of five panoramic photomicrographs in 2 mmHg (slide A, section 1) with H & E stained.

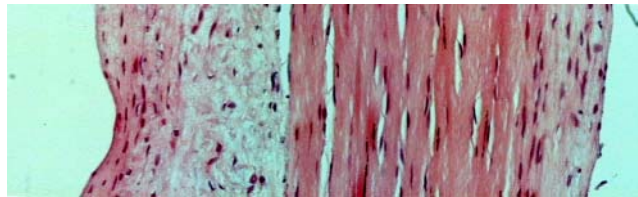
12. 2 mmHg (slide A, section 2) with H & E stained



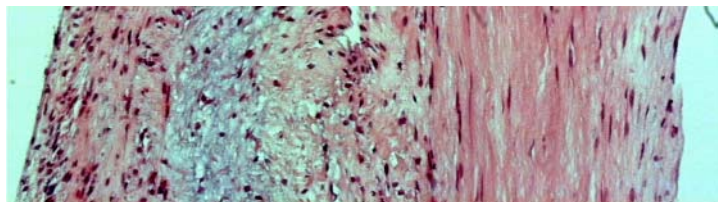
2 mmHg; H & E; Slide A; Section 2(Y); Cross-section location 1



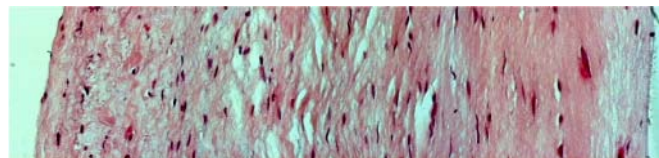
2 mmHg; H & E; Slide A; Section 2(Y); Cross-section location 2



2 mmHg; H & E; Slide A; Section 2(Y); Cross-section location 3



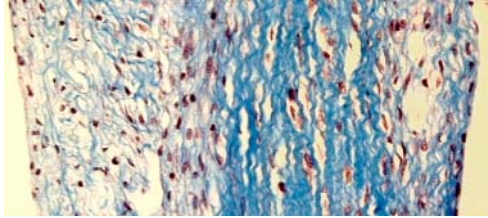
2 mmHg; H & E; Slide A; Section 2(Y); Cross-section location 4



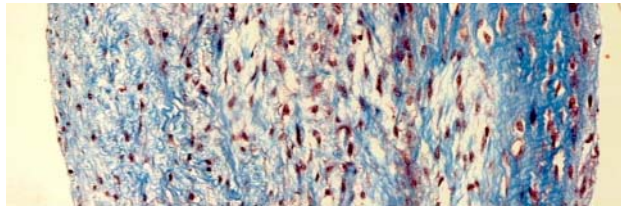
2 mmHg; H & E; Slide A; Section 2(Y); Cross-section location 5

Figure C-12 Sample of five panoramic photomicrographs in 2 mmHg (slide A, section 2) with H & E stained.

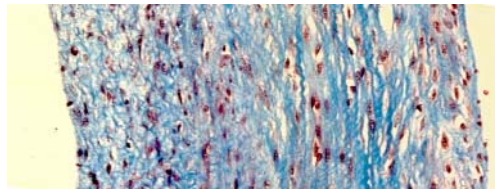
13. 4 mmHg (slide A, section 1) with Masson stained



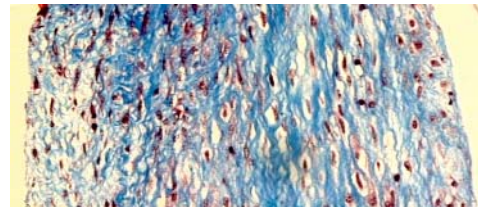
4 mmHg; Masson; Slide A; Section 1(X); Cross-section location 1



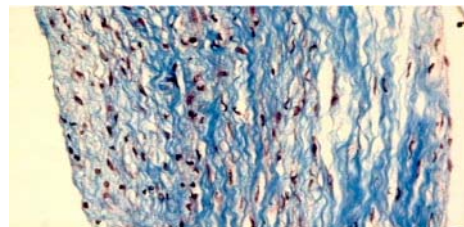
4 mmHg; Masson; Slide A; Section 1(X); Cross-section location 2



4 mmHg; Masson; Slide A; Section 1(X); Cross-section location 3



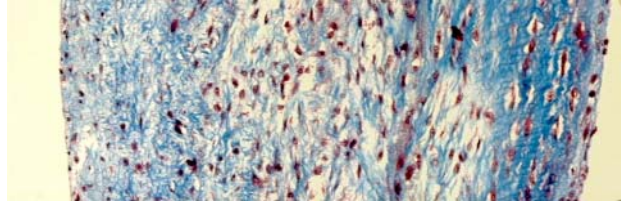
4 mmHg; Masson; Slide A; Section 1(X); Cross-section location 4



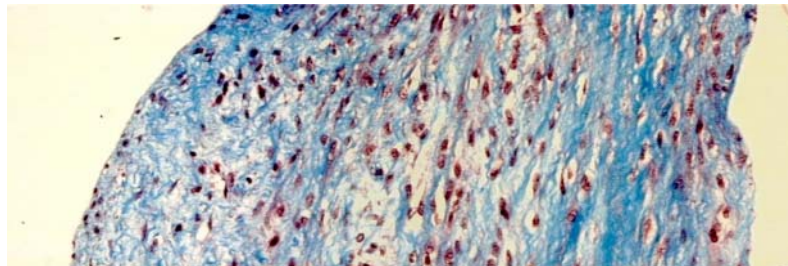
4 mmHg; Masson; Slide A; Section 1(X); Cross-section location 5

Figure C-13 Sample of five panoramic photomicrographs in 4 mmHg (slide A, section 1) with Masson stained.

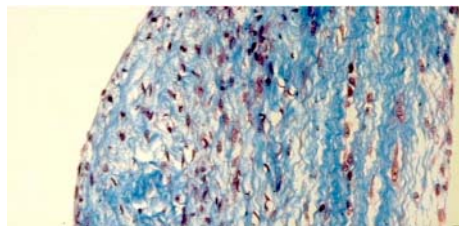
14. 4 mmHg (slide A, section 2) with Masson stained



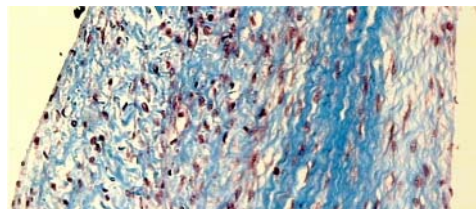
4 mmHg; Masson; Slide A; Section 2(Y); Cross-section location 1



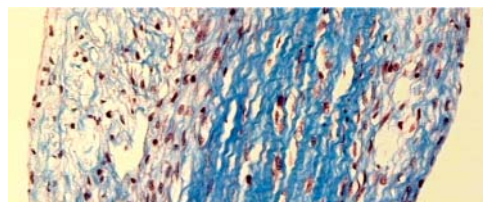
4 mmHg; Masson; Slide A; Section 2(Y); Cross-section location 2



4 mmHg; Masson; Slide A; Section 2(Y); Cross-section location 3



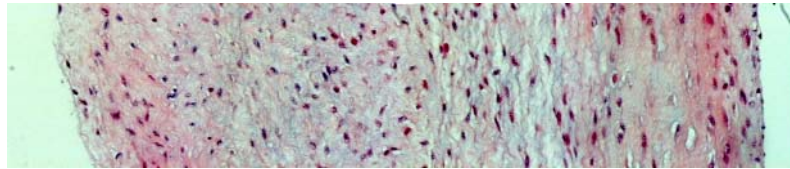
4 mmHg; Masson; Slide A; Section 2(Y); Cross-section location 4



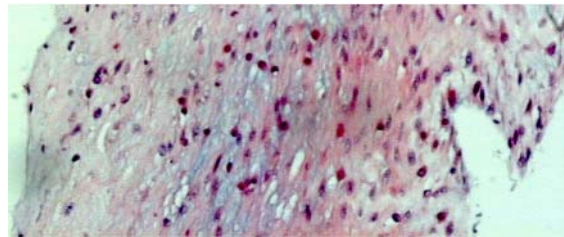
4 mmHg; Masson; Slide A; Section 2(Y); Cross-section location 5

Figure C-14 Sample of five panoramic photomicrographs in 4 mmHg (slide A, section 2) with Masson stained.

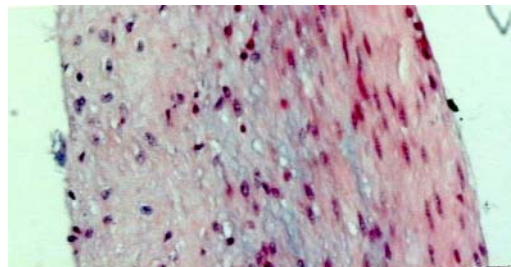
15. 4 mmHg (slide B, section 1) with H & E stained



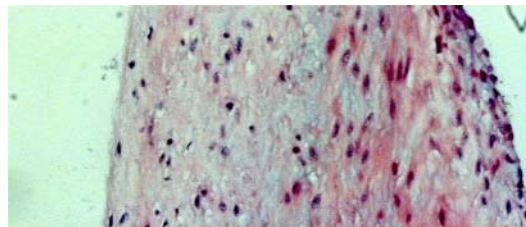
4 mmHg; H & E; Slide B; Section 1(X); Cross-section location 1



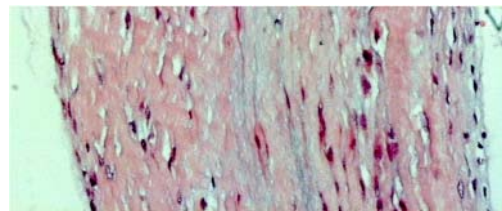
4 mmHg; H & E; Slide B; Section 1(X); Cross-section location 2



4 mmHg; H & E; Slide B; Section 1(X); Cross-section location 3



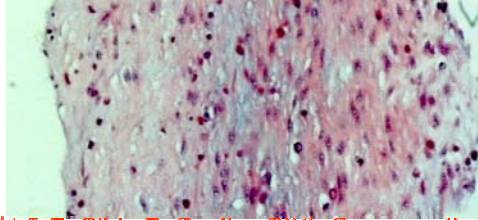
4 mmHg; H & E; Slide B; Section 1(X); Cross-section location 4



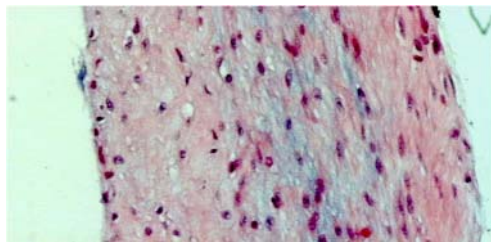
4 mmHg; H & E; Slide B; Section 1(X); Cross-section location 5

Figure C-15 Sample of five panoramic photomicrographs in 4 mmHg (slide B, section 1) with H & E stained.

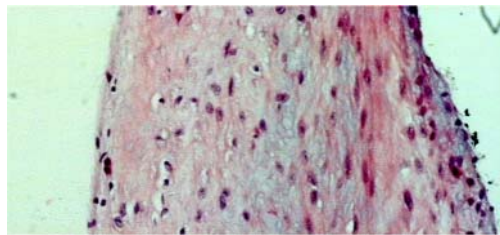
16. 4 mmHg (slide B, section 2) with H & E stained



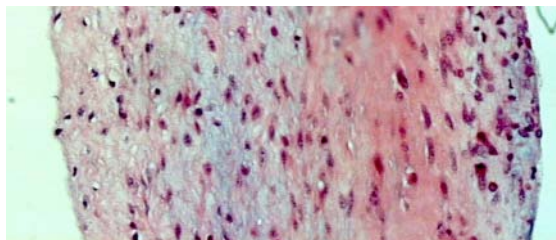
4 mmHg; H & E; Slide B; Section 2(Y); Cross-section location 1



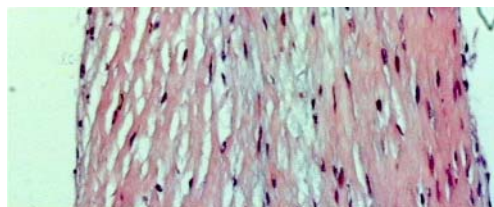
4 mmHg; H & E; Slide B; Section 2(Y); Cross-section location 2



4 mmHg; H & E; Slide B; Section 2(Y); Cross-section location 3



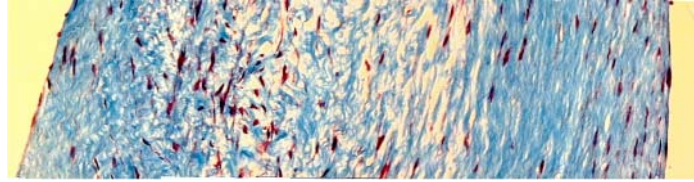
4 mmHg; H & E; Slide B; Section 2(Y); Cross-section location 4



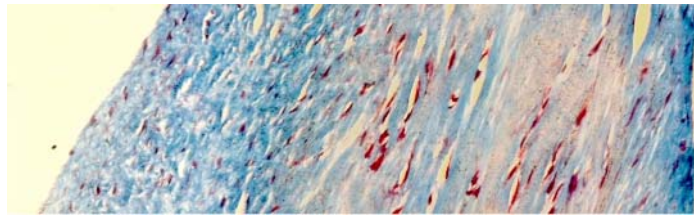
4 mmHg; H & E; Slide B; Section 2(Y); Cross-section location 5

Figure C-16 Sample of five panoramic photomicrographs in 4 mmHg (slide B, section 2) with H & E stained.

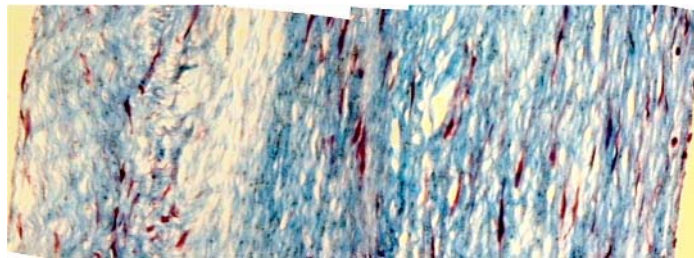
17. 60 mmHg (slide A, section 1) with Masson stained



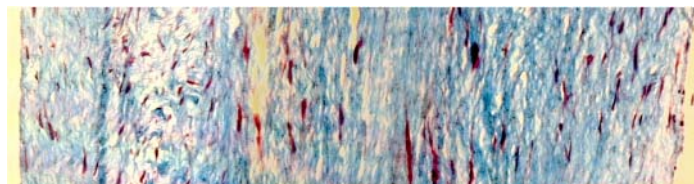
60 mmHg; Masson; Slide A; Section 1; Cross-section location 1



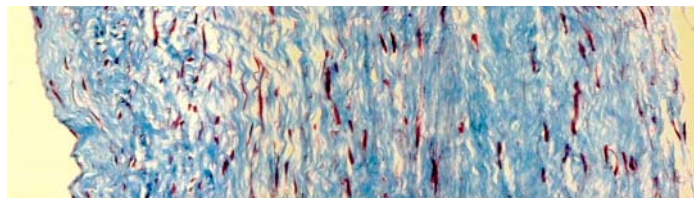
60 mmHg; Masson; Slide A; Section 1; Cross-section location 2



60 mmHg; Masson; Slide A; Section 1; Cross-section location 3



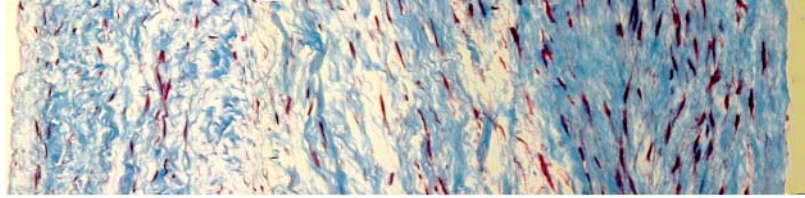
60 mmHg; Masson; Slide A; Section 1; Cross-section location 4



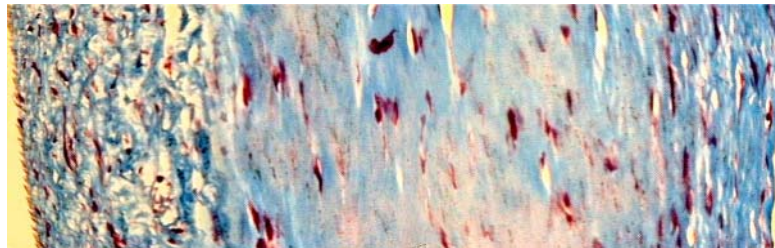
60 mmHg; Masson; Slide A; Section 1; Cross-section location 5

Figure C-17 Sample of five panoramic photomicrographs in 60 mmHg (slide A, section 1) with Masson stained.

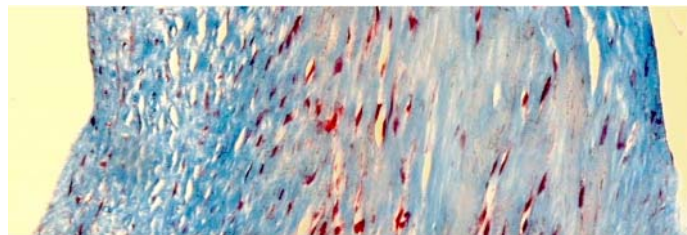
18. 60 mmHg (slide A, section 2) with Masson stained



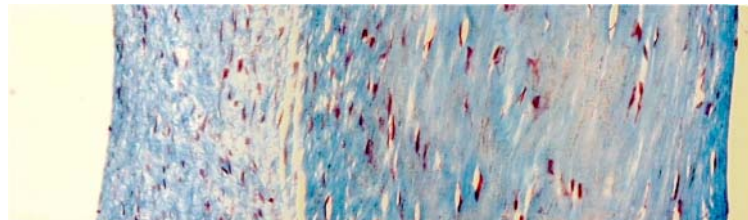
60 mmHg; Masson; Slide A; Section 2(Y); Cross-section location 1



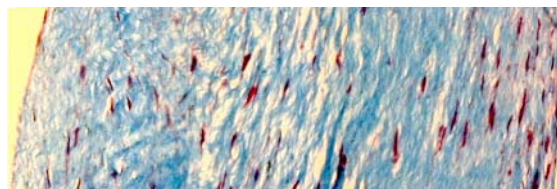
60 mmHg; Masson; Slide A; Section 2(Y); Cross-section location 2



60 mmHg; Masson; Slide A; Section 2(Y); Cross-section location 3



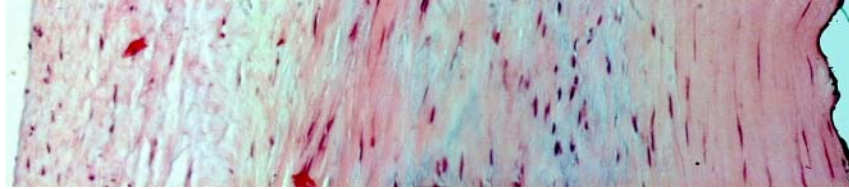
60 mmHg; Masson; Slide A; Section 2(Y); Cross-section location 4



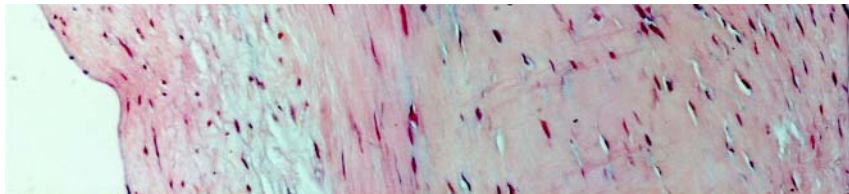
60mmHg; Masson; Slide A; Section 2(Y); Cross-section location 5

Figure C-18 Sample of five panoramic photomicrographs in 60 mmHg (slide A, section 2) with Masson stained.

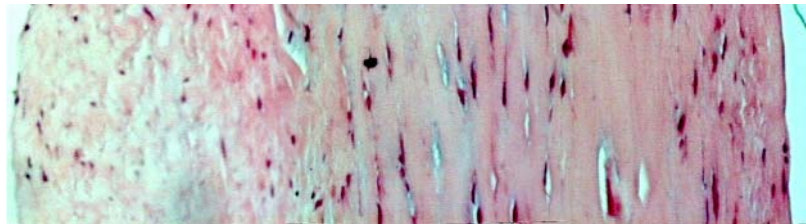
19. 60 mmHg (slide A, section 1) with H & E stained



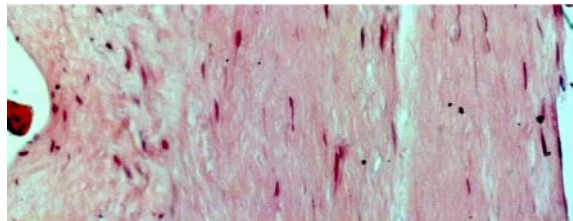
60 mmHg; H & E; Slide A; Section 1(X); Cross-section location 1



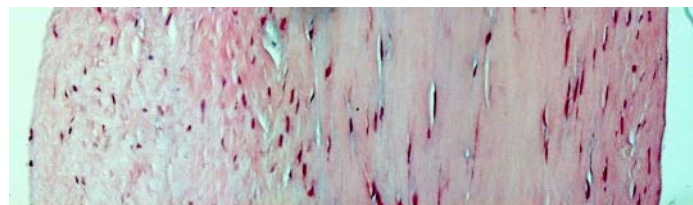
60 mmHg; H & E; Slide A; Section 1(X); Cross-section location 2



60 mmHg; H & E; Slide A; Section 1(X); Cross-section location 3



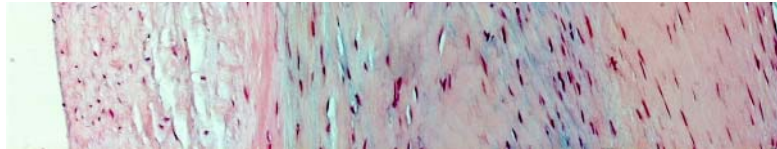
0 mmHg; H & E; Slide A; Section 1(X); Cross-section location 4



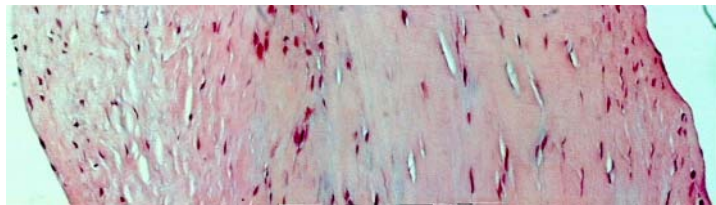
0 mmHg; H & E; Slide A; Section 1(X); Cross-section location 5

Figure C-19 Sample of five panoramic photomicrographs in 60 mmHg (slide A, section 1) with H & E stained.

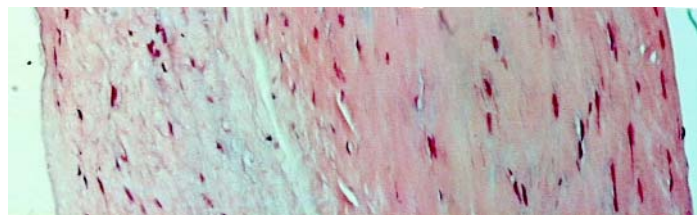
20. 60 mmHg (slide A, section 2) with H & E stained



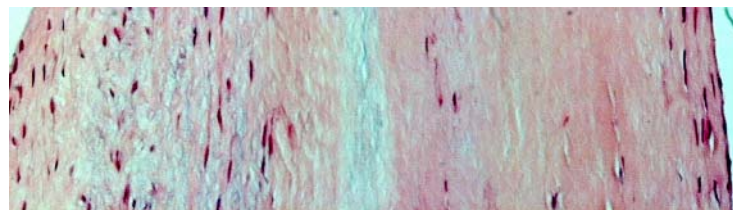
60 mmHg; H & E; Slide A; Section 2(Y); Cross-section location 1



60 mmHg; H & E; Slide A; Section 2(Y); Cross-section location 2



60 mmHg; H & E; Slide A; Section 2(Y); Cross-section location 3



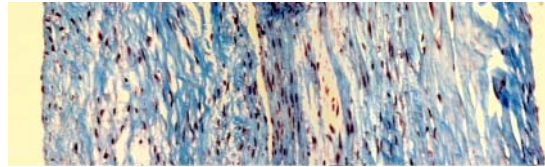
0 mmHg; H & E; Slide A; Section 2(Y); Cross-section location 4



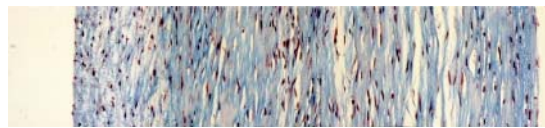
0 mmHg; H & E; Slide A; Section 2(Y); Cross-section location 5

Figure C-20 Sample of five panoramic photomicrographs in 60 mmHg (slide A, section 2) with H & E stained.

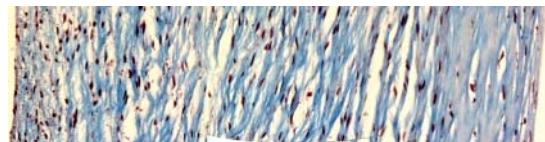
21. 90 mmHg (slide A, section 1) with Masson stained



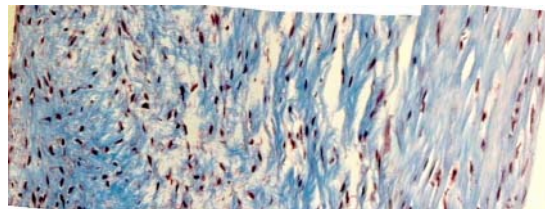
90 mmHg; Masson; Slide A; Section 1(X); Cross-section location 1



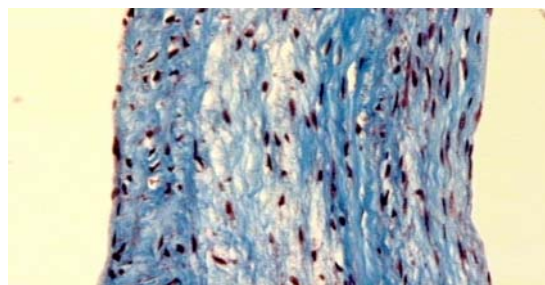
90 mmHg; Masson; Slide A; Section 1(X); Cross-section location 2



90 mmHg; Masson; Slide A; Section 1(X); Cross-section location 3



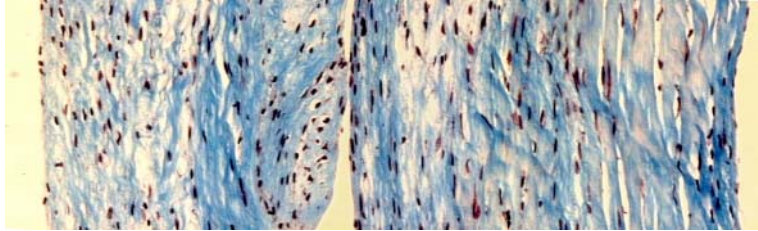
90 mmHg; Masson; Slide A; Section 1(X); Cross-section location 4



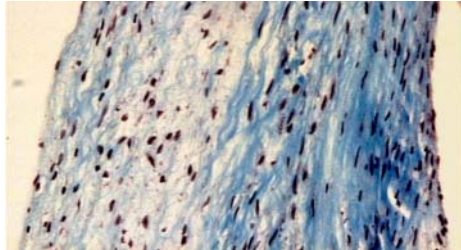
90 mmHg; Masson; Slide A; Section 1(X); Cross-section location 5

Figure C-21 Sample of five panoramic photomicrographs in 90 mmHg (slide A, section 1) with Masson stained.

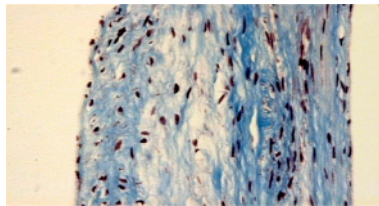
22. 90 mmHg (slide A, section 2) with Masson stained



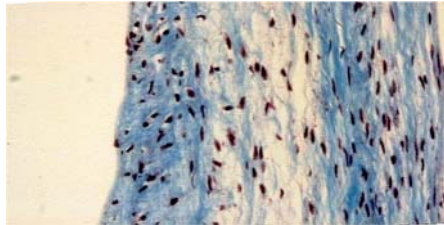
90 mmHg; Masson; Slide A; Section 2(Y); Cross-section location 1



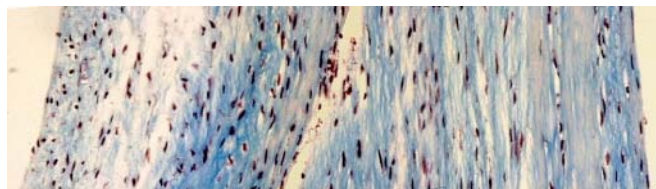
90 mmHg; Masson; Slide A; Section 2(Y); Cross-section location 2



90 mmHg; Masson; Slide A; Section 2(Y); Cross-section location 3



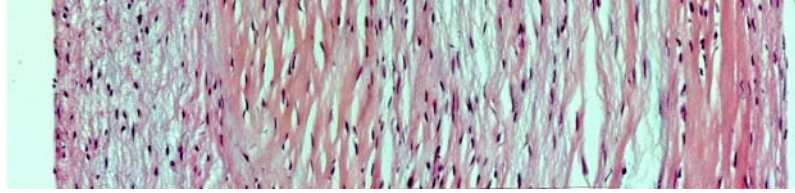
90 mmHg; Masson; Slide A; Section 2(Y); Cross-section location 4



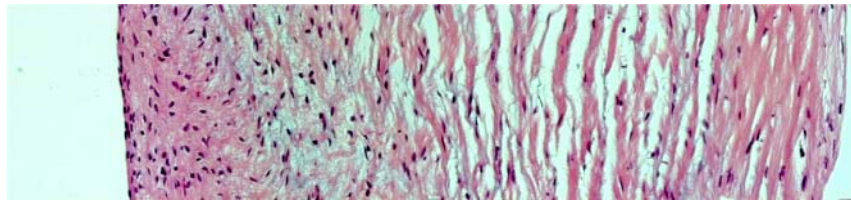
90mmHg; Masson; Slide A; Section 2(Y); Cross-section location 5

Figure C-22 Sample of five panoramic photomicrographs in 90 mmHg (slide A, section 2) with Masson stained.

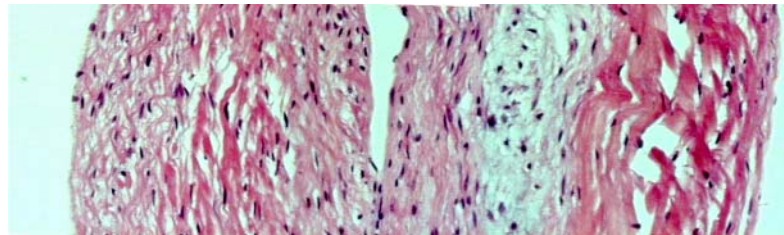
23. 90 mmHg (slide A, section 1) with H & E stained



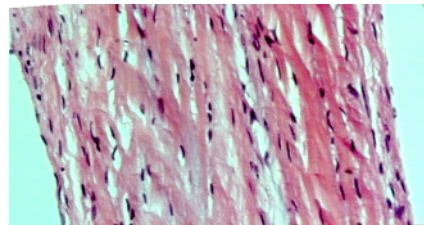
90 mmHg; H & E; Slide A; Section 1(X); Cross-section location 1



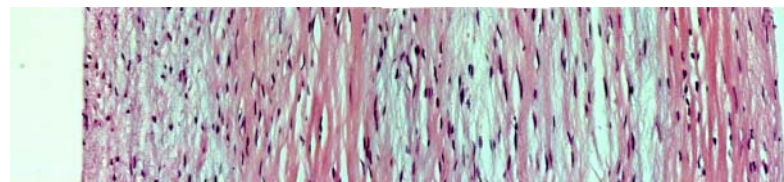
90 mmHg; H & E; Slide A; Section 1(X); Cross-section location 2



90 mmHg; H & E; Slide A; Section 1(X); Cross-section location 3



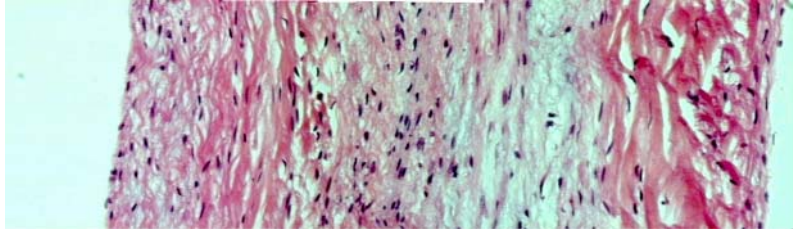
90 mmHg; H & E; Slide A; Section 1(X); Cross-section location 4



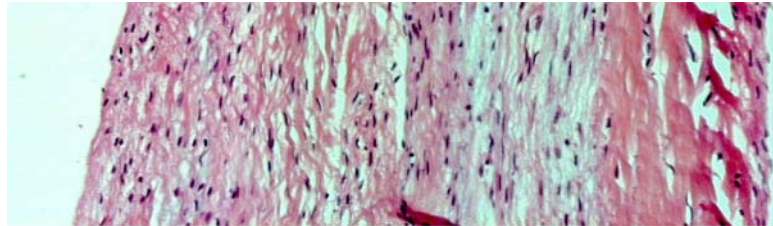
90 mmHg; H & E; Slide A; Section 1(X); Cross-section location 5

Figure C-23 Sample of five panoramic photomicrographs in 90 mmHg (slide A, section 1) with H & E stained.

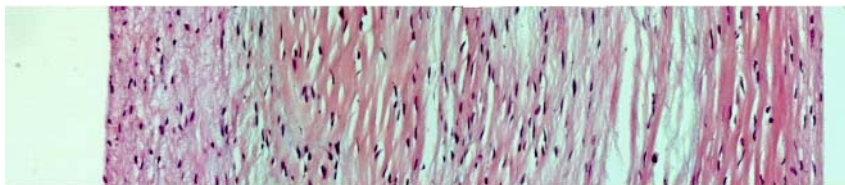
24. 90 mmHg (slide A, section 2) with H & E stained



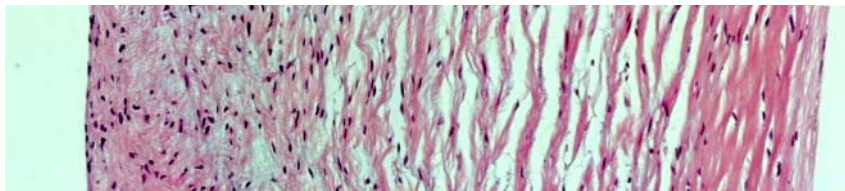
90 mmHg; H & E; Slide A; Section 2(Y); Cross-section location 1



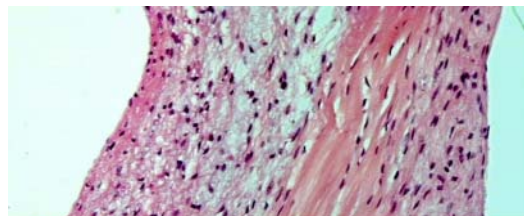
90 mmHg; H & E; Slide A; Section 2(Y); Cross-section location 2



90 mmHg; H & E; Slide A; Section 2(Y); Cross-section location 3



90 mmHg; H & E; Slide A; Section 2(Y); Cross-section location 4



90 mmHg; H & E; Slide A; Section 2(Y); Cross-section location 5

Figure C-24 Sample of five panoramic photomicrographs in 90 mmHg (slide A, section 2) with H & E stained.

APPENDIX D: INTRA-SLIDE AND INTRA-PRESSURE VARIABILITY

1. Bar-charts showed below indicating intra-slide variability under 0, 1, 2, 4, 60 and 90 mmHg transvalvular pressures.

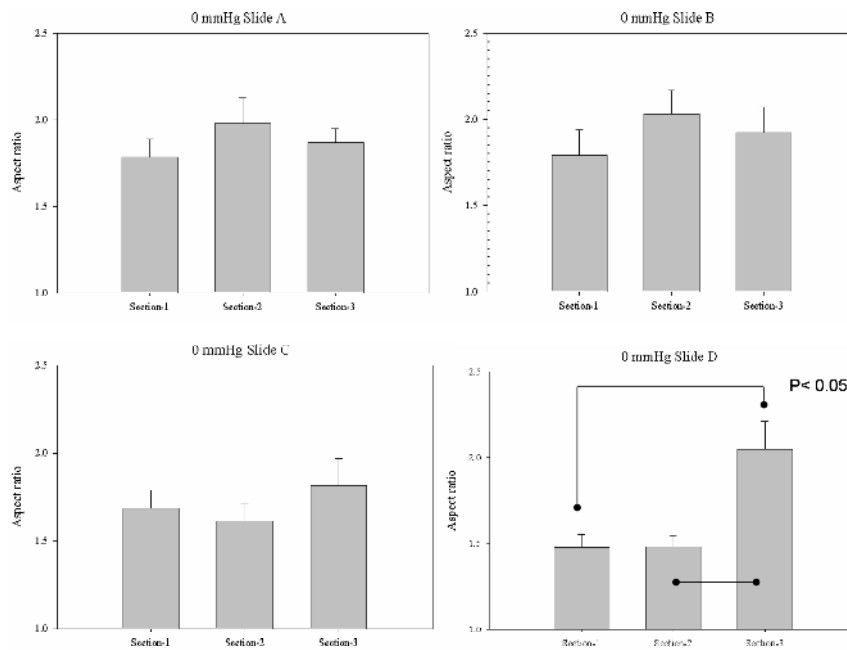


Figure D-1 Averaged cellular aspect ratio of specimen under 0 mmHg was measured, and intra-slide variability from slide A – D was observed.

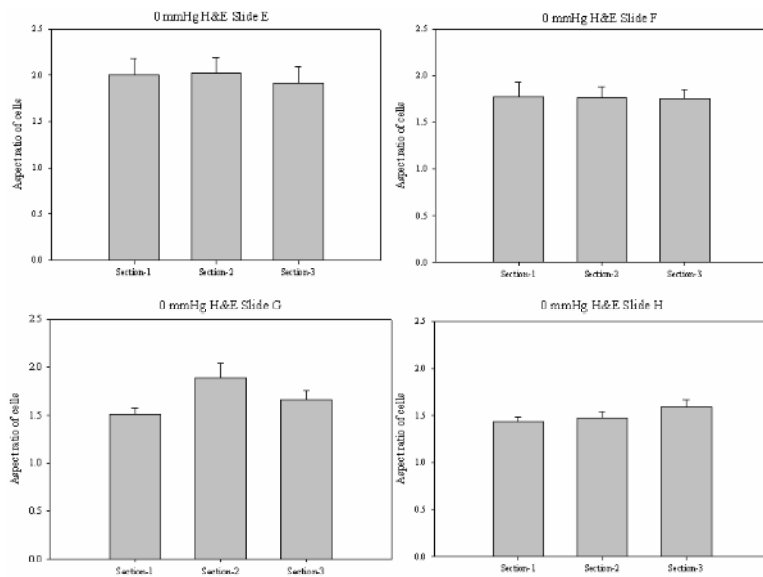


Figure D-2 Averaged VIC nuclei aspect ratio of specimen under 0 mmHg was measured, and no intra-slide variability from slide E – H was observed.

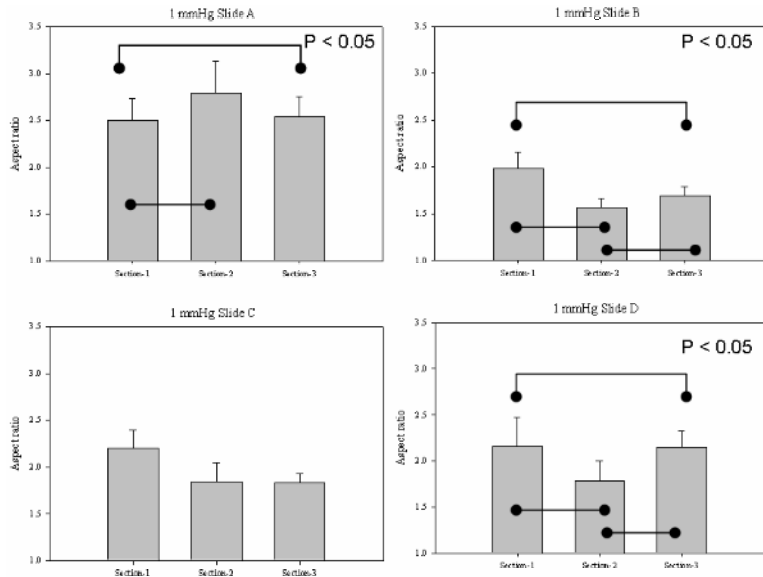


Figure D-3 Averaged VIC nuclei aspect ratio of specimen under 1 mmHg was measured, and intra-slide variability from slide A – D was observed.

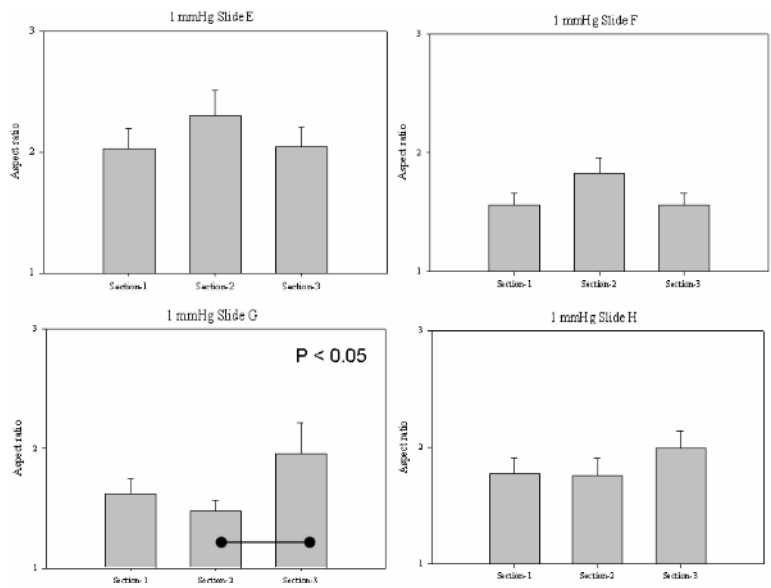


Figure D-4 Averaged VIC nuclei aspect ratio of specimen under 1 mmHg was measured, and intra-slide variability from slide E – H was observed.

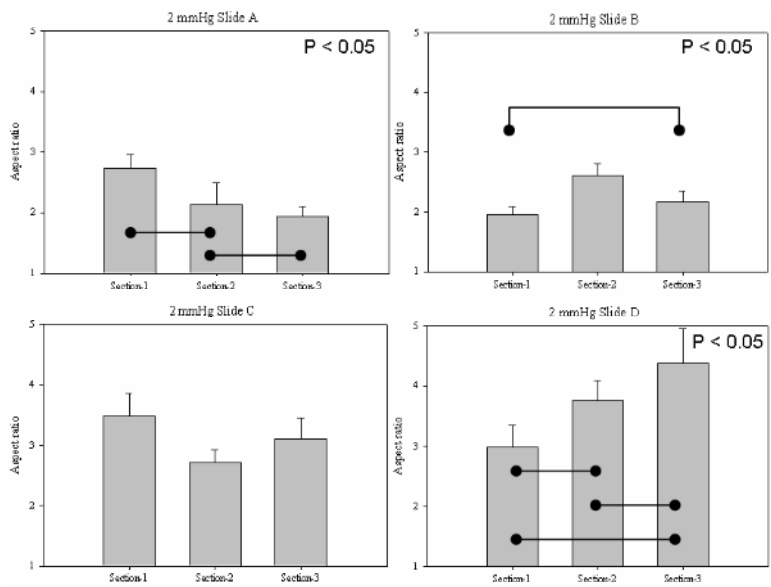


Figure D-5 Averaged VIC nuclei aspect ratio of specimen under 2 mmHg was measured, and intra-slide variability from slide A – D was observed.

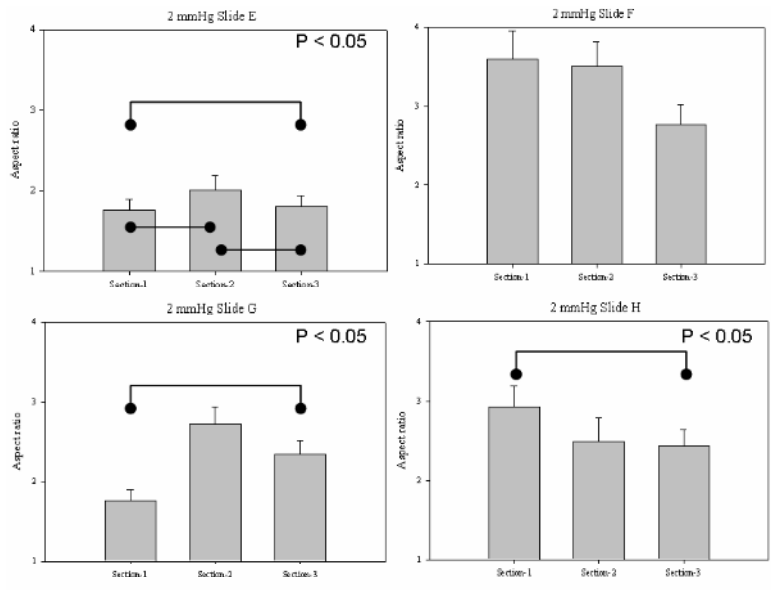


Figure D-6 Averaged VIC nuclei aspect ratio of specimen under 2 mmHg was measured, and intra-slide variability from slide E – H was observed.

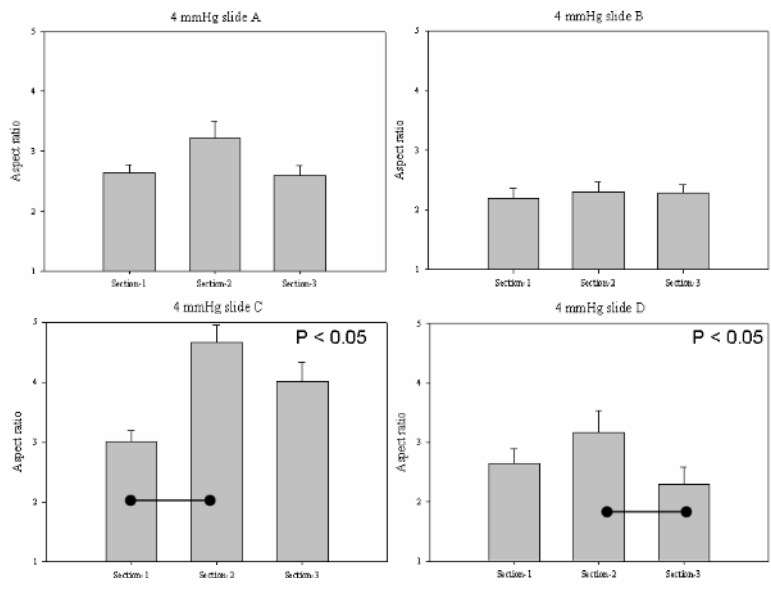


Figure D-7 Averaged VIC nuclei aspect ratio of specimen under 4 mmHg was measured, and intra-slide variability from slide A – D was observed.

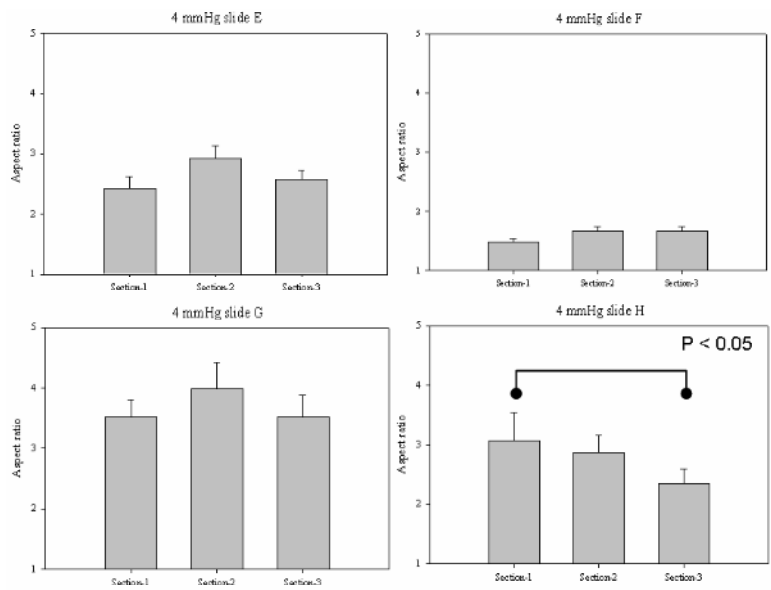


Figure D-8 Averaged VIC nuclei aspect ratio of specimen under 4 mmHg was measured, and intra-slide variability from slide E – H was observed.

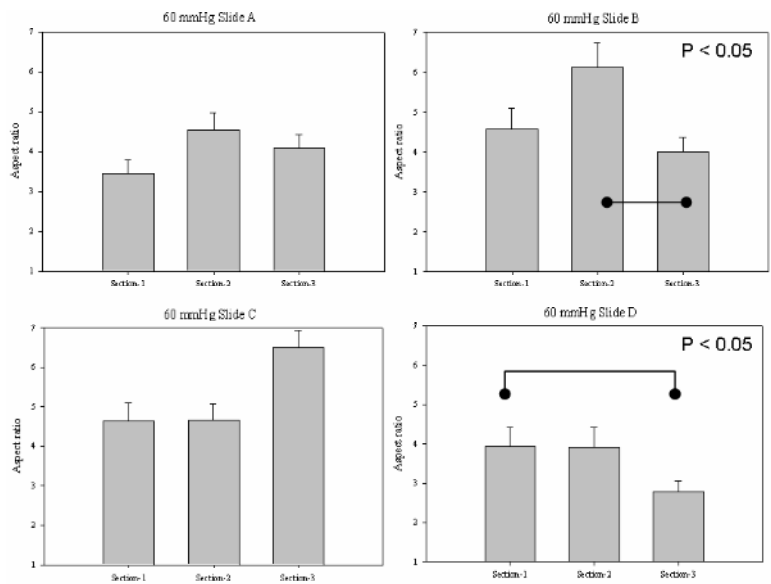


Figure D-9 Averaged VIC nuclei aspect ratio of specimen under 60 mmHg was measured, and intra-slide variability from slide A – D was observed.

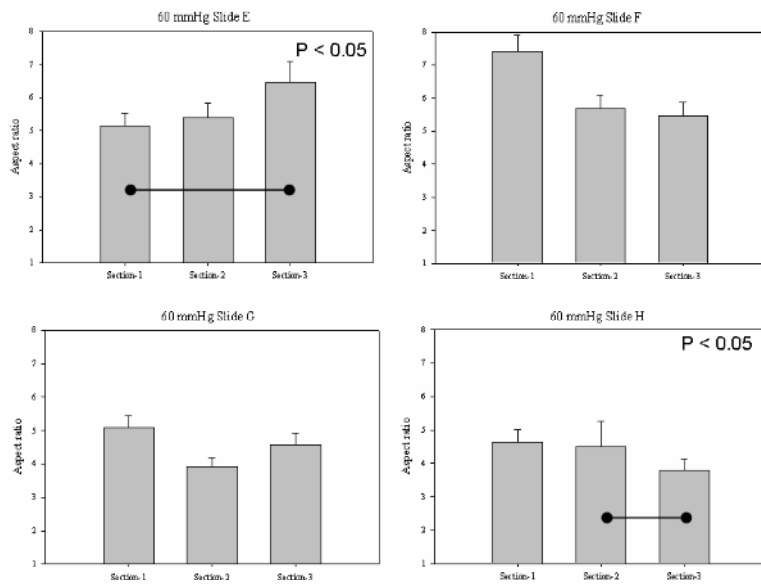


Figure D-10 Averaged VIC nuclei aspect ratio of specimen under 60 mmHg was measured, and intra-slide variability from slide E – H was observed.

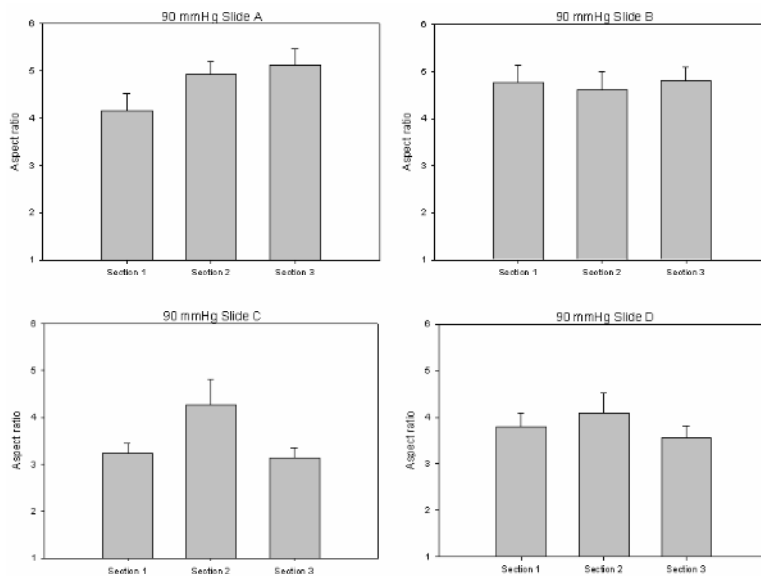


Figure D-11 Averaged VIC nuclei aspect ratio of specimen under 90 mmHg was measured, and no intra-slide variability from slide A – D was observed.

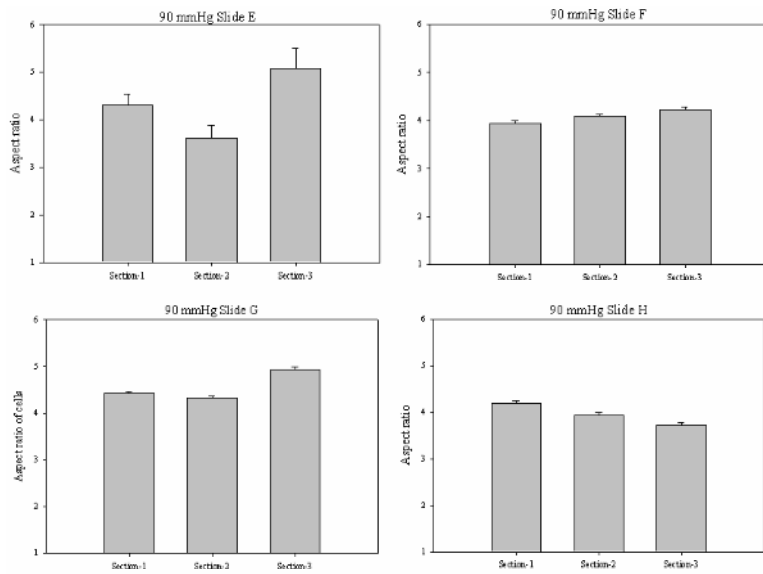


Figure D-12 Averaged VIC nuclei aspect ratio of specimen under 90 mmHg was measured, and no intra-slide variability from slide E – H was observed.

2. Bar-charts showed below indicating intra-pressure variability under 0, 1, 2, 4, 60 and 90 mmHg transvalvular pressures.

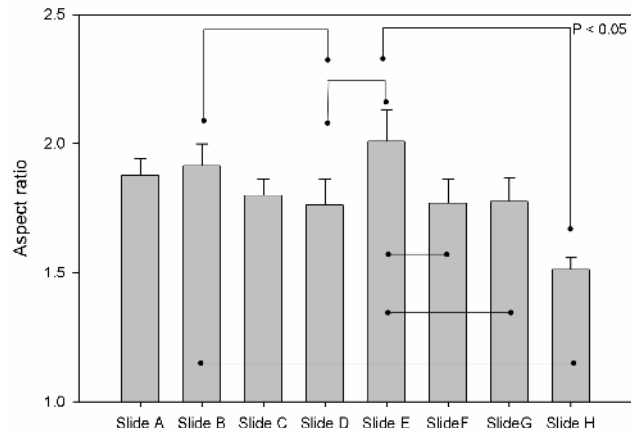


Figure D-13 Averaged VIC nuclei aspect ratio of specimen under 0 mmHg was measured, and intra-pressure variability from slide A – H was observed.

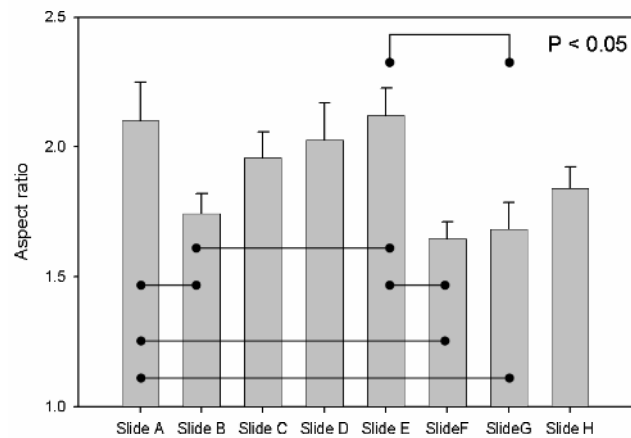


Figure D-14 Averaged VIC nuclei aspect ratio of specimen under 1 mmHg was measured, and intra-pressure variability from slide A – H was observed.

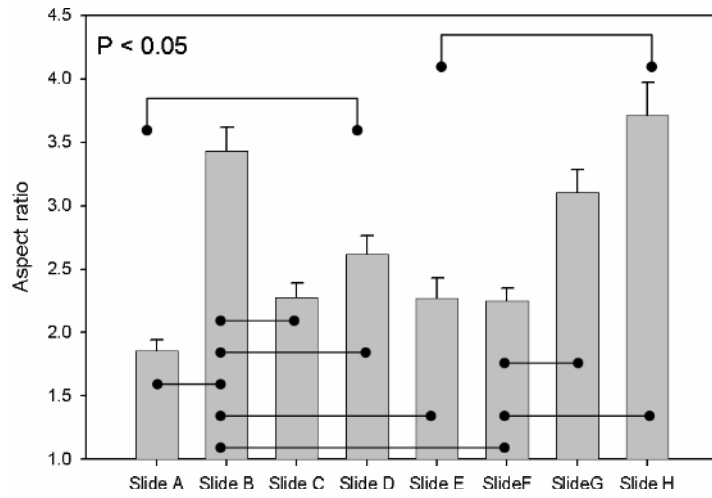


Figure D-15 Averaged VIC nuclei aspect ratio of specimen under 2 mmHg was measured, and intra-pressure variability from slide A – H was observed.

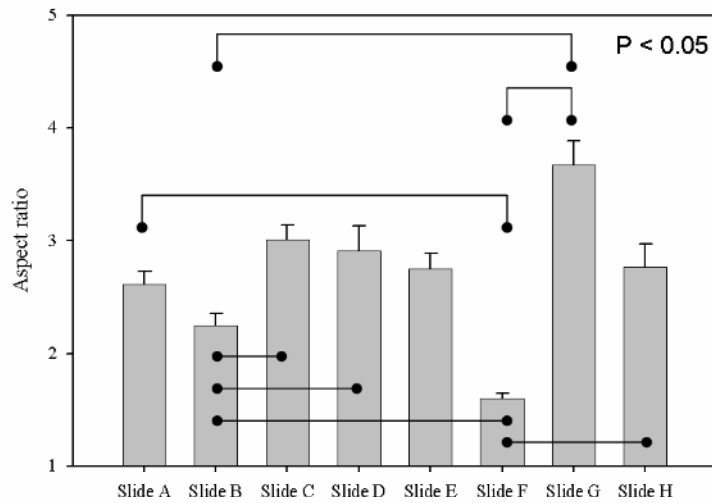


Figure D-16 Averaged VIC nuclei aspect ratio of specimen under 4 mmHg was measured, and intra-pressure variability from slide A – H was observed.

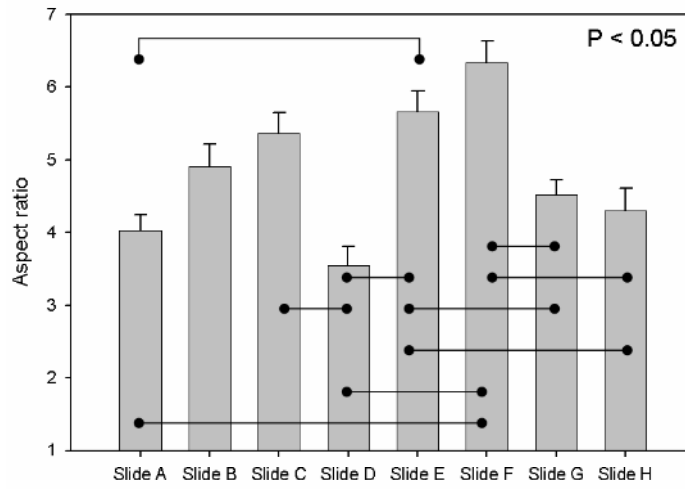


Figure D-17 Averaged VIC nuclei aspect ratio of specimen under 60 mmHg was measured, and intra-pressure variability from slide A – H was observed.

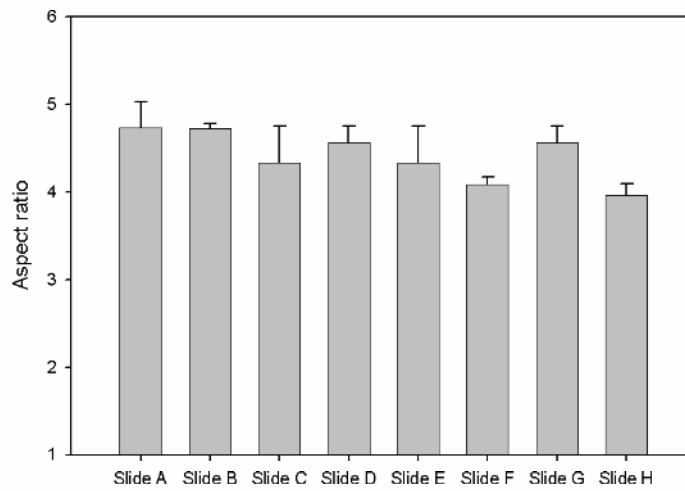


Figure D-18 Averaged VIC nuclei aspect ratio of specimen under 90 mmHg was measured, and no intra-pressure variability from slide A – H was observed.

APPENDIX E: CALCULATION OF NUCLEI ASPECT RATIOS

1. Results of the RVE model: LEHI circular VIC nuclei with elastic property, $E = 9 \times 10^{-2}$ MPa.

Table E-1 Calculation of major axis lengths in the circumferential, radial and transmural directions, calculation of aspect ratio and percent change in aspect ratio (%) under 1 – 90 mmHg.

	1 mmHg	2 mmHg	4 mmHg	60 mmHg	90 mmHg
a	7.5563	7.607	7.6922	8.576	8.607
b	7.6089	7.7225	7.9565	11.137	11.161
c	7.3376	6.981	6.891	4.4175	4.392
Aspect ratio	1.0298	1.1205	1.1167	1.9414	1.9597
Change in aspect ratio (%)	2.98 %	12.05 %	11.67 %	94.14 %	95.97 %

2. Results of the RVE model LEHI circular VIC nuclei with elastic property, $E = 9 \times 10^{-6}$ MPa.

Table E-2 Calculation of major axis lengths in the circumferential, radial and transmural directions, calculation of aspect ratio and percent change in aspect ratio (%) under 1 – 90 mmHg.

	1 mmHg	2 mmHg	4 mmHg	60 mmHg	90 mmHg
a	7.536	7.577	7.666	8.44	8.719
b	7.86	8.167	8.66	10.752	11.434
c	7.122	6.815	6.35	4.649	4.23
Aspect ratio	1.058	1.112	1.20656	1.8158	2.061
Change in aspect ratio (%)	5.8 %	11.22 %	20.65 %	81.58 %	106.1 %

3. Results of the RVE model: circular VIC nuclei with Neo-Hookean hyperelastic property, $G = 4 \times 10^{-4}$ MPa.

Table E-3 Calculation of major axis lengths in the circumferential, radial and transmural directions, calculation of aspect ratio and percent change in aspect ratio (%) under 1 – 90 mmHg.

	1 mmHg	2 mmHg	4 mmHg	60 mmHg	90 mmHg
a	7.538	7.58	7.668	8.576	8.719
b	7.852	8.158	8.643	11.133	11.431
c	7.125	6.824	6.368	4.42	4.245
Aspect ratio	1.0575	1.1105	1.2	1.94	2.05
Change in aspect ratio (%)	5.75 %	11.05 %	20 %	94 %	105 %

APPENDIX F: LOCAL MECHANICAL ENVIRONMENT OF VIC NUCLEI

1. Stress and strain distributions of the RVE model under 90 mmHg: circular LEHI VIC nuclei elastic moduli = 9×10^{-2} MPa.

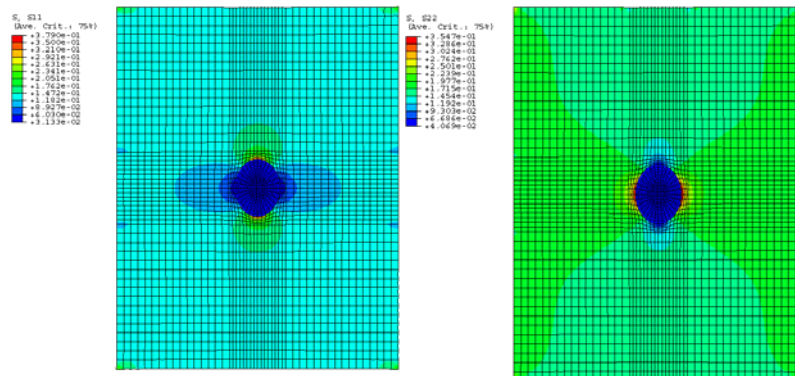


Figure F-1 Stress distributions (S11: left panel, and S22: right panel) of the RVE model in the circumferential and radial directions under 90 mmHg transvalvular pressures.

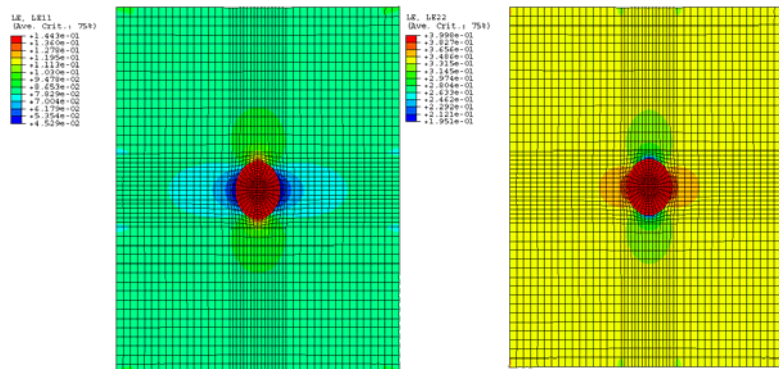


Figure F-2 Strain distributions (LE11: left panel, and LE22: right panel) of the RVE model in the circumferential and radial directions under 90 mmHg transvalvular pressures.

2. Stress and strain distributions of the RVE model under 90 mmHg: circular LEHI VIC nuclei with elastic moduli = 9×10^{-6} MPa.

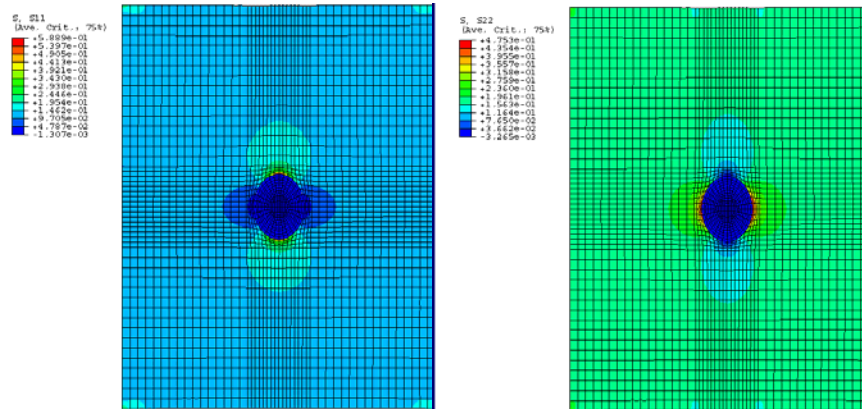


Figure F-3 Stress distributions (S11: left panel, and S22: right panel) of the RVE model in the circumferential and radial directions under 90 mmHg transvalvular pressures.

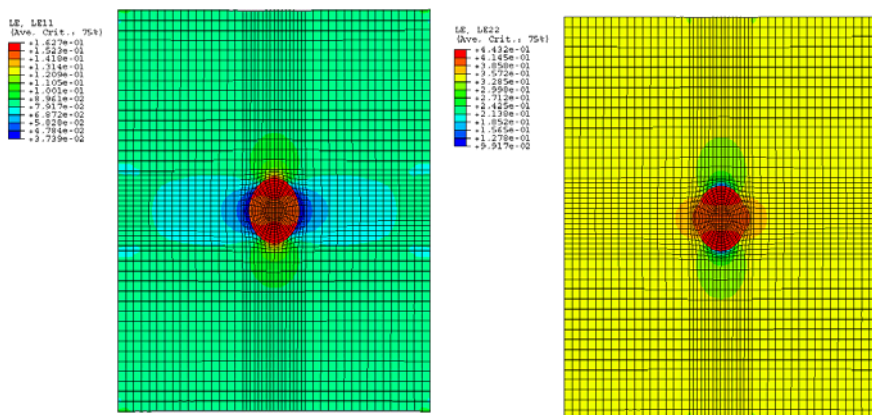


Figure F-4 Strain distributions (LE11: left panel, and LE22: right panel) of the RVE model in the circumferential and radial directions under 90 mmHg transvalvular pressures.

3. Stress and strain distributions of the RVE model under 90 mmHg: circular VIC nuclei with Neo-Hookean hyperelastic material property ($G = 4 \times 10^{-4}$ MPa).

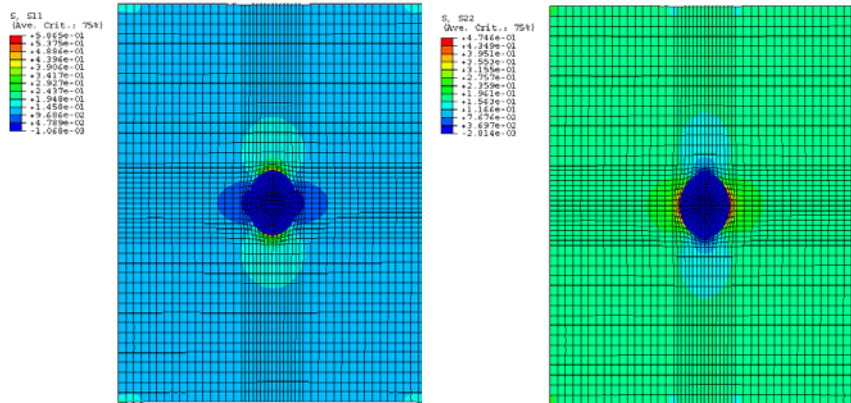


Figure F-5 Stress distributions (S11: left panel, and S22: right panel) of the RVE model in the circumferential and radial directions under 90 mmHg transvalvular pressures.

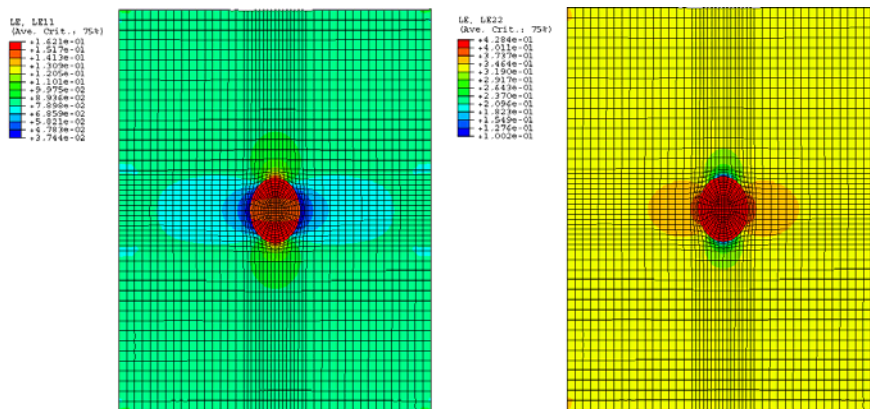


Figure F-6 Strain distributions (LE11: left panel, and LE22: right panel) of the RVE model in the circumferential and radial directions under 90 mmHg transvalvular pressures.

BIBLIOGRAPHY

1. Fisher, J., Whestley, D.J., Douglas, I., *et al.*, Failure Modes in Pericardial and Porcine Bioprostheses (Paris: Dr. A. Aneur, Communication Medicale, 1987).
2. Sacks, M.S. and Schoen, F.J., "Collagen fiber disruption occurs independent of calcification in clinically explanted bioprosthetic heart valves," *Journal of Biomedical Materials Research*, (2002).
3. Sacks, M.S., "The Biomechanical Effects of Fatigue on the Porcine Bioprosthetic Heart Valve," *Journal of Long-Term Effects of Medical Implants*, Vol. 11, (2001), pp. 231-247.
4. Schoen, F.J. and Levy, R.J., "Founder's Award, 25th Annual Meeting of the Society for Biomaterials, perspectives. Providence, RI, April 28-May 2, 1999. Tissue heart valves: current challenges and future research perspectives," *J Biomed Mater Res*, Vol. 47, No. 4. (1999), pp. 439-465.
5. "Hurst's The Heart Arteries and Veins, by Alexander, R.W., Schilant, R.C., and Fuster, V." (9th edition; New York: McGraw-Hill, 1998).
6. Sutton, J.P., 3rd, Ho, S.Y., and Anderson, R.H., "The forgotten interleaflet triangles: a review of the surgical anatomy of the aortic valve," *Ann Thorac Surg*, Vol. 59, No. 2. (1995), pp. 419-427.
7. Thubrikar, M., *The aortic valve* (Boca Raton: CRC Press, Inc., 1990).
8. Keele, K.D., *Leonardo da Vinci on movement of the heart and blood* (London: Harvey and Blythe, 1952).
9. Henderson, Y. and Johnson, F.E., "Two models of closure of the heart valves," *Heart*, Vol. 4, (1912), p. 69.
10. Bellhouse, B.J., *The fluid mechanics of the aortic valve*, in *Biological tissue in heart valve replacement*, Ionescu, M.I., *et al.*, Editors. 1972, Butterworths: London.

11. Thubrikar, M., Piepgrass, W.C., Deck, J.D., *et al.*, "Stresses of natural versus prosthetic aortic valve leaflets in vivo," *Ann Thorac Surg*, Vol. 30, No. 3. (1980), pp. 230-239.
12. Yearwood, T.L., Misbach, G.A., and Chandran, K.B., "Experimental fluid dynamics of aortic stenosis in a model of the human aorta," *Clin Phys Physiol Meas*, Vol. 10, No. 1. (1989), pp. 11-24.
13. Burwash, I.G., Thomas, D.D., Sadahiro, M., *et al.*, "Dependence of Gorlin formula and continuity equation valve areas on transvalvular volume flow rate in valvular aortic stenosis," *Circulation*, Vol. 89, No. 2. (1994), pp. 827-835.
14. ANTONINI-CANTERIN, F., FAGGIANO, P., ZANUTTINI, D., *et al.*, "Is aortic valve resistance more clinically meaningful than valve area in aortic stenosis?," *Heart*, Vol. 82, No. 1. (1999), pp. 9-10.
15. Gross, L. and Kugel, M.A., "Topographical anatomy and histology of the valves in the human heart," *Am J Pathol*, Vol. 7, (1931), pp. 225-276.
16. Thubrikar, M.J., Aouad, J., and Nolan, S.P., "Comparison of the in vivo and in vitro mechanical properties of aortic valve leaflets," *J Thorac Cardiovasc Surg*, Vol. 92, No. 1. (1986), pp. 29-36.
17. Lo, D. and Vesely, I., "Biaxial strain analysis of the porcine aortic valve," *Ann Thorac Surg*, Vol. 60, No. 2 Suppl. (1995), pp. S374-378.
18. Vesely, I. and Boughner, D., "Analysis of the bending behavior of porcine xenograft leaflets and of neutral aortic valve material: bending stiffness, neutral axis and shear measurements," *J Biomech*, Vol. 22, No. 6-7. (1989), pp. 655-671.
19. Billiar, K.L. and Sacks, M.S., "Biaxial Mechanical Properties of the Natural and Glutaraldehyde Treated Aortic Valve Cusp-Part I: Experimental Results," *Journal of Biomechanical Engineering: Transactions of the ASME*, Vol. 122, (2000), pp. 23-30.
20. Sacks, M.S., *Biaxial mechanical behavior of fixed bovine pericardium*, in *Proceedings of the 5th World Biomaterials Congress*. 1996.
21. Proceedings of the 11th Conference Engineering, Engineering Mechanics Division/ASCE, "Biaxial mechanical behavior of bovine pericardium as a bioprosthetic material", by Sacks, M.S., pp. 200-203, 1996.
22. Sacks, M.S., "Biaxial mechanical evaluation of planar biological materials," *Journal of Elasticity*, Vol. 61, (2000), pp. 199-246.

23. Sun, W., Sacks, M.S., Sellaro, T.L., *et al.*, "Biaxial mechanical response of bioprosthetic heart valve biomaterials to high in-plane shear," *J Biomech Eng*, Vol. 125, No. 3. (2003), pp. 372-380.
24. Sacks, M.S. and Sun, W., "Multiaxial mechanical behavior of biological materials," *Annu Rev Biomed Eng*, Vol. 5, (2003), pp. 251-284.
25. Christie, G.W., "Anatomy of aortic heart valve leaflets: the influence of glutaraldehyde fixation on function," *Eur J Cardiothorac Surg*, Vol. 6 Suppl 1, (1992), pp. S25-32; discussion S33.
26. Deck, J.D., "Endothelial cell orientation on aortic valve leaflets," *Cardiovasc Res*, Vol. 20, No. 10. (1986), pp. 760-767.
27. Lupu, F. and Simionescu, M., "Organization of the intercellular junctions in the endothelium of cardiac valves," *J Submicrosc Cytol*, Vol. 17, No. 2. (1985), pp. 119-132.
28. Leask, R.L., Jain, N., and Butany, J., "Endothelium and valvular diseases of the heart," *Microsc Res Tech*, Vol. 60, No. 2. (2003), pp. 129-137.
29. Sacks, M.S., Smith, D.B., and Hiester, E.D., "The aortic valve microstructure: effects of transvalvular pressure," *J Biomed Mater Res*, Vol. 41, No. 1. (1998), pp. 131-141.
30. Filip, D.A., Radu, A., and Simionescu, M., "Interstitial cells of the heart valves possess characteristics similar to smooth muscle cells," *Circ Res*, Vol. 59, No. 3. (1986), pp. 310-320.
31. Messier, R.H., Jr., Bass, B.L., Aly, H.M., *et al.*, "Dual structural and functional phenotypes of the porcine aortic valve interstitial population: characteristics of the leaflet myofibroblast," *J Surg Res*, Vol. 57, No. 1. (1994), pp. 1-21.
32. Mulholland, D.L. and Gotlieb, A.I., "Cell biology of valvular interstitial cells," *Can J Cardiol*, Vol. 12, No. 3. (1996), pp. 231-236.
33. Roy, A., Brand, N.J., and Yacoub, M.H., "Molecular characterization of interstitial cells isolated from human heart valves," *J Heart Valve Dis*, Vol. 9, No. 3. (2000), pp. 459-464; discussion 464-455.
34. Taylor, P.M., Batten, P., Brand, N.J., *et al.*, "The cardiac valve interstitial cell," *Int J Biochem Cell Biol*, Vol. 35, No. 2. (2003), pp. 113-118.
35. Weston, M.W., LaBorde, D.V., and Yoganathan, A.P., "Estimation of the shear stress on the surface of an aortic valve leaflet," *Ann Biomed Eng*, Vol. 27, No. 4. (1999), pp. 572-579.

36. Weston, M.W. and Yoganathan, A.P., "Biosynthetic activity in heart valve leaflets in response to in vitro flow environments," *Ann Biomed Eng*, Vol. 29, No. 9. (2001), pp. 752-763.
37. Rodriguez-Niedenfuhr, M., Papoutsis, M., Christ, B., *et al.*, "Prox1 is a marker of ectodermal placodes, endodermal compartments, lymphatic endothelium and lymphangioblasts," *Anat Embryol (Berl)*, Vol. 204, No. 5. (2001), pp. 399-406.
38. Dare, A.J., Veinot, J.P., Edwards, W.D., *et al.*, "New observations on the etiology of aortic valves disease: a surgical pathologic study of 236 cases from 1990," *Hum Pathol*, Vol. 24, (1993), pp. 1330-1338.
39. Freeman, W.K., Schaff, H.V., and Orszulak, T.A., "Ultrasonic aortic valve decalcification: serial Doppler echocardiographic follow-up," *J Am Coll Cardiol*, Vol. 16, (1990), pp. 623-630.
40. McBride, L.R., Naunheim, K.S., and Fiore, A.C., "Aortic Valve decalcification," *J Thorac Cardiovasc Surg*, Vol. 100, (1990), pp. 36-42.
41. Bernal, J.M., Fernandez-Vals, M., Rabasa, J.M., *et al.*, "Repair of nonsevere rheumatic aortic valve disease during other valvular procedures: is it safe?," *J Thorac Cardiovasc Surg*, Vol. 115, No. 5. (1998), pp. 1130-1135.
42. Harken, D.E., Taylor, W.J., Lefemine, A.A., *et al.*, "Aortic valve replacement with a caged ball valve," *Am J Cardiol*, Vol. 9, (1962), pp. 292-299.
43. Harken, D., Soroff, H.S., and Taylor, W.J., "Partial and complete prosthesis in aortic insufficiency," *J Thorac Cardiovasc Surg*, Vol. 40, (1960), pp. 744-762.
44. Bjork, V.O., "A new tilting disc valve prosthesis," *Scand J Thorac Cardiovasc Surg*, Vol. 3, (1969), pp. 1-10.
45. Schoen, F., Levy, R., and Piehler, H., "Pathological Considerations in Replacement Cardiac Valves," *Cardiovascular Pathology*, Vol. 1, No. 1. (1992), pp. 29-52.
46. Schoen, F.J., *Modes of Failure and other Pathology of Mechanical and Tissue Heart Valve Prostheses*, in *Replacement Cardiac Valves*, Bondar, E. and Frater, R., Editors. 1991, Pergamon Press: New York. p. 99-124.
47. Jamieson, W.R.E., Gallucci, V., Thiene, G., *et al.*, *Porcine Valves*, in *Replacement Heart Valves*, Bondar, E. and Frater, R., Editors. 1991, Replacement Cardiac Valves: New York. p. 229-275.
48. Rizzoli, G., Bottio, T., Thiene, G., *et al.*, "Long-term durability of the Hancock II porcine bioprosthesis," *J Thorac Cardiovasc Surg*, Vol. 126, No. 1. (2003), pp. 66-74.

49. Schoen, F.J., Collins, J.J., and Cohn, L.H., "Long-term failure rate and morphologic correlations in porcine bioprosthetic heart valves," *Am J Cardiol*, Vol. 51, (1983), p. 957.
50. Schoen, F.J. and Levy, R.J., *Calcification of Bioprosthetic Heart Valves*, in *Replacement Cardiac Valves*, Bondar, E. and Frater, R., Editors. 1991, Pergamon Press: New York. p. 125-148.
51. Vyavahare, N., Ogle, M., Schoen, F.J., *et al.*, "Mechanisms of Bioprosthetic Heart Valve failure: Fatigue Causes Collagen Denaturation and Glycosaminoglycan Loss," *Journal of Biomedical Materials Research*, Vol. 46, (1999), pp. 44-50.
52. Ellsmere, J.C., Khanna, R.A., and Lee, J.M., "Mechanical loading of bovine pericardium accelerates enzymatic degradation," *Biomaterials*, Vol. 20, No. 12. (1999), pp. 1143-1150.
53. Vesely, I. and Noseworthy, R., "Micro mechanics of the Fibrosa and the Ventricularis in Aortic Valve Leaflets," *J Biomech*, Vol. 25, No. 1. (1992), pp. 101-113.
54. Haziza, F., Papouin, G., Barratt-Boyes, B., *et al.*, "Tears in bioprosthetic heart valve leaflets without calcific degeneration," *J Heart Valve Dis*, Vol. 5, No. 1. (1996), pp. 35-39.
55. Walley, V.M., Aul, S., and Keon, W.J., *Primary Failure Due to Tears in Standard-Profile Ionescu-Shiley Cardiac Valve Bioprostheses*, in *Calcification and Degeneration of Heart Valve Bioprostheses*, Gabbay, S. and Cabrol, C., Editors. 1987, Dr. A. Ameur Communication Medicale: Paris. p. 119-128.
56. Sacks, M.S., Smith, D.B., and Hiester, E.D., "A small angle light scattering device for planar connective tissue microstructural analysis," *Ann Biomed Eng*, Vol. 25, No. 4. (1997), pp. 678-689.
57. "Valvular Heart Disease, by Otto, C.M." (1st edition; Philadelphia: W. B. Saunders Company, 1999), p.^pp. Pages.
58. Deiwick, M., Glasmacher, B., Pettenazzo, E., *et al.*, "Primary tissue failure of bioprostheses: new evidence from in vitro tests," *Thorac Cardiovasc Surg*, Vol. 49, No. 2. (2001), pp. 78-83.
59. Levy, R., Schoen, F., Levy, J., *et al.*, "Biologic determinants of dystrophic calcification and osteocalcin deposition in glutaraldehyde-preserved porcine aortic valve leaflets implanted subcutaneously in rats," *American Journal of Pathology*, Vol. 113, (1983), pp. 143-155.

60. Thubrikar, M.J., Deck, J.D., Aouad, J., *et al.*, "Role of mechanical stress in calcification of aortic bioprosthetic valves," *J Thorac Cardiovasc Surg*, Vol. 86, No. 1. (1983), pp. 115-125.
61. De Biasi, S., Pilotto, F., and Pozzoni, F., "The glutaraldehyde-treated porcine aortic valve. A study of the leaflets' mechanical properties," *Int J Artif Organs*, Vol. 3, No. 5. (1980), pp. 271-276.
62. Purinya, B., Kasyanov, V., Volkolakov, J., *et al.*, "Biomechanical and structural properties of the explanted bioprosthetic valve leaflets," *J Biomech*, Vol. 27, No. 1. (1994), pp. 1-11.
63. Vesely, I., "A mechanism for the decrease in stiffness of bioprosthetic heart valve tissues after cross-linking," *ASAIO J*, Vol. 42, No. 6. (1996), pp. 993-999.
64. Courtman, D.W., Pereira, C.A., Omar, S., *et al.*, "Biomechanical and ultrastructural comparison of cryopreservation and a novel cellular extraction of porcine aortic valve leaflets," *J Biomed Mater Res*, Vol. 29, No. 12. (1995), pp. 1507-1516.
65. Adamczyk, M.M., Lee, T.C., and Vesely, I., "Biaxial strain properties of elastase-digested porcine aortic valves," *J Heart Valve Dis*, Vol. 9, No. 3. (2000), pp. 445-453.
66. Gloeckner, D.C., Billiar, K.L., and Sacks, M.S., "Effects of Mechanical Fatigue on the Bending Properties of the Porcine Bioprosthetic Heart Valve," *American Society for Artificial Internal Organs (ASAIO)*, Vol. 45, (1999), pp. 59-63.
67. Frisch-Fay, R., *Flexible Bars* (Washington: Butter Worths, 1962).
68. Sacks, M.S., Gloeckner, D.C., Vyavahare, N., *et al.*, "Alterations in the Flexural Behavior of Porcine Bioprosthetic Heart Valves with Fatigue," *Journal of Heart Valve Disease*, (2002).
69. Broom, N.D., "The Stress/Strain and Fatigue Behavior of Glutaraldehyde Preserved Heart-Valve Tissue," *Journal of Biomechanics*, Vol. 10, (1977), pp. 707-724.
70. Vesely, I., Boughner, D.R., and Leeson-Dietrich, J., "Bioprosthetic valve tissue viscoelasticity: implications on accelerated pulse duplicator testing," *Ann Thorac Surg*, Vol. 60, No. 2 Suppl. (1995), pp. S379-382; discussion S383.
71. Vyavahare, N., Ogle, M., Schoen, F.J., *et al.*, "Mechanisms of bioprosthetic heart valve failure: fatigue causes collagen denaturation and glycosaminoglycan loss," *J Biomed Mater Res*, Vol. 46, No. 1. (1999), pp. 44-50.
72. Sacks, M.S. and Smith, D.B., "Effects of Accelerated Testing on Porcine Bioprosthetic Heart Valve Fiber Architecture," *Biomaterials*, Vol. 19, (1998), pp. 1027-1036.

73. Rabkin, E. and Schoen, F.J., "Cardiovascular tissue engineering," *Cardiovasc Pathol*, Vol. 11, No. 6. (2002), pp. 305-317.
74. Stock, U.A., Vacanti, J.P., Mayer, J.E., *et al.*, "Tissue Engineering of Heart Valves-Current Aspects," *Thoracic Cardiovascular Surgery*, Vol. 50, (2002), pp. 184-193.
75. Schoen, F.J. and Levy, R.J., "Pathology of substitute heart valves: new concepts and developments," *J Card Surg*, Vol. 9, No. 2 Suppl. (1994), pp. 222-227.
76. Jansson, K., Bengtsson, L., Swedenborg, J., *et al.*, "In vitro endothelialization of bioprosthetic heart valves provides a cell monolayer with proliferative capacities and resistance to pulsatile flow," *J Thorac Cardiovasc Surg*, Vol. 121, No. 1. (2001), pp. 108-115.
77. Trantina-Yates, A.E., Human, P., Bracher, M., *et al.*, "Mitigation of bioprosthetic heart valve degeneration through biocompatibility: in vitro versus spontaneous endothelialization," *Biomaterials*, Vol. 22, No. 13. (2001), pp. 1837-1846.
78. Tran, H.S., Puc, M.M., Hewitt, C.W., *et al.*, "Diamond-like carbon coating and plasma or glow discharge treatment of mechanical heart valves," *J Invest Surg*, Vol. 12, No. 3. (1999), pp. 133-140.
79. Bengtsson, L.A. and Haegerstrand, A.N., "Endothelialization of mechanical heart valves in vitro with cultured adult human cells," *J Heart Valve Dis*, Vol. 2, No. 3. (1993), pp. 352-356.
80. Zhu, L., Williams, W.G., Bellhouse, B., *et al.*, "Effective endothelialization of polyurethane surfaces. Response to shear stress and platelet adhesion," *ASAIO Trans*, Vol. 36, No. 4. (1990), pp. 811-816.
81. Langer, R. and Vacanti, J.P., "Tissue engineering," *Science*, Vol. 260, No. 5110. (1993), pp. 920-926.
82. Hoerstrup, S.P., Sodian, R., Daebritz, S., *et al.*, "Functional living trileaflet heart valves grown in vitro," *Circulation*, Vol. 102, No. 19 Suppl 3. (2000), pp. III44-49.
83. Mol, A., Bouten, C.V., Zund, G., *et al.*, "The relevance of large strains in functional tissue engineering of heart valves," *Thorac Cardiovasc Surg*, Vol. 51, No. 2. (2003), pp. 78-83.
84. Engelmayer, G.C., Hildebrand, D.K., Sutherland, F.W., *et al.*, "A novel bioreactor for the dynamic flexural stimulation of tissue engineered heart valve biomaterials," *Biomaterials*, Vol. 24, No. 14. (2003), pp. 2523-2532.
85. O'Brien, M.F., Goldstein, S., Walsh, S., *et al.*, "The SynerGraft valve: a new acellular (nonglutaraldehyde-fixed) tissue heart valve for autologous recellularization first

- experimental studies before clinical implantation," *Semin Thorac Cardiovasc Surg*, Vol. 11, No. 4 Suppl 1. (1999), pp. 194-200.
86. Simon, P., Kasimir, M.T., Seebacher, G., *et al.*, "Early failure of the tissue engineered porcine heart valve SYNERGRAFT in pediatric patients," *Eur J Cardiothorac Surg*, Vol. 23, No. 6. (2003), pp. 1002-1006; discussion 1006.
 87. Weinberg, C.B. and Bell, E., "A blood vessel model constructed from collagen and cultured vascular cells," *Science*, Vol. 231, No. 4736. (1986), pp. 397-400.
 88. Niklason, L.E., Gao, J., Abbott, W.M., *et al.*, "Functional arteries grown in vitro," *Science*, Vol. 284, No. 5413. (1999), pp. 489-493.
 89. Bertipaglia, B., Ortolani, F., Petrelli, L., *et al.*, "Cell characterization of porcine aortic valve and decellularized leaflets repopulated with aortic valve interstitial cells: the VESALIO Project (Vitalitate Exornatum Succedaneum Aorticum Labore Ingenioso Obtenibitur)," *Ann Thorac Surg*, Vol. 75, No. 4. (2003), pp. 1274-1282.
 90. Dvorin, E.L., Wylie-Sears, J., Kaushal, S., *et al.*, "Quantitative evaluation of endothelial progenitors and cardiac valve endothelial cells: proliferation and differentiation on poly-glycolic acid/poly-4-hydroxybutyrate scaffold in response to vascular endothelial growth factor and transforming growth factor beta1," *Tissue Eng*, Vol. 9, No. 3. (2003), pp. 487-493.
 91. Perry, T.E., Kaushal, S., Nasser, B., *et al.*, "Peripheral blood as a cell source for tissue engineering heart valves," *Surgical Forum*, Vol. LII, (2001), pp. 99-101.
 92. Wells, S.M. and Sacks, M.S., "Effects of fixation pressure on the biaxial mechanical behavior of porcine bioprosthetic heart valves with long-term cyclic loading," *Biomaterials*, Vol. 23, No. 11. (2002), pp. 2389-2399.
 93. Jockenhoevel, S., Zund, G., Hoerstrup, S.P., *et al.*, "Cardiovascular tissue engineering: a new laminar flow chamber for in vitro improvement of mechanical tissue properties," *Asaio J*, Vol. 48, No. 1. (2002), pp. 8-11.
 94. O'Callaghan, C.J. and Williams, B., "Mechanical strain-induced extracellular matrix production by human vascular smooth muscle cells: role of TGF-beta(1)," *Hypertension*, Vol. 36, No. 3. (2000), pp. 319-324.
 95. ASME, Bioengineering, "Nonlinear Finite Element Modeling of Cell Mechanical Environment in Hydrogels for Intervertebral Disc Repair", by Baer, A., E., Grinstaff, M.W., Smeds, K.A., *et al.*, pp. 113-114, 2001.
 96. ASME, Bioengineering, "A Finite-Deformation, Anisotropic, Biphasic Finite element Model of Cell-Matrix Interactions in the Intervertebral Disc", by Baer, A., E., Laursen, T.A., and Setton, L., A., pp. 799-800, 2001.

97. Baer, A.E. and Setton, L.A., "The Micromechanical Environment of Intervertebral Disc Cells: Effect of Matrix Anisotropy and Cell Geometry Predicted by a Linear Model," *Journal of Biomechanical Engineering: Transactions of the ASME*, Vol. 122, (2000), pp. 245-251.
98. Guilak, F. and Mow, V.C., "The Mechanical Environment of the Chondrocyte: A Biphasic Finite Element Model of Cell-Matrix Interactions in Articular Cartilage," *Journal of Biomechanics*, Vol. 33, (2000), pp. 1663-1673.
99. Baer, A.E., Laursen, T.A., Guilak, F., *et al.*, "The micromechanical environment of intervertebral disc cells determined by a finite deformation, anisotropic, and biphasic finite element model," *J Biomech Eng*, Vol. 125, No. 1. (2003), pp. 1-11.
100. Kouznetsova, V., Brekelmans, W.A.M., and Baaijens, F.P.T., "An Approach to Micro-Macro Modeling of Heterogeneous Materials," *Computational Mechanics*, Vol. 27, (2001), pp. 37-48.
101. Bouten, C.V.C., Knight, M.M., Lee, D.A., *et al.*, "Compressive Deformation and Damage of Muscle Cell Subpopulations in a Model System," *Annals of Biomedical Engineering*, Vol. 29, No. 2. (2001), pp. 153-163.
102. Hill, R., "Elastic properties of reinforced solids: some theoretical principles," *J. Mech. Phys. Solids*, Vol. 11, (1963), pp. 357-372.
103. Kanit, T., Forest, S., Galliet, I., *et al.*, "Determination of the size of the representative volume element for random composites: statistical and numerical approach," *International Journal of Solids and Structures*, Vol. 40, (2003), pp. 3647-3679.
104. Agoram, B. and Barocas, V.H., "Coupled Macroscopic and Microscopic Scale Modeling of Fibrillar Tissue and Tissue Equivalents," *Journal of Biomechanical Engineering: Transactions of the ASME*, Vol. 123, (2001), pp. 362-369.
105. Barocas, V.H. and Tranquillo, R.T., "A Finite Element Solution for the anisotropic Biphasic theory of Tissue-Equivalent Mechanics: The Effect of Contact Guidance on Isometric Cell Traction Measurement," *Journal of Biomechanical Engineering*, Vol. 119, (1997), pp. 261-268.
106. Barocas, V.H. and Tranquillo, R.T., "An Anisotropic Biphasic Theory of Tissue-Equivalent Mechanics: The Interplay Among Cell Traction, Fibrillar Network Deformation, fibril Alignment, and Cell Contact Guidance," *Journal of Biomechanical Engineering*, Vol. 119, (1997), pp. 137-145.
107. Breuls, R.G.M., Sengers, B.G., Oomens, C.W.J., *et al.*, "Predicting Local Cell Deformations in Engineered Tissue Constructs: A Multilevel Finite Element Approach," *Journal of Biomechanical Engineering*, Vol. 124, (2002), pp. 198-204.

108. Breuls, R.G., Sengers, B.G., Oomens, C.W., *et al.*, "Predicting local cell deformations in engineered tissue constructs: a multilevel finite element approach," *J Biomech Eng*, Vol. 124, No. 2. (2002), pp. 198-207.
109. Wakatsuki, T., Kolodney, M.S., Zahalak, G.I., *et al.*, "Cell Mechanics Studied by a Reconstituted Model Tissues," *Biophysical Journal*, Vol. 79, (2000), pp. 2353-2368.
110. Zahalak, G.I., Wagenseil, J.E., Wakatsuki, T., *et al.*, "A Cell-Based constitutive Relation for Bio-Artificial Tissues," *Biophysical Journal*, Vol. 79, (2000), pp. 2369-2381.
111. Lanir, Y., "A Structural Theory for the Homogeneous Biaxial Stress-Strain Relationships in Flat Collagenous Tissues," *Journal of Biomechanics*, Vol. 12, (1979), pp. 423-436.
112. Lanir, Y., "Plausibility of Structural Constitutive Equations for Isotropic soft Tissue in Finite Static Deformations," *Journal of Applied Mechanics*, Vol. 61, (1994), pp. 695-702.
113. Lanir, Y., "Constitutive Equations for Fibrous Connective Tissues," *Journal of Biomechanics*, Vol. 16, (1983), pp. 1-12.
114. Horowitz, A., Lanir, Y., Yin, F.C.P., *et al.*, "Structural Three Dimensional Constitutive Law for the Passive Myocardium," *Journal of Biomechanical Engineering*, Vol. 110, (1988), pp. 200-207.
115. Driessen, N.J.B., Peters, G.W.M., Huyghe, J.M., *et al.*, "Remodelling of continuously distributed collagen fibres in soft connective tissues," *Journal of Biomechanics*, Vol. 36, No. 8. (2003), pp. 1151-1158.
116. Billiar, K.L. and Sacks, M.S., "Biaxial Mechanical Properties of Native and Glutaraldehyde Treated Aortic Valve Cusps. Part II-A Structurally Guided Constitutive Model," *Journal of Biomechanical Engineering: Transactions of the ASME*, Vol. 122, No. 4. (2000), pp. 327-335.
117. Lanir, Y., "Plausibility of structural constitutive equations for swelling tissues-implications of the C-N and S-E conditions," *J Biomech Eng*, Vol. 118, No. 1. (1996), pp. 10-16.
118. Lanir, Y., O., L., and O., I., "Optimal Design of Biaxial Tests for Structural Material characterization of Flat Tissues," *Journal of Biomechanical Engineering*, Vol. 118, (1996), pp. 41-47.
119. Sacks, M.S., Smith, D.B., and Hiester, E.D., "A Small Angle Light Scattering Device for Planar Connective Tissue Microstructural Analysis," *Ann Biomed Eng*, Vol. 25, No. 4. (1997), pp. 678-689.

120. Grande-Allen, K.J., Cochran, R.P., Reinhall, P.G., *et al.*, "Re-creation of sinuses is important for sparing the aortic valve: a finite element study," J Thorac Cardiovasc Surg, Vol. 119, No. 4 Pt 1. (2000), pp. 753-763.
121. Grande-Allen, K.J., Cochran, R.P., Reinhall, P.G., *et al.*, "Mechanisms of aortic valve incompetence: finite-element modeling of Marfan syndrome," J Thorac Cardiovasc Surg, Vol. 122, No. 5. (2001), pp. 946-954.
122. Grande-Allen, K.J., Cochran, R.P., Reinhall, P.G., *et al.*, "Finite-element analysis of aortic valve-sparing: influence of graft shape and stiffness," IEEE Trans Biomed Eng, Vol. 48, No. 6. (2001), pp. 647-659.
123. Grande, K.J., Cochran, R.P., Reinhall, P.G., *et al.*, "Mechanisms of aortic valve incompetence: finite element modeling of aortic root dilatation," Ann Thorac Surg, Vol. 69, No. 6. (2000), pp. 1851-1857.
124. Grande, K.J., Cochran, R.P., Reinhall, P.G., *et al.*, "Stress variations in the human aortic root and valve: the role of anatomic asymmetry," Ann Biomed Eng, Vol. 26, No. 4. (1998), pp. 534-545.
125. Gnyaneshwar, R., Kumar, R.K., and Balakrishnan, K.R., "Dynamic analysis of the aortic valve using a finite element model," The Annals of Thoracic Surgery, Vol. 73, No. 4. (2002), pp. 1122-1129.
126. De Hart, J., Peters, G.W., Schreurs, P.J., *et al.*, "A three-dimensional computational analysis of fluid-structure interaction in the aortic valve," J Biomech, Vol. 36, No. 1. (2003), pp. 103-112.
127. Carew, E.O., Talman, E.A., Boughner, D.R., *et al.*, "Quasi-Linear Voice Theory Applied to Internal Shearing of Porcine Aortic Valve Leaflets," Journal of Biomechanical Engineering: Transactions of the ASME, Vol. 121, (1999), pp. 386-392.
128. Chew, G.G., Howard, I.C., and Patterson, E.A., "Simulation of damage in a porcine prosthetic heart valve," J Med Eng Technol, Vol. 23, No. 5. (1999), pp. 178-189.
129. Krucinski, S., Vesely, I., Dokainish, M.A., *et al.*, "Numerical simulation of leaflet flexure in bioprosthetic valves mounted on rigid and expansible stents," J Biomech, Vol. 26, No. 8. (1993), pp. 929-943.
130. Thornton, M.A., Howard, I.C., and Patterson, E.A., "Three-dimensional stress analysis of polypropylene leaflets for prosthetic heart valves," Med Eng Phys, Vol. 19, No. 6. (1997), pp. 588-597.

131. Patterson, E.A., Howard, I.C., and Thornton, M.A., "A comparative study of linear and nonlinear simulations of the leaflets in a bioprosthetic heart valve during the cardiac cycle," *J Med Eng Technol*, Vol. 20, No. 3. (1996), pp. 95-108.
132. Burriesci, G., Howard, I.C., and Patterson, E.A., "Influence of anisotropy on the mechanical behaviour of bioprosthetic heart valves," *J Med Eng Technol*, Vol. 23, No. 6. (1999), pp. 203-215.
133. Einstein, D.R., Reinhall, P., Nicosia, M., *et al.*, "Dynamic finite element implementation of nonlinear, anisotropic hyperelastic biological membranes," *Comput Methods Biomech Biomed Engin*, Vol. 6, No. 1. (2003), pp. 33-44.
134. Humphrey, J.D., *Cardiovascular solid Mechanics: Cells, Tissues and Organs* (New York: Springer, 2001).
135. Thubrikar, M. and Eppink, R.T., "A method for analysis of bending and shearing deformations in biological tissue," *Journal of Biomechanics*, Vol. 15, (1982), pp. 529-535.
136. Vesely, I. and Noseworthy, R., "Micromechanics of the fibrosa and the ventricularis in aortic valve leaflets," *Journal of Biomechanics*, Vol. 25, No. 1. (1992), pp. 101-113.
137. Fung, Y.C., *Biomechanics: mechanical properties of living tissues*. (2nd edition; New York: Springer Verlag, 1993).
138. Yu, Q., Zhou, J., and Fung, Y., "Neutral axis location in bending and Young's modulus of different layers of the arterial wall," *American Journal of Physiology*, Vol. 265, (1993), pp. H52-H60.
139. Timoshenko, S.P. and Goodier, J.N., *Theory of Elasticity* (3rd edition; New York: McGraw-Hill, Inc., 1970).
140. Curnier, A., He, Q.-C., and Zysset, P., "Conewise Linear Elastic Materials," *Journal of Elasticity*, Vol. 37, (1995), pp. 1-38.
141. Beer, F.R. and Johnston, E.R., *Mechanics of materials* (2nd edition; New York: McGraw-Hill, Inc., 1992).
142. Taylor, P.M., Allen, S.P., and Yacoub, M.H., "Phenotypic and functional characterization of interstitial cells from human heart valves, pericardium and skin," *J Heart Valve Dis*, Vol. 9, No. 1. (2000), pp. 150-158.
143. Taylor, P.M., Allen, S.P., Dreger, S.A., *et al.*, "Human cardiac valve interstitial cells in collagen sponge: a biological three-dimensional matrix for tissue engineering," *J Heart Valve Dis*, Vol. 11, No. 3. (2002), pp. 298-306; discussion 306-297.

144. Cimini, M., Rogers, K.A., and Boughner, D.R., "Aortic valve interstitial cells: an evaluation of cell viability and cell phenotype over time," *J Heart Valve Dis*, Vol. 11, No. 6. (2002), pp. 881-887.
145. Young, W.C., *Roark's formulas for stress and strain* (6th edition; New York: McGraw-Hill Book Company, 1989).
146. Lenth, R.V., "Some practical guidelines for effective sample-size determination," *The American Statistician*, Vol. 55, (2001), pp. 187-193.
147. Clarke, G.M., *Statistics and experimental design* (New York: John Wiley & Sons Inc., 1994).
148. Hogg, R.V. and Johannes, L., *Applied Statistics for Engineers and Physical Scientists* (2 edition; New York: Macmillan Publishing Company, 1992).
149. Ott, R.L., *An Introduction to Statistical Methods and Data Analysis* (5th edition; Pacific Grove: Duxbury, 2001).
150. Smith, D.B., Sacks, M.S., Vorp, D.A., *et al.*, "Surface geometric analysis of anatomic structures using biquintic finite element interpolation," *Ann Biomed Eng*, Vol. 28, No. 6. (2000), pp. 598-611.
151. Calladine, C.R., *Theory of shell structures* (Cambridge: Cambridge University Press, 1983).
152. Butler, D.L., Goldstein, S., and Guilak, F., "Functional Tissue Engineering: The role of biomechanics," *Journal of Biomechanical Engineering*, Vol. 122, (2000), pp. 570-575.
153. Sugimoto, H., *Effects of leaflet stiffness on the dynamic motion of the aortic heart valve*, in *Bioengineering*. 2003, University of Pittsburgh: Pittsburgh. p. 113.
154. Mayne, A.S., Christie, G.W., Smaill, B.H., *et al.*, "An assessment of the mechanical properties of leaflets from four second-generation porcine bioprostheses with biaxial testing techniques," *J Thorac Cardiovasc Surg*, Vol. 98, No. 2. (1989), pp. 170-180.
155. Sun, W., *Biomechanical simulations of heart valve biomechanics*, in *Bioengineering*. 2003, University of Pittsburgh: Pittsburgh. p. 201.
156. Slaughter, W.S., *The Linearized Theory of Elasticity* (1 edition; Boston: Birkhauser, 2001).
157. Levy, R.J., Vyavahare, N., Ogle, M., *et al.*, "Inhibition of cusp and aortic wall calcification in ethanol- and aluminum-treated bioprosthetic heart valves in sheep:

- background, mechanisms, and synergism," *J Heart Valve Dis*, Vol. 12, No. 2. (2003), pp. 209-216; discussion 216.
158. Lovekamp, J. and Vyavahare, N., "Periodate-mediated glycosaminoglycan stabilization in bioprosthetic heart valves," *J Biomed Mater Res*, Vol. 56, No. 4. (2001), pp. 478-486.
159. Schoen, F. and Levy, R., "Tissue heart valves: Current challenges and future research perspectives," *Journal of Biomedical Materials Research*, Vol. 47, (1999), pp. 439-465.
160. 7th World biomaterialscongress, "Active contractile properties of aortic valve leaflets under flexure", by Merryman, W. and Sacks, M., 2004.
161. Satta, J., Melkko, J., Pollanen, R., *et al.*, "Progression of human aortic valve stenosis is associated with tenascin-C expression," *J Am Coll Cardiol*, Vol. 39, No. 1. (2002), pp. 96-101.
162. Jian, B., Jones, P.L., Li, Q., *et al.*, "Matrix metalloproteinase-2 is associated with tenascin-C in calcific aortic stenosis," *Am J Pathol*, Vol. 159, No. 1. (2001), pp. 321-327.
163. Vyavahare, N., Jones, P.L., Tallapragada, S., *et al.*, "Inhibition of matrix metalloproteinase activity attenuates tenascin-C production and calcification of implanted purified elastin in rats," *Am J Pathol*, Vol. 157, No. 3. (2000), pp. 885-893.
164. Asanuma, K., Magid, R., Johnson, C., *et al.*, "Uniaxial strain upregulates matrix-degrading enzymes produced by human vascular smooth muscle cells," *Am J Physiol Heart Circ Physiol*, Vol. 284, No. 5. (2003), pp. H1778-1784.
165. Yamaguchi, S., Yamaguchi, M., Yatsuyanagi, E., *et al.*, "Cyclic strain stimulates early growth response gene product 1-mediated expression of membrane type 1 matrix metalloproteinase in endothelium," *Lab Invest*, Vol. 82, No. 7. (2002), pp. 949-956.
166. Seliktar, D., Nerem, R.M., and Galis, Z.S., "The role of matrix metalloproteinase-2 in the remodeling of cell-seeded vascular constructs subjected to cyclic strain," *Ann Biomed Eng*, Vol. 29, No. 11. (2001), pp. 923-934.
167. Seliktar, D., Nerem, R.M., and Galis, Z.S., "Mechanical strain-stimulated remodeling of tissue-engineered blood vessel constructs," *Tissue Eng*, Vol. 9, No. 4. (2003), pp. 657-666.
168. Dreger, S.A., Taylor, P.M., Allen, S.P., *et al.*, "Profile and localization of matrix metalloproteinases (MMPs) and their tissue inhibitors (TIMPs) in human heart valves," *J Heart Valve Dis*, Vol. 11, No. 6. (2002), pp. 875-880; discussion 880.

169. Solan, A., Mitchell, S., Moses, M., *et al.*, "Effect of pulse rate on collagen deposition in the tissue-engineered blood vessel," *Tissue Eng*, Vol. 9, No. 4. (2003), pp. 579-586.
170. ABAQUS, ABAQUS/Standard User's Manual, Version 6.3. (Hibbitt, Karlsson & Sorensen, Inc., 2002).
171. Timoshenko, S. and Gere, J., *Mechanics of Materials* (New York: D. Van Nostrand, 1972).
172. Fung, Y.C., *Foundations of Solid Mechanics* (Englewood Cliffs: Prentice-Hall, 1965).